Structure−Performance Relationships of Copper and Post−Transition Metals in Electrochemical CO₂ Reduction

Structure−Performance Relationships of Copper and Post−Transition Metals in Electrochemical CO$_2$ Reduction

Structuur-activiteitsrelaties van Koper en Laat-overgangsmetalen in de Elektrochemische Reductie van Koolstofdioxide

(met een samenvatting in het Nederlands)

Proefschrift

ter verkrijging van de graad van doctor aan de
Universiteit Utrecht
op gezag van de
rector magnificus, prof.dr. H.R.B.M. Kummeling,
ingevolge het besluit van het college voor promoties
in het openbaar te verdedigen op

maandag 8 januari 2024 des middags te 12.15 uur

door

Shuang Yang

geboren op 22 oktober 1993
te Guizhou, China

Promotor:

  Prof. dr. ir. B.M. Weckhuysen

Copromotor:

  Dr. W. van der Stam

Beoordelingscommissie:

  Prof. dr. P.C.A. Bruijnincx
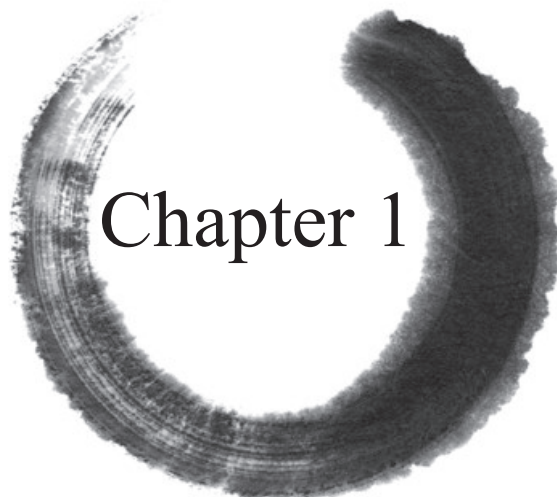 Prof. dr. M.T.M. Koper
  Prof. dr. G.J. Kramer
  Prof. dr. A. Meijerink
  Prof. dr. B. Roldán Cuenya

Table of Contents

Chapter 1

General Introduction

Abstract

As fossil resources are used worldwide to produce chemicals, materials, and fuels, carbon dioxide (CO_2) continues to build up in the atmosphere, leading to concerns about the environment and climate change. One solution is to convert CO_2 into valuable chemicals through electrochemical CO_2 reduction reactions (eCO$_2$RR), which can store renewable electricity and produce base chemicals, such as carbon monoxide, formate, methane, ethylene, and ethanol. However, due to the complicated reaction pathways and sluggish reaction kinetics of eCO$_2$RR, the selectivity and activity of most catalysts remain low, along with limited stability. Therefore, the selection and design of electrocatalysts with high selectivity, activity, and stability are critical for the practical application of eCO$_2$RR. The composition of electrode materials is a significant factor in determining product selectivity. Based on the main products, metal electrocatalysts can be divided into four groups: CO−active metal (*e.g.,* silver, gold, and zinc), hydrocarbons−active metal (*i.e.,* copper), formate−active metal (*e.g.,* indium, tin, lead, and bismuth) and hydrogen−active metal (*e.g.,* iron, nickel, and platinum). Among them, as the unique candidate to produce C_{2+} products, copper unfortunately still suffers from low product selectivities and high hydrogen production. In contrast, post−transition metals (*e.g.,* lead, tin, and bismuth) exhibit high selectivity towards formate and strongly suppress the hydrogen evolution reaction. In this PhD Thesis, copper and post−transition metals are combined to catalyze the eCO$_2$RR to approach high catalytic selectivity, activity, and stability. Meanwhile, the structure−performance relationships of the monometallic and bimetallic copper/post−transition metals are studied through multiscale characterization. The first half of the Chapter introduces the basic theory, current progress, and challenges of eCO$_2$RR research. The second half of the Chapter will discuss the development and obstacles of copper and post−transition metals catalyzing eCO$_2$RR. The Chapter closes with a discussion on the state−of−the−art *in situ* characterization techniques and an outline of this PhD Thesis.

1.1 Motivations and Challenges

The industrial revolution led to a significant expansion in the utilization of fossil resources, and in almost chronological order coal, crude oil, and natural gas, thereby accelerating global economic growth and at the same time resulting in anthropogenic carbon dioxide (CO_2) emissions, which bring negative consequences for the environment, resources, and climate.[1] Carbon sequestration, carbon recycling, and decarbonization are recognized as the three principal categories of strategies that can reduce net CO_2 emissions. Among these, carbon recycling, which is based on converting CO_2 into fuels and value−added chemicals, is one of the most promising ways to mitigate the negative effects of the current fossil fuel−based energy system and facilitate the energy system transition to a more sustainable form. CO_2 recycling can be approached through diverse ways, including (a) biochemical transformation or enzymatic catalysis;[2–5] (b) electrochemical or photochemical reduction;[6–9] (c) radiochemical conversion;[10] and (d) thermochemical reactions.[11–14] However, the chemical stability of the linear CO_2 molecule requires high energy barriers for the dissociation of the C=O bond.[15] Among the various CO_2 conversion strategies, thermally driven processes have received the most extensive research in the past decades.[16] In these processes, hydrogen (H_2) is typically the ultimate proton source, which is normally in the form of gas and strongly relies on the traditional hydrogen production industry, *i.e.*, steam methane reforming and coal gasification, which often releases CO_2 at the same time.[17] Moreover, traditional thermal CO_2 hydrogenation often runs at high pressures and temperatures, presenting potential safety risks and requiring additional energy consumption.

The direct electrochemical CO_2 reduction reaction (eCO$_2$RR) using water (H_2O) as the proton source can avoid the dependence on traditional hydrogen production, which is envisioned a sustainable cycle in which CO_2 is converted into based chemicals and fuels (**Figure 1.1**). In addition, it is powered by renewable electricity and is well compatible with the energy storage system of sustainable energies (such as solar, tidal, and wind). Furthermore, the eCO$_2$RR operates under mild and controllable conditions (*i.e.,* room temperature and pressure), making it highly feasible from an engineering and economic standpoint.[18–20] The eCO$_2$RR is considered one of the most feasible CO_2
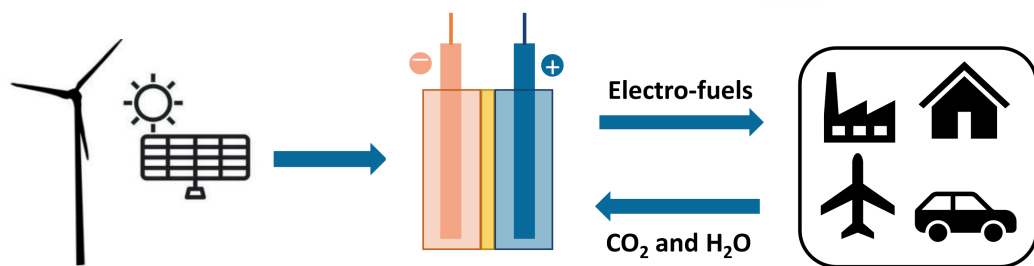

Figure 1.1. The electrochemical CO_2 reduction electrolyzer is integrated with renewable power source and industrial applications. As a result, the emission of CO_2 from industries, transportation, and domestic activities can be converted into value−added chemicals and fuels.

recycling methods. Therefore, a variety of electrocatalysts have been explored over the past decades. However, achieving high product selectivity, activity, and stability in eCO$_2$RR remains challenging, which hinders the practical applications of electrochemical CO$_2$ conversion. Apart from electrocatalysts, development and testing work have been conducted in reactor component design and fundamental reaction mechanisms in eCO$_2$RR. However, despite the advancements that have been achieved, the key problem of low selectivity, activity, and stability is still not resolved because of the lack of highly effective electrocatalysts. Although precious metals, such Au and Ag, have been found to be very selective to certain products with prolonged stability, the scarcity and high cost present practical difficulties to their application.[21–23] To date, substantial efforts have been directed toward developing more cost−effective catalysts.

The rational design of advanced electrocatalysts often requires a comprehensive understanding of how catalysts work in actual catalysis conditions.[24] To this end, the application and development of multiscale *in situ* characterization are crucial due to their ability to identify active reaction sites and reaction pathways. Combined with product analysis techniques, such as Gas Chromatography /Mass Spectrometry (GC/MS), one can build valuable structure−performance relationships for certain types of electrocatalysts, which can guide the design and fabrication of electrocatalyst materials with high catalytic efficiency.

1.2 Fundamentals of eCO$_2$RR

1.2.1 Electrochemical Cell Components

The eCO$_2$RR generally occurs at the interface between electrode/electrocatalyst, which strongly depends on the materials of electrode, electrolyte, and the electrochemical cell configurations. Various cell designs have been used to study the electrochemical behavior of eCO$_2$RR. Most of the material research on eCO$_2$RR has been carried out using an H−cell (**Figure 1.2a**), especially for
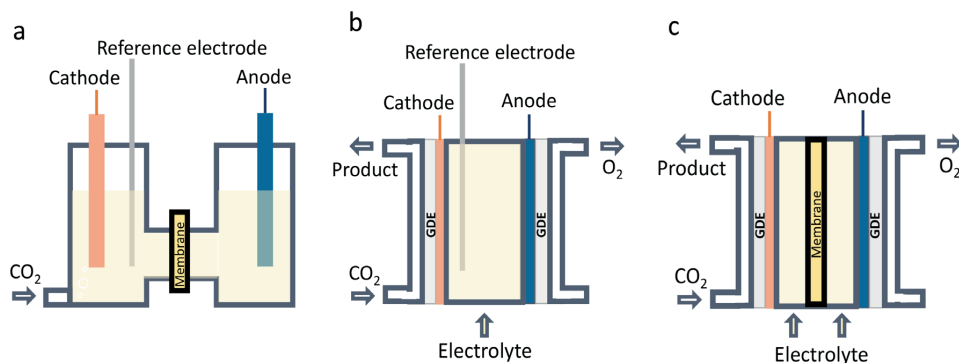

Figure 1.2. Schematic illustration of designs of H−cell (a), microfluidic cell (b), and continuous flow cell (c).

fundamental studies, such as catalyst−electrolyte interactions, reaction conditions and eCO$_2$RR efficiency and product distribution.[25] In a typical H−cell with a three−electrode configuration, the working electrode (cathode) and reference electrode are located in the cathode chamber, whereas the counter electrode (anode) is located in the anode chamber. A cation−exchange or anion−exchange polymer membrane separates the cathode and anode. As a result of this design, cathodic products cannot be transported to the anode.

A reference electrode is often needed to evaluate the cathodic potential of the working electrode in practical electrocatalysis. It is critical to correctly design and locate the reference electrode to accurately measure the cathodic potential versus (vs.) the reference electrode. The most commonly known reference electrodes include standard hydrogen electrode (SHE), reversible hydrogen electrode (RHE), Ag/AgCl electrode, and Hg/Hg$_2$Cl$_2$ electrode. The conversion of potential vs. SHE and RHE can be obtained by using Equation 1.1:

$$E \text{ (vs. RHE)} = E^0 \text{ (vs. SHE)} + 0.059 \times pH \tag{1.1}$$

In practical circumstances, Ag/AgCl and Hg/Hg$_2$Cl$_2$ electrodes are often used for experimental potential determination, whose potentials are known and chemically stable with saturated electrolytes. They are widely used to experimentally determine potentials vs. RHE (see more details in Method Section in each Chapter).

One of the key problems of the H−type cell is mass transfer limitation owing to the low solubility of CO$_2$ and low reactant concentration on the surface of the electrode/electrocatalyst, especially for long−term operation and under high cathodic potentials and currents. Therefore, increasing attention has moved to porous catalyst layers and Gas Diffusion Electrodes (GDE), which not only increase the electrochemical active surface area but also allow for CO$_2$ supply in the form of gas and consequently eliminate the solubility restriction to the eCO$_2$RR.

Based on the design of GDE, microfluidic cells, and continuous flow cells have been developed to obtain better catalytic activity and stability. A microfluidic cell typically contains a microlayer of liquid electrolyte and gaseous CO$_2$ injected from the backside of the electrode.[26] Membrane free is the main feature of a microfluidic reactor (**Figure 1.2b**), where a thin spacer (<1 mm) is used to separate the anode and cathode instead of a membrane, allowing liquid electrolyte to flow through. To realize a better practical performance of CO$_2$ reduction, a continuous flow electrolyzer (**Figure 1.2c**) has been developed. A cathode and an anode with an electrolyte layer in between are separated by a membrane, often with forced convection.[27] The use of a membrane has a similar function as within an H−cell of preventing product crossover. The most employed membranes in recent eCO$_2$RR research are ion−exchange membranes, including cation−exchange membranes, anion−exchange membranes, and bipolar membranes.[32] They are chosen due to their ability to allow certain ions to pass through and block other ions or neutral molecules. The proton exchange membrane (*i.e.,* Nafion 117), which allows for the passage of the proton and blocks the anions, was used for all studies in this Thesis. In a continuous flow cell, the CO$_2$ and catholyte are supplied to the cathode in the gas and liquid phase, respectively, while the anode is fed with an anolyte that can be different in

composition from the catholyte if needed.

Both aqueous and non−aqueous electrolytes are developed and used in eCO$_2$RR investigation.[28] This Thesis will only discuss aqueous media since non−aqueous media was not used in all work involved. The eCO$_2$RR has primarily been studied using weakly alkaline or acidic CO$_2$−saturated aqueous electrolytes containing Na$^+$ or K$^+$ alkali metal cations and HCO$_3^-$, SO$_4^{2-}$, or Cl$^-$ anions. Cations can affect relative concentrations of charged species (such as radical anion intermediates) close to electrodes, which further influence current density and product selectivity.[29] Anions including HCO$_3^-$, SO$_4^{2-}$, H$_2$PO$_4^{4-}$, ClO$_4^-$, and Cl$^-$ play a crucial role in the local pH on the surface of the electrode and, consequently, the product selectivity.[30] Generally, bicarbonate solutions are commonly used for eCO$_2$RR due to their good buffering capability and proton donation ability. The dissolved CO$_2$ exists in equilibrium with bicarbonate between a bulk pH range of 6 and 8.[31] In studies involved in this Thesis, KHCO$_3$ solution was used as the electrolyte.

1.2.2 From CO$_2$ to Value−Added Products

In an electrochemical system, reduction reactions occur at the cathode and oxidation reactions occur at the anode (**Figure 1.3**). In the case of an aqueous electrolyte, both the eCO$_2$RR (Equation 1.2) and the hydrogen evolution reaction (HER, Equation 1.3) can occur at the cathode. However, the eCO$_2$RR is often in competition with HER because of the similarity of their standard reduction potential $E°$ (**Table 1.1**, $E°_{HER} = -0.42$ V vs. SHE, pH = 7).

$$xCO_2 + nH^+ + ne^- \rightarrow product + yH_2O \tag{1.2}$$

$$2H^+ + 2e^- \rightarrow H_2 \tag{1.3}$$

On the anode side of a general electrochemical system, the anodic reaction is typically oxygen
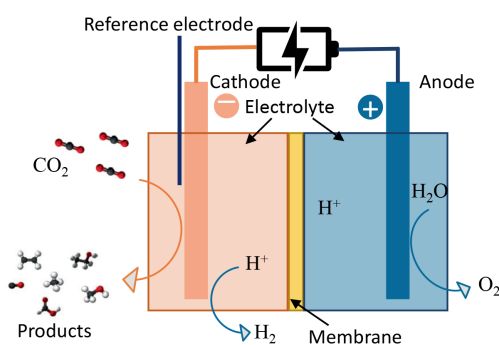

Figure 1.3. Representative scheme of an eCO$_2$RR electrolyzer in a three−electrode configuration, containing a working electrode (cathode), a counter electrode (anode), a reference electrode, a membrane and electrolyte. The CO$_2$ is converted at the cathode into possible products, competing with the hydrogen evolution reaction. Oxygen evolution reaction (OER) will happen at the anode to balance the total transferred charges.

evolution reaction (OER, Equation 1.4, $E°_{OER} = 0.81$ V vs. SHE, pH = 7) with proton formation and transfer to the cathode to balance the overall reaction, along with electron transfer.

$$2H_2O \rightarrow O_2 + 4H^+ + 4e^- \tag{1.4}$$

In practical eCO_2RR systems, the total cell voltage is a combination of anodic and cathodic potentials, and the rate of OER must also be optimized to ensure efficient eCO_2RR. In addition, the potential required to drive the reaction is typically greater than the thermodynamic potential (**Table 1.1**).

Various parameters are used to evaluate the performance of an electrocatalyst in eCO_2RR, including partial current density, overpotential, onset potential, Faradaic Efficiency (FE) and stability. Partial current density is the current density that effectively drives the formation of the desired product, which is influenced by both the intrinsic activity of the electrocatalyst and the experimental conditions. Overpotential refers to the difference between the theoretical reduction potential and the actual electrode reduction potential, while onset potential is the potential at which the target product

Table 1.1. Electrochemical potentials of possible processes at the cathode during eCO_2RR in aqueous solutions for different products.

Possible half–reactions at the cathode	$E°$ (V vs. SHE) at pH 7
$CO_2\ (g) + e^- \rightarrow CO_2^{*-}$	−1.90
$2H^+ + 2e^- \rightarrow H_2\ (g)$	−0.42
$CO_2\ (g) + 2H^+ + 2e^- \rightarrow HCOOH\ (l)$	−0.61
$CO_2\ (g) + H_2O\ (l) + 2e^- \rightarrow HCOO^-\ (aq) + OH^-$	−0.43
$CO_2\ (g) + 2H^+ + 2e^- \rightarrow CO\ (g) + H_2O\ (l)$	−0.53
$CO_2\ (g) + H_2O + 2e^- \rightarrow CO\ (g) + 2OH^-$	−0.52
$2CO_2\ (g) + 2H^+ + 2e^- \rightarrow H_2C_2O_4\ (l)$	−0.91
$2CO_2\ (g) + 2e^- \rightarrow C_2O_2^-\ (aq)$	−1.00
$CO_2\ (g) + 4H^+ + 4e^- \rightarrow C\ (s) + 2H_2O\ (l)$	−0.20
$CO_2\ (g) + 2H_2O\ (l) + 4e^- \rightarrow C\ (s) + 4OH^-$	−1.04
$CO_2\ (g) + 4H^+ + 2e^- \rightarrow HCHO\ (l) + H_2O\ (l)$	−0.48
$CO_2\ (g) + 3H_2O + 4e^- \rightarrow HCHO\ (l) + 4OH^-$	−0.89
$CO_2\ (g) + 6H^+\ (l) + 6e^- \rightarrow CH_3OH\ (l) + H_2O\ (l)$	−0.38
$CO_2\ (g) + 5H_2O\ (l) + 6e^- \rightarrow CH_3OH\ (l) + 6OH^-$	−0.81
$CO_2\ (g) + 8H^+ + 8e^- \rightarrow CH_4\ (g) + 2H_2O\ (l)$	−0.24
$CO_2\ (g) + 6H_2O\ (l) + 8e^- \rightarrow CH_4\ (g) + 8OH^-$	−0.25
$2CO_2\ (g) + 12H^+ + 12e^- \rightarrow C_2H_4\ (g) + 4H_2O\ (l)$	0.06
$2CO_2\ (g) + 8H_2O\ (l) + 12e^- \rightarrow C_2H_4\ (g) + 12OH^-$	−0.34
$2CO_2\ (g) + 12H^+ + 12e^- \rightarrow CH_3CH_2OH\ (l) + 3H_2O\ (l)$	0.08
$2CO_2\ (g) + 9H_2O\ (l) + 12e^- \rightarrow CH_3CH_2OH\ (l) + 12OH^-$	−0.33
$2CO_2\ (g) + 14H^+ + 14e^- \rightarrow C_2H_6\ (g) + 4H_2O\ (l)$	−0.27
$3CO_2\ (g) + 18H^+ + 18e^- \rightarrow C_3H_7OH\ (l) + H_2O\ (l)$	−0.31

is first detected. A lower overpotential or onset potential indicates that the electrocatalyst can more easily initiate eCO$_2$RR. FE is a metric that expresses the percentage of charges transferred to the target product compared to the total charges passed during the reaction, representing product selectivities. It can be calculated using Equation 1.5:

$$FE = \alpha nF/Q \times 100\%$$ (1.5)

Where n represents the number of electrons transferred, α is the number of moles for a given product, F is Faraday's constant (96485 C mol^{-1}), and Q is the total charge passed during electrolysis. Stability is the capacity of an electrocatalyst to maintain its activity and selectivity under prolonged operation at constant current or constant potential conditions.

To determine the above−mentioned parameters, electrochemical characterization and product analysis techniques are often combined. In general, a potentiostatic test, also called chronoamperometry (CA), is often applied to evaluate FE of products at certain potentials, in which the potential at the working electrode is held at a constant level for a given period of time. This technique can determine onset potential and overpotential through varying applied potentials. Sometimes, chronopotentiometry (CP) is employed to study chemical reaction mechanisms and kinetics, in which the current at the working electrode is held at a constant level for a given period, and dynamic potentials are measured. Cyclic voltammetry (CV) is usually used to study the redox property of catalysts within a defined potential window. The non−Faradaic region in the CV curves reflects the behavior of the double layer, which consists of the charged electrode and a layer of charged ions that are physically adsorbed on the surface of the electrode. The built−up double layer capacitance (C_{dl}) can be used to determine the electrochemical active surface area (ECSA), according to Equation 1.6:

$$ECSA = (I_c / v) / C_s \times S$$ (1.6)

Where I_c is the charging current determined by the current difference between positive and negative scans in the non−Faradaic region, v is the scan rate (V s^{-1}) of the CV measurement. During the CV scans, the I_c is linear with the scan rate v, and the slope of the line is equal to the C_{dl}. C_s and S are the double layer capacitance and geometric surface area of the reference materials, respectively.

1.2.3 Reaction Pathways

The eCO$_2$RR encounters challenges such as the activation of CO$_2$ and multiple single−step reactions. Moreover, the involvement of proton donors in the reaction, either directly or through proton−coupled electron transfer steps, further complicates the eCO$_2$RR process (**Figure 1.4**). As a result, a wide range of possible products may be obtained depending on the number of electrons and protons involved. In the case of aqueous electrolytes, all possible half−reactions for eCO$_2$RR are listed in **Table 1.1**. The Gibbs free energy ΔG of the reaction can be calculated based on Equation 1.7:

$$\Delta G = -nFE°$$ (1.7)

Redox reactions with a more positive $E°$ are thermodynamically more favorable, where n refers to the number of electrons transferred during a redox reaction and F represents the Faraday constant. Based

on this, CO_2 reductions toward hydrocarbons or alcohol products should have better thermodynamics than CO, HCOOH, HCHO, and H_2. However, since CO_2 reduction also kinetically depends on the concentration of protons and other factors such as electrolyte composition and electrode property, in practical experiments, these reactions often occur at larger onset potentials.

In **Figure 1.4**, all the complicated reaction pathways are classified into four routes according to different products.[33] Initially, CO_2 is dissolved in the solution, resulting in the first electron transfer to form aqueous $*CO_2{}^-$. This CO_2 activation process follows solvation and equilibration of the electrocatalytic surface. To do this, CO_2 is often adsorbed on the surface of the catalyst in the form of $*CO_2{}^-$. Two other possible intermediates of $*COOH$ and $*OCHO$ can also be formed during the CO_2 activation for further reactivity.[34] Four redox reactions (Equations 1.8−1.11) have been considered to be related to the CO_2 activation:

$$* + CO_2 + H^+ + e^- \rightarrow {}^*COOH \qquad (1.8)$$

$$* + CO_2 + H^+ + e^- \rightarrow {}^*OCHO \qquad (1.9)$$

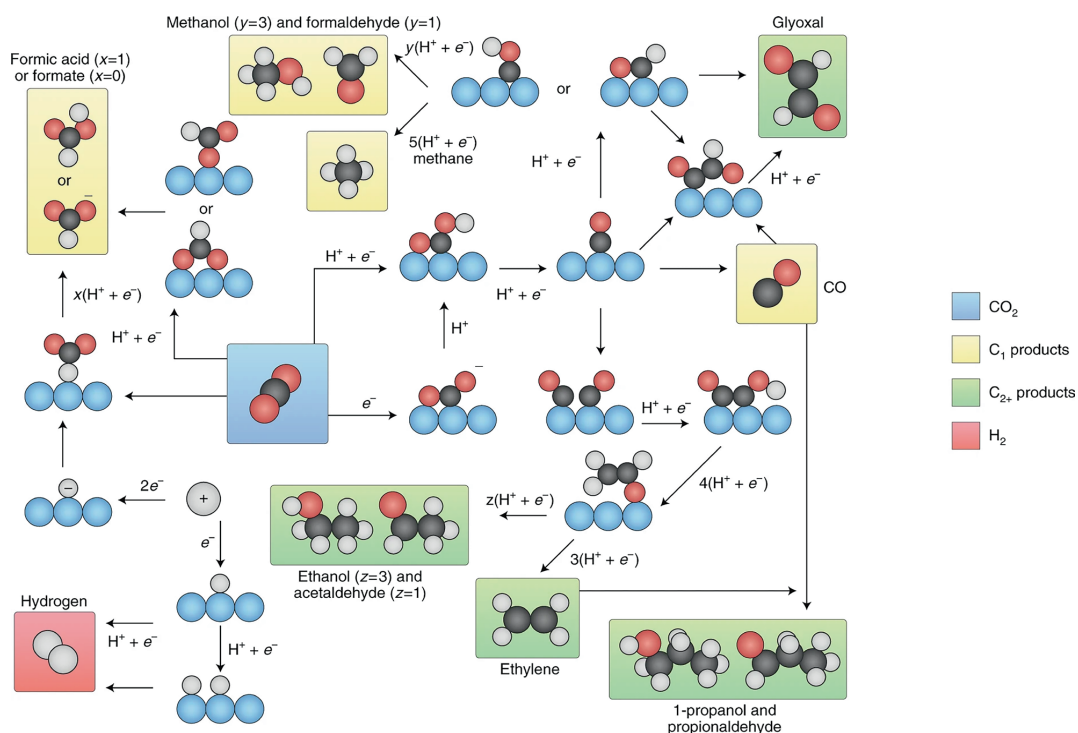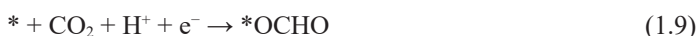$$* + CO_2 + e^- \rightarrow {}^*CO_2{}^- \qquad (1.10)$$

Figure 1.4. The possible paths from CO_2 to valuable products. Black sphere, carbon; red sphere, oxygen; white spheres, hydrogen; blue spheres, metal catalysts. The arrows represent whether proton, electron, or concerted proton–electron transfer (CPET) take place. Reproduced from *Ref. 33*.

$$* + H^+ + 2e^- \rightarrow *H^-$$ (1.11)

Equations 1.8 and 1.9 are thought to be the concerted proton–electron transfer (CPET) reactions, which have been considered to determine the selectivity among (post−)transition metal surfaces. [35] After adsorption, these two intermediates are reduced to formic acid and CO. It has been reported that *COOH is likely the intermediate for CO formation, and *OCHO is more likely responsible for formic acid production.[36] This calculated prediction has been in agreement with experimental results, that post−transition metals prefer to bind CO_2 via oxygen and are selective towards formic acid, whereas transition−metal electrodes, such as Ag and Au, prefer to bind via carbon and are selective for CO formation. The intermediate *COOH would be further converted into *CO, which has been proposed to be the key intermediate for the more complicated reductions. If the formed *CO is adsorbed long enough, prominently on Cu, it can trigger a series of proton and electron transfers through a *COH or *CHO intermediate, which leads to more C_1 products, such as methanol, methane, or glyoxal. At the same time, *CO dimerization occurs, resulting in C−C bond formation, after which a wide range of products can be produced.[22,37] However, it is challenging to target multi−carbon products, where competing reaction pathways can generate many chemically similar bounded intermediates. Understanding these pathways and electrode materials design must be unified to achieve selectivity that approaches unity.

1.2.4 Electrode Materials

1.2.4.1 Electrode Composition

Since the reaction kinetics of the anode also determine the reaction efficiency of the total cell, an anode with high conversion efficiency is favored. Traditional OER anodes are generally made by precious metal−based catalysts, such as Pt, IrO_2 and RuO_2. Nevertheless, as practical applications dictate, these noble catalysts are expected to be replaced by more cost−effective anode catalysts in the future, such as manganese, cobalt, and nickel−based materials.[39]

In the other half−cell, the cathode catalyzes CO_2 to value−added products. Catalysts that can activate the C=O double bond and overcome the energy barrier of CO_2 reduction are crucial for the process. [40] The distribution of products obtained through the eCO_2RR process depends on various factors, including the physical characteristics and form of the material used as the cathode, the electrolyte, and the operational conditions (*e.g.,* pressure and temperature).[41] In particular, the intrinsic electronic properties of the cathode surface strongly govern the kinetics and product selectivity of eCO_2RR by affecting the intermediate species binding energies and activation barriers.[20] Given that the HER competes with eCO_2RR, strategies for suppressing HER should also be taken into account when designing electrocatalysts. Numerous efforts to develop cathodic electrocatalysts have been made in the past decades. Most existing electrocatalysts can be divided into three groups: metallic, nonmetallic, and molecular catalysts.[42]

Nonmetallic electrocatalysts, as one of the most investigated electrocatalysts for OER and HER, have also been developed for eCO_2RR during the past decades. However, their conversion efficiency and selectivity in eCO_2RR are not comparable to metallic catalysts because the competing HER
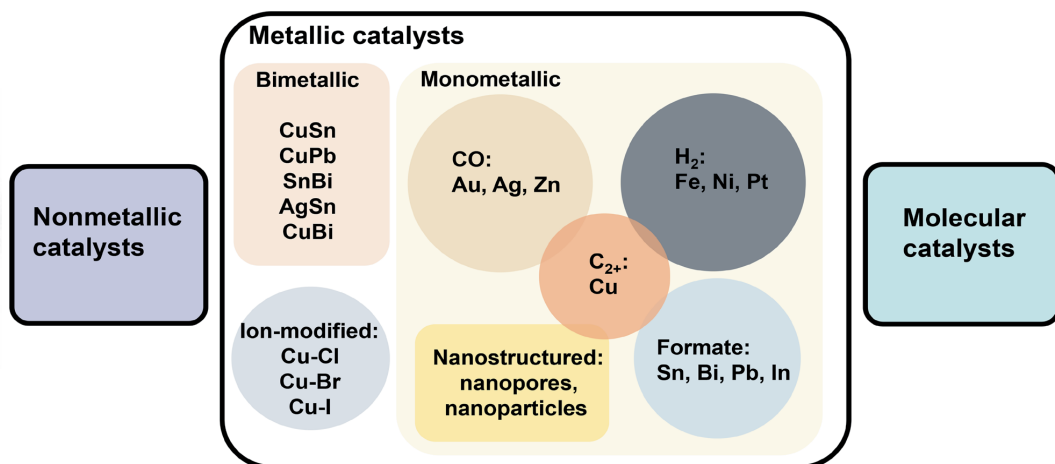
Figure 1.5. An outline of three groups of electrocatalysts for eCO$_2$RR, including nonmetallic catalysts, metallic catalysts, and molecular catalysts. Metallic catalysts can be classified into monometallic electrocatalysts, bimetallic electrocatalysts and ion−modified metal electrocatalysts.

cannot be effectively suppressed. Molecular catalysts have also attracted massive attention in the field of eCO$_2$RR. However, due to the ligand effects, which share similar vibrational modes as many reaction intermediates in eCO$_2$RR, the structure−performance relationship is difficult to be identified using current characterization techniques, such as Raman Spectroscopy, compared to metallic catalysts. In this Thesis, metallic catalysts will be the focus.

Due to their structural simplicity, ease of handling, and robust properties, polycrystalline monometallic catalysts were initially the preferred materials for studies on eCO$_2$RR. A monometallic catalyst can be further classified into four subgroups depending on what it predominantly produces (**Figure 1.5**): CO (*e.g.*, gold, silver, and zinc), formate (*e.g.,* tin (Sn), indium (In), bismuth (Bi) and lead (Pb)), hydrocarbons (copper (Cu)) and H$_2$ (*e.g.,* iron (Fe), nickel (Fe), and platinum (Pt)).[22] Among all these monometallic electrocatalysts, Cu stands out because of its unique capability to reduce CO$_2$ into hydrocarbon fuels with acceptable FEs.[43] However, bulk Cu electrocatalysts often suffer from low selectivity and activity. The use of catalysts beyond bulk monometallics has been demonstrated in recent years as a promising means of reducing CO$_2$, such as nanostructured metals,[44] bimetallics,[45] and ion−modified metals.[46] Therefore, designing electrodes has gained a lot of attention.

1.2.4.2 Electrode Morphology
Apart from the composition of electrode materials, the morphology also plays an important role in the catalytic behavior of electrodes. Understanding how the morphology of an electrode affects the performance of CO$_2$ reduction reactions requires looking at different scales. At the nanoscale level, the surface structure of the electrode includes the surface low coordinated sites (such as steps and

terraces), open facets (normally on single crystal), and grain boundaries (**Figures 1.6a−d**). For example, different low−index facets exposed on the Cu electrode have shown different selectivities in eCO$_2$RR. The simulated identification of active sites of the Cu single crystal found that Cu(111) gives methane, Cu(110) gives acetaldehyde, Cu(100) gives ethylene and the n(100)×(110) step produces ethanol.[47] High−index facets, which constitute terraces and steps with variable orientations, are usually rich in undercoordinated sites. **Figure 1.6e** shows the influence of undercoordinated sites on product distribution. By comparing the ratio of C$_2$H$_4$ to CH$_4$ upon different structures, it was found that the steps can enhance the selectivity of C$_2$H$_4$ over CH$_4$ compared to the planar single crystals.[48] Grain boundaries have also been shown to have boosted activity in eCO$_2$RR, possibly due to the increased stabilization of the CO$_2$ anionic adsorbate (*CO$_2^-$, **Figure 1.4**) and *CO.[49] The activity and selectivity of eCO$_2$RR can

Figure 1.6. Illustration of step (a), terrace (b), open facet (c) and grain boundary (d) in crystalline Cu; The log (C$_2$H$_4$/CH$_4$) is as a function of the crystal orientation with reference of Cu(100) (b), adapted from *Ref. 48*.

also be influenced by the nanostructure and mesostructure of catalysts at the microscale level based on factors such as the number of active sites, the size of the catalyst particles, the distance between the particles, and reactant transport to active sites. For example, the impact of particle size in Au nanoparticles has been revealed that smaller nanoparticles significantly increased the H$_2$/CO ratio in eCO$_2$RR.[50] The influence of morphology will be discussed in detail in the next Section with examples related to this Thesis.
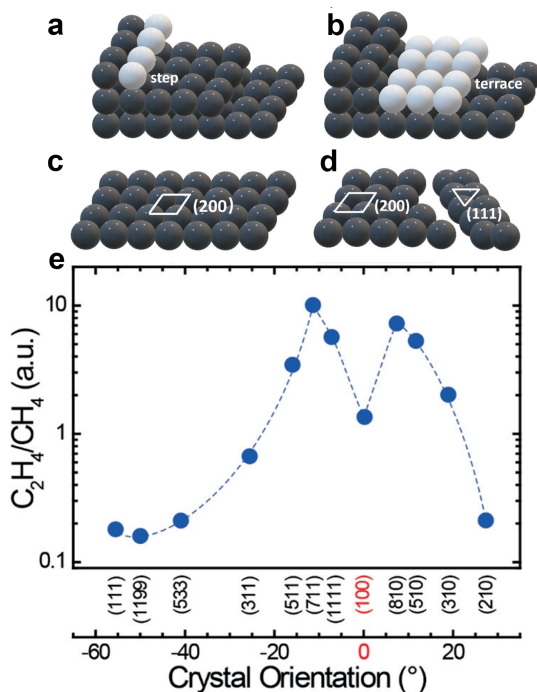
1.3 Metal−Based Electrocatalysts for eCO$_2$RR

1.3.1 Monometallic Catalysts

Early research in this field, which began in the 1980s, focused on bulk metal catalyst activity.[51] Therefore, commonly available, single−element metallic electrodes were first explored in the bulk polycrystalline phase.[20] The main reasons for the difference in selectivity for different metals will be discussed in the following Sections, together with some state−of−the−art examples.

1.3.1.1 Cu

The special property of Cu to catalyze the CO_2 reduction toward hydrocarbons originates from its negative adsorption energy for *CO and positive adsorption of *H (**Figure 1.7a**), distinguishing Cu from the other metals.[52] In contrast, the bonding energy of *CO is found to be relatively weak on Ag, Au, and Zn, leading to the selective formation of CO after *CO desorption. Metals having weak bonding energy of *CO and negligible hydrogen coverage mainly produce formate, such as post−transition metals. Therefore, during the past decades, Cu has received a lot of attention as electrocatalytic material for eCO_2RR. Despite being active in producing hydrocarbons, the overpotential needed is large and the observed product distribution over polycrystalline Cu is yet too diverse (**Figures 1.7b−e**).[48] For instance, on polycrystalline Cu, H_2 dominates at potentials lower than −0.6 V vs. RHE. The onset potential for hydrocarbons is found to be around −0.8 V vs. RHE, which is much larger than their standard reduction potential. [53] Various strategies have been employed to improve the catalytic performance of Cu for CO_2 reduction, including oxide−derived electrodes, selectively exposed facets, nanostructured electrodes, mixed valence states of Cu, and bimetallic or alloy nanocrystals.[54–56]

The oxidized Cu foil (OD−Cu) was reported in 2012 by Li *et al*.[57] They observed that prepared OD−Cu electrode generated a current density per geometric area of the electrode 30 times higher
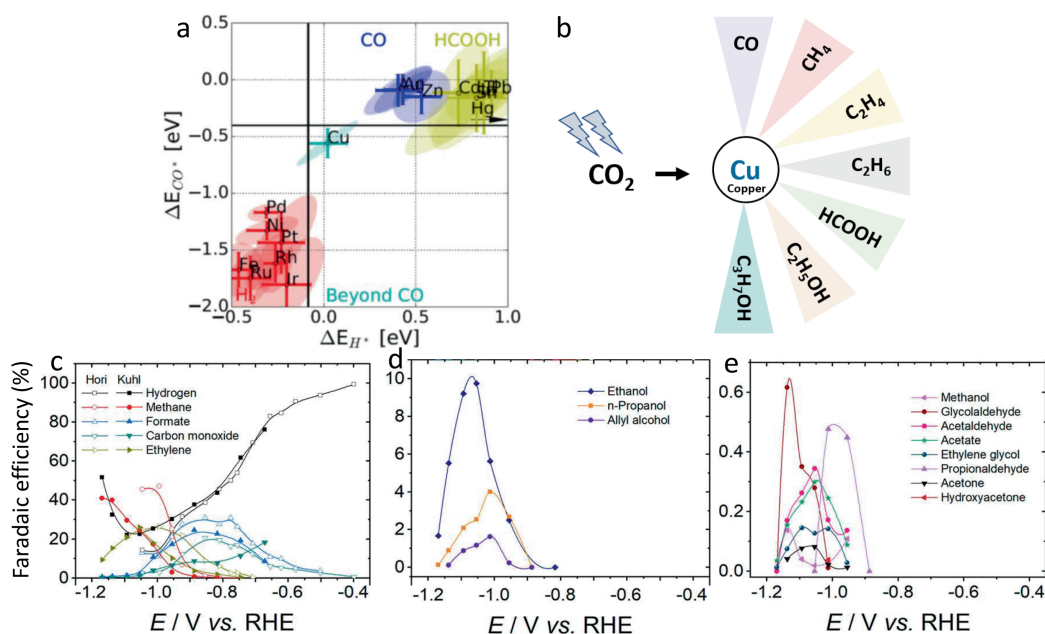

Figure 1.7. The calculated binding energies of the intermediates ΔE_{CO^*} and ΔE_{H^*} of different metal electrodes (a), reproduced from *Ref. 52*. Scheme (b) and Faradaic Efficiencies (FEs, c−e) of different products in electrochemical CO_2 conversion on polycrystalline Cu, adapted from *Ref. 48*.

than that of polycrystalline Cu. CO and formate were found to be the main products on OD−Cu at low overpotentials, achieving a peak FE toward CO and formate of 45.0% at −0.3 V vs. RHE and 38.0% at −0.5 V vs. RHE, respectively. At high overpotentials, the FEs toward CO and formate dropped dramatically, approaching nearly zero at −1.0 V vs. RHE, while the selectivities for hydrocarbon products slowly increased, with ethylene and ethane obtained at < 10.0% FEs. Kanan *et al.* followed this work and identified the active sites to be abundant grain boundaries. Using Transmission Electron Microscopy (TEM)−based automated crystal orientation mapping (**Figure 1.8a**) and temperature−programmed desorption of CO, they found that random, noncoherent grain boundaries have strong CO−binding sites which were believed to be the active sites for C−C coupling (**Figure 1.8b**).[58] However, Feng *et al.* found that the unique role of surface sites associated with grain boundaries
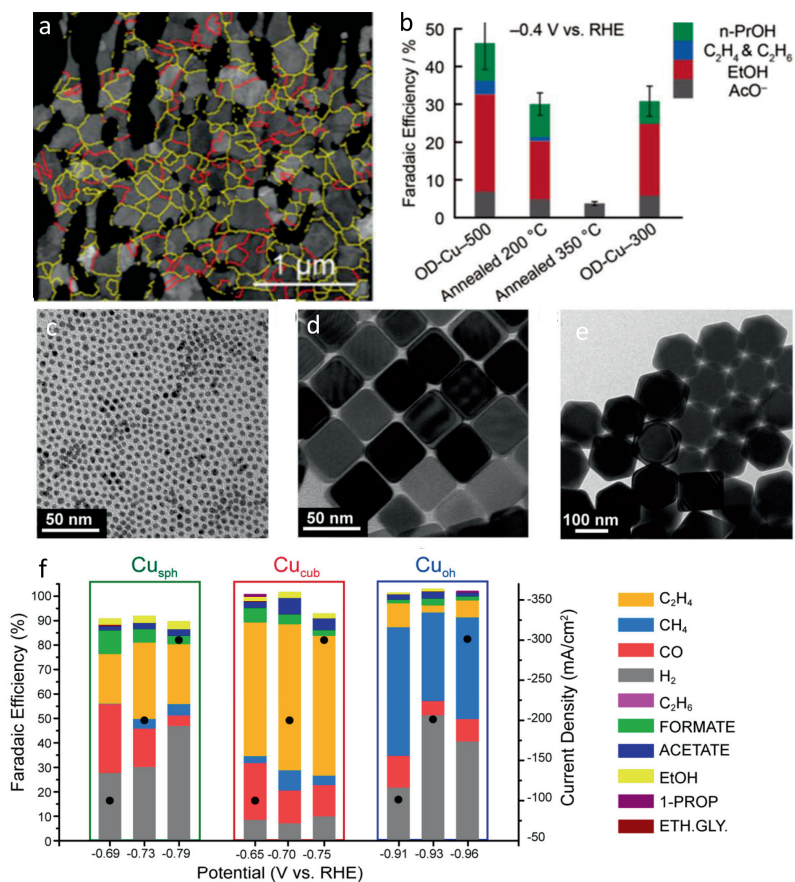

Figure 1.8. Crystal orientation map (a) of the oxidized Cu foil−500 (OD−Cu−500) electrode showing the coherent (red) and random (yellow) grain boundaries (GBs) and comparison of product distribution for the different OD−Cu electrodes (b), reproduced from *Ref. 58.* Transmission Electron Microcopy (TEM) images of the reported Cu$_{sph}$ (c), Cu$_{cub}$ (d), and Cu$_{oh}$ (e), respectively, and their catalytic performances (f) in eCO$_2$RR, reproduced from *Ref 60.*

in the eCO_2RR could also be ascribed to the strain effect through synchrotron−based X−ray Diffraction (XRD), which revealed the presence of microstrain in the grain boundaries−rich Cu nanoparticles.[59] Although this confirms the density of grain boundaries found on the OD−Cu electrodes, it remains unclear whether the observed microstrain could account for the strong binding of *CO observed over Cu−based materials.

As mentioned in Section 1.2.4.2, facet−sensitive selectivity of Cu in the electrochemical CO_2 reduction has been explored in the early study done by Hori.[22] It was revealed that open facets such as (100) and (110), as well as the stepped surfaces with (100) terrace, selectively promote C_{2+} products, whereas (111) and stepped surfaces with (111) terrace prefer the production of CH_4. C_2H_4 was the main product obtained on (100), while oxygenated hydrocarbons such as acetaldehyde, ethanol, and acetic acid dominated on (110). Buonsanti *et al.* reported facet−dependent selectivity of Cu nanocrystals (**Figures 1.8c−d**).[60] It was observed that the Cu_{cub} nanocrystals were highly selective toward C_2H_4, Cu_{oh} nanocrystals were selective toward CH_4, and Cu_{sph} nanocrystals were not selective toward any specific product (**Figure 1.8f**). Despite the evidence for the open facets being active and selective for CO_2 reduction, it is much less straightforward to correlate the electrocatalytic performances of nanostructured Cu catalysts to their surface structures. The single crystals often behave differently from nanocatalysts because the latter is usually abundant with undercoordinated surface sites, such as corners, edges, steps, and defects, which do not only give rise to distinct catalytic performance from the corresponding single crystal facets but also complicate surface characterization.[61] Recently, the Roldan Cuenya group reported an almost inert catalytic eCO_2RR performance on Cu single crystal surfaces that are clean, flat, and atomically ordered, whereas defective and higher index surfaces showed the generation of hydrocarbons.[62] This again emphasizes the importance of electrode surface morphology and structure in eCO_2RR.

Additionally, Cu catalysts can improve electrochemical performance in eCO_2RR by creating mixed valence states between Cu^0 and Cu^+ species. Using an oxygen plasma treatment, Roldan Cuenya and co−workers pre−oxidized Cu foil surfaces and *in situ* reduced them to Cu.[63] These experiments resulted in increased selectivity of C_2H_4, which was measured to be a FE of 60.0% at −0.9 V vs. RHE. The study demonstrated that Cu^+ species could exist stable under eCO_2RR conditions, which were more prone to interact with *CO intermediates during hydrogenation reactions and, therefore, directed the reduction pathway to C_2H_4.[64–65]

Nanostructured catalysts have been reported to have different catalytic behavior from their bulk counterparts. More increased active specific surface areas in nanostructured catalysts can provide more active sites and expose a large portion of edge or low−coordinated sites. For example, Yang *et al.* reported that greater hydrocarbon selectivity and activity were observed on Cu nanowires compared to bulk Cu.[66] Nam *et al.* reported that Cu mesopore electrodes fabricated by a sputtering method could improve the FE of C_2H_4 from 8.0% to 38.0% as the pore width was narrowed from 300 nm to 30 nm, whereas the FE of CH_4 and CO decreased by 28.0%. With the same pore width of 30 nm, when the pore depth size increased from 40 nm to 70 nm, saturated hydrocarbon (C_2H_6) became the major product (**Figures 1.9a−d**).[67] Systematical work was done by Strasser and co−workers on

the size effect in electrocatalytic CO_2 reduction over Cu nanoparticles (**Figure 1.9e**).[56] It was found that the particle size ranging from 5 nm to 10 nm can dramatically increase the overall catalytic activity of CO_2 reduction, with boosted selectivity for CO and H_2 production, whereas particle sizes
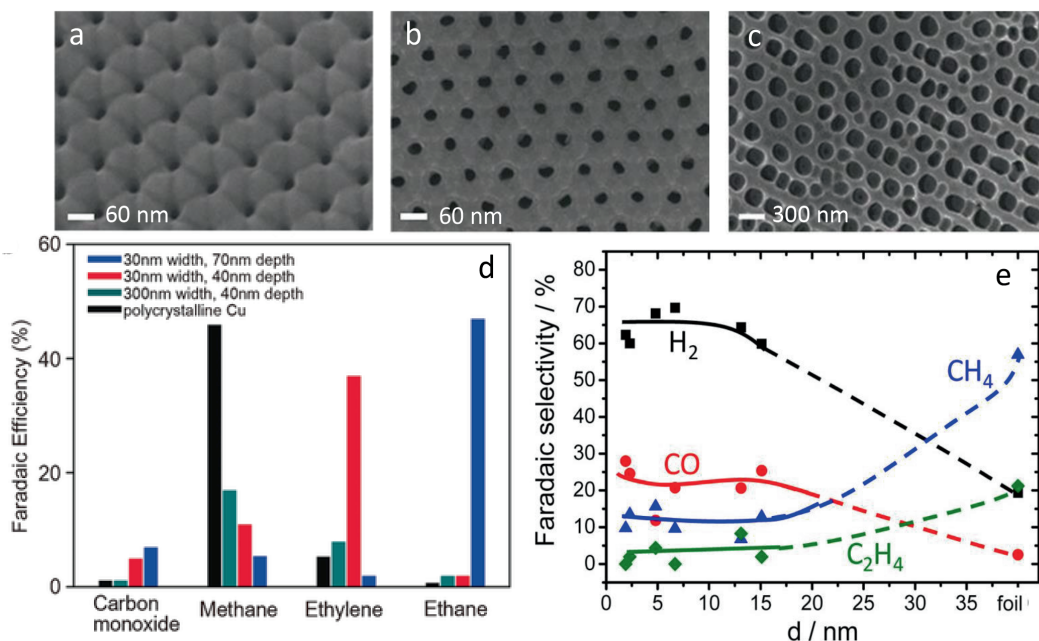
Figure 1.9. Scanning Electron Microscopy (SEM) images of Cu mesopores with 30 nm width/40 nm depth (a), 30 nm width/70 nm depth (b), and 300 nm width/40 nm depth (c). Comparison of Faradaic Efficiencies (FEs) (d) in Cu catalysts with different pore sizes and Cu foil, reproduced from *Ref. 67.* The FEs of reaction products during the CO_2 electroreduction on Cu NPs with different sizes (e), reproduced from *Ref. 56.*

over 15 nm showed an increased selectivity toward hydrocarbon formation.

Alloying or doping different atoms is one of the most promising ways to change the product distribution of Cu by tuning the binding energy of crucial intermediates and reaction pathways. A bimetallic Cu−based electrocatalyst can be engineered to have multiple active sites for adsorbing key intermediates in the C_{2+} pathway, which can modulate the efficiency and selectivity of CO_2 conversion. This part will be discussed in more detail in Section 1.3.2.

1.3.1.2 Post−Transition Metals

As one of the most important hydrogen carriers and raw materials for the production of various organic agents, formate has attracted attention in the field of eCO_2RR as a valuable product.[68] In

contrast to other products beyond CO, for which at least four electrons are needed, the two−electron route for formate has more opportunities to achieve a high FE and production rate for practical applications.[66] Metals in the p−block, also known as post−transition metals, such as Sn, In, Bi, Pb, and their oxides (**Figure 1.10**), not only have excellent abilities to suppress the competitive HER
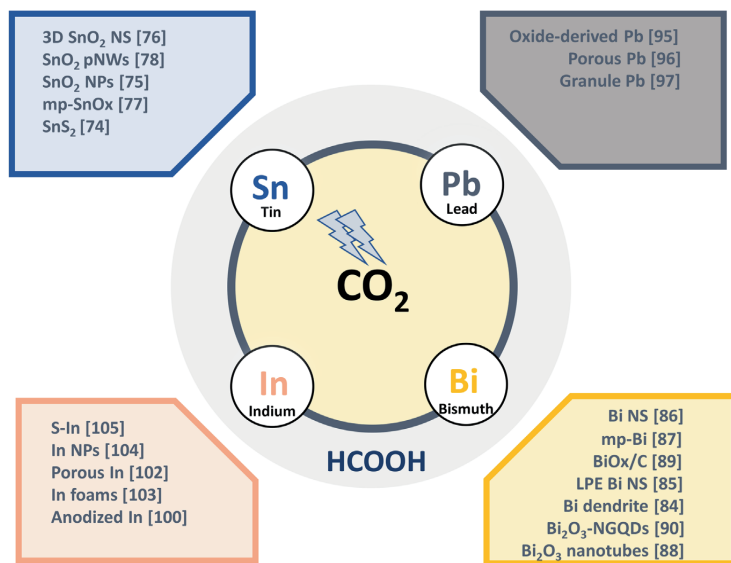

Figure 1.10. Overview of the post−transition metal based electrocatalysts in eCO$_2$RR, which will be discussed in the coming Sections. They are classified into four groups: Tin−based electrocatalysts, Lead−based electrocatalysts, Indium−based electrocatalysts and Bismuth−based electrocatalysts.

from eCO$_2$RR but also catalyze the reduction of CO$_2$ into formate and formic acid as major products with a FE greater than 90.0% in an aqueous solution saturated with CO$_2$.[70] In this Section, state−of−the−art developments and challenges of monometallic post−transition metals will be briefly discussed.

Sn−based electrocatalyst materials

Due to their good activity, high selectivity, non−toxicity, and large abundance in the Earth's crust, Sn−based materials have been identified as attractive electrocatalysts for selective CO$_2$ reduction to formate for large−scale applications.[71] Polycrystalline Sn metal was reported by Hori *et al.* in 1994 to have high formate selectivity (FE 88.0%) for electrochemical CO$_2$ reduction in 0.1 M KHCO$_3$ aqueous solution.[22] Significant follow−up research has been dedicated to improving the catalytic performance, including strategies of oxidation treatment, morphology control, electronic modulation by doping, alloying and defects. Additionally, revealing the active site and mechanism of eCO$_2$RR on Sn−based electrocatalysts has also been extensively investigated.

Most recent reports have found the existence of metastable metal oxides on Sn surfaces during cathodic reactions.[72] For example, Kanan *et al.* applied different pretreatments to Sn electrodes and found that SnO_x was essential for formate formation in eCO$_2$RR.[73] Sn electrodes with native SnO_x layers demonstrated a potential−dependent CO$_2$ reduction activity in agreement with previous
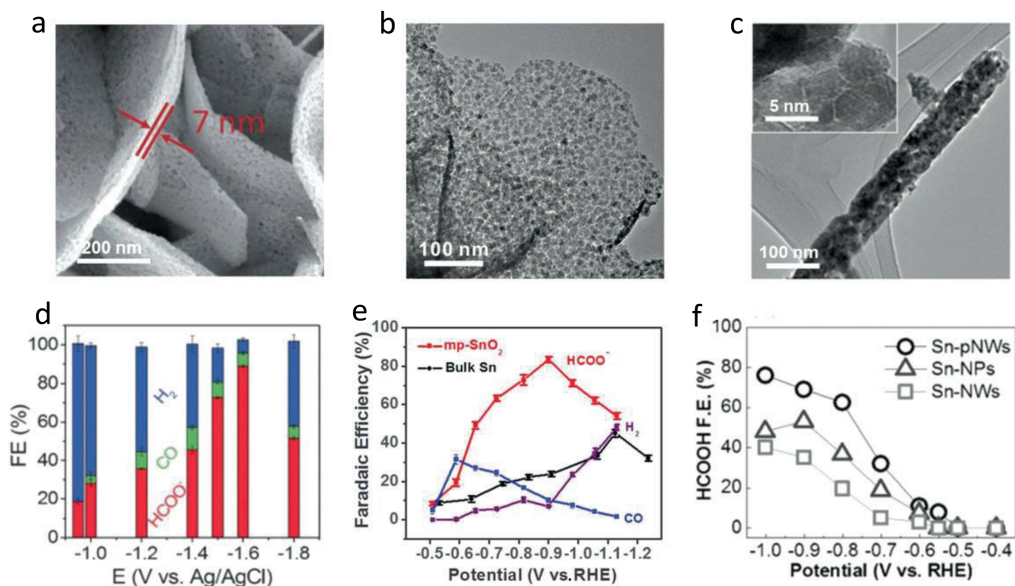

Figure 1.11. Scanning Electron Microscopy (SEM) image of porous 3D SnO$_2$ nanosheets (a). eCO$_2$RR product distribution on SnO$_2$ at different applied potentials (d), reproduced *from ref. 76.* Transmission Electron Microscopy (TEM) image of mesoporous SnO$_2$ nanosheets (mp−SnO$_2$) (b). Faradaic Efficiencies (FEs) at different potentials on mp−SnO$_2$ in comparison with the FEs on commercial Sn foil (e), reproduced from *ref. 77.* TEM images of porous Sn nanowires (Sn−pNWs) with abundant grain boundaries (c). Potential−dependent HCOOH FE on Sn−pNWs and other Sn electrocatalysts (f), reproduced from *Ref. 78.*

studies by Hori *et al*. In contrast, etching off the SnO$_x$ layer from the electrode resulted in negligible eCO$_2$RR activity and higher HER selectivity. An electrode prepared from a mixed phase of Sn and SnO$_x$, however, showed nearly eightfold higher current density and fourfold higher formate FE than one prepared with the pristine Sn foil.[73]

Apart from O, sulfur (S) on the surface may also enhance the eCO$_2$RR. As with SnO$_x$, SnS$_x$ could also be electrochemically reduced to metallic Sn with residual S on the surface, facilitating the eCO$_2$RR performance. Zheng and co−workers deposited SnS$_x$ atomic layer on Au substrates to fabricate S−modulated Sn catalysts through electrochemical reduction.[74] It was found that the prepared Sn(S) facilitated the eCO$_2$RR with a FE of 93.0% for formate formation at −0.75 V vs. RHE. Furthermore,

prolonged stability (more than 40 h of operation) was obtained using the Sn(S) catalysts. As evidenced by the DFT calculation, the authors correlated the improved catalytic performance to S−induced uncoordinated sites.

Since the surface oxide layer may have a uniquely important role, a number of researchers used SnO_2 rather than Sn metal directly as the starting material or "precatalyst". Prior to eCO_2RR, SnO_2 is electrochemically reduced to metallic Sn with some residual surface oxide. By carefully controlling the morphology, the catalytic performance of Sn−based catalysts could be enhanced due to the enlarged specific area and increased exposed active sites. Zhang *et al.* synthesized a series of SnO_2 nanocrystals with sizes ranging from 3 nm to 200 nm, loaded on high surface area carbon supports to maximize the specific surface area.[75] It was demonstrated that 5 nm SnO_2 nanocrystals supported on graphene had the highest FE (over 93.0%) for formate, resulting from a compromise between the strength of the interaction between $*CO_2^-$ and kinetic activation toward protonation on the nanoscale catalyst surface. Li and co−workers prepared three−dimensional (3D) hierarchical mesoporous SnO_2 nanosheets through a hydrothermal method.[76] Electrochemical measurements showed that a formate partial current density of 45 mA cm^{-2} with a FE of 87.0% was achieved for eCO_2RR at the potential of −1.6 V vs. Ag/AgCl. The improved performance was ascribed to the advantageous 3D hierarchical structure (**Figures 1.11a, d**), which enlarged the electrochemical active surface area, facilitated the charge transfer at the surface, and promoted the mass transport of reactant and product. This is confirmed by similar SnO_2 nanostructures, which also showed boosted formate formation in eCO_2RR (**Figures 1.11b, e**).[77] A team led by Spurgeon synthesized porous SnO_2 nanowires, which were electrochemically reduced to metallic Sn nanowires with a high grain boundary density (**Figure 1.11c**).[78] As a result, the catalyst produced formate with improved activity and selectivity, starting at a low overpotential of 350 mV and reaching a steady efficiency of 80.0% at −1.0 V vs. RHE (**Figure 1.11f**). Tuning surface electronic structure by doping or alloying has been proven as a promising strategy to improve the intrinsic activity of a catalyst. An *et al.* introduced Bi into SnO and found that the Bi−doped SnO presented a FE of around 93.0% toward formate.[79] Jiao *et al.* synthesized a Ag−Sn core−shell structure and the FE of formate was boosted to 80.0%.[80] The reaction pathway could even be tuned from formate to CO when combining Sn and Cu. Takanabe and co−workers reported a Cu−Sn bimetallic catalyst that promotes CO formation with a FE up to 90.0% at −0.6 V vs. RHE.[81] More details about bimetallic Cu−Sn electrocatalysts will be discussed in Section 1.3.2.1 and Chapter 3.

Bi−based electrocatalyst materials

As one of the p−block metals, Bi has shown the potential of electrochemically converting CO_2 into formate with an activity comparable to Sn−based materials. Unlike Sn, in which metal oxide species have been proven to play an important role in eCO_2RR performance for Sn−based electrocatalysts, literatures on the active sites and mechanism of Bi−based electrocatalysts are still in disagreement about whether BiO_x species are involved. According to Pander *et al.*, who used *in situ* Attenuated Total Reflection−Fourier Transform Infrared (ATR−FTIR) Spectroscopy to analyze Bi surfaces during CO_2 electrochemical reduction, the oxide layer on the Bi surface did not change after initial

reduction, and no reaction intermediates were detected under working conditions.[82] However, many theoretical works emphasized the crucial role of Bi−O interaction during eCO₂RR. For example, a DFT calculation revealed that O_2 is the only species that adsorbs on the Bi(111) surface.[83]

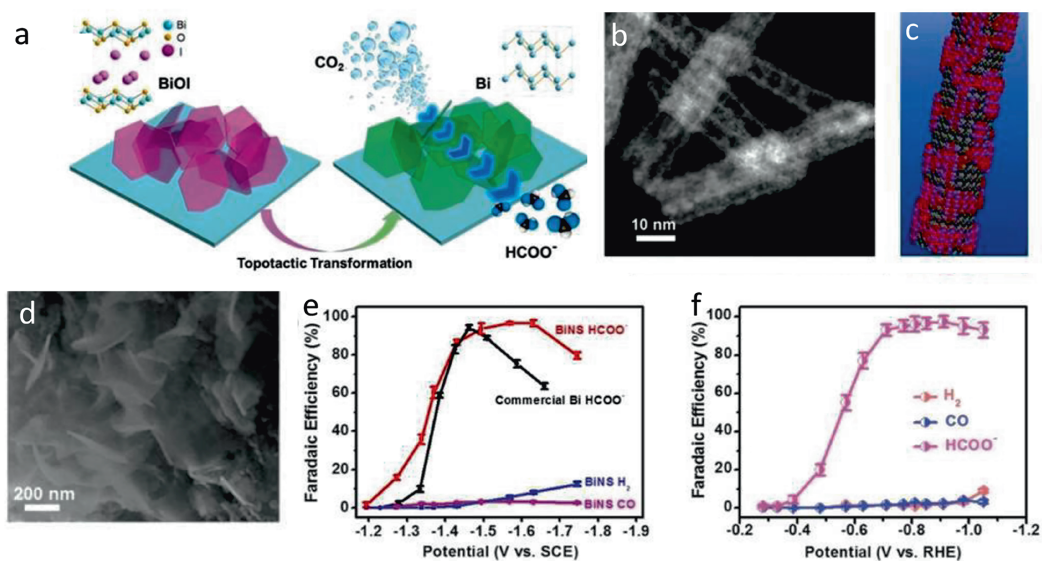Despite the high selectivity toward formate, the catalytic activity of bulk Bi metal electrodes still

Figure 1.12. Schematic illustration of the topotactic transformation of BiOI nanosheets to metallic Bi nanosheets for eCO₂RR (a). Scanning Electron Microscopy (SEM) image of reduced Bi nanosheets (Bi NS) (d) and potential−dependent Faradaic Efficiencies (FEs) of formate, CO, and H₂ on Bi NS in comparison with the FEs on commercial Bi nanopowder (e), reproduced from *ref. 86.* High−angle annular dark field scanning transmission electron microscopy image (b) and structural model of Bi₂O₃ double−walled nanotubes with highly defective outer walls (c). Potential−dependent FEs on metallic Bi nanotubes converted from Bi₂O₃ double−walled nanotubes (f), reproduced from *Ref. 88.*

needs to be improved to meet the requirement for practical applications (unity selectivity and low overpotential). Strategies include morphology control and electronic structure modulations. Manipulation of the morphology of Bi−based materials can be approached by various methods. Electrodeposition is a common technique to directly deposit metallic Bi nanostructures onto current collectors. Precise control of experimental parameters such as deposition potential and time can lead to fine−tuned morphology and, thus, optimal electrocatalytic performance. Min and co−workers created hierarchical Bi dendrites through the electrodeposition of Bi³⁺ precursors in ethylene glycol in multiple steps.[84] The prepared Bi dendrites with rich unsaturated sites and high index surfaces delivered the maximum formate FE of 89.0% at −0.74 V vs. RHE and improved stability for 12 h.

Two−dimensional (2D) structures in catalysts have attracted tremendous attention because they often lead to improved performance due to a high partial density of states of the Bi p band around the Fermi level.[85] Bulk Bi has a layered structure similar to black phosphorus that can be exfoliated to form 2D structures. Zhang *et al*. synthesized ultrathin 2D Bi nanosheets by means of liquid−phase exfoliation (LPE) and observed an enhanced formate FE of 86.0% at −1.1 V vs. RHE.[85] Transformation of Bi compounds (such as layered Bi oxide, oxyhalides, and carbonate) is also an effective way to achieve 2D structures.[86,87] Han and co−workers prepared 2D Bi nanosheets through electrochemical reduction of BiOI nanosheets, which showed a near unity selectivity toward formate in eCO2RR (**Figures 1.12a, d, e**).[86] Follow−up work showed that mesoporous Bi (mp−Bi) nanosheets were obtained from $Bi_2O_2CO_3$ nanosheets under cathodic potentials due to structure mismatch.[87] Gong *et al*. reported the defective Bi nanotubes achieved by the use of double−walled Bi_2O_3 nanotubes with fragmented outer surfaces as the precatalyst through electrochemical reduction transformation, which presented a formate FE close to 100.0% with a great formate partial current density around 60 mA cm^{-2} at −1.05 V vs. RHE (**Figures 1.12b, c, f**).[88]

Hybrid nanostructures supported by carbonaceous materials are also an effective strategy for tuning the properties of Bi−based electrocatalysts. Nam *et al*. fabricated a hybrid structure of Bi_2O_3 nanoparticles supported on carbon black through a solvothermal method.[89] This hybrid electrocatalyst exhibited an average Faradaic Efficiency of 93.4% between −1.37 and −1.70 V vs. Ag/AgCl and a partial current density up to 18 mA cm^{-2} for selective formate production. Liu and co−workers decorated Bi_2O_3 nanosheets with N−doped graphene quantum dots, which displayed high formate FE of >90.0% within a wide potential range from −0.9 to −1.2 V vs. RHE as well as good stability for >14 h.[90] Bi electrodes have also been found to have a higher intrinsic CO_2 reduction activity by forming bimetallic structures with other metals. Sun *et al*. reported a Mo−Bi bimetallic chalcogenide as an electrocatalyst for eCO2RR, which changed the reaction pathway towards methanol with a FE of 71.2% at −0.70 V vs. SHE.[91] Details about bimetallic CuBi electrocatalysts will be discussed in Section 1.3.2.2, and Bi−based electrocatalysts will be discussed in Chapter 4.

Pb−based electrocatalyst materials

Despite having excellent selectivity for formate formation, Pb−based electrocatalysts have been regarded as not ideal for eCO2RR due to their intrinsic toxicity and concomitant environmental unfriendliness, and so are receiving less attention than other p−block metals.[92] Early DFT mechanistic studies revealed that the high selectivity of Pb electrocatalysts for formate originates from the strong O−affinity and weak C− and H−affinity properties of Pb. This led to the participation of *OCHO species (**Figure 1.4**) as key intermediates exclusively producing formate, while preventing unwanted H_2 production.[93] However, when the effects of solvent and cation formation in the electrolyte were considered, later theoretical studies suggested that the reaction may proceed preferentially via direct carbon−bonded *COOH intermediates (**Figure 1.4**), which share the same high formate selectivity.[94] Experimental studies have indicated that a metallic Pb surface plays an important role in producing formate from CO_2, evidenced by *in situ* ATR−FTIR measurement. [82] However, they found that a higher FE of formate was obtained in the electrode after anodic

treatment. Similar results were reported by Kanan *et al.* that a reduced PbO_2 electrode (~100.0% at −0.80 V vs. RHE) behaved better than Pb foil (~30.0% at −0.80 V vs. RHE) in electrochemical CO_2 conversion to formate.[95] This suggests that surface oxide species boost the catalytic performance of Pb−based electrocatalysts, similar to the observations for Sn and Bi.

A close relationship exists between the catalytic properties of Pb electrodes and the morphologies and composition of the electrodes, especially with respect to their FE. A honeycomb−like structure of Pb electrodes was fabricated along the [100]−axis by Fan *et al*. Using this structure, ample electrode/electrolyte contact surface area was provided, as well as strong structural stability, which facilitated the formation of formate with a FE around 97.0% at −0.99 V vs. RHE.[96] Apart from room temperature and pressure, Balun *et al*. reported Pb granule electrodes for eCO_2RR at high−pressure conditions and high temperatures in a fixed−bed reactor.[97] The maximum FE for formate was found to be 94.0% at −1.8 V vs. SHE with a yield of the reaction of 1.3×10^{-3} kg L^{-1} h^{-1}. Like other p−block metals, combining Pb with a secondary metal could possibly shift the product distribution. For example, Ismail *et al*. reported a series of Au–Pb bimetallic electrocatalysts with different Au/Pb interfaces, which effectively enhanced the formation of CH_4.[98] The maximum CH_4 production was obtained when the most Au/Pb interfaces were present. DFT calculation suggested a moderate binding strength for the key intermediates to CH_4 on the Au/Pb interface. Details about bimetallic CuPb electrocatalysts will be discussed in Section 1.3.2.3 and Chapter 2.

In−based electrocatalyst materials

Similar to the other p−block metals, In is also highly selective for formate production from CO_2. However, the relatively high cost (about 10 times that of Sn or Bi) brings concerns for its potential industrial implementation. The early exploration of the In−based electrode was done by Hori *et al*., which showed a FE of 94.4% for formate on In electrode, which was even higher than that of Sn (88.4%).[99] Another similar aspect to Sn is that In is a strongly oxophilic metal and the surface of an In electrode tends to be covered by a layer of oxide. A strong dependency between the catalytic behavior and the surface conditions of In electrodes has been reported by Bocarsly *et al*.[100] They demonstrated that an etched electrode with the removal of In oxides showed a lower FE toward formate, compared to the anodized electrode with In oxide layer. To reveal the role of In oxide in eCO_2RR, *in situ* ATR−FTIR measurements were employed. It was found that the In_2O_3 surface layer could first react with H_2O to form $In(OH)_3$ during the eCO_2RR process. The formed $In(OH)_3$ could further interact with the dissolved CO_2, by which In−carbonate species were generated for the formate formation at low overpotentials. The proposed mechanism was confirmed by a follow−up work that compared the deliberately prepared $In(OH)_3$ and In_2O_3 nanoparticles, in which the former achieved almost 100.0% FE for formate at −1.3 V vs. Ag/AgCl.[101]

Despite the high selectivity toward formate, In−based electrocatalysts still face the same issue as the other p−block metals do, *i.e.,* low catalytic activity to meet the requirement for industrial applications (current density higher than 1 A cm^{-2}). Various strategies based on the morphology effect and electronic effect have been applied to improve the catalytic activity and stability. In order

to further promote the current density and production rate, strategies are pursued to prepare In nanostructures, one of which is electrodeposition. Luo and co−workers fabricated a 3D porous In electrode through electrodeposition. The porous structure provided an enhanced formate formation for eCO$_2$RR with a FE of 90.0% at a production rate of 1.14 mmol cm^{-2} h^{-1}. The authors ascribed the enhancement mechanism to the increased local pH in the vicinity of the electrode, which suppressed the competitive HER.[102] Hou and co−workers electrodeposited dendritic In foams from Cl$^-$−containing aqueous solution by means of templating dynamic hydrogen bubbles, which also showed a similar enhanced formate production.[103] Different from the observation that an In oxide layer acts as an active site for CO$_2$ conversion to formate, Leonard and co−workers reported *in situ* electrochemically reduced In$_2$O$_3$ nanocatalysts, in which a metastable oxide layer was removed and an In^0–In$_2$O$_3$ composite was created.[104] This In^0–In$_2$O$_3$ composite material changed the reaction pathway and was able to electrochemically reduce CO$_2$ to CO with near 100% selectivity at relatively low potentials (*c.a.* −1.0 V vs. Ag/AgCl). The authors attributed the change in selectivity to the direct exposure of In^0 to CO$_2$ in solution. A promising method to manipulate the product distribution of eCO$_2$RR on In is combining In with a secondary component, such as Cu, which can tune the absorption energy of crucial intermediates and thus change the reaction pathway to products. More details will be discussed in Section 1.3.2.4.

1.3.2 Cu/Post−Transition Metal Bimetallics

As a new class of catalysts, bimetallic catalysts are prepared by mixing two metal components within a single catalyst. Such catalysts may include core−shell structures (**Figure 1.13a**), intermetallic alloys (**Figure 1.13b**), solid solution alloys (**Figure 1.13c**), and heterostructures (**Figure 1.13d**). Compared with monometallic catalysts, bimetallic catalysts exhibit significantly different properties due to their different electronic structures.[105,106] The presence of other metals also provides new active sites, which optimizes the binding strength between intermediates and active sites. It is, therefore, possible to obtain catalyst structures with optimal properties that may not otherwise be accessible to drive catalytic reactions. As introduced in 1.3.1.1, Cu is the unique metal for catalyzing electrochemical CO$_2$ conversion to hydrocarbons, but it still suffers from a wide product distribution. This has led to the development of a number of bimetallic catalysts that are capable of converting CO$_2$ into certain products, especially copper−based bimetallic catalysts. Many Cu−based bimetallic
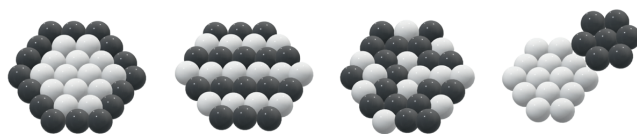

Figure 1.13. Schematic diagram of the Cu−based bimetallic structures: core−shell (a), intermetallic alloy (b), solid solution alloy (c), and heterostructure (d).

catalysts have been investigated for applications in eCO$_2$RR, but most of them still have significant limitations, including high cost and inevitable HER (*e.g.,* the noble metals Pt and Pd). As HER−inert and earth−abundant metals, alloying post−transition metals with Cu is considered one of the most promising strategies to improve the catalytic performance of Cu−based bimetallic materials. The combination of Cu and transition metals, such as CuAg, CuAu, and CuZn, has also attracted a lot of attention for decades and shown a promising selectivity improvement in eCO$_2$RR. This Thesis will focus on Cu integrated with post-transition metals as electrocatalysts in eCO$_2$RR. More details about Cu−transition metal bimetallic electrocatalysts will be discussed in the Outlook Section.

1.3.2.1 CuSn Bimetallic Catalysts

As mentioned in Section 1.3.1.2, Sn has an excellent ability to electrochemically catalyze CO$_2$ to formate. Due to its stronger O affinity and weaker H affinity than Cu, Sn metal is relatively inactive for HER and active for formate production.[107] This implies that the eCO$_2$RR proceeds overwhelmingly via *COOH or *OCHO intermediates (**Figure 1.4**) on the Sn electrode surface.[35] When combining Sn with Cu, the *CO intermediates are theoretically unaffected by O−binding sites (*i.e.,* Sn) since they are inclined to bind in configurations with little contribution from the O atom. Instead, O atoms play a more critical role in stabilizing the *COOH intermediate and potentially increasing its binding energy if O−binding sites are present.[108] When eCO$_2$RR occurs via the
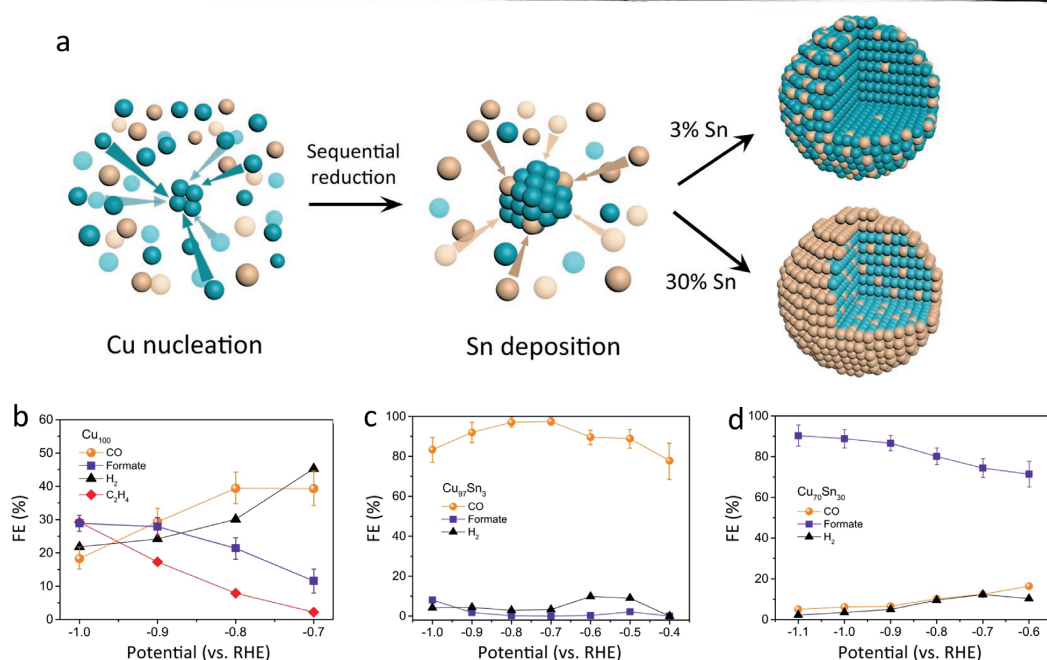
Figure 1.14. Schematic diagram of the CuSn bimetallic nanoparticles with different concentrations of Sn (a); Potential dependence of Faradaic Efficiencies (FEs) for eCO$_2$RR on Cu$_{100}$ (b), Cu$_{97}$Sn$_3$ (c), and Cu$_{70}$Sn$_{30}$ (d). Adapted from *Ref. 109.*

*OCHO intermediate, the O−binding sites likely play an even greater role, since both oxygen atoms are bound to the surface.[35] Therefore, it is expected that Cu/Sn bimetallic catalysts will improve selectivity to a *COOH or *HCHO intermediate pathway, resulting in an enhancement in CO or formate production. Ren *et al*. reported a structure of Cu and Sn surface alloy with isolated Sn sites anchoring on a Cu host with high surface densities for efficient electrocatalytic CO_2 reduction (**Figure 1.14a**).[109] Typically, the Cu_{100} showed a variety of products (**Figure 1.14b**). The selectivity shifted a lot to CO with FEs over 80.0% in the same potential window on $Cu_{97}Sn_3$ catalyst (**Figure 1.14c**), whereas the formate formation dominated in $Cu_{10}Sn_{30}$ (**Figure 1.14d**). Li *et al.* reported a structure of core−shell $Cu−SnO_2$ nanoparticles, with a maximum FE of 93.0% at −0.7 V vs. RHE for samples with a 0.8 nm thick SnO_2 shell.[110] A significant effect of Sn shell thickness on product selectivity was found in this study. It was observed that a thicker (1.8 nm) shell tended to generate formate whereas the thinner (0.8 nm) shell yielded CO in a more selective manner with a conversion efficiency of 93.0% at −0.7 V vs. RHE. DFT calculations indicated that the 0.8 nm thick SnO_2 shell induced a large compressive strain on the surface (10.0%), resulting in Cu atoms diffusing out as well. Therefore, unlike the 1.8−nm thick SnO_2 shell model with an energetically more favorable formate production potential, the overpotential for CO production was less negative on the Cu−doped model with both compression and doping. Apart from two−electron products, a recent work has reported the enhanced production of C_2H_4 from CO_2 over $SnO_2−CuO$ nanosheets by Lan and co−workers.[111] Using DFT calculations, it was revealed that the dopant Sn increased the electron density of CuO, where CO_2 molecules were easier to be activated in the Cu region.

1.3.2.2 CuBi Bimetallic Catalysts

The most reported CuBi electrocatalysts are highly selective and stable toward formate at low overpotential, reaching FEs of around 90.0% for formate. The main product seemed limited to formate when Cu coexisted with Bi in early studies. For example, Hoffman *et al.* synthesized dendritic bimetallic CuBi electrocatalysts with nanosized grains.[112] They found that highly dense defect sites were created in the CuBi structure due to the lattice mismatch of Cu and Bi, leading to suppressed HER and CO formation and enhanced formation of formate (90.0% at −0.8 V vs. RHE). Ren *et al. in situ* constructed a CuBi bimetallic catalyst and observed a promoted electrochemical CO_2 to formate conversion with a FE of 98.0% at −0.98 V vs. RHE.[113] Through *in situ* Raman Spectroscopy measurements, it was revealed that abundant Cu−Bi interface structures on the catalyst surface can provide active sites for eCO2RR.Combining Bi with Cu was recently found to change the reaction pathway toward products beyond formate. Wang *et al.* fabricated four bimetallic CuBi aerogel electrocatalysts with adjustable composition (**Figure 1.15a**).[114] The FE of CO (FE of 86.6%) and formate (FE of 60.8%) were found for $Cu_{100}Bi$ and Cu_5Bi, respectively, which were 1.2 and 5.5 times higher than that over the Cu catalyst. $Cu_{50}Bi$ exhibited enhanced selectivity for CH_4 (FE of 26.0%), while $Cu_{10}Bi$ displayed C_2H_4 FE (31.6%) which was 1.6 times higher than with Cu (**Figure 1.15b**). Willian A. *et al.* successfully synthesized CuBi nanoparticles, which exhibited a CH_4 FE as high as 70.6% at −1.2 V vs. RHE.[115] DFT calculations showed that alloying Cu with Bi significantly decreased the formation energy of *COH, the rate−determining step, which explained the improved performance.
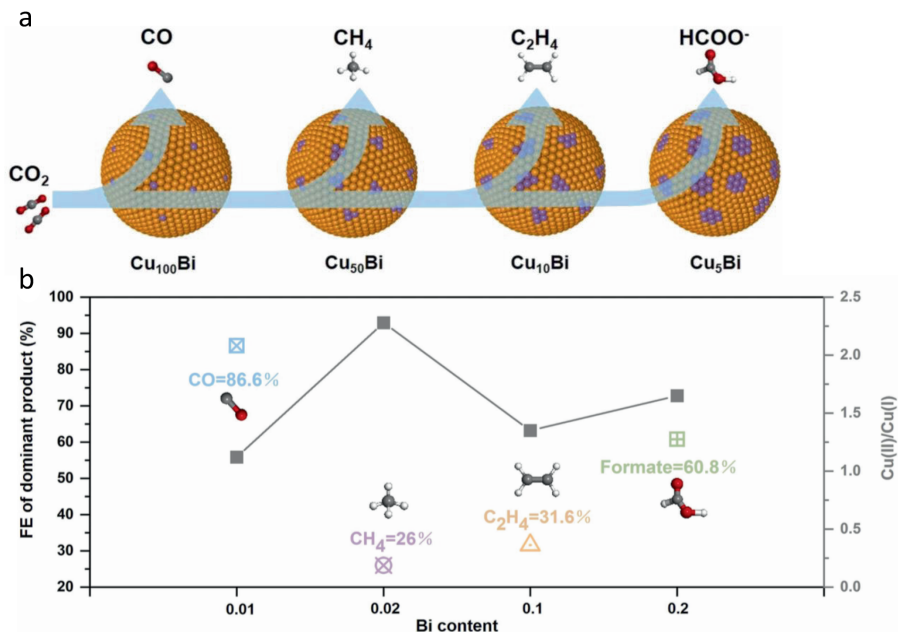
Figure 1.15. Schematic illustration of the product distribution over different Cu−Bi ratios (a) and selectivities for eCO$_2$RR and Cu(II)/Cu(I) ratios as a function of Bi content (b). Adapted from *Ref. 114.*

1.3.2.3 CuPb Bimetallic Catalysts

The research on CuPb bimetallic electrocatalysts for eCO$_2$RR is less in−depth and extensive than Sn and Bi due to the relatively higher toxicity of Pb. According to early reports, CuPb bimetallic electrodes at −1.15 V vs. SHE enhanced the FE for formate by 50% from 22%.[116] Yang and co−workers reported a 3D hierarchical nanostructure of CuPb catalyst via an electrodepositing−annealing−electroreduction approach.[117] The nanostructured CuPb electrodes catalyzed electrochemical CO$_2$ conversion to CO with a FE of 29.6% at −0.93 V vs. RHE. Strasser *et al*. prepared a series of CuPb bimetallic electrocatalysts through underpotential electro−deposition, with which the adapted Pb coverage was precisely controlled (**Figure 1.16a**).[118] The authors found that as little as 0.16 monolayer (ML) Pb surface adatoms on a polycrystalline Cu surface improved the formate production 15 times compared to Cu foil. The 0.78 ML Pb surface adatoms showed the most favorable formate production with the most effective H$_2$ suppression (**Figures 1.16b, c**). It was inferred that the favorable product efficiency was due to the selective poisoning of Pb adatoms at the strongest hydrogen adsorption sites, which changed the chemisorption of reactive intermediates due to the electronic effects of Pb adatoms. A study done by Wang *et al*. demonstrated that a strong synergy between the Cu core and ultrathin Pb shell in Cu/Pb core/shell nanocrystals significantly
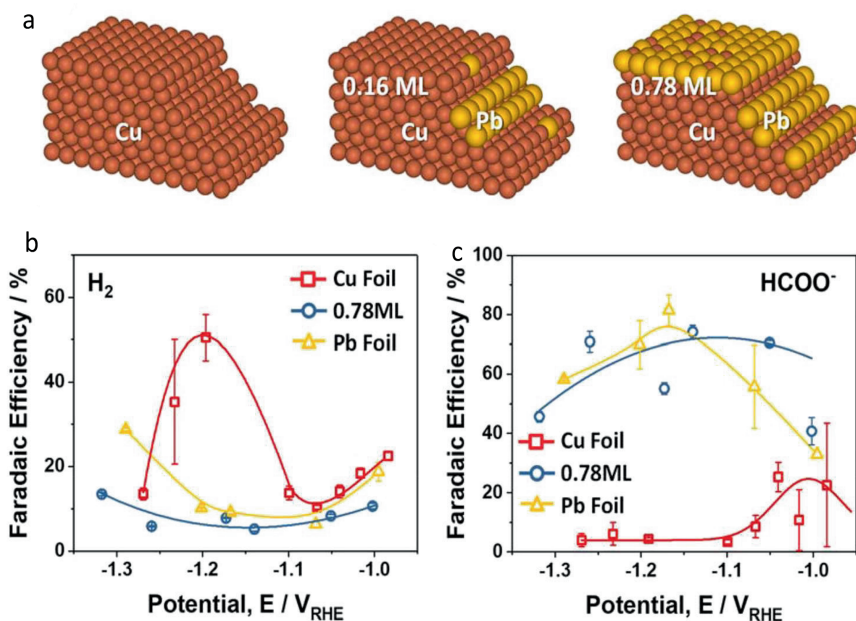
Figure 1.16. Scheme of Cu and Pb modified Cu system (0.16 and 0.78 monolayer (ML) Pb/Cu), Pb adatoms are decorated preferentially on HER and eCO$_2$RR sites, *i.e.,* on the edge and step sites of Cu (a). Faradaic Efficiencies (FEs) of H$_2$ (b) and HCOO$^-$ (c) for Cu foil, 0.78 ML Pb/Cu and Pb foil. Adapted from *Ref. 118.*

boosted the electrocatalytic reduction of CO$_2$ toward C$_{2+}$ products with a maximum FE of 81.6%.[119] According to DFT calculations, the synergistic Cu/Pb core/shell nanocrystals had reduced formation energies for *COOH and *OCCOH intermediates, which were critical intermediates in reducing CO$_2$ to CO and C$_{2+}$ products, respectively. This was shown to result in significant increases in the selectivity for C$_{2+}$ liquids.

1.3.2.4 CuIn Bimetallic Catalysts

As with Sn, the binding of *CO remains unchanged over CuIn bimetallic catalysts, and *COOH is relatively stable for CO production. It was proven to increase the energy barrier for *H adsorption while stabilizing the *COOH intermediate by 0.1 eV.[120] Hoffman and co−workers electrodeposited dendritic CuIn alloys of various compositions.[121] These CuIn electrodes produced formate and CO from CO$_2$ with a tunable selectivity, *i.e.,* high formate selectivity (up to 62.0%) with an 80.0 at% In alloy and an ideal syngas (CO FE of 35.0%, H$_2$ FE of 15.0%) flow at In 40.0 at%. In particular, CuIn alloys have been prepared by Rasul and co−workers using electrochemical reduction of thermally oxidized Cu metal foil in an In sulfate solution. High−resolution Transmission Electron Microscopy (HR−TEM) and Energy−dispersive X−ray spectroscopy (EDS) mapping images (**Figures 1.17a,**
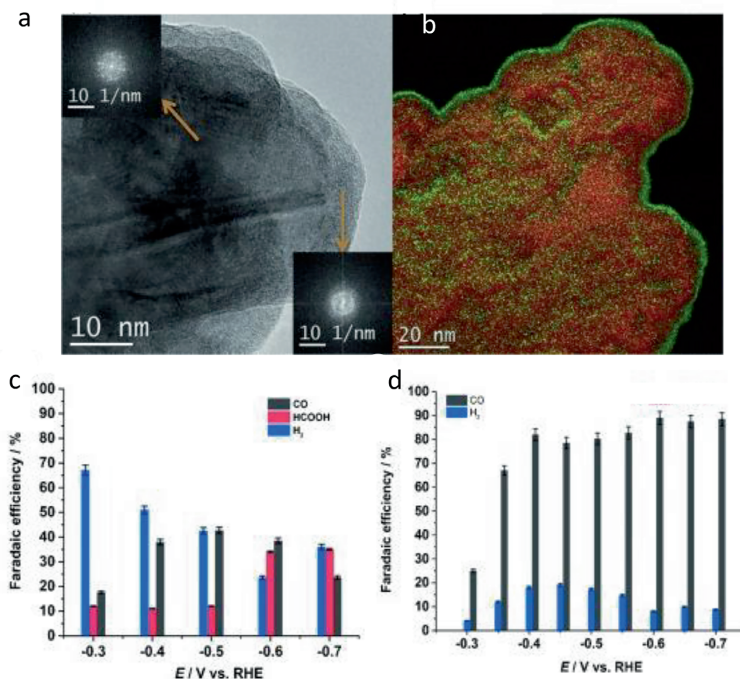
Figure 1.17. High–resolution Transmission Electron Microscopy (HRTEM) images of CuIn with fast Fourier transform images from the bulk and the surface (inset) (a); Energy Dispersive X–ray Spectroscopy (EDS) element mapping (b) of the selected area: In (green), Cu (red). Faradaic Efficiencies (FEs) distribution of pure Cu (c) and CuIn electrode (d). Adapted from *Ref. 120.*

b) suggested that In atoms preferentially located at the surface of the Cu foil. The prepared CuIn electrode showed a FE toward CO of 90% at −0.5 V vs. RHE, in contrast to the pure Cu electrode that generated mixed products of CO and formic acid with FE of 45.0% and 10.0%, respectively at the same condition (**Figures 1.17c, d**).[120]

Bimetallic CuIn catalysts with a core/shell structure were also widely used for eCO$_2$RR because of their controllable selectivity by tuning the thickness of the shell. Xie *et al.* synthesized a series of monodisperse core/shell Cu/In$_2$O$_3$ nanoparticles for eCO$_2$RR.[122] It was found that tunable syngas formation (larger than 90.0%) was observed on the Cu/In$_2$O$_3$ nanoparticles with different thicknesses of the In$_2$O$_3$ shell. The author ascribed the boosted CO formation to the synergistic effect of lattice compression and doping in the In$_2$O$_3$ shell.

1.4 Multiscale *in situ* Characterization in eCO$_2$RR

Developing suitable catalysts that can achieve high activity and selectivity towards valuable

products is a crucial requirement for the commercial viability of eCO$_2$RR. Catalyst discovery typically involves a long process of ab initio and kinetics simulation combined with experimental and characterization data. While free energy calculations of adsorbed reaction intermediates have shown a good correlation with experimental reaction rate and selectivity on simple and well−ordered catalytic systems, screening of new and less ordered catalysts computationally remains challenging due to the diverse active sites, intermediates, and reaction steps.[50] The traditional method of electrochemical experiments, including voltammetry and amperometry, when combined with product analysis, offers only a single facet of a multifaceted challenge. There are also ambiguities about how the conversion of CO$_2$ proceeds to create complex (and more valuable) products, such as CO, CH$_4$, C$_2$H$_4$, and C$_2$H$_5$OH, and about how to design materials that are selective for certain products with high activity and stability.
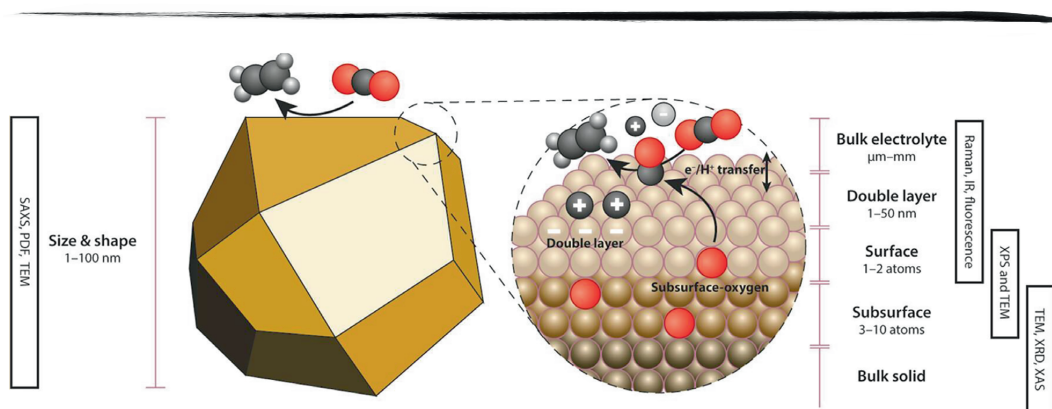
Figure 1.18. Length scales of relevant characterization techniques for *ex situ* and *in situ* studies of electrocatalyst, ranging from single atoms at the surface to the catalyst scale (1–100 nm) and the electrolyte (several micrometers to millimeters). Reproduced from *Ref. 125.*

As a way to solve this problem, multiscale characterization gained considerable attention in recent years.[123] The use of *ex situ* and *in situ* multiscale characterization techniques, which enable probing of the catalytic system before/after and under actual operating conditions, has proven to be valuable in uncovering reaction mechanisms, visualizing catalyst dynamics and surface−bound intermediates, and capturing the behavior at the catalyst−electrolyte interface.[124] The knowledge gained from these techniques, combined with theoretical insights, has played a crucial role in the rational design of subsequent generations of catalysts.

Figure 1.18 depicts multiscale characterization techniques for catalyst materials, including their respective ranges of lateral resolution and atomic detection limits.[125] Vibrational spectroscopies such as infrared (IR) and Raman,[126,127] microscopies including Atomic Force Microscopy (AFM) and Transmission Electron Microscopy (TEM),[128–130] and X−ray characterization techniques such as X−ray Absorption Spectroscopy (XAS),[131,132] X−ray Photoelectron Spectroscopy (XPS),[133,134]

and X−ray Diffraction (XRD)[135] have been utilized to investigate the morphology, composition, and surface chemical state of electrocatalysts. In addition, these techniques have been used to track the interaction between adsorbed intermediates and electrode−electrolyte interfaces. Some techniques cannot readily be applied to electrocatalysis research due to their incompatibility in a real working environment, such as XPS and TEM, that require an (ultra) high vacuum in electrocatalytic cells. In addition, the attenuation of X−rays by water presents a challenge to performing sophisticated surface−sensitive studies such as Grazing Incidence X−ray Diffraction (GIXRD) and Small−Angle X−ray Scattering (SAXS).[136,137] However, the surface is of particular interest due to the structural sensitivity of electrocatalytic CO_2 conversion. Therefore, multiscale approaches, including *ex situ* and *in situ* techniques, are needed for the elucidation of the catalyst structure−performance relationship.

1.4.1 Vibrational Spectroscopy

Vibrational spectroscopy techniques yielded a vast amount of information on both the reactants and catalysts. These techniques explore the interactions between molecular vibrations and light, typically in the ultraviolet and visible frequency range (in the case of Raman Spectroscopy) or the infrared frequency range (in the case of IR Spectroscopy).[138] In this Thesis, only Raman Spectroscopy will be discussed.

1.4.1.1 *In situ* Raman Spectroscopy

The combination of Raman Spectroscopy with electrochemistry is gaining popularity as a potent approach to investigate electrocatalytic CO_2 reduction due to its ability to detect possible reaction intermediates in an aqueous environment with negligible water interaction. This technique commonly involves a visible light laser for excitation and measuring inelastically scattered photons from a sample. Raman Spectroscopy provides *in situ* information on potential−induced transformations of the catalyst structure, the reactants, and the catalytic active species, which may not be detected with commonly employed *ex situ* methods such as XPS. This technique is especially useful for studying metal−oxide and oxide−derived eCO_2RR catalysts due to their characteristic metal−oxygen vibrational modes at low Raman shifts, indicating the metal's coordination and oxidation state. Apart from the zero water interference, this is the other advantage of using Raman Spectroscopy over IR spectroscopy in eCO_2RR. For example, Dutta and co−workers used Raman spectro−electrochemistry to investigate the changes in SnO_2 nanoparticles on reduced graphene oxide supports during eCO_2RR to produce formate.[139] By monitoring the characteristic SnO_2 Raman vibrations at 482 cm^{-1}, 623 cm^{-1}, and 762 cm^{-1}, they observed structural transformations in the SnO_2 catalyst (**Figure 1.19**). The SnO_2 was present at moderate potentials (−0.25 V vs. RHE), while partial reduction of Sn(IV) to Sn(II) occurred at more negative potentials. Complete conversion to metallic Sn(0) was observed beyond −1.2 V vs. RHE. Controlled potential electrolysis experiments indicated that the formate formation rate was highest when $Sn(IV)/SnO_2$ was the main catalytic species, while Sn(0) formation resulted in mainly H_2 generation.
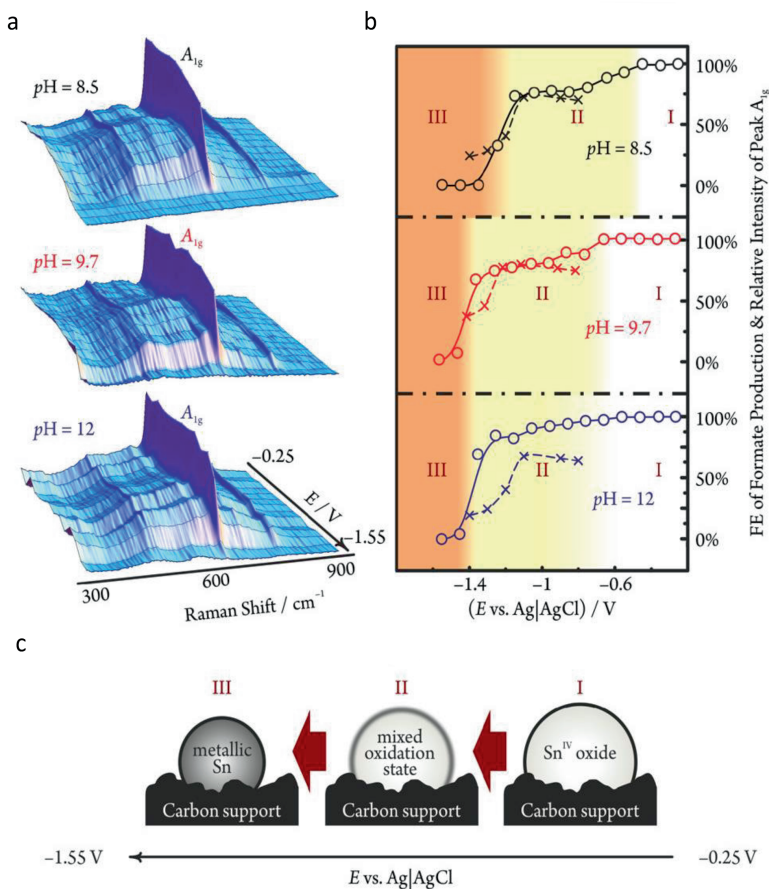
Figure 1.19. *In situ* Raman spectra collected at different pH and potentials (a). A_{1g} Raman peaks related to Sn(IV) (marked with o and solid line) and the Faradaic Efficiency (FE) of formate production (marked with × and dashed line) were presented as a function of electrode potential (b). The catalyst exists in three potential regions (c), represented by the shaded background: fully oxidized SnO_2 (I), a partially reduced mixed oxidation state compound (II), and completely reduced metallic Sn(III). Adapted from *Ref. 139.*

Surface Enhanced Raman Spectroscopy (SERS) is that Raman signals are enhanced on plasmonic interfaces by generating strong local electromagnetic fields upon light excitation.[140] Due to the sharp decay of these fields with distance, SERS is highly surface−selective and ideal for studying interfacial electrochemical reactions. SERS is conducted similarly to ordinary Raman measurement but requires an appropriate substrate that can create a plasmonic interface and a proper excitation wavelength. An *et al.* utilized the time−resolved SERS technique to monitor the dynamics of eCO₂RR intermediates and Cu surfaces with sub−second time resolution.[126] Through anodic treatment and subsequent reduction of the Cu electrodes, nanostructures were formed via redeposition of dissolved
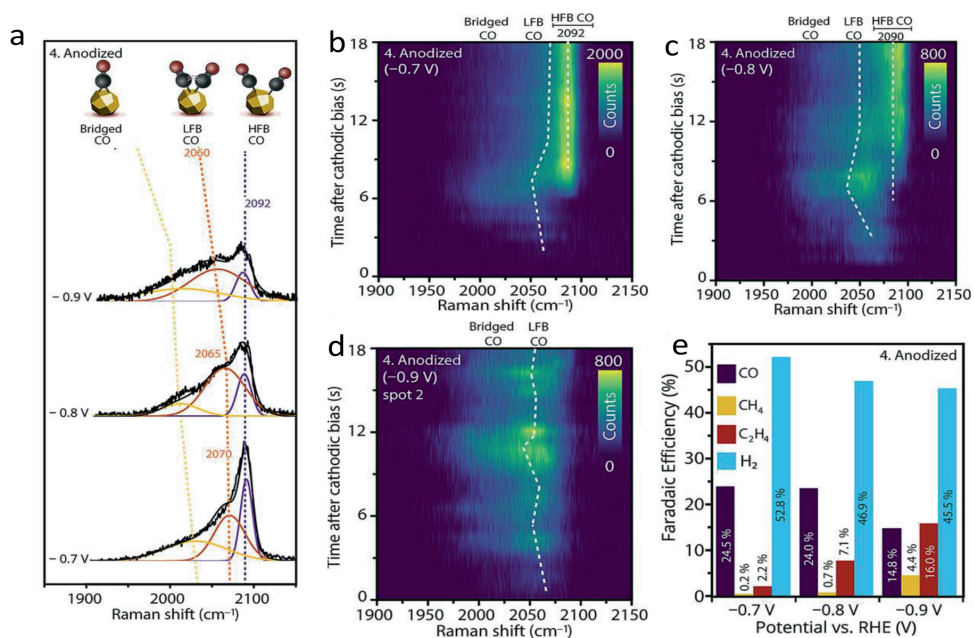
Figure 1.20. Comparison of steady−state Raman spectra (15 min after reduction) of anodized Cu−electrode during reduction at −0.7 V vs. RHE, −0.8 V vs. RHE and −0.9 V vs. RHE (a). Collection time is 5 s. Time resolved−Surface Enhanced Raman Spectroscopy (SERS) heatmap of anodized Cu electrode during reduction at −0.7 V vs. RHE (b), −0.8 V vs. RHE (c) and −0.9 V vs. RHE (d) in the CO region (Raman shift between 1900–2150 cm^{-1}). The color bars of the heatmaps are based on the photon counts of the Raman spectra. FE of anodized Cu electrode during eCO$_2$RR at −0.7 V, −0.8 V and −0.9 V (e). Reproduced from *Ref. 126.*

Cu species. These structures acted as "hotspots" for SERS and active sites for C−C coupling. In **Figure 1.20a**, steady−state *in situ* Raman spectra collected about 15 minutes after cathodic bias onset indicated that the (high−frequency band linear CO) HFB−CO peak positions were slightly different for varying potentials. As the potential became more cathodic, the relative intensity of HFB−CO compared to (low−frequency band linear CO) LFB−CO decreased while the relative peak intensity of LFB−CO increased. Additionally, the LFB−CO peak underwent a more significant shift towards lower Raman wavenumbers under more cathodic potential, from 2070 cm^{-1} at −0.7 V to approximately 2050 cm^{-1} at −0.9 V. In the time−dependent *in situ* SERS heatmaps at −0.7 V and −0.8 V vs. RHE (**Figures 1.20b, c**), *CO was primarily statically adsorbed with a Raman band at approximately 2092 cm^{-1}. This static *CO was associated with the desorption of gaseous CO product. At −0.9 V vs. RHE (**Figure 1.20d**), an activated *CO intermediate was dominant and characterized by a dynamic Raman band below 2060 cm^{-1}. Its dynamic behavior over time and

potential was correlated to a tendency towards dimerization and the formation of ethylene at a more cathodic bias (**Figure 1.20e**).

1.4.2 X−ray Techniques

X−ray techniques can complement vibrational spectroscopes to overcome limitations in probing catalyst surfaces. Recent advances in fourth−generation synchrotron radiation sources have made *operando* hard and soft X−rays more applicable to catalysis, providing sensitive probing capabilities for element, orientation, and chemical state detection.

1.4.2.1 *In situ* X−ray Absorption Spectroscopy

X−ray Absorption Spectroscopy (XAS) is a widely used method for studying catalysts under various experimental conditions. Due to its ability to identify specific elemental states, it is particularly useful for identifying active sites in complex systems and can be applied to a wide range of materials, including ordered, disordered, nano−structured, and liquid materials. XAS plays a significant role in−catalyst research because it can provide a wealth of information about a catalyst in a single reaction. By analyzing XAS features, one can detect tiny changes in bond lengths (on the picometer scale) caused by thermal expansion, surface relaxation, and interactions with the support, ligands, and adsorbates. Additionally, XAS can be used to investigate the nanoscale morphology, macroscopic evolution of composition and crystallographic structure, and heterogeneous distribution of different species in large materials.[141–143]
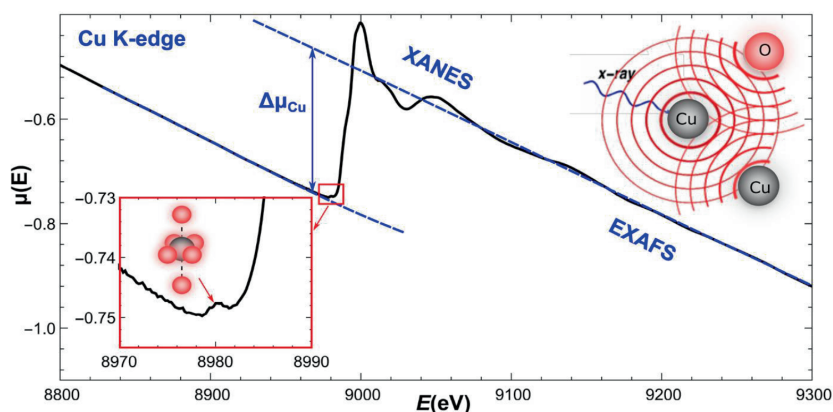
Figure 1.21. Cu K−edge X−ray Absorption Spectroscopy (XAS) data for an as−prepared Cu nanocatalyst used for eCO$_2$RR. Schematics of the photoelectron scattering process, and pre−edge at the Cu K−edge are shown in the insets. Adapted from *Ref. 144.*

The X−ray Absorption Near Edge Structure (XANES), spanning a region of 50–200 eV above the absorption edge, provides valuable information about electron transitions between occupied and unoccupied states, reflecting local atomic and electronic structure information, such as the

coordination numbers, bond distances and angles and oxidation state (**Figure 1.21**).[144] The presence of pre−edge peaks may indicate orbital hybridization caused by coordinating species such as ligands. The edge position is also important as it reveals the oxidation state of elements, which is related to the effective nuclear charge. However, the quantitative analysis of these spectra is not straightforward due to its complexity. The extended X−ray Absorption Fine Structure (EXAFS) technique derives local structural information by studying the oscillating intensity produced by interference between ejected and backscattered photoelectrons in the vicinity of the absorbing atom.[145] This analysis provides reliable structural information concerning the local, short−range coordination environment and the chemical and electronic structure of specific sites within materials, including the number, chemical nature, and distance of neighboring atoms from the atomic site of interest. While the in−depth quantitative analysis of XANES results can be challenging, EXAFS data can be approached
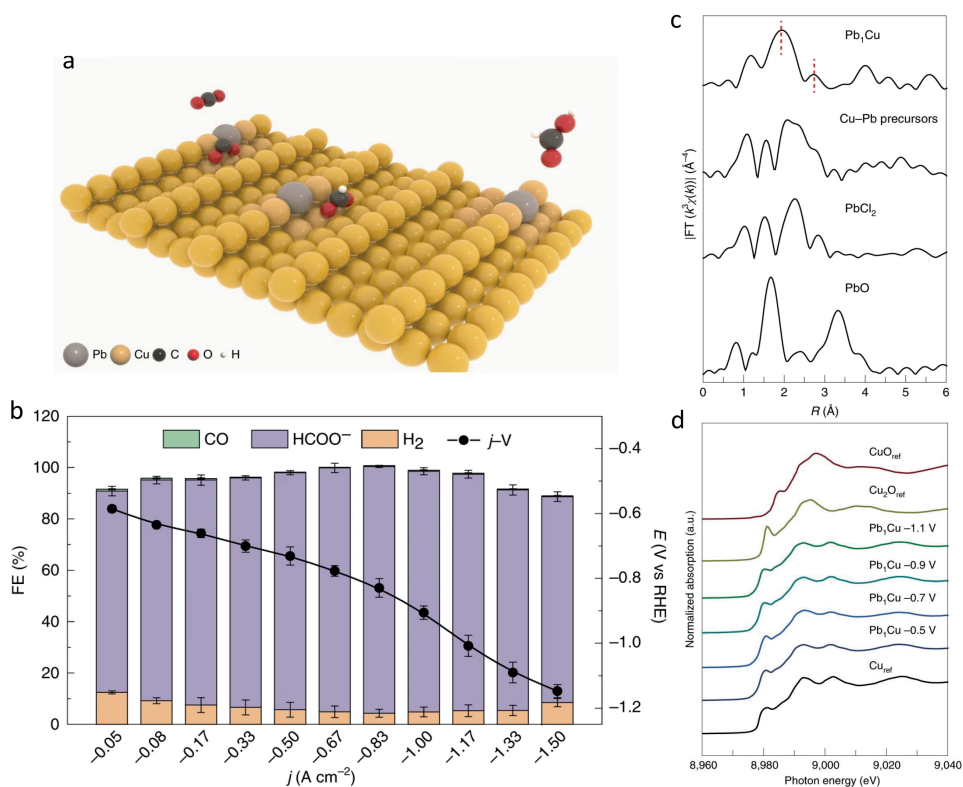
Figure 1.22. Schematic illustration of CO_2 conversion into HCOOH over a Pb_1Cu single−atom alloy (SAA) (a); Faradaic Efficiencies (FEs) of all CO_2RR products at different current densities and the corresponding $j–V$ curve of Pb_1Cu SAAs (b). *Ex situ* extended X−ray Absorption Fine Structure (EXAFS) spectra at the Pb L_3−edge of the Pb_1Cu catalyst (c). *In situ* X−ray Absorption Near Edge Structure (XANES) spectra at the Cu K−edge of the Pb_1Cu catalyst under formate evolution conditions, along with the spectra of CuO, Cu_2O and Cu as references (d). Adapted from *Ref. 146*.

by fitting with the pre−existing material parameters from a crystal database. Zheng and co−workers reported a single−atom Pb−alloyed Cu catalyst (Pb$_1$Cu) that could exclusively convert CO_2 into formate with high selectivity of around 96% and high activity of $1\,A\,cm^{-2}$ (**Figures 1.22a, b**).[146] The coordination environment of Pb atoms in Pb$_1$Cu was revealed using EXAFS measurements (**Figure 1.22c**). The EXAFS curve for the Cu−Pb precursor showed a peak at approximately 2.67 Å, ascribed to Pb−Cl bonds. In contrast, Pb$_1$Cu showed two peaks at around 1.93 Å and 2.73 Å, which corresponded to Pb−O and Pb−Cu bonds, respectively, confirming the exclusive existence of atomically dispersed Pb atoms. They used *in situ* XAS to further study the electronic structure of the Pb$_1$Cu catalyst during reactions. In **Figure 1.22d,** the Cu K−edge absorption spectra of the Pb$_1$Cu catalyst at different voltages were compared to control samples (Cu foil, CuO, and Cu_2O), in which the Pb$_1$Cu catalyst Cu matrix was metallic during formate evolution. Despite the limitation of detecting Pb signals due to the strong Cu fluorescence, they concluded that the active phase of the catalyst during eCO$_2$RR is a Pb$_1$Cu single−atom alloy (SAA) catalyst consisting of metallic Cu alloyed with Pb single atoms. *In situ* EXAFS is also capable of detecting structural changes, as reported by Weng *et al.,* and the transformation of Cu (II)phthalocyanine into 2 nm Cu nanoclusters during eCO$_2$RR was tackled. Notably, the nanoclusters returned to their original form of Cu (II) phthalocyanine upon removal of the voltage, indicating the process was reversible.[147]

1.4.2.2 *In situ* X−ray Diffraction

X−ray Diffraction (XRD) is a common characterization technique for nanoscale materials. The most prevalent type of X−ray diffraction is known as Bragg diffraction (**Figure 1.23a**), which is defined as the scattering of waves from a crystalline structure. Formulated by William Lawrence Bragg, the equation of Bragg's law relates wavelength to an angle of diffraction and lattice spacing:

$$n\lambda = 2d\,sin(\theta) \tag{1.11}$$

Where *n* is a numeric constant known as the order of the diffracted beam, λ is the wavelength of the beam, *d* denotes the distance between lattice planes, and θ represents the angle of the diffracted wave. Because of the nature of diffraction, waves will experience either constructive or destructive interference with other waves. In the same way, when an X−ray beam is diffracted off a crystal, the different parts of the diffracted beam will have seemingly stronger energy, while other parts will seem to lose energy. This is dependent mostly on the wavelength of the incident beam, and the spacing between the crystal lattices of the sample. XRD pattern analysis, such as Rietveld refinement, can provide more information that is complementary to various microscopic and spectroscopic methods. From peak intensity, atomic parameter information such as porosity can be obtained (**Figure 1.23b**). Unit cell parameters can be achieved from 2θ positions, which is widely used for phase identification and sample purity. Peak shape provides crystallinity, disorder and defects information, such as grain size, strain and stress.

In situ XRD is a powerful technique used in the study of eCO$_2$RR. It allows researchers to monitor the structural changes of catalysts during the reaction in real time, providing valuable insights into the reaction mechanisms and the performance of the catalysts. By analyzing the diffraction
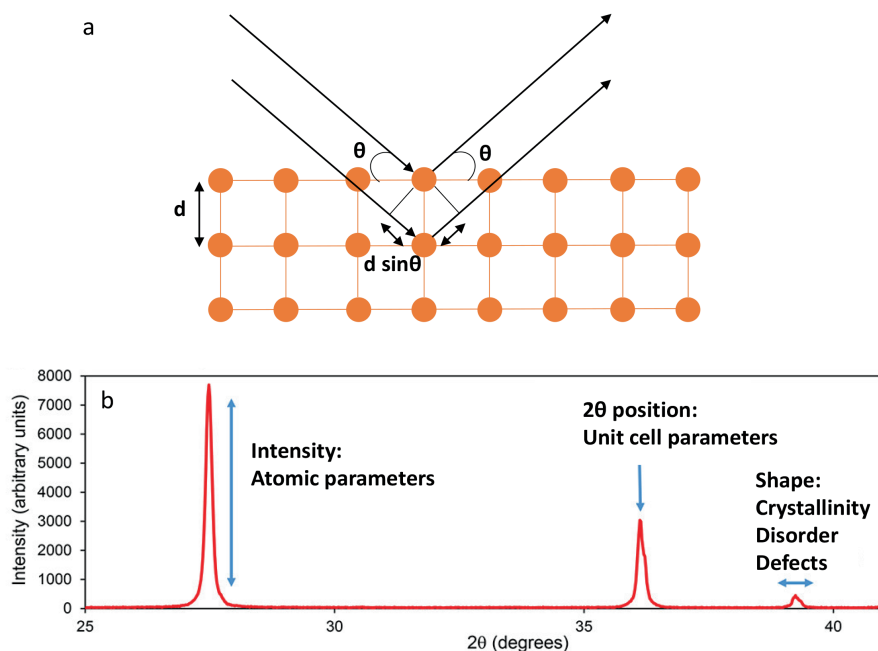
Figure 1.23. Schematic illustration of Bragg's law (a); A diffraction pattern as a plot of diffracted intensity as a function of angle 2θ (b), adapted form *Ref. 148.*

patterns of the materials under reaction conditions, *in situ* XRD can reveal information on the crystal structure, phase transformations, and even the size and morphology of the catalyst particles. This information is crucial for the development of new and more efficient catalysts for eCO$_2$RR.

For example, Zhang and co−workers utilized *in situ* Synchrotron Radiation X−ray Diffraction (SR−XRD) to investigate the structural changes of PbS catalysts during eCO$_2$RR.[149] The *in situ* SR−XRD analysis showed that the PbS nanocrystals underwent a rapid structural transformation to Pb thin films during eCO$_2$RR, which served as the catalytic surface. The structural change was found to be involving the conversion of PbS to PbCO$_3$ and further reduction to Pb. Janis and co−workers *in situ* monitored the changes in the amount of metallic copper phase and the size of the crystalline copper domains under potential pulses in eCO$_2$RR, through the alterations in the metallic Cu(311) Bragg peak area and width, respectively.[135] Specifically, the quantity of metallic copper and the size of the copper domains were found to be reduced during pulsed eCO$_2$RR compared to static eCO$_2$RR at −1.0 V vs. RHE (**Figure 1.24a**). The periodic reoxidation of the catalyst is also observed in *in situ* XRD measurement, as evidenced by the changes in the Cu(311) diffraction peak parameters, including the peak area, relative peak broadening (the coherence length of Cu domains), and lattice spacing (strain) (**Figures 1.24b**). In addition, the Bragg peak parameters from a Cu$_2$O−like phase were found during the pulsed treatment (**Figure 1.24c**). As a bulk technique, the XRD analysis is
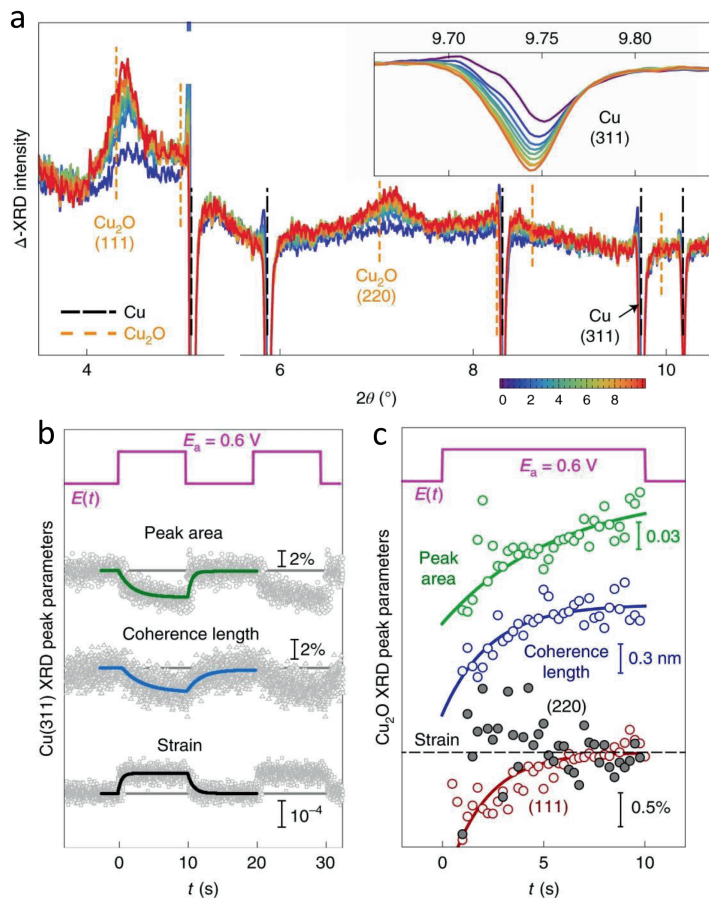
Figure 1.24. The alterations in the differential X−ray Diffraction (XRD) patterns during pulsed eCO$_2$RR, where the XRD intensities corresponding to t = 0 were subtracted (a). The inset depicts a magnified view of the (311) Bragg peak for metallic copper. The corresponding development of Cu(311) Bragg peak parameters is shown in (b), including the relative changes in the Bragg peak area, copper coherence length, and lattice strain. The progression of Cu$_2$O−like Bragg peak parameters during the anodic pulse(c). Adapted from *Ref. 135*.

limited in providing average structure information. It can be correlated with other techniques, such as XAS and TEM, which can provide more local and comprehensive structure information, and X−ray Photoelectron Spectroscopy (XPS) which is sensitive to surface structure, to fully understand the catalysts under reaction conditions.

1.5 Thesis Scope and Outline

The primary objective of this PhD Thesis is to study the electrocatalytic behavior of transition metal Cu and post−transition metals (*i.e.,* Pb, Sn, and Bi) in eCO_2RR. The structure–composition–performance relationships of these electrocatalysts are understood through a comprehensive analysis of *ex situ* and *in situ* characterizations across multiple scales. The Thesis encompasses various catalyst systems, from initial design and synthesis to critical structure identification, electrocatalytic performance evaluation, and *in situ* characterization. In specific cases, DFT calculations were also employed through extended collaboration to shed light on the reaction mechanisms. The ultimate goal is to reveal the reaction mechanism from diverse perspectives and provide new insights into the design of advanced electrocatalysts for eCO_2RR.

Chapter 2 focuses on the bimetallic CuPb electrocatalysts derived from industrial metallurgical waste for eCO_2RR. The metal ions were extracted from the waste through chemical treatment with ammonium chloride, and electrocatalysts with tunable compositions were fabricated through electrodeposition at varying cathodic potentials. The study found a volcano−shape relationship between eCO_2RR selectivity towards CO and the elemental ratio of Cu and Pb, with $Cu_{9.00}Pb_{1.00}$ achieving a maximum FE towards CO of 41.1% at –1.05 V vs. RHE, which is four times higher than that of pure Cu (9.7%, at –1.05 V vs. RHE), under the same electrocatalytic conditions. *In situ* Raman Spectroscopy measurements revealed that the optimal amount of Pb effectively improved the reducibility of the pristine Cu^+ and Pb^{2+} domains to metallic Cu and Pb, which boosted the selectivity towards CO by synergistic effects. This Chapter provides a framework for designing and tuning the selectivity of bimetallic electrocatalysts for CO_2 reduction through the valorization of metallurgical waste.

Chapter 3 explores the bimetallic CuSn system for eCO_2RR. It is found that a small doping concentration of Sn in CuO has a profound influence on the catalytic performance, boosting the FE up to 98% for CO at –0.75 V vs. RHE, with prolonged stable performance (FE > 90%) up to 15 h. Through a combination of *ex situ* and *in situ* characterization techniques, the *in situ* activation and reaction mechanism of the electrocatalyst at work was elucidated. *In situ* X−ray Diffraction and *in situ* Raman Spectroscopy measurements showed the reduction process of CuO to metallic Cu structure. Besides, *in situ* Raman Spectroscopy measurements revealed that the binding strength of the crucial adsorbed *CO intermediate was weakened through Sn doping, thereby favoring gaseous CO desorption. Meanwhile, the DFT calculation suggested that the Sn doping could indeed suppress the competitive HER and facilitate CO formation. This Chapter sheds light on the intimate relationship between bimetallic structure and catalytic behavior, resulting in stable and selective oxide−derived Sn−doped Cu electrocatalysts.

Chapter 4 focuses on the identification of the active site in Bi−based electrocatalysts for eCO_2RR, using Bi oxyhalide as a platform. Bismuth oxyhalide nanoplatelets were synthesized and found to be efficient in electrocatalytic CO_2 to formic acid (HCOOH FE of 91%, 76%, and 69% for BiOBr (BOB), BiOI (BOI), and BiOCl (BOC), at −1.05, −1.08, and −1.09 V vs. RHE, respectively).

The *in situ* generated metallic Bi structure was identified as the active site for CO_2 to formic acid conversion through *in situ* X−ray Diffraction. In both potential−dependent and time−dependent *in situ* XRD measurements, Bi(003) facets were observed for BiOBr and Bi(012) facets for BiOCl during reaction, whereas both contributed equally in BiOI. It was discovered that Bi(003) was more catalytically active than Bi(012) for formic acid production. Additionally, *in situ* X−ray Absorption Spectroscopy measurements revealed that the reconstruction of BiOCl proceeded rapidly, as shown by the short−lived transition state, whereas in BiOBr and BiOI the transition state lasted longer. This suggests that halogens in BiOX could determine the facet exposure of the formed Bi electrocatalyst during catalysis. These findings provide new insights into the active phase of Bi−based electrocatalysts during eCO$_2$RR and could potentially lead to the design of superior electrocatalysts for CO_2 conversion to liquid fuels.

1.6 References

[1]   S. J. Davis, K. Caldeira, H. D. Matthews, *Science* **2010**, *329*, 1330–1333.

[2]   C. Y. Chen, K. L. Yeh, R. Aisyah, D. J. Lee, J. S. Chang, *Bioresour. Technol.* **2011**, *102*, 71–81.

[3]   C. K. Savile, J. J. Lalonde, *Curr. Opin. Biotechnol.* **2011**, *22*, 818–823.

[4]   A. Alissandratos, C. J. Easton, *Beilstein J. Org. Chem.* **2015**, *11*, 2370–2387.

[5]   M. K. Lam, K. T. Lee, *Biotechnol. Adv.* **2012**, *30*, 673–690.

[6]   N. Russo, M. Piumetti, D. Fino, *J. Adv. Catal. Sci. Technol.* **2014**, *1*, 16–25.

[7]   S. N. Habisreutinger, L. Schmidt−Mende, J. K. Stolarczyk, *Angew. Chem. Int. Ed.* **2013**, *52*, 7372–7408.

[8]   E. E. Benson, C. P. Kubiak, A. J. Sathrum, J. M. Smieja, *Chem. Soc. Rev.* **2009**, *38*, 89–99.

[9]   C. Costentin, M. Robert, J. M. Savéant, *Chem. Soc. Rev.* **2013**, *42*, 2423–2436.

[10]   J. Grodkowski, P. Neta, *J. Phys. Chem. B* **2002**, *105*, 4967–4972.

[11]   L. E. I. Shi, G. Yang, K. A. I. Tao, *Acc. Chem. Res.* **2013**, *46*, 2–11.

[12]   S. Saeidi, N. A. S. Amin, M. R. Rahimpour, *J. CO$_2$ Util.* **2014**, *5*, 66–81.

[13]   D. Pakhare, J. Spivey, *Chem. Soc. Rev.* **2014**, *43*, 7813–7837.

[14]   S. G. Jadhav, P. D. Vaidya, B. M. Bhanage, J. B. Joshi, *Chem. Eng. Res. Des.* **2014**, *92*, 2557–2567.

[15]   Z. Sun, T. Ma, H. Tao, Q. Fan, B. Han, *Chem* **2017**, *3*, 560–587.

[16]   W. Zhou, K. Cheng, J. Kang, C. Zhou, V. Subramanian, Q. Zhang, Y. Wang, *Chem. Soc. Rev.* **2019**, *48*, 3193–3228.

[17]   S. Rönsch, J. Schneider, S. Matthischke, M. Schlüter, M. Götz, J. Lefebvre, P. Prabhakaran, S. Bajohr, *Fuel* **2016**, *166*, 276–296.

[18]   J. L. Inglis, B. J. MacLean, M. T. Pryce, J. G. Vos, *Coord. Chem. Rev.* **2012**, *256*, 2571–2600.

[19]   X. Mao, T. A. Hatton, *Ind. Eng. Chem. Res.* **2015**, *54*, 4033–4042.

[20]   J. Qiao, Y. Liu, F. Hong, J. Zhang, *Chem. Soc. Rev.* **2014**,43, 631−675.

[21]   N. S. Spinner, J. A. Vega, W. E. Mustain, *Catal. Sci. Technol.* **2012**, *2*, 19–28.

[22]   Y. Hori, *Mod. Asp. Electrochem.* **2008**, 89–189.

[23]   Y. Kwon, J. Lee, *Electrocatalysis* **2010**, *1*, 108–115.

[24]   Y. Yang, Y. Xiong, R. Zeng, X. Lu, M. Krumov, X. Huang, W. Xu, H. Wang, F. J. Disalvo, J. D. Brock, D. A. Muller, H. D. Abruñã, *ACS Catal.* **2021**, *11*, 1136–1178.

[25]   W. Luo, J. Zhang, M. Li, A. Züttel, *ACS Catal.* **2019**, *9*, 3783–3791.

[26]   D. T. Whipple, E. C. Finke, P. J. A. Kenis, *Electrochem. Solid−State Lett.* **2010**, *13*, 109–111.

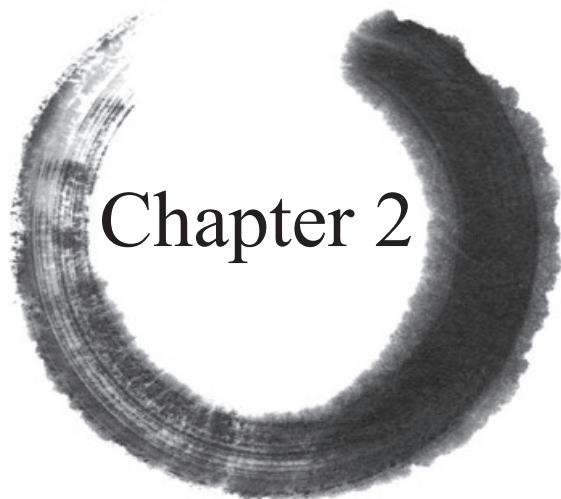[27]   D. A. Salvatore, D. M. Weekes, J. He, K. E. Dettelbach, Y. C. Li, T. E. Mallouk, C. P. Berlinguette, *ACS*

Energy Lett. **2018**, *3*, 149–154.

[28]   Y. Tomita, S. Teruya, O. Koga, Y. Hori, *J. Electrochem. Soc.* **2000**, *147*, 4164.

[29]   M. R. Thorson, K. I. Siil, P. J. A. Kenis, *J. Electrochem. Soc.* **2013**, *160*, F69–F74.

[30]   Y. Hori, A. Murata, R. Takahashi, *J. Chem. Soc. Faraday Trans. 1 Phys. Chem. Condens. Phases* **1989**, *85*, 2309–2326.

[31]   A. S. Varela, W. Ju, T. Reier, P. Strasser, *ACS Catal.* **2016**, *6*, 2136–2144.

[32]   M. Ramdin, A. R. T. Morrison, M. De Groen, R. Van Haperen, R. De Kler, L. J. P. Van Den Broeke, J. P. Martin Trusler, W. De Jong, T. J. H. Vlugt, *Ind. Eng. Chem. Res.* **2019**, *58*, 1834–1847.

[33]   Y.Y. Birdja, E. Pérez−Gallent, M.C. Figueiredo, A.J. Göttle, F. Calle−Vallejo, M.T.M. Koper, *Nat. Energy* **2019**, 4, 732–745.

[34]   C. W. Lee, N. H. Cho, K. D. Yang, K. T. Nam, *ChemElectroChem* **2017**, *4*, 2130–2136.

[35]   J. T. Feaster, C. Shi, E. R. Cave, T. Hatsukade, D. N. Abram, K. P. Kuhl, C. Hahn, J. K. Nørskov, T. F. Jaramillo, *ACS Catal.* **2017**, 7, 4822–4827.

[36]   H. A. Hansen, J. B. Varley, A. A. Peterson, J. K. Nørskov, *J. Phys. Chem. Lett.* **2013**, *4*, 388–392.

[37]   K. P. Kuhl, E. R. Cave, D. N. Abram, T. F. Jaramillo, *Energy Environ. Sci.* **2012**, *5*, 7050–7059.

[38]   Y. Hori, R. Takahashi, Y. Yoshinami, A. Murata, *J. Phys. Chem. B* **1997**, *101*, 7075–7081.

[39]   N. T. Suen, S. F. Hung, Q. Quan, N. Zhang, Y. J. Xu, H. M. Chen, *Chem. Soc. Rev.* **2017**, *46*, 337–365.

[40]   R. Z. Zhang, B. Y. Wu, Q. Li, L. Le Lu, W. Shi, P. Cheng, *Coord. Chem. Rev.* **2020**, *422*, 1–28.

[41]   S. Kaneco, K. Iiba, K. Ohta, T. Mizuno, A. Saji, *J. Electroanal. Chem.* **1998**, *441*, 215–220.

[42]   Q. Lu, F. Jiao, *Nano Energy* **2016**, *29*, 439–456.

[43]   R. Kortlever, I. Peters, S. Koper, M. T. M. Koper, *ACS Catal.* **2015**, *5*, 3916–3923.

[44]   Y. Lum, Y. Kwon, P. Lobaccaro, L. Chen, E. L. Clark, A. T. Bell, J. W. Ager, *ACS Catal.* **2016**, *6*, 202–209.

[45]   Y. Wang, L. Cao, N. J. Libretto, X. Li, C. Li, Y. Wan, C. He, J. Lee, J. Gregg, H. Zong, D. Su, J. T. Miller, T. Mueller, C. Wang, *J. Am. Chem. Soc.* **2019**, *141*, 16635–16642.

[46]   Q. Zhang, T. Gao, J. M. Andino, Y. Li, *Appl. Catal. B Environ.* **2012**, *123–124*, 257–264.

[47]   A. Bagger, W. Ju, A.S. Varela, P. Strasser, J. Rossmeisl, *ACS Catal.* **2019**, 9, 7894–7899.

[48]   S. Nitopi, E. Bertheussen, S. B. Scott, X. Liu, A. K. Engstfeld, S. Horch, B. Seger, I. E. L. Stephens, K. Chan, C. Hahn, J. K. Nørskov, T. F. Jaramillo, I. Chorkendorff, *Chem. Rev.* **2019**, *119*, 7610–7672.

[49]   R. G. Mariano, K. McKelvey, H. S. White, M. W. Kanan, *Science* **2017**, *358*, 1187–1192.

[50]   W. Zhu, R. Michalsky, Ö. Metin, H. Lv, S. Guo, C. J. Wright, X. Sun, A. A. Peterson, S. Sun, *J. Am. Chem. Soc.* **2013**, *135*, 16833–16836.

[51]   D. P. Summers, K. W. Frese, *J. Electrochem. Soc.* **1988**, *135*, 264–265.

[52]   A. Bagger, W. Ju, A. S. Varela, P. Strasser, J. Rossmeisl, *ChemPhysChem* **2017**, *18*, 3266–3273.

[53]   A. A. Peterson, F. Abild−Pedersen, F. Studt, J. Rossmeisl, J. K. Nørskov, *Energy Environ. Sci.* **2010**, *3*, 1311–1315.

[54]   D. Kim, J. Resasco, Y. Yu, A. M. Asiri, P. Yang, *Nat. Commun.* **2014**, *5*, 3002.

[55]   A. Dutta, M. Rahaman, N. C. Luedi, M. Mohos, P. Broekmann, *ACS Catal.* **2016**, *6*, 3804–3814.

[56]   R. Reske, H. Mistry, F. Behafarid, B. Roldan Cuenya, P. Strasser, *J. Am. Chem. Soc.* **2014**, *136*, 6978–6986.

[57]   C. W. Li, M. W. Kanan, *J. Am. Chem. Soc.* **2012**, *134*, 7231–7234.

[58]   A. Verdaguer−Casadevall, C. W. Li, T. P. Johansson, S. B. Scott, J. T. McKeown, M. Kumar, I. E. L. Stephens, M. W. Kanan, I. Chorkendorff, *J. Am. Chem. Soc.* **2015**, *137*, 9808–9811.

[59]   X. Feng, K. Jiang, S. Fan, M. W. Kanan, *ACS Cent. Sci.* **2016**, *2*, 169–174.

[60]   G. L. De Gregorio, T. Burdyny, A. Loiudice, P. Iyengar, W. A. Smith, R. Buonsanti, *ACS Catal.* **2020**, *10*, 4854–4862.

[61]   D. Raciti, C. Wang, *ACS Energy Lett.* **2018**, *3*, 1545–1556.

[62]   F. Scholten, K.C. Nguyen, J.P. Bruce, M. Heyde, B. Roldan Cuenya, *Angew. Chem. Int. Ed.* **2021**, *60*, 19169-19175.

[63] H. Mistry, A. S. Varela, C. S. Bonifacio, I. Zegkinoglou, I. Sinev, Y. W. Choi, K. Kisslinger, E. A. Stach, J. C. Yang, P. Strasser, B. R. Cuenya, *Nat. Commun.* **2016**, *7*, 12123.

[64] S. Lee, D. Kim, J. Lee, *Angew. Chem. Int. Ed.* **2015**, *54*, 14701–14705.

[65] D. Kim, S. Lee, J. D. Ocon, B. Jeong, J. K. Lee, J. Lee, *Phys. Chem. Chem. Phys.* **2015**, *17*, 824–830.

[66] Y. Li, F. Cui, M. B. Ross, D. Kim, Y. Sun, P. Yang, *Nano Lett.* **2017**, *17*, 1312–1317.

[67] K. D. Yang, W. R. Ko, J. H. Lee, S. J. Kim, H. Lee, M. H. Lee, K. T. Nam, *Angew. Chem. Int. Ed.* **2017**, *56*, 796–800.

[68] L. An, R. Chen, *J. Power Sources* **2016**, *320*, 127–139.

[69] X. Yang, P. Pachfule, Y. Chen, N. Tsumori, Q. Xu, *Chem. Commun.* **2016**, *52*, 4171–4174.

[70] R. L. Melen, *Science.* **2019**, *363*, 479–484.

[71] H. Wang, A. L. Rogach, *Chem. Mater.* **2014**, *26*, 123–133.

[72] A. Dutta, A. Kuzume, V. Kaliginedi, M. Rahaman, I. Sinev, M. Ahmadi, B. Roldán Cuenya, S. Vesztergom, P. Broekmann, *Nano Energy* **2018**, *53*, 828–840.

[73] Y. Chen, M. W. Kanan, *J. Am. Chem. Soc.* **2012**, *134*, 1986–1989.

[74] X. Zheng, P. De Luna, F. P. García de Arquer, B. Zhang, N. Becknell, M. B. Ross, Y. Li, M. N. Banis, Y. Li, M. Liu, O. Voznyy, C. T. Dinh, T. Zhuang, P. Stadler, Y. Cui, X. Du, P. Yang, E. H. Sargent, *Joule* **2017**, *1*, 794–805.

[75] S. Zhang, P. Kang, T. J. Meyer, *J. Am. Chem. Soc.* **2014**, *136*, 1734–1737.

[76] F. Li, L. Chen, G. P. Knowles, D. R. MacFarlane, J. Zhang, *Angew. Chem. Int. Ed.* **2017**, *129*, 520–524.

[77] N. Han, Y. Wang, J. Deng, J. Zhou, Y. Wu, H. Yang, P. Ding, Y. Li, *J. Mater. Chem. A* **2019**, *7*, 1267–1272.

[78] B. Kumar, V. Atla, J. P. Brian, S. Kumari, T. Q. Nguyen, M. Sunkara, J. M. Spurgeon, *Angew. Chem. Int. Ed.* **2017**, *56*, 3645–3649.

[79] X. An, S. Li, A. Yoshida, T. Yu, Z. Wang, X. Hao, A. Abudula, G. Guan, *ACS Appl. Mater. Interfaces* **2019**, *11*, 42114–42122.

[80] W. W. Luc, C. Collins, S. Wang, H. Xin, K. He, Y. Kang, F. Jiao, *J. Am. Chem. Soc.* **2017**, *139*, 1885−1893.

[81] S. Sarfraz, A. T. Garcia−Esparza, A. Jedidi, L. Cavallo, K. Takanabe, *ACS Catal.* **2016**, *6*, 2842–2851.

[82] J. E. Pander, M. F. Baruch, A. B. Bocarsly, *ACS Catal.* **2016**, *6*, 7824–7833.

[83] W. Oh, C. K. Rhee, J. W. Han, B. Shong, *J. Phys. Chem. C* **2018**, *122*, 23084–23090.

[84] J. H. Koh, D. H. Won, T. Eom, N. K. Kim, K. D. Jung, H. Kim, Y. J. Hwang, B. K. Min, *ACS Catal.* **2017**, *7*, 5071–5077.

[85] W. Zhang, Y. Hu, L. Ma, G. Zhu, P. Zhao, X. Xue, R. Chen, S. Yang, J. Ma, J. Liu, Z. Jin, *Nano Energy* **2018**, *53*, 808–816.

[86] N. Han, Y. Wang, H. Yang, J. Deng, J. Wu, Y. Li, Y. Li, *Nat. Commun.* **2018**, *9*, 1320.

[87] H. Yang, N. Han, J. Deng, J. Wu, Y. Wang, Y. Hu, P. Ding, Y. Li, Y. Li, J. Lu, *Adv. Energy Mater.* **2018**, *8*, 1–6.

[88] Q. Gong, P. Ding, M. Xu, X. Zhu, M. Wang, J. Deng, Q. Ma, N. Han, Y. Zhu, J. Lu, Z. Feng, Y. Li, W. Zhou, Y. Li, *Nat. Commun.* **2019**, *10*, 2807.

[89] C. W. Lee, J. S. Hong, K. D. Yang, K. Jin, J. H. Lee, H. Y. Ahn, H. Seo, N. E. Sung, K. T. Nam, *ACS Catal.* **2018**, *8*, 931–937.

[90] Z. Chen, K. Mou, X. Wang, L. Liu, *Angew. Chem. Int. Ed.* **2018**, *57*, 12790–12794.

[91] X. Sun, Q. Zhu, X. Kang, H. Liu, Q. Qian, Z. Zhang, B. Han, *Angew. Chem. Int. Ed.* **2016**, *128*, 6883–6887.

[92] S. Back, J. H. Kim, Y. T. Kim, Y. Jung, *Phys. Chem. Chem. Phys.* **2016**, *18*, 9652–9657.

[93] J. S. Yoo, R. Christensen, T. Vegge, J. K. Nørskov, F. Studt, *ChemSusChem* **2016**, *9*, 358–363.

[94] C. X. Zhao, Y. F. Bu, W. Gao, Q. Jiang, *J. Phys. Chem. C* **2017**, *121*, 19767–19773.

[95] C. H. Lee, M. W. Kanan, *ACS Catal.* **2015**, *5*, 465–469.

[96] M. Fan, S. Garbarino, G. A. Botton, A. C. Tavares, D. Guay, *J. Mater. Chem. A* **2017**, *5*, 20747–20756.

[97] F. Köleli, D. Balun, *Appl. Catal. A Gen.* **2004**, *274*, 237–242.

[98] A. M. Ismail, G. F. Samu, H. C. Nguyën, E. Csapó, N. López, C. Janáky, *ACS Catal.* **2020**, *10*, 5681–5690.

[99]   J. H. C. Smith, *Plant Physiol.* **1943**, *18*, 207–223.

[100]   Z. M. Detweiler, J. L. White, S. L. Bernasek, A. B. Bocarsly, *Langmuir* **2014**, *30*, 7593–7600.

[101]   J. L. White, A. B. Bocarsly, *J. Electrochem. Soc.* **2016**, *163*, H410–H416.

[102]   W. Luo, W. Xie, M. Li, J. Zhang, A. Züttel, *J. Mater. Chem. A* **2019**, *7*, 4505–4515.

[103]   Z. Xia, M. Freeman, D. Zhang, B. Yang, L. Lei, Z. Li, Y. Hou, *ChemElectroChem* **2018**, *5*, 215.

[104]   C. I. Shaughnessy, D. T. Jantz, K. C. Leonard, *J. Mater. Chem. A* **2017**, *5*, 22743–22749.

[105]   A. Wang, X. Y. Liu, C. Y. Mou, T. Zhang, *J. Catal.* **2013**, *308*, 258–271.

[106]   M. Sankar, N. Dimitratos, P. J. Miedziak, P. P. Wells, C. J. Kiely, G. J. Hutchings, *Chem. Soc. Rev.* **2012**, *41*, 8099–8139.

[107]   W. Lv, R. Zhang, P. Gao, L. Lei, *J. Power Sources* **2014**, *253*, 276–281.

[108]   Y. Li, Q. Sun, *Adv. Energy Mater.* **2016**, *6*, 1600463.

[109]   W. Ren, X. Tan, J. Qu, S. Li, J. Li, X. Liu, S. P. Ringer, J. M. Cairney, K. Wang, S. C. Smith, C. Zhao, *Nat. Commun.* **2021**, *12*, 1449.

[110]   Q. Li, J. Fu, W. Zhu, Z. Chen, B. Shen, L. Wu, Z. Xi, T. Wang, G. Lu, J. J. Zhu, S. Sun, *J. Am. Chem. Soc.* **2017**, *139*, 4290–4293.

[111]   Y. Lan, G. Niu, F. Wang, D. Cui, Z. Hu, *ACS Appl. Mater. Interfaces* **2020**, *12*, 36128–36136.

[112]   Z. B. Hoffman, T. S. Gray, Y. Xu, Q. Lin, T. B. Gunnoe, G. Zangari, *ChemSusChem* **2019**, *12*, 231–239.

[113]   H. Ren, X. Wang, X. Zhou, T. Wang, Y. Liu, C. Wang, Q. Guan, W. Li, *J. Energy Chem.* **2023**, *79*, 263–271.

[114]   Y. Wang, L. Cheng, Y. Zhu, J. Liu, C. Xiao, R. Chen, L. Zhang, Y. Li, C. Li, *Appl. Catal. B Environ.* **2022**, *317*, 121650.

[115]   Z. Wang, Q. Yuan, J. Shan, Z. Jiang, P. Xu, Y. Hu, J. Zhou, L. Wu, Z. Niu, J. Sun, T. Cheng, W. A. Goddard, *J. Phys. Chem. Lett.* **2020**, *11*, 7261–7266.

[116]   M. Watanabe, M. Shibata, A. Katoh, T. Sakata, M. Azuma, *J. Electroanal. Chem.* **1991**, *305*, 319–328.

[117]   Y. Wang, H. Hu, Y. Sun, Y. Tang, L. Dai, Q. Hu, A. Fisher, X. J. Yang, *Adv. Mater. Interfaces* **2019**, *6*, 1–7.

[118]   C. Kim, T. Möller, J. Schmidt, A. Thomas, P. Strasser, *ACS Catal.* **2019**, *9*, 1482–1488.

[119]   P. Wang, H. Yang, Y. Xu, X. Huang, J. Wang, M. Zhong, T. Cheng, Q. Shao, *ACS Nano* **2021**, *15*, 1039–1047.

[120]   S. Rasul, D. H. Anjum, A. Jedidi, Y. Minenkov, L. Cavallo, K. Takanabe, *Angew. Chem. Int. Ed.* **2015**, *127*, 2174–2178.

[121]   Z. B. Hoffman, T. S. Gray, K. B. Moraveck, T. B. Gunnoe, G. Zangari, *ACS Catal.* **2017**, *7*, 5381–5390.

[122]   H. Xie, S. Chen, F. Ma, J. Liang, Z. Miao, T. Wang, H. L. Wang, Y. Huang, Q. Li, *ACS Appl. Mater. Interfaces* **2018**, *10*, 36996–37004.

[123]   A. D. Handoko, F. Wei, Jenndy, B. S. Yeo, Z. W. Seh, *Nat. Catal.* **2018**, *1*, 922–934.

[124]   K. Tran, Z. W. Ulissi, *Nat. Catal.* **2018**, *1*, 696–703.

[125]   W. Van Der Stam, *Chem. Mater.* **2022**, *35*, 386−394.

[126]   H. An, L. Wu, L. D. B. Mandemaker, S. Yang, J. de Ruiter, J. H. J. Wijten, J. C. L. Janssens, T. Hartman, W. van der Stam, B. M. Weckhuysen, *Angew. Chem. Int. Ed.* **2021**, *60*, 16576–16584.

[127]   K. Yang, R. Kas, W. A. Smith, *J. Am. Chem. Soc.* **2019**, *141*, 15891–15900.

[128]   P. Grosse, A. Yoon, C. Rettenmaier, A. Herzog, S. W. Chee, B. Roldan Cuenya, *Nat. Commun.* **2021**, *12*, 6736.

[129]   G. H. Simon, C. S. Kley, B. Roldan Cuenya, *Angew. Chem. Int. Ed.* **2021**, *60*, 2561–2568.

[130]   R. M. Arán−Ais, R. Rizo, P. Grosse, G. Algara−Siller, K. Dembélé, M. Plodinec, T. Lunkenbein, S. W. Chee, B. Roldan Cuenya, *Nat. Commun.* **2020**, *11*, 3489.

[131]   J. Timoshenko, B. Roldan Cuenya, *Chem. Rev.* **2021**, *121*, 882–961.

[132]   X. Wang, K. Klingan, M. Klingenhof, T. Möller, J. Ferreira de Araújo, I. Martens, A. Bagger, S. Jiang, J. Rossmeisl, H. Dau, P. Strasser, *Nat. Commun.* **2021**, *12*, 794.

[133]   D. Gao , F. Scholten, B. R. Cuenya, *ACS Catal.* **2017,** 7, 5112–5120.

[134]   H. Mistry, Y. W. Choi, A. Bagger, F. Scholten, C. S. Bonifacio, I. Sinev, N. J. Divins, I. Zegkinoglou, H. S. Jeon, K. Kisslinger, E. A. Stach, J. C. Yang, J. Rossmeisl, B. Roldan Cuenya, *Angew. Chem. Int. Ed.* **2017**, *56*,

11394–11398.

[135] J. Timoshenko, A. Bergmann, C. Rettenmaier, A. Herzog, R. M. Arán–Ais, H. S. Jeon, F. T. Haase, U. Hejral, P. Grosse, S. Kühl, E. M. Davis, J. Tian, O. Magnussen, B. Roldan Cuenya, *Nat. Catal.* **2022**, *5*, 259–267.

[136] M. Farmand, A. T. Landers, J. C. Lin, J. T. Feaster, J. W. Beeman, Y. Ye, E. L. Clark, D. Higgins, J. Yano, R. C. Davis, A. Mehta, T. F. Jaramillo, C. Hahn, W. S. Drisdell, *Phys. Chem. Chem. Phys.* **2019**, *21*, 5402–5408.

[137] W. Van Der Stam, F. T. Rabouw, S. J. W. Vonk, J. J. Geuchies, H. Ligthart, A. V. Petukhov, C. De Mello Donega, *Nano Lett.* **2016**, *16*, 2608–2614.

[138] N. Heidary, K. H. Ly, N. Kornienko, *Nano Lett.* **2019**, *19*, 4817–4826.

[139] A. Dutta, A. Kuzume, M. Rahaman, S. Vesztergom, P. Broekmann, *ACS Catal.* **2015**, *5*, 7498–7502.

[140] P. L. Stiles, J. A. Dieringer, N. C. Shah, R. P. Van Duyne, *Annu. Rev. Anal. Chem.* **2008**, *1*, 601–626.

[141] J. Timoshenko, A. I. Frenkel, *ACS Catal.* **2019**, *9*, 10192–10211.

[142] S. Bordiga, E. Groppo, G. Agostini, J. A. Van Bokhoven, C. Lamberti, *Chem. Rev.* **2013**, *113*, 1736–1850.

[143] J. D. Grunwaldt, B. Kimmerle, A. Baiker, P. Boye, C. G. Schroer, P. Glatzel, C. N. Borca, F. Beckmann, *Catal. Today* **2009**, *145*, 267–278.

[144] J. Timoshenko, H. S. Jeon, I. Sinev, F. T. Haase, A. Herzog, B. Roldan Cuenya, *Chem. Sci.* **2020**, *11*, 3727–3736.

[145] H. Mistry, A. S. Varela, C. S. Bonifacio, I. Zegkinoglou, I. Sinev, Y. W. Choi, K. Kisslinger, E. A. Stach, J. C. Yang, P. Strasser, B. R. Cuenya, *Nat. Commun.* **2016**, *7*, 12123.

[146] T. Zheng, C. Liu, C. Guo, M. Zhang, X. Li, Q. Jiang, W. Xue, H. Li, A. Li, C. W. Pao, J. Xiao, C. Xia, J. Zeng, *Nat. Nanotechnol.* **2021**, *16*, 1386–1393.

[147] Z. Weng, Y. Wu, M. Wang, J. Jiang, K. Yang, S. Huo, X. F. Wang, Q. Ma, G. W. Brudvig, V. S. Batista, Y. Liang, Z. Feng, H. Wang, *Nat. Commun.* 2018, 9, 415.

[148] J. S. O. Evans, I. R. Evans, *J. Chem. Educ.* **2021**, *98*, 495–505.

[149] Z. Zhang, C. Liu, J. T. Brosnahan, H. Zhou, W. Xu, S. Zhang, *J. Mater. Chem. A* **2019**, *7*, 23775–23780.

Chapter 2

Waste−Derived Copper−Lead Electrocatalysts for CO$_2$ Reduction

Abstract

It remains a real challenge to control the selectivity of the electrocatalytic CO$_2$ reduction (eCO$_2$RR) reaction to valuable chemicals and fuels. Most of the electrocatalysts are made of non−renewable metal resources, which hampers their large−scale implementation. This Chapter reports the preparation of bimetallic copper−lead (CuPb) electrocatalysts from industrial metallurgical waste. The metal ions were extracted from the metallurgical waste through simple chemical treatment with ammonium chloride, and Cu$_x$Pb$_y$ electrocatalysts with tunable compositions were fabricated through electrodeposition at varying cathodic potentials. X−ray spectroscopy techniques showed that the pristine electrocatalysts consist of Cu^0, Cu^{1+} and Pb^{2+} domains, and no evidence for alloy formation was found. A volcano−shape relationship between eCO$_2$RR selectivity toward two electron products was found, such as CO, and the elemental ratio of Cu and Pb. A maximum Faradaic Efficiency towards CO (41.1%) was found for Cu$_{9.00}$Pb$_{1.00}$, which was four times higher than that of pure Cu (9.7%), under the same electrocatalytic conditions. *In situ* Raman Spectroscopy revealed that the optimal amount of Pb effectively improved the reducibility of the pristine Cu^{1+} and Pb^{2+} domains to metallic Cu and Pb, which boosted the selectivity towards CO by synergistic effects. This Chapter provides a framework of thinking to design and tune the selectivity of bimetallic electrocatalysts for CO$_2$ reduction through valorization of metallurgical waste.

2.1 Introduction

Capture and electrochemical conversion of carbon dioxide (CO_2) to value−added products with renewably generated electricity is a promising strategy towards mitigation of the large scale emission of greenhouse gases into the atmosphere.[1,2] Copper (Cu) is a unique metal because of its moderate binding energy of crucial reaction intermediates, which enables Cu to produce both simple (*i.e.*, CO and HCOOH) and more complex reduction products (*i.e.*, C_{2+} hydrocarbons and oxygenates) through electrocatalytic CO_2 reduction reaction (eCO_2RR).[3,4] However, it is still a challenge to direct and control the selectivity of Cu for eCO_2RR, and an increase in the demand for Cu calls for alternative sources of this metal.[5–7] In this regard, using metal residues produced in the metallurgical industry as raw material to prepare electrocatalysts for CO_2 conversion, has gained researchers' attention recently. Fayalite slags, the residue from the zinc ore metallurgical industry, are rich in many potentially useful electrocatalytic elements, such as iron (Fe), zinc (Zn), copper (Cu), and lead (Pb) (**Table 2.1**).Compared to the traditional landfilling of these slags, which may change the original geological structures and worsen the quality of groundwater, unlocking the potential of this industrial waste to produce catalytic materials that convert CO_2 into valuable chemicals has the potential to create a self−sustainable cycle.[8–11]

A promising approach to improve the electrocatalytic selectivity of Cu for eCO_2RR is the utilization of bimetallic systems.[12–14] Many reports have demonstrated that the binding strength of specific intermediates on the bimetallic catalyst surface could be rationally modified based on the relative oxygen (O) and hydrogen (H) affinities of the two metals.[15,16] Post−transition metals, such as tin (Sn), bismuth (Bi), lead (Pb) and indium (In), are known to have weak H binding and strong O binding, which resulted in excellent abilities to suppress the competitive hydrogen evolution reaction (HER) in eCO_2RR.[17–20] Bimetallic Cu−based catalysts including post−transition metals, such as Cu/In, Cu/Sn and Cu/Bi, have been recently reported to boost the selectivity for C_1 products at moderate current density.[21–23] Furthermore, it is known that product selectivity in a Cu−based bimetallic system is highly sensitive to the composition of the catalysts, and variations in metal ratios can

Table 2.1 The Inductively Coupled Plasma−Optical Emission Spectrometry (ICP−OES) result of the raw fayalite slags.

Elements	Fe %	Si %	Zn %	Al %	Pb %	Cu %	Na %	Ga %	Mg %	Mn %	Cr %
Conc.	43.65	16.06	4.24	1.55	0.76	0.51	0.43	0.32	0.26	0.20	0.14
Elements	Ti %	S %	P %	K %	Co %	Ba ppm	Zr ppm	Mo ppm	Sr ppm	V ppm	Be ppm
Conc.	0.09	0.09	0.07	0.07	0.05	176	107	88	65	23	14
Elements	Sb ppm	Li ppm	B ppm	Cd ppm	Sc ppm	Y ppm					
Conc.	12	6	5	5	3	2					

lead to an enhanced selectivity for specific products.[24–29] Tuning the structure and composition of electrocatalysts therefore constitutes an attractive strategy to improve the selectivity of eCO$_2$RR catalysts.

In this Chapter, a series of Cu$_x$Pb$_y$ (x + y = 10) electrocatalysts with tunable compositions were fabricated directly from industrial metallurgical waste through chemical extraction and electrodeposition at varying potentials, and deployed them in eCO$_2$RR. The morphology and structure of the Cu$_x$Pb$_y$ electrocatalysts were identified by *ex situ* Scanning Electron Microscopy (SEM), high−resolution High Angle Annular Dark Field Scanning Transmission Electron Microscopy (HAADF−STEM), X−ray Photoelectron Spectroscopy (XPS), X−ray Diffraction (XRD) and X−ray Absorption Spectroscopy (XAS), which indicate that the pristine Cu$_x$Pb$_y$ electrocatalysts are phase−separated structures with Cu^0, Cu^{1+} and Pb^{2+} domains. The electrocatalytic performance showed that the selectivity towards CO could be tuned by varying the amount of Pb and the maximum Faradaic Efficiency (41.1% CO at −1.05 V vs. RHE) was found for Cu$_{9.00}$Pb$_{1.00}$ in 0.1 M KHCO$_3$ aqueous solution, which was four−times higher than that of pure Cu (9.7 % CO at −1.05 V vs. RHE) under the same electrochemical conditions. We found that the Cu^{1+} and Pb^{2+} domains were reduced *in situ* to their active metallic counterparts, as evidenced by *in situ* Raman Spectroscopy and *ex situ* XRD measurements, and that the reducibility of the metal species was influenced by the electrocatalyst composition. These results suggest that there is a synergy between electrochemically reduced Cu and Pb, which tunes the reaction pathway to CO formation. This study provides a new understanding of synergistic effects in Cu−based bimetallic system for eCO$_2$RR and constructs a framework for rational design of bimetallic electrocatalysts from industrial waste.

2.2 Methods

2.2.1 Waste Extraction

The studied fayalite slags were provided by Aurubis Beerse NV. Four different extraction strategies were applied to the fayalite slags under study. Before taking these treatments, the fayalite slags (0.5−1.0 cm diameter, **Figure 2.1a**) were ground into fine powders with a particle size of 75 μm. Acid treatment was conducted by mixing sulfuric acid and the ground fayalite slags. When a concentrated sulfuric acid was used, the fayalite slags almost stayed unchanged because of surface passivation. 5 M sulfuric acid was also tried with and without heating. A black gel was formed and difficult to be further separated when heated at 40 °C for 1 h, whereas no obvious change was observed under 25 °C. To remove silicon from the residue system, alkali solution (NaOH, Sigma−Aldrich, powder, reagent grade, ≥ 98.0%) was added to the fayalite slags. A certain amount of the ground powders was added to the NaOH aqueous solution (from 1 M to 10 M), stirring for a certain time (from 2 h to 24 h). The treatment temperatures ranged from 50 °C to 150 °C. Filtration was applied to separate liquid and solid phases. After the treatment, iron oxides were formed on the surface of fayalite slag with an increased roughness (**Figures 2.1b, c**). However, the main phase of the treated samples remains fayalite structure (**Figures 2.1e, g**) and inactive for most possible applications. Thermal treatment was employed by annealing the ground fayalite slags at temperatures ranging from 500 °C to 1100 °C for 2 h
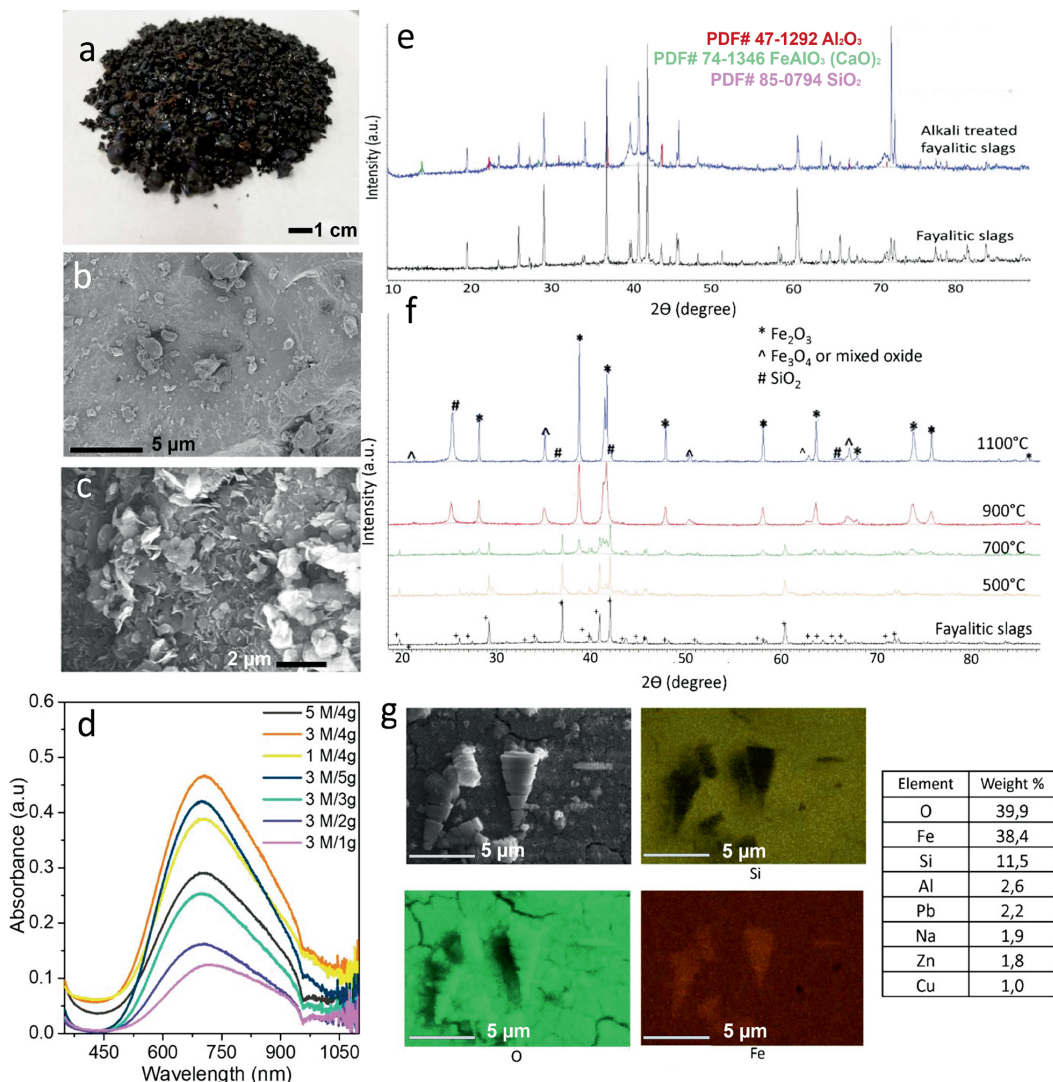
Figure 2.1. Picture of the fayalite slags under study (a); Scanning Electron Microscopy (SEM) images of the fayalite slags (b) and the alkali–treated fayalite slags (c); UV–Vis spectra (d) of precursor solutions collected from complexing extraction of the fayalite slags. Different amounts of fayalite slags were mixed with NH_4Cl aqueous solution with different concentrations, marked as X M/Y g (X=1, 3, 5; Y=1, 2, 3, 4, 5) in the graph. The highest concentration of Cu complex can be obtained by using 3 M NH_4Cl solution and 4 g fayalite slags. X–ray Diffraction (XRD) patterns of the fayalite slags and the alkali–treated fayalite slags (e); XRD patterns of the fayalite slags and the thermal–treated fayalite slags under different temperatures (f); SEM Energy Dispersive X–ray Spectroscopy (EDS)–mapping of the alkali–treated fayalite slags (g), with an inserted table showing element ratios.

in air. Although the structure of the fayalite slags has transferred into iron oxides and SiO_2 (**Figure 2.1f**) under the temperature as high as 1100 °C, the whole chemical environment inside the treated samples was complicated since all impurities still remain. Acid treatment was further applied to the thermal−treated slags. Unfortunately, surface passivation occurred. The only working treatment is the complexing treatment. Different amounts (1, 2, 3, 4, 5 g) of ground powders were mixed with 12 mL NH_4Cl (Sigma−Aldrich, powder, ACS reagent, $\geq$ 99.5%) aqueous solution with different concentration (1, 3, 5 M), followed by stirring for 24 h at room temperature. After filtration, a blue solution was collected. 0.5 mL of the filtrate was used for UV−Vis spectroscopy measurements, to analyze the complex concentration of $[Cu(NH_3)_4]^{2+}/[CuCl_4]^{2-}$. As suggested in **Figure 2.1d**, the strongest intensity can be obtained in the filtrate collected from the combination of 4 g fayalite slags and 3 M NH_4Cl aqueous solution, suggesting the highest extraction efficiency.

2.2.2 Catalyst Preparation

The Cu−based electrocatalysts were obtained by one−step electrodeposition. 12 mL filtrate, collected from the complexing extraction using 4 g fayalite slags and 3 M NH_4Cl solution, was diluted by mixing with 12 mL deionized water. The diluted filtrate (24 mL) was used as electrolyte for all samples, except for control samples Cu−1 and Pb−1. The NH_4Cl can be reused for subsequent extraction of metals from industrial waste residues. Carbon paper (effective geometric surface area 1 cm^2) was used as substrate during electrodeposition, Pt wire was used as counter electrode and Ag/AgCl electrode was used as reference electrode (ET069−3, −0.205 V vs. SHE, eDAQ). The electrocatalysts were prepared by applying various potentials (−0.6 V, −0.8 V and −1.0 V vs. Ag/AgCl) for 600 s with a stirring rate of 350 rpm to achieve $Cu_{9.20}Pb_{0.80}$, $Cu_{9.00}Pb_{1.00}$ and $Cu_{8.65}Pb_{1.35}$, respectively. The obtained samples were washed with MilliQ water before the electrochemical measurements. The reference Cu−1 was obtained by electrodeposition at −0.8 V vs. Ag/AgCl from an aqueous solution containing 0.1 M $CuCl_2$ (Sigma−Aldrich, powder, 99.0%) and 3 M NH_4Cl. The reference Pb−1 was prepared through galvanostatic electrodeposition at −10 mA in 0.1 M $PbCl_2$ (Sigma−Aldrich, powder, 98.0%) solution.

2.2.3 Characterization

2.2.3.1 Basic Characterization

UV−Vis Spectroscopy was performed by using an Avantes DH−2000−BAL Deuterium lamp and an Avantes StarLine AvaSpec−2048 L spectrometer with a liquid−immersed probe head. The spectra were obtained in the range 200–1100 nm. The elemental composition of the pristine samples was characterized by Inductively Coupled Plasma−Optical Emission Spectrometry (ICP−OES, PerkinElmer Optima 8300 Optical Emission Spectrometer). The calibration solutions were prepared by diluting standard calibration solutions (PerkinElmer, N9300233) by 5% HNO_3 solution into different concentrations: 0.0 ppm, 0.2 ppm, 0.4 ppm, 0.6 ppm, 0.8 ppm and 1.0 ppm. The fayalite slags were dissolved in aqua regia for 48 hours, followed by a filtration to remove the undissolved species. Electrodeposited samples were dissolved in 65% HNO_3 (2 mL, Suprapur) before oxidation. The obtained solutions were diluted with 5% HNO_3 solution to achieve an optimal measurement concentration. Atomic Force Microscopy (AFM) measurements were performed with a Bruker Multimode microscope instrument, using silicon NSC−16 SCANASYST−AIR in ScanAsyst mode. X−ray Diffraction (XRD) measurements were performed on a Bruker D8 Phaser diffractometer, equipped

with a Cu Kα source (λ=1.54 Å). The morphology and elemental distribution were determined with Scanning Electron Microscopy (SEM, FEI Helios NanoLab 600) and high−resolution High Angle Annular Dark Field Scanning Transmission Electron Microscopy (HAADF−STEM) and coupled STEM Energy Dispersive X−ray (STEM−EDX) measurement (FEI Titan^3, 200 keV). To do this, the catalyst materials were stripped off the carbon paper electrodes by sonication in absolute ethanol for the HAADF−STEM measurements. In the X−ray Photoelectron Spectroscopy (XPS) measurements, a K−Alpha X−ray photoelectron spectrometer by ThermoFisher scientific with an aluminum (K=1486.68 eV) X−ray source was used to collect the X−ray photoelectron spectra. All spectra were calibrated with reference to the C 1s at 284.8 eV. The curve fitting was carried out using Shirley/Linear background and a combination of Gaussian and Lorentzian functions. X−ray Absorption Spectroscopy (XAS) measurements were performed in air by the Beijing Synchrotron Radiation Facility (1W1B, BSRF) at the Cu K−edge and Pb L$_3$−edge.

2.2.3.2 *In situ* Raman Spectroscopy Measurements

In situ Raman spectra were collected using a Renishaw InVia Raman microscope and 785 nm excitation laser, coupled with a Nikon N40X−NIR water−dipping objective. To avoid laser damage, the laser power was set to below 1.5 mW. The time interval for each spectrum is 1 s for all measured samples. An Autolab PGSTAT 101 potentiostat was used for cyclic voltammetry (CV) measurements which was carried out under a scanning rate of 50 mV s^{-1} in CO$_2$−saturated 0.1 M KHCO$_3$ (Sigma−Aldrich, powder, ACS reagent, 99.7%) electrolyte solution (pH 6.8), from −1.0 V to 1.6 V vs. RHE.

2.2.4 Electrochemical Measurements

The Ivium compactstat.h10800 potentiostat was used for all electrochemical measurements. The samples were loaded in a standard three−electrode system in a two−compartment H−cell separated by a proton exchange membrane (Nafion 117, Dupont). Fresh samples were used for the activity measurements at different applied potentials, and averaged over four measurements. Ag/AgCl (ET072−3, −0.205 V vs. SHE) and a Pt−mesh were employed as reference electrode and counter electrode, respectively. 0.1 M KHCO$_3$ aqueous solution saturated with CO$_2$ (pH=6.8) was applied as electrolyte for all CO$_2$ reduction experiments. During the experiments, CO$_2$ was continuously delivered into the cathodic compartment at a constant rate of 8.7 mL min^{-1}. The as−prepared samples were employed as working electrode directly and held for 40 min at least under different constant biases (−0.85 V, −0.95 V, −1.05 V, −1.15 V, −1.25 V vs. RHE). To calculate the Electrochemical Active Surface Area (ECSA), the double layer capacitance (C$_{dl}$) was determined through the Cyclic Voltammetry (CV) measurements in the non−Faradaic region at 30, 50, 70, 100, 150 mV s^{-1} scan rate by a linear fit of the charging current. The ECSA of as−prepared sample was obtained by subtracting C$_{dl}$ of carbon paper and normalizing the C$_{dl}$ difference to that of Cu foil. Regarding the *iR* correction, the solution resistance was calculated by Electrochemical Impedance Spectroscopy (EIS) with a frequency range of 0.01 to 100 kHz.

The measured potential values were converted to the Reversible Hydrogen Electrode (RHE) using Equation 2.1:

$$E \ (vs. \ RHE) = E \ (vs. \ Ag/AgCl) + 0.205 \ V + 0.059 \times pH - iR \tag{2.1}$$

2.2.5 Products Analysis

The gas products at each fixed potential were quantified by an online Gas Chromatograph (GC) equipped with a Thermal Conductivity Detector (TCD) and a Flame Ionization Detector (FID). ^{1}H Nuclear Magnetic Resonance (NMR) spectroscopy was employed to determine the liquid products using water suppression mode. 0.5 mL of electrolyte was mixed with 0.1 mL of deuterated water (D_2O) as lock solvent. Then, 0.05 μL of dimethyl sulfoxide (DMSO) was used as the internal reference.

The Faradaic Efficiency (FE) of gas products was calculated using Equation 2.2:

$$FE = (n \cdot F \cdot c \cdot f) / (Vm \cdot I \cdot 60\ sec/min \cdot 1000000\ ppm) \times 100\% \qquad (2.2)$$

Where n represents the number of electrons involved to produce the related products from CO_2 or H_2O (*e. g.,* 2 for CO and H_2, 12 for C_2H_4); F is the Faraday constant (96485 C mol^{-1}); c is the concentration of the product measured by GC; f is the gas flow rate (mL min^{-1}); I is the average measured current in 1 min (A); Vm is the volume of 1 mol gas at room temperature and pressure (24451 mL mol^{-1}).

The FE of liquid products was calculated by using Equation 2.3:

$$FE = (n \cdot F \cdot M \cdot V) / (I \cdot t) \times 100\% \qquad (2.3)$$

Where n is the number of electrons transferred to form the desired product (*e. g.,* 2 for HCOOH); F is the Faraday constant (96485 C mol^{-1}); M is the Molar concentration of the liquid product (mol L^{-1}); V is the liquid volume (L); I is the average measured current in 1 minute (A); t is the duration time (s).

Production rate of all products were calculated by using Equation 2.4:

$$production\ rate = (FE \cdot I) / (n \cdot F \cdot S) \qquad (2.4)$$

Where n represents the number of electrons needed to produce the related products; F is the Faraday constant (96485 C mol^{-1}); I is the average measured current in 1 min (A); S represents the geometric area of the electrode (cm^2).

2.3 Results and Discussion

2.3.1 Catalyst Preparation and Characterization

As the main solid residue from the metallurgical industry, fayalite slags are composed of irregular particles with diameters from 0.50 cm to 1.00 cm. Their main crystal structure is found to be fayalite ($Fe_2(SiO_4)$ mineral), as evidenced by X−ray Diffraction (XRD) measurements (**Figure A1**), in which over twenty different elements co−exist as analyzed with Inductively Coupled Plasma−Optical Emission Spectrometry (ICP−OES, **Table 2.1**). Due to their complicated composition and high chemical resistance, degradation in a natural environment and direct reuse of the fayalite slags are difficult to achieve. To find the most effective extraction strategy, we have performed different treatments to the fayalite slags and compared their feasibility for metal ion extraction, as shown in **Figure 2.2**.

Most commonly employed extraction techniques were first conducted to fayalite slags, including acid treatment, alkali treatment and thermal treatment. It was found that neither the use of acid or alkali
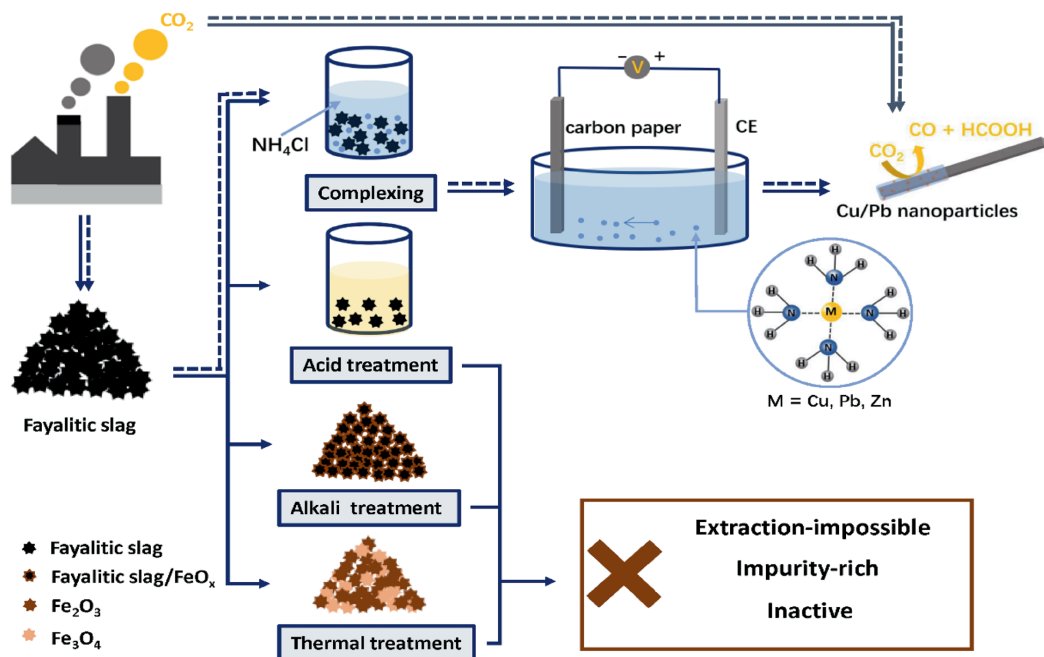
Figure 2.2. Comparison of different residue treatments and the preparation of waste−derived copper−lead bimetallic electrocatalysts through chemical extraction and electrodeposition.

was capable of further processing the fayalite slags due to the passivation and the residual impurities, which makes the separation and extraction impossible (see more details in Method section). Thermal treatment successfully changed the fayalite slags into iron oxide and SiO_2 **(Figure 2.1f)** but still kept most impurities inside. In contrast to the above−mentioned treatments, complexing with ammonium chloride (NH_4Cl) presents a more facile, sustainable and safer way to reuse this industrial residue. By complexing with NH_3 and Cl^-, certain elements could be selectively extracted from the fayalite slags (such as copper (Cu), lead (Pb) and zinc (Zn), as shown in **Table 2.2**). With the subsequent electrodeposition, we managed to fabricate the electrocatalysts with controllable composition and structure.

As illustrated in **Figure 2.2**, the metal elements were extracted from the fayalite slags by mixing with concentrated NH_4Cl aqueous solution. The Cu^{2+} and Pb^{2+} cations from the fayalite slags could form stable complexes with NH_3 and Cl^- ($[Cu/Pb (NH_3)_4]^{2+}$ and $[CuCl_4]^{2-}$) after one day of stirring at room temperature (see **Figure 2.1d** for the corresponding UV−vis spectra).[34,35] The resulting solution was filtrated to remove undissolved species and the obtained filtrate was subsequently transferred into a one−cell electroplating bath to fabricate the working electrode for eCO_2RR catalysis. Different potentials (–0.6 V to –1.4 V with steps of –0.2 V, potentials are given vs. Ag/AgCl) were used during electrodeposition in order to tune the electrocatalyst composition. For comparison, Cu−1 and Pb−1 were also prepared from commercial highly purified Cu− and Pb−salts by electrodeposition under

Table 2.2. Element concentration of the filtrate after NH$_4$Cl complexing, determined by Inductively Coupled Plasma−Optical Emission Spectrometry (ICP−OES).

Elements	Cu	Pb	Na	Ni	Zn	Ga	K	Mg
Conc. (ppm)	321.775	47.966	18.133	13.608	12.587	9.921	5.206	4.747
	Si	Al	B	Fe	Mn	Co	Li	Ba
	4.416	1.373	1.004	0.604	0.444	0.318	0.254	0.112

Table 2.3 The ICP−OES results of materials prepared by electrodeposition at different applied potentials ranging from −0.40 V to −1.40 V vs. Ag/AgCl.

Cathodic bias (V vs. Ag/AgCl)	Cu (mol%)	Pb (mol%)	Zn (mol%)	Ni (mol%)
−0.40	100.00			
−0.60 (Cu$_{9.20}$Pb$_{0.80}$)	91.99	8.01		
−0.80 (Cu$_{9.00}$Pb$_{1.00}$)	89.86	10.14		
−1.00 (Cu$_{8.65}$Pb$_{1.35}$)	86.58	13.42		
−1.20	85.52	9.63	2.79	2.06
−1.40	83.52	11.40	2.93	2.15

similar conditions. The elemental ratio of the pristine electrocatalysts was studied by ICP−OES (**Table 2.3**). From this analysis, it is evidenced that Cu dominates under all applied potentials, but Pb is incorporated from –0.6 V vs. Ag/AgCl onward. The Pb content regularly increases with increasing applied cathodic bias until –1.2 V vs. Ag/AgCl, at which zinc and nickel start to appear. The XRD measurements (**Figure 2.3a**) confirm the formation of a metallic Cu fcc phase, in which dominant Cu(111) and Cu(200) reflections can be discerned. We also observe the XRD reflections of Cu$_2$O in Cu$_{9.00}$Pb$_{1.00}$, Cu$_{8.65}$Pb$_{1.65}$ and Cu−1, which can be attributed to the inevitable oxidation of the copper surface due to air exposure, contact with the aqueous electrolyte, or the strong oxygen evolution at the anode under high applied bias during electrodeposition. However, no reflections from Pb or Pb−containing compounds were found, which might be due to their relatively low content, poor crystallinity, or small crystalline domain size. Furthermore, no shifts of Cu reflections are observed, which indicates that pure Cu phases are formed, and no alloy formation with Pb occurred.

The local morphological structure of the pristine bimetallic electrocatalysts were investigated using Scanning Electron Microcopy (SEM). Cu$_{9.20}$Pb$_{0.80}$ (**Figure 2.3b**) shows the particle−like structure in which small particles aggregate together to form larger particles. Cu$_{9.00}$Pb$_{1.00}$ (**Figure 2.3c**) has a dendrite−like structure, which is also composed of small particles. It was found that Cu$_{9.20}$Pb$_{0.80}$ has a larger particle size (100−200 nm) compared to Cu$_{9.00}$Pb$_{1.00}$, in which a uniform distribution of particles with sizes ranging between 30 and 50 nm was observed. Cu$_{8.65}$Pb$_{1.35}$ (**Figure 2.3d**) also shows a dendrite−like shape, while two distinct types of structures are observed, namely nanoparticles and
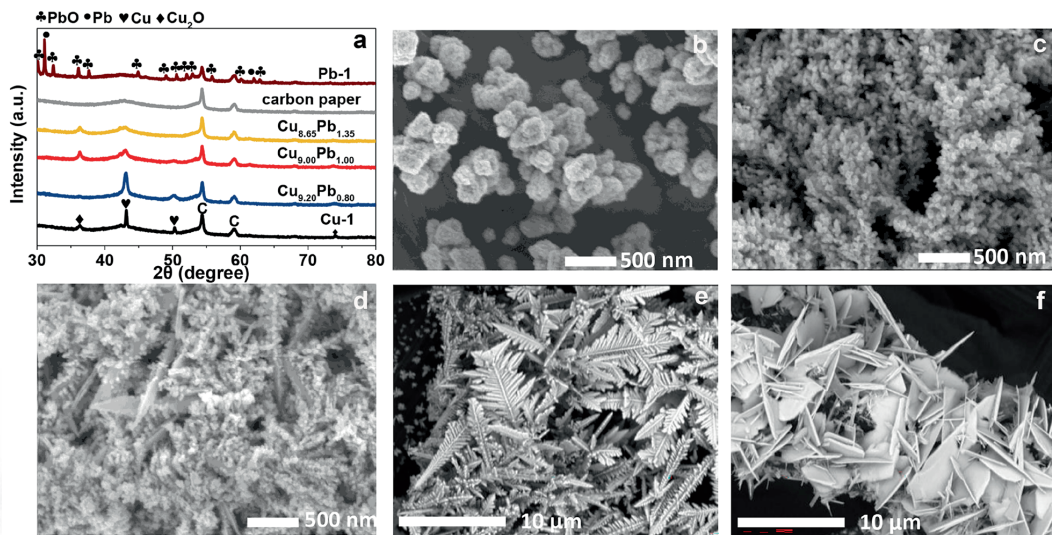
Figure 2.3. X–ray Diffraction (XRD) patterns (a) of the Cu_xPb_y supported on carbon paper, including reference patterns for pure Cu (PDF 00–004–0836) and the carbon paper electrode, indicating the formation of metallic Cu and surface Cu oxide (PDF 04–007–9767) species. No crystalline Pb or Pb compound domains are observed. Scanning Electron Microscopy (SEM) images of the electrodeposited $Cu_{9.20}Pb_{1.0}$ (b), $Cu_{9.00}Pb_{1.00}$ (c), $Cu_{8.65}Pb_{1.35}$ (d), Cu–1 (e) and Pb–1 (f) materials supported on carbon paper.

nanorods. SEM−Energy Dispersive X−ray Spectroscopy (EDS) experiments (**Figures 2.4a−f**) suggest that the increased amount of Pb resulted in aggregation of Pb into nanorods.[36] The thickness of the studied catalysts grown on carbon papers was determined by Atomic Force Microscopy (AFM). As observed in SEM images, small particles aggregated into big particles in $Cu_{9.20}Pb_{1.0}$, and further formed dendrites in $Cu_{8.65}Pb_{1.35}$ as well as $Cu_{8.65}Pb_{1.35}$, leading to the uneven catalyst layers in AFM images. Apart from the shape of catalyst, the crossed bare carbon fibers also make the catalyst layer uneven. The thickness of the catalyst layer on carbon paper substrate was determined to be around 2.5 µm, 1.1 µm and 1.5 µm in $Cu_{9.20}Pb_{1.0}$ (**Figures 2.4g, j**), $Cu_{9.00}Pb_{1.00}$ (**Figures 2.4h, k**) and $Cu_{8.65}Pb_{1.35}$ (**Figures 2.4i, l**), respectively.

To further determine the morphology and chemical composition of the target catalyst $Cu_{9.00}Pb_{1.00}$. Transmission Electron Microscopy (TEM), High−resolution High Angle Annular Dark Field Scanning Transmission Electron Microscopy (HAADF−STEM) and STEM Energy Dispersive X−ray Spectroscopy (STEM−EDS) measurements were employed. **Figure 2.5a** shows the typical TEM image of $Cu_{9.00}Pb_{1.00}$, confirming the particle size is ranging from 30−50 nm. From the high resolution HAADF−STEM data and the corresponding Fourier Transforms (FTs) (**Figure 2.5b**), it can be clearly observed that Cu, Cu_2O and PbO are present in the $Cu_{9.00}Pb_{1.00}$ sample. We also found
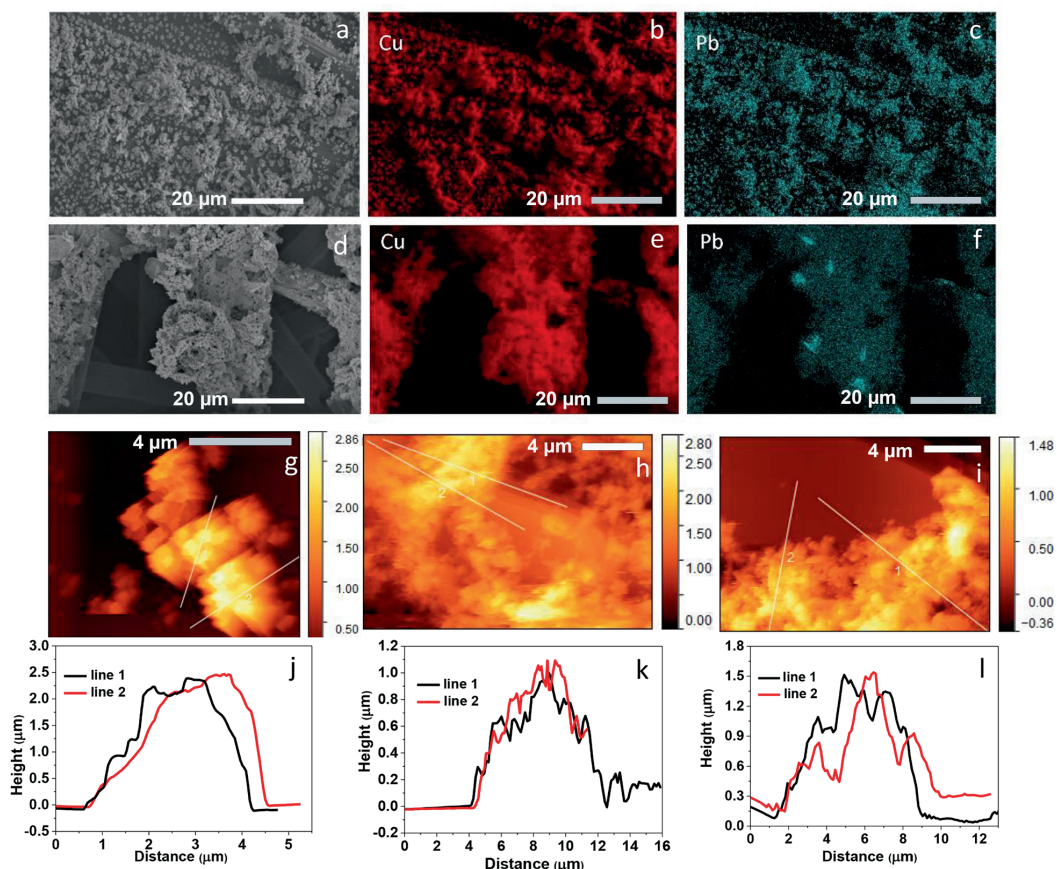
Figure 2.4. Scanning Electron Microscopy (SEM) image and the corresponding Energy Dispersive X–ray Spectroscopy (EDS)–mapping of Cu and Pb in $Cu_{9.20}Pb_{0.80}$ (a–c) and $Cu_{8.65}Pb_{1.35}$ (d–f), showing an aggregation of Pb in $Cu_{8.65}Pb_{1.35}$; Atomic Force Microscopy (AFM) images of $Cu_{9.20}Pb_{1.0}$ (g), $Cu_{9.00}Pb_{1.00}$ (h) and $Cu_{8.65}Pb_{1.35}$ (i) with two lines marking the position where the thickness was measured and thickness profile of the marked lines in $Cu_{9.20}Pb_{1.0}$ (j), $Cu_{9.00}Pb_{1.00}$ (k) and $Cu_{8.65}Pb_{1.35}$ (l), showing an uneven surface and the micrometer–level thickness of the catalyst layers.

a very small fraction of regions in which the lattice fringes correspond to metallic Pb (**Figure 2.5c**). The HAADF−STEM measurements (**Figure 2.5d**) and the related STEM−EDS mapping (**Figure 2.5e**) confirm the homogeneous distribution of Cu and Pb, suggesting that Pb species do not form individual nanoparticles.

To gain insight into the chemical state of the surface of the pristine electrocatalysts, X−ray Photoelectron Spectroscopy (XPS) measurements were performed. **Table 2.4 (Figure 2.6a)** shows the atomic ratio of Cu and Pb at the surface, as determined by XPS measurements. Compared with
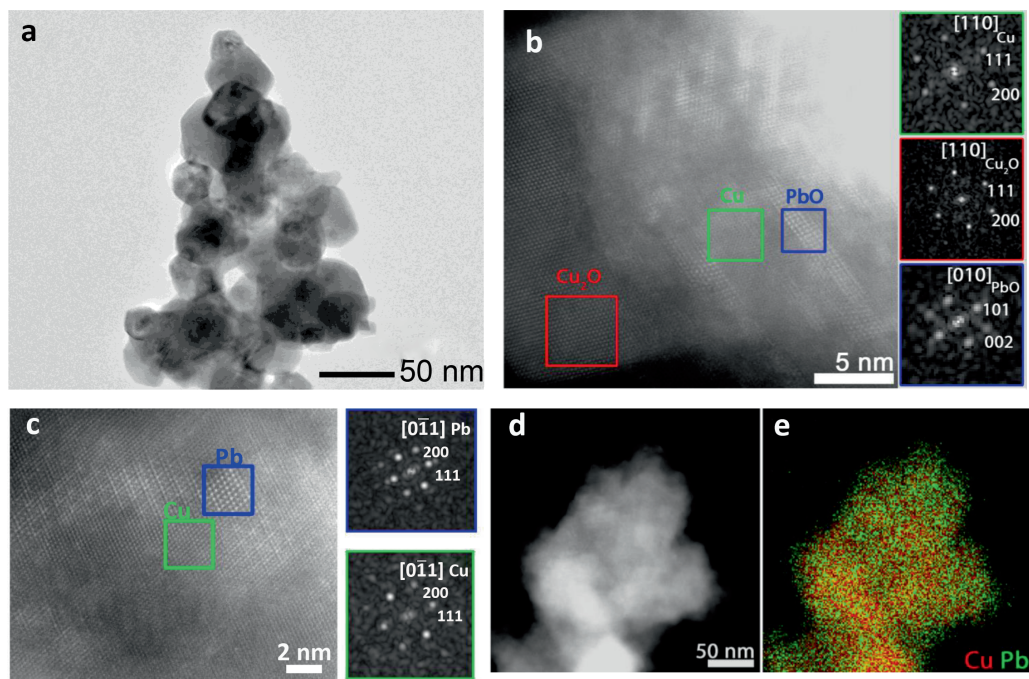
Figure 2.5. Transmission Electron Microscopy (TEM) image of the $Cu_{9.00}Pb_{1.00}$ electrode (a), indicating a particle size of 30 to 50 nm; High Angle Annular Dark Field Scanning Transmission Electron Microscopy (HAADF−STEM) image (b) of $Cu_{9.00}Pb_{1.00}$ together with the corresponding Fourier Transforms (FTs, insets) from the regions indicated by squares of different color, clearly revealing crystalline Cu, Cu_2O and PbO domains; HAADF−STEM image of $Cu_{9.00}Pb_{1.00}$, which shows a small area of the lattice fringe of metallic Pb, evidenced by the FTs of the marked area. Magnified HAADF−STEM image (d) of the region indicated by the white rectangle in (c), together with the corresponding EDS map (e) of the $Cu_{9.00}Pb_{1.00}$ sample.

the ratios obtained by ICP−OES (**Table 2.3**), the surface Pb/Cu ratio is found to be quite similar, showing that Pb is homogeneously distributed throughout the electrodeposited catalyst. Small variations could be caused by the different surface morphologies of the prepared catalysts. As shown in **Figure 2.6b**, the Cu $2p_{3/2}$ XPS spectra were deconvoluted into peaks at 932.6 eV and 934.6 eV, corresponding to $Cu^{0/1+}$ and Cu^{2+}, respectively.[37–39] For all samples, a higher contribution of Cu^{1+} was observed from Cu LMM spectra than Cu^0 (**Figure 2.6c**), which indicates that the surface of Cu−based electrocatalysts is prone to surface oxidation. This is consistent with the XRD results, in which reflections of Cu_2O were observed in all cases. The XPS Pb 4f spectra (**Figure 2.6d**) show the domination of Pb^{2+} species on the surface of all measured samples, as evidenced by the binding energy of the Pb 4f electrons, along with a negligibly small peak of metallic Pb (136.5 eV) observed in the XPS measurements, consistent with the high resolution HAADF−STEM data.[40,41] The
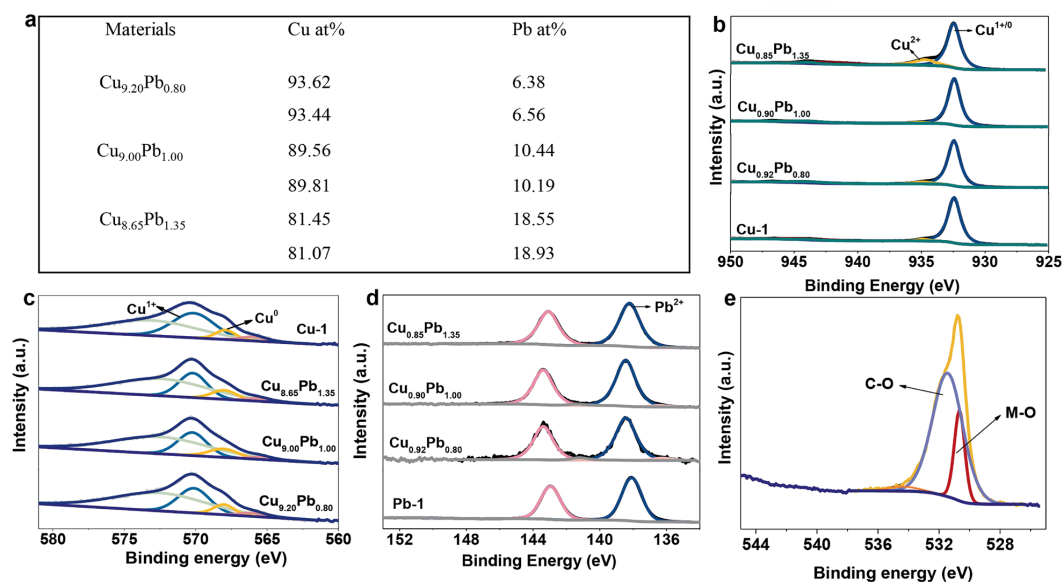
Figure 2.6. The atomic percentage of Cu and Pb (a) from X−ray Photoelectron Spectroscopy (XPS) results (**Table 2.4**); XPS results of Cu 2p spectra (b) and Cu LMM Auger spectra (c) of all Cu_xPb_y catalysts and Cu reference (Cu−1); Pb 4f XPS spectra (d) of different Cu_xPb_y catalyst and Pb reference (Pb−1); O 1s XPS spectrum of $Cu_{9.00}Pb_{1.00-}$ (e).

representative O 1s spectrum (**Figure 2.6e**) showed three types of O species, which are identified as metal−oxygen (M−O, 530 eV) bond, carbon−oxygen (C−O, 531.4 eV) bond and oxygen−hydrogen bond (534.0eV) respectively.[42,43] Taken together, it is evident that both Cu and Pb have been oxidized on the surface. This might be caused by inevitable air exposure of these two metals during the preparation by electrodeposition, or due to the aqueous electrolyte solution that was used for the electrocatalyst preparation.[44]

The local structure and the electronic nature of the pristine electrocatalysts were determined by X−ray Absorption Spectroscopy (XAS), including X−ray Absorption Near Edge Spectroscopy (XANES) and Extended X−ray Absorption Fine Structure (EXAFS) measurements. In **Figure 2.7a**, the Cu K−edge XANES spectrum of $Cu_{9.00}Pb_{1.00}$ displays a similar shape as that of Cu foil and Cu−1, indicating that these samples have similar structures.[45] Their identical Cu K−edge positions in XANES reveal that the bulk oxidation state of Cu in $Cu_{9.00}Pb_{1.00}$ is close to the metallic Cu^0 phase. From the Fourier−transformed k^3−weighted EXAFS spectra (**Figure 2.7b** and **Figure 2.7c**), the main characteristic peaks are found to be Cu−Cu scattering for these three samples, indicating the predominant existence of metallic Cu and the absence of significant Cu−Pb bonds. This observation suggests that Cu and Pb do not form alloys under the present preparation conditions.[46]

The coordination number (CN) of Cu−Cu bonds in $Cu_{9.00}Pb_{1.00}$ is fitted to be 5.2 (**Table A1**), which
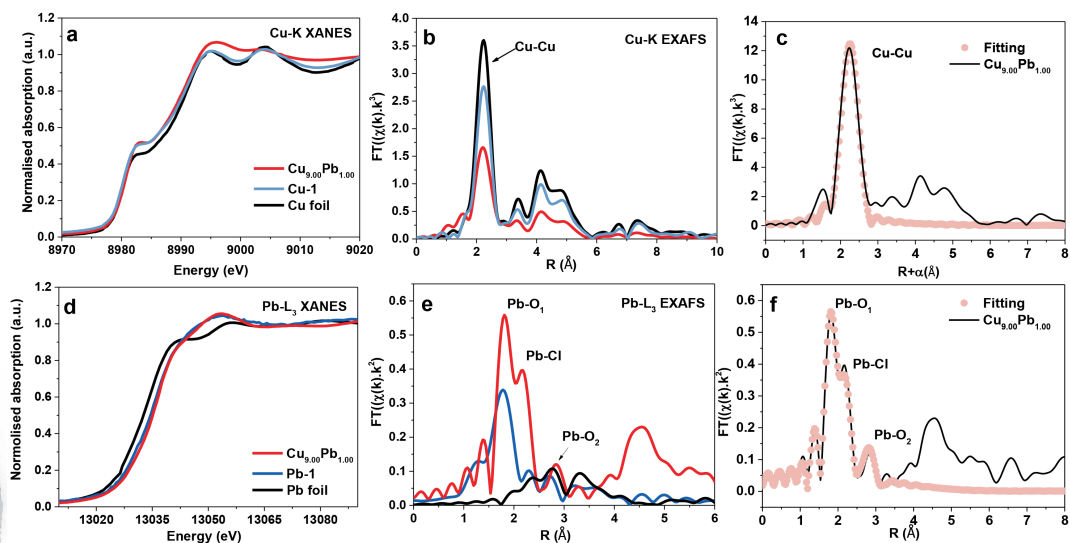
Figure 2.7. Cu K−edge X−ray Absorption Near Edge Spectroscopy (XANES) spectra (a) of $Cu_{9.00}Pb_{1.00}$, Cu−1 and Cu foil and the corresponding Extended X−ray Absorption Fine Structure (EXAFS) spectra (b); The fitting curve of $Cu_{9.00}Pb_{1.00}$ Cu K edge in R−space (c); Pb L_3−edge XANES spectra (d) of $Cu_{9.00}Pb_{1.00}$, Pb−1 and Pb foil, and the corresponding EXAFS spectra (e); The fitting curve of $Cu_{9.00}Pb_{1.00}$ Pb L_3 edge in R−space (f). No Cu−Pb bonds were observed, indicating that the waste−derived bimetallic Cu_xPb_y electrocatalysts are not alloys.

is smaller than that of Cu foil (12.0) and Cu−1 (8.4). This is probably caused by the presence of abundant atomic defects within the $Cu_{9.00}Pb_{1.00}$ structure.[47] In the Pb L_3 XANES spectra (**Figure 2.7d**), it is suggested that $Cu_{9.00}Pb_{1.00}$ contains a higher oxidation state than Pb^{2+} in Pb−1 and Pb^0 in Pb foil, evidenced by a slight shift of the edge position to higher energy. Pb−O and Pb−Cl bonds are confirmed by the quantitative fitting results of the Pb L_3−edge (**Figure 2.7e** and **Figure 2.7f**). The formation of Pb−Cl bonds could be from the NH_4Cl involved in the electrocatalyst synthesis. Similarly, there is no Pb−Cu bond observed in $Cu_{9.00}Pb_{1.00}$ (expected at larger bond lengths compared to the Cu−Cu bond), confirming that the pristine $Cu_{9.00}Pb_{1.00}$ electrocatalyst is not an alloy, but instead consists of phase−separated Cu− and Pb−rich domains. Based on the observation above, we can draw the intermediate conclusion that Cu predominantly formed in the metallic state in the waste−derived electrocatalyst, while Pb is mainly present in its oxidized form and partially bonded with Cl^- from the aqueous NH_4Cl solution used for the chemical extraction procedure.

2.3.2 Electrocatalytic Performance

The eCO_2RR performance of the different Cu_xPb_y electrocatalysts was explored using a three electrode H−type cell containing CO_2−saturated 0.1 M $KHCO_3$ aqueous electrolyte solution. To analyze the product distribution and selectivity, electrolysis experiments were operated at constant
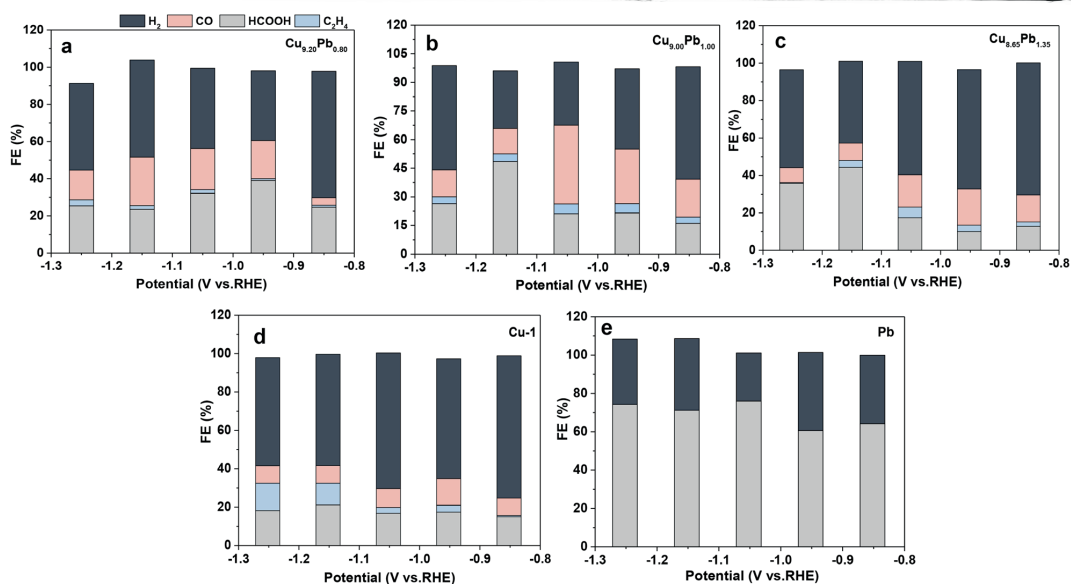
Figure 2.8. Potential−dependent Faradaic Efficiencies (FEs) of $Cu_{9.20}Pb_{0.80}$ (a), $Cu_{9.00}Pb_{1.00}$ (b) and $Cu_{8.65}Pb_{1.35}$ (c) and Cu−1 (d) and Pb−1 (e) in CO_2 saturated 0.1 M $KHCO_3$ solution.

potentials ranging from –0.85 to –1.25 V vs. RHE, and the products were analyzed with online GC and offline NMR measurements (representative results shown in **Figures A2** and **A3**). **Figure 2.8** and **Figure A4** show the potential−dependent Faradaic Efficiency (FE) profiles of CO, HCOOH, C_2H_4 and H_2 for the different waste−derived Cu_xPb_y electrodes, in contrast to pure Cu and Pb electrode. It was found that the $Cu_{9.00}Pb_{1.00}$ electrode (**Figure 2.8b**) shows relatively lower H_2 and higher CO FE than all the other samples in the given potential window. The maximum FE of CO is 41.1% at –1.05 V vs. RHE, which is around four times higher than that of Cu−1 (9.7%, **Figure 2.8d**) at this applied potential, suggesting synergistic effects between the Cu−rich and Pb−rich domains compared to pure Cu and Pb electrode (no CO formation, **Figure 2.8e**). The enhanced HCOOH formation is also observed in these Cu_xPb_y catalysts, which can be attributed to the Pb species which are originally active for electrochemical CO_2 to HCOOH conversion. A very small amount of C_2H_4 was also found in all Cu_xPb_y samples due to the exposed active sites for ethylene production on the Cu surface.

Both $Cu_{9.00}Pb_{1.00}$ and Cu−1 behave similarly in their stability test (**Figure 2.9**). It can be seen that the production of CO on $Cu_{9.00}Pb_{1.00}$ decreases from 41.1% to 17.5% after 15 h of operation at −1.05 V vs. RHE (**Figure 2.9a**), which is similar to the great loss of FE (from 9.7 % to 5.1%) on Cu−1 (**Figure 2.9d**). The observed degradation in catalytic performance over time could be attributed to partial detachment of active material during catalysis, as evidenced by the *ex situ* SEM images of $Cu_{9.00}Pb_{1.00}$ and Cu−1 before (**Figures 2.9b, e**) and after (**Figures 2.9c, f**) catalysis.

To investigate the composition effect of the Cu_xPb_y electrocatalysts in more detail, we compared the FE and production rate for the electrodes with different Cu/Pb metal ratios at a fixed potential of
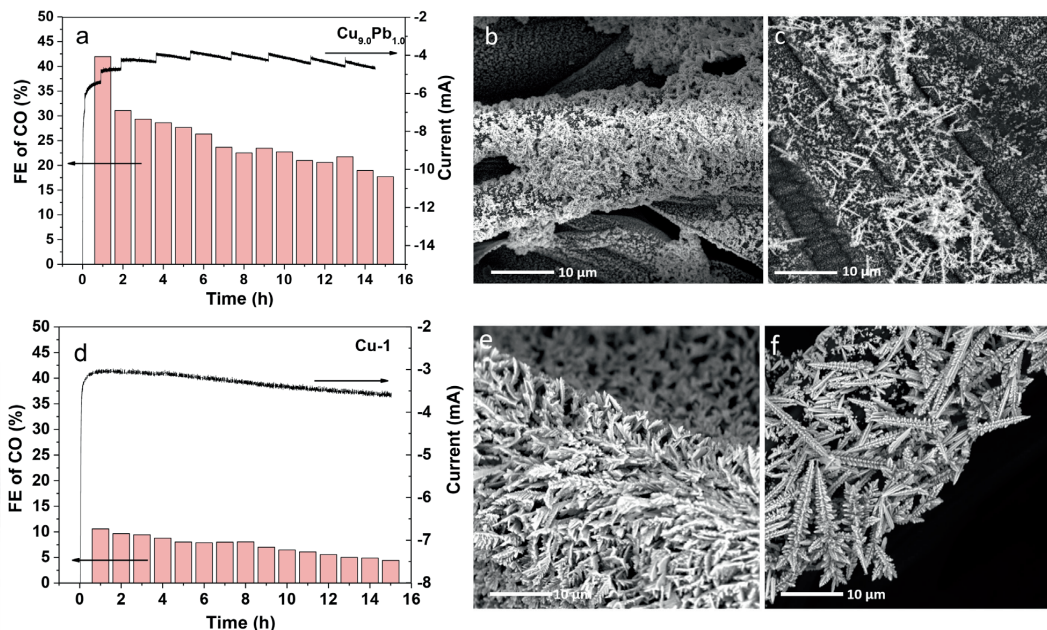
Figure 2.9. The stability test result (a), Scanning Electron Microscopy (SEM) images before (b) and after (c) of $Cu_{9.0}Pb_{1.0}$ at −1.05 Vs vs. RHE for 15 h; The stability test result (d), SEM images before (e) and after (f) of Cu−1 at −1.05 Vs vs. RHE for 15 h.

–1.05 V vs. RHE. In **Figure 2.10a**, compared to the pure Cu electrode (Cu−1), incorporation of a small amount of Pb ($Cu_{9.20}Pb_{0.80}$) enhances the eCO$_2$RR selectivity toward HCOOH and CO by twofold (31.8% and 22.8%, respectively, compared to 17.1% and 9.7% for Cu−1) along with a lower H$_2$ production (around 30.1% for $Cu_{9.20}Pb_{0.80}$ compared to 70.9% for Cu−1). The CO production is further enhanced when a slightly higher amount of Pb is introduced ($Cu_{9.00}Pb_{1.00}$), reaching over
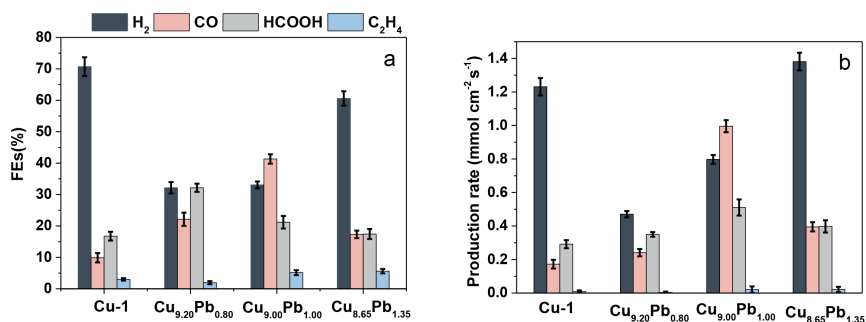
Figure 2.10. Faradaic Efficiencies (FEs) (a) and production rates (b) of the main products (CO, HCOOH, H$_2$ and C$_2$H$_4$) for the different Cu$_x$Pb$_y$ samples at −1.05 V vs. RHE.

41.1% FE for CO. In $Cu_{8.65}Pb_{1.35}$, both CO and HCOOH productions are hindered, and a dramatic increase of H_2 FE is observed (60.6%, comparable to 70.8% for Cu−1). This leads to a volcano−shaped dependence of the CO selectivity based on the amount of Pb present in the Cu_xPb_y electrodes. A similar trend is also found in the production rate distribution (**Figure 2.10b**), confirming the synergistic effect on CO selectivity. In general, the partial current density normalized by the geometric surface area of the electrodes does not reflect the intrinsic activity.[48]

To understand the intrinsic activity of these waste−derived Cu_xPb_y electrocatalysts, we analyzed the electrochemical active surface area (ECSA) and evaluated their ECSA−normalized partial current densities for CO and H_2. ECSA can be evaluated by measuring Cyclic voltammetry (CV) in non−Faradaic region (**Figure 2.11a**) and comparing the double layer capacitance (C_{dl}). **Figures 2.11b−f** show the CV curves of Cu_xPb_y electrocatalysts, Cu−1 and carbon paper collected at different scan rates. Based on the current difference between positive scan and negative scan, the C_{dl} can be calculated. The calculated and fitted C_{dl} is shown in **Figure 2.12a**, by which the geometric area can be normalized to ECSA−normalized area (**Table 2.5**). In agreement with the trend that we found in the FE and production rate (**Figures 2.7a, b**), $Cu_{9.00}Pb_{1.00}$ shows a significantly higher ECSA−normalized activity for CO (**Figure 2.8b**) compared to Cu−1, $Cu_{8.65}Pb_{1.35}$ and $Cu_{9.20}Pb_{0.80}$, along with the lowest activity for H_2 at –1.05 V vs. RHE (**Figure 2.8c**). This trend indicates that an optimal amount of Pb co−existing with Cu provides a means to suppress the competitive HER in favor of CO production.
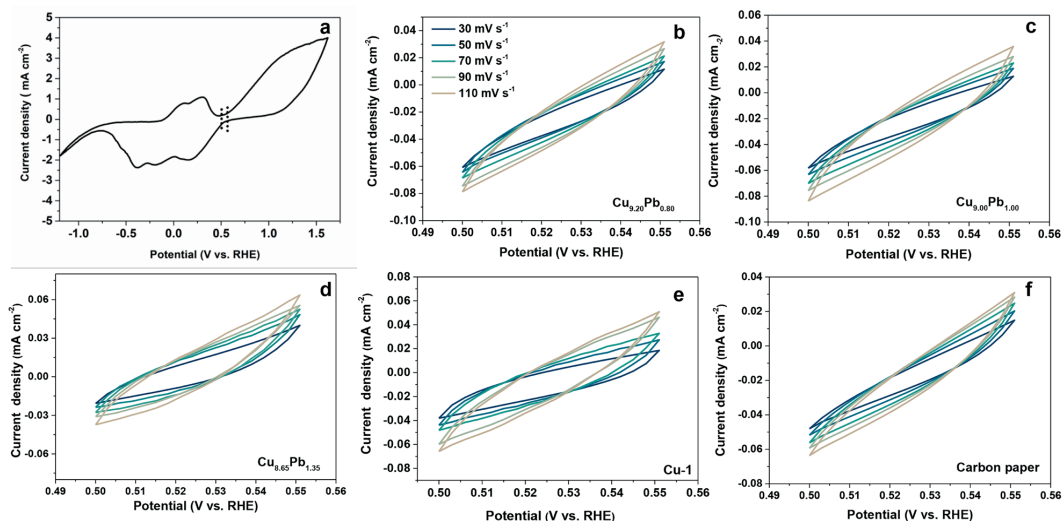
Figure 2.11. Cyclic voltammetry (CV) curve of $Cu_{8.65}Pb_{1.35}$ in an H−cell (a). The dashed lines mark the potential window (0.50 V − 0.55 V vs. RHE) used for electrochemical active surface area (ECSA) measurements, representing the non−Faradaic region of the CV curve. CV curves collected at different scan rates for ECSA measurements of $Cu_{9.00}Pb_{1.00}$ (b) and $Cu_{9.20}Pb_{0.80}$ (c), $Cu_{8.65}Pb_{1.35}$ (d), Cu−1 (e) and carbon paper (f).
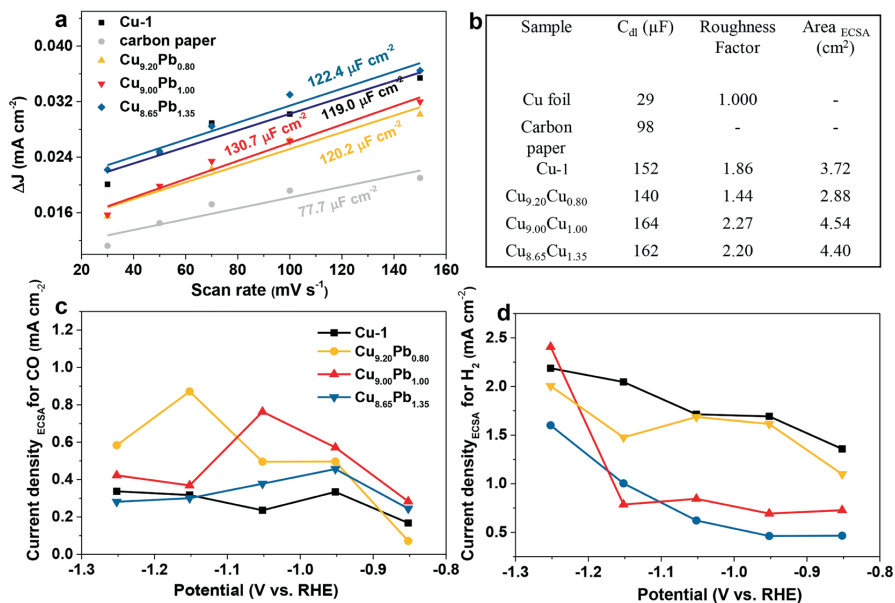
Figure 2.12. Charging current density differences at 0.525 V vs. RHE for all samples against scan rate (a), calculated from Figure 2.11; Table 2.5 (b) shows the roughness factors and electrochemical active surface area (ECSA) for the studied materials; The ECSA−normalized partial current density of CO (c) and H_2 (d) for the different Cu_xPb_y catalysts at varying cathodic potentials.

2.3.3 *In situ* Raman Spectroscopy Measurements

To analyze the observed effect of the Cu/Pb ratio on the catalytic performance in more detail, we monitored the structural changes in these Cu_xPb_y catalysts at the eCO_2RR onset by *in situ* Raman Spectroscopy measurements. These *in situ* Raman measurements were performed in CO_2−saturated 0.1 M $KHCO_3$ electrolyte solution. The CV curves were achieved by scanning between −1.0 V to 1.6 V vs. RHE using a scan rate of 50 mV s⁻¹, and Raman spectra were collected at a rate of one spectrum per second in order to construct the Raman Spectroscopy heatmaps as a function of applied potential (**Figure 2.13**).

As shown in **Figure 2.13a**, the first reduction peak occurs at 0.2 V vs. RHE for the $Cu_{9.20}Pb_{0.80}$ electrode, which is attributed to the reduction of Cu^+ to Cu^0.[49–51] The corresponding Raman Spectroscopy heatmap (**Figure 2.13b**) reveals that the signals associated with CuO_x (at 504 and 619 cm⁻¹) disappear at 0.13 V vs. RHE, corresponding to the end of the Cu^+ to Cu^0 reduction peak in the CV (indicated with a dashed line in **Figure 2.13a**). When an increased cathodic bias is applied, a second reduction peak appears at −0.03 V vs. RHE. Since Cu^+ is already fully reduced to Cu^0, as evidenced by the *in situ* Raman Spectroscopy measurement, this reduction peak is tentatively ascribed to the *in*
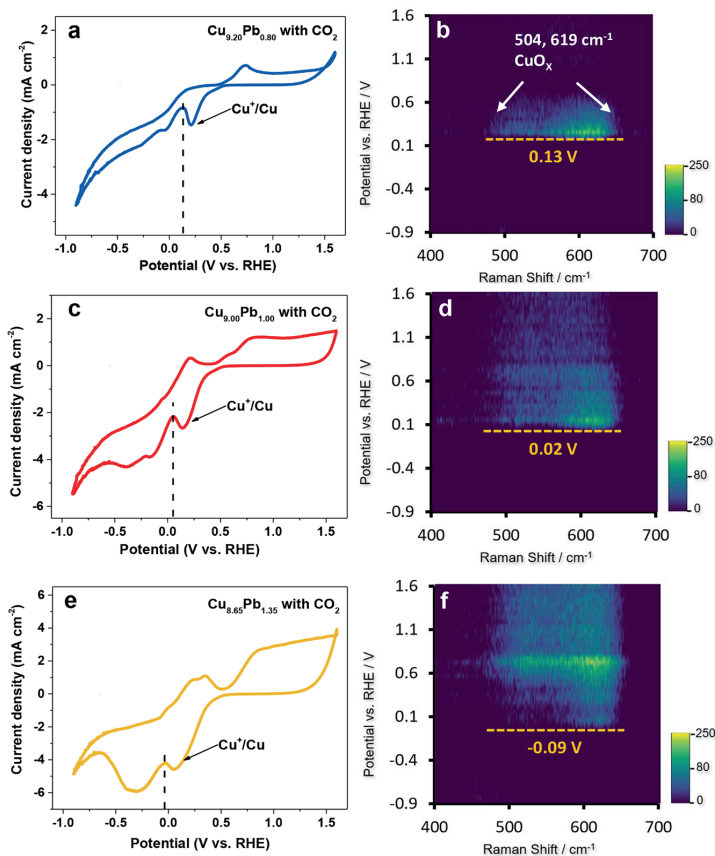
Figure 2.13. Cyclic voltammetry (CV) curves and *in situ* Raman spectra of (a, b) $Cu_{9.20}Pb_{0.80}$, (c, d) $Cu_{9.00}Pb_{1.00}$ and (e, f) $Cu_{8.65}Pb_{1.35}$ waste–derived electrocatalysts, showing a shift of the Cu reduction onset to more negative cathodic bias when more Pb is present in the electrocatalyst. Dashed lines (black and yellow) represent the potentials at which the Cu reduction is finished, as evidenced by the *in situ* Raman spectra.

situ reduction of Pb^{2+} species. A similar phenomenon of Cu^+ reduction to Cu^0 can be found in the *in situ* Raman Spectroscopy heatmaps for $Cu_{9.00}Pb_{1.00}$ and $Cu_{8.65}Pb_{1.35}$, although the absolute reduction potential varies slightly. However, there are two Pb reduction peaks observed in the CV of the $Cu_{9.00}Pb_{1.00}$ electrode after the disappearance of the CuO_x Raman signal (**Figures 2.13c, d**). These two reduction features in the CV potentially correspond to two different types of Pb, which is well in line with the Pb−L_3 edge EXAFS fitting results (**Figure 2.7f**) that indicated the presence of Pb−O and Pb−Cl bonds.

In $Cu_{8.65}Pb_{1.35}$ (**Figures 2.13e, f**), the Cu reduction peak shifts to more negative cathodic bias compared to $Cu_{9.20}Pb_{0.80}$ and $Cu_{9.00}Pb_{1.00}$. Only one reduction peak of Pb is found in this CV curve,
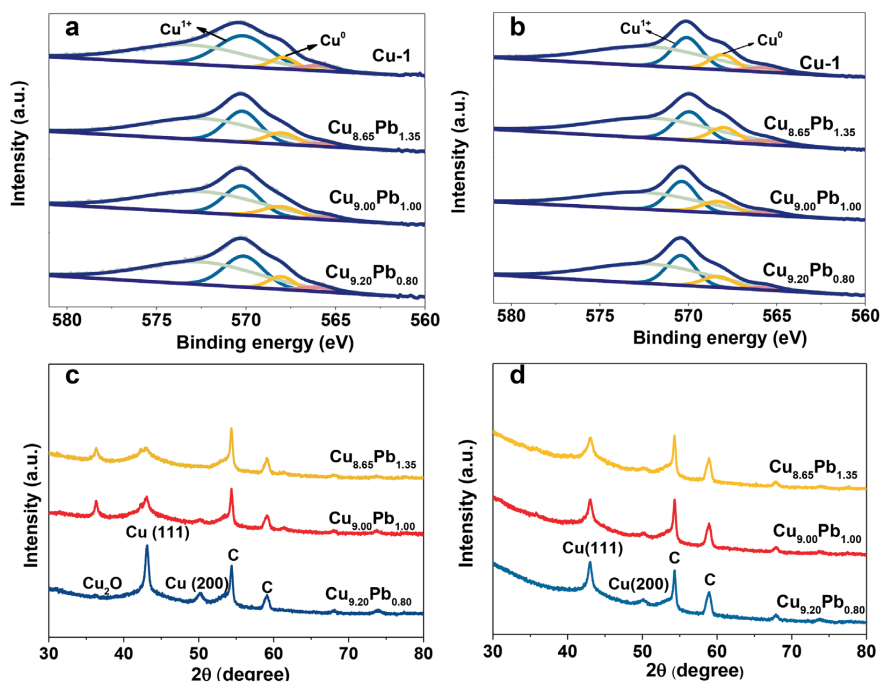
Figure 2.14. *Ex situ* Cu LMM Auger spectra of all Cu_xPb_y and Cu−1 before (a) and after (b) 1 h of catalysis at −1.05 V vs. RHE; *Ex situ* X−ray Diffraction (XRD) patterns of Cu_xPb_y before (c) and after (d) 1 h of catalysis at −1.05 V vs. RHE.

implying that the reduction of Pb species is inhibited under such electrochemical reduction conditions. The observed shift of the Cu reduction peak to more negative cathodic bias suggests that more driving force is needed for the reduction of Cu^+ to the metallic state when too much Pb coexists with Cu. The difficulty of Pb reduction in $Cu_{8.65}Pb_{1.35}$ can be ascribed to the aggregation of Pb species (**Figure 2.14**), while the aggregation is absent in the other two samples (**Figure 2.4 and Figure 2.5**).[52] To confirm the *in situ* electrochemical reduction of Pb and Cu species, we analyzed Cu LMM Auger spectroscopy and observed that the contribution of Cu^0 increases after catalysis (**Figure 2.10b**) compared to before catalysis (**Figure 2.14a**). This is further corroborated by the XRD pattern of the $Cu_{9.00}Pb_{1.00}$ electrocatalyst before (**Figure 2.14c**) and after catalysis (**Figure 2.14d**), where we observe that the reflections of Cu_2O have disappeared after eCO_2RR and only metallic Cu reflections are present after one hour of electrolysis.

2.3.4 Mechanism

The relationship between metal ratio and performance of the waste−derived Cu_xPb_y electrocatalysts is summarized in **Figure 2.15**. First, when a small amount of Pb is present in the bimetallic catalyst ($Cu_{9.20}Pb_{0.80}$), hydrogen evolution is suppressed and the formation of HCOOH and CO is enhanced. As shown in **Figure 2.8**, H_2 evolution is dominant in pure Cu (Cu−1) electrodes, while pure Pb
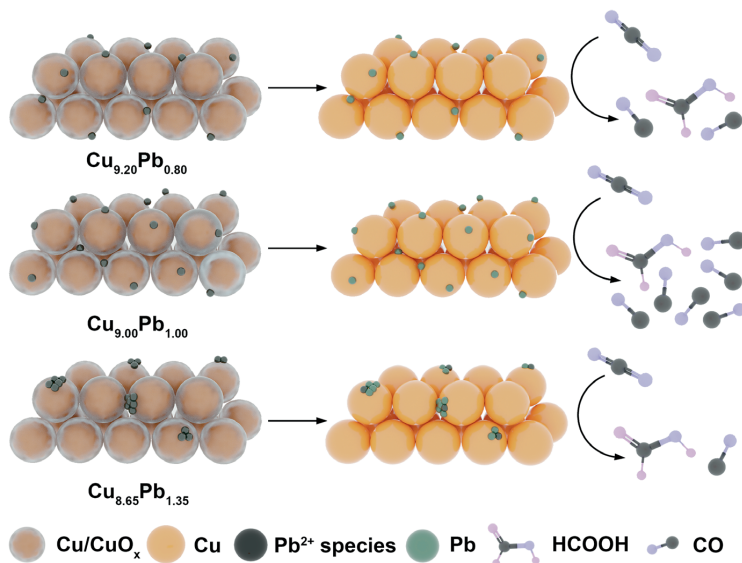
Figure 2.15. Schematic illustration of the pristine waste–derived Cu_xPb_y electrocatalysts and their compositional transformation under eCO_2RR conditions. $Cu_{9.20}Pb_{0.80}$ and $Cu_{9.00}Pb_{1.00}$ have the ability to form metallic Pb under reaction conditions, thereby enhancing the selectivity for C_1 products through a nanoscale synergistic effect between Cu and Pb. This synergistic effect is relatively weaker in $Cu_{8.65}Pb_{1.35}$, since the formation of metallic Pb is prohibited, which results in a similar catalytic performance as pure Cu.

(Pb−1) mainly produces HCOOH. Therefore, the enhancement of the CO formation for the bimetallic electrodes cannot be solely ascribed to Cu or Pb domains in the bimetallic electrocatalyst. Instead, the combination of *in situ* reduced metallic Cu and Pb, evidenced by CV and *in situ* Raman Spectroscopy results, is necessary for enhanced CO formation. The enhancement of the CO formation reaches a maximum of 41.1% at –1.05 V vs. RHE when more Pb is present in the form of a Cu/Pb ratio of 9.0, resulting from the formation of more metallic Pb and the subsequent stronger Cu−Pb synergy under reaction conditions. The increase in HCOOH FE for $Cu_{9.00}Pb_{1.00}$ compared to $Cu_{9.20}Pb_{0.80}$ suggests that the HCOOH formation is intrinsically promoted by Pb species.[53–56] However, when even more Pb is introduced, the enhancement effect for CO production is weakened, which is explained by the lower tendency of $Cu_{8.65}Pb_{1.35}$ to form metallic Cu and Pb under these reaction conditions. Therefore, CO production dramatically decreases in $Cu_{8.65}Pb_{1.35}$ due to the absence of a synergistic effect between metallic Cu and Pb, and the catalytic performance is similar to pure Cu. [57–60] The small decrease in HCOOH formation for $Cu_{8.65}Pb_{1.35}$ is caused by the aggregation of Pb^{2+} species which is also responsible for their inferior reducibility. Overall, we have found that coexistence of Cu and

Pb in Cu−based waste−derived bimetallic electrocatalysts promotes the formation of CO through a synergistic effect between *in situ* reduced Pb and Cu, while the presence of a larger amount of PbO in the pristine electrocatalyst hampers the *in situ* formation of metallic Cu and Pb, which limits the synergistic effect and lowers the electrocatalytic performance.

2.4 Conclusions

We have prepared a series of copper−lead (Cu_xPb_y, x+y=10) materials from industrial metallurgical waste, which were evaluated for the electrochemical CO_2 reduction reaction. The Cu and Pb species were obtained from the industrial waste through chemical extraction with ammonium chloride, and the composition of the waste−derived electrocatalysts was tailored through the electrodeposition conditions. The composition of the pristine waste−derived electrocatalysts was analyzed with X−ray Diffraction, X−ray Photoelectron Spectroscopy and X−ray Absorption Spectroscopy, which revealed that the bimetallic electrocatalysts consist of Cu^0, Cu^+ and Pb^{2+} domains, and no alloy formation was observed. Improved selectivity towards CO was observed in these bimetallic systems compared to pure Cu. The optimized $Cu_{9.00}Pb_{1.00}$ electrocatalyst showed a fourfold improvement of CO formation compared to pure Cu under the same electrochemical conditions. Through *in situ* Raman Spectroscopy, it was revealed that the reducibility of pristine Cu^{1+} and Pb^{2+} species into metallic Cu^0 and Pb^0 played a crucial role in the enhanced formation of CO. With a proper amount of Pb coexisting with Cu, a synergy between *in situ* reduced Cu and Pb facilitated enhanced CO selectivity, whereas these reduction processes were hampered when the amount of Pb species was increased because of Pb species aggregation, resulting in a decrease of CO selectivity and an increase in hydrogen evolution reaction. Our results show the potential of industrial waste−derived bimetallic electrocatalysts for the rational and sustainable design of C_1 product selective eCO$_2$RR electrocatalysts.

2.5 Acknowledgements

2.6 References

[1]   B. M. Tackett, E. Gomez, J. G. Chen, *Nat. Catal.* **2019**, *2*, 381–386.

[2]   J. Artz, T. E. Müller, K. Thenert, J. Kleinekorte, R. Meys, A. Sternberg, A. Bardow, W. Leitner, *Chem. Rev.* **2018**, *118*, 434–504.

[3]   D. Gao, R. M. Arán−Ais, H. S. Jeon, B. Roldan Cuenya, *Nat. Catal.* **2019**, *2*, 198–210.

[4]   D. Raciti, C. Wang, *ACS Energy Lett.* **2018**, *3*, 1545–1556.

[5]   P. Sebastián−Pascual, S. Mezzavilla, I. E. L. Stephens, M. Escudero−Escribano, *ChemCatChem* **2019**, *11*, 3626–3645.

[6]   M. Ma, K. Djanashvili, W. A. Smith, *Angew. Chem. Int. Ed.* 2016, *55*, 6680–6684.

[7]   R. Kortlever, J. Shen, K. J. P. Schouten, F. Calle−Vallejo, M. T. M. Koper, *J. Phys. Chem. Lett.* **2015**, *6*, 4073–4082.

[8]   J. He, K. E. Dettelbach, A. Huang, C. P. Berlinguette, *Angew. Chem. Int. Ed.* **2017**, *4*, 16806–16809.

[9]   A. Vasileff, C. Xu, L. Ge, Y. Zheng, S. Qiao, Chem **2018**, *4*, 1809−1831.

[10]   H. Guo, Y. Hou, A. Dutta, S. R. Waldvogel, P. Broekmann, *ChemElectroChem* **2019**, *6*, 2324–233.

[11]   S. Stojkovikj, G. A. El−nagar, F. Firschke, L. C. Pardo, L. Choubrac, M. Najdoski, M. T. Mayer, *ACS Appl. Mater. Interfaces* **2021**, *13*, 38161−38169.

[12]   B. Zhang, K. hung Lai, B. Wang, Z. Wang, *Resour. Conserv. Recycl.* **2018**, *139*, 40–47.

[13]   M. Palmiotto, E. Fattore, V. Paiano, G. Celeste, A. Colombo, E. Davoli, *Environ. Int.* 2014, *68*, 16–24.

[14]   A. Yılmaz, E. Atmaca, *Environ. Geol.* **2006**, *50*, 677–689.

[15]   S. Mor, K. Ravindra, R. P. Dahiya, A. Chandra, *Environ. Monit. Assess.* **2006**, *118*, 435–456.

[16]   J. Albo, A. Sáez, J. Solla−Gullón, V. Montiel, A. Irabien, *Applied Catal.ysis B: Environmental* **2015**, *177*, 709–717.

[17]   J. Huang, M. Mensi, E. Oveisi, V. Mantella, R. Buonsanti, *J. Am. Chem. Soc.* **2019**, *141*, 2490–2499.

[18]   J. Albo, D. Vallejo, G. Beobide, O. Castillo, P. Castaço, *ChemSusChem* **2017**, *10*, 1100–1109.

[19]   C. J. Chang, S. C. Lin, H. C. Chen, J. Wang, K. J. Zheng, Y. Zhu, H. M. Chen, *J. Am. Chem. Soc.* **2020**, *142*, 12119–12132.

[20]   C. G. Morales−Guio, E. R. Cave, S. A. Nitopi, J. T. Feaster, L. Wang, K. P. Kuhl, A. Jackson, N. C. Johnson, D. N. Abram, T. Hatsukade, C. Hahn, T. F. Jaramillo, *Nat. Catal.* **2018**, *1*, 764–771.

[21]   S. Nitopi, E. Bertheussen, S. B. Scott, X. Liu, A. K. Engstfeld, S. Horch, B. Seger, I. E. L. Stephens, K. Chan, C. Hahn, J. K. Nørskov, T. F. Jaramillo, I. Chorkendorff, *Chem. Rev.* **2019**, *119*, 7610–7672.

[22]   J. E. Pander, M. F. Baruch, A. B. Bocarsly, *ACS Catal.* **2016**, *6*, 7824–7833.

[23]   C. Kim, T. Möller, J. Schmidt, A. Thomas, P. Strasser, *ACS Catal.* 2019, *9*, 1482–1488.

[24]   Y. Kwon, J. Lee, *Electrocatalysis* **2010**, *1*, 108–115.

[25]   A. Bagger, W. Ju, A. S. Varela, P. Strasser, J. Rossmeisl, *ChemPhysChem* **2017**, *18*, 3266–3273.

[26]   M. Schreier, F. Héroguel, L. Steier, S. Ahmad, J. S. Luterbacher, M. T. Mayer, J. Luo, M. Grätzel, *Nat. Energy* **2017**, *2*, 17087.

[27]   W. Lv, J. Zhou, J. Bei, R. Zhang, L. Wang, Q. Xu, W. Wang, *Appl. Surf. Sci.* **2017**, *393*, 191–196.

[28]   S. Rasul, D. H. Anjum, A. Jedidi, Y. Minenkov, L. Cavallo, K. Takanabe, *Angew. Chem. Int. Ed.* **2015**, *127*, 2174–2178.

[29]   M. Bernal, A. Bagger, F. Scholten, I. Sinev, A. Bergmann, M. Ahmadi, J. Rossmeisl, B. R. Cuenya, *Nano Energy* **2018**, 53, 27–36.

[30]   Z. Chang, S. Huo, W. Zhang, J. Fang, H. Wang, *J. Phys. Chem. C* **2017**, *121*, 11368–11379.

[31]   Z. B. Hoffman, T. S. Gray, K. B. Moraveck, T. B. Gunnoe, G. Zangari, *ACS Catal.* **2017**, *7*, 5381–5390.

[32]   J. P. Grote, A. R. Zeradjanin, S. Cherevko, A. Savan, B. Breitbach, A. Ludwig, K. J. J. Mayrhofer, *J. Catal.* **2016**, *343*, 248–256.

[33]   S. Lee, G. Park, J. Lee, *ACS Catal.* **2017**, *7*, 8594–8604.

[34]   D. Kim, J. Resasco, Y. Yu, A. M. Asiri, P. Yang, *Nat. Commun.* **2014**, *5*, 4948.

[35]   B. Morosin, A. C. Larson, *Acta Cryst.* **1969**, *B25*, 1417–1419.

[36]   S. Yancoillie, K. Pierloot, *J. Phys. Chem. A* **2008**, *112*, 4011–4019.

[37] J. Li, A. Xu, F. Li, Z. Wang, C. Zou, C. M. Gabardo, Y. Wang, A. Ozden, Y. Xu, D. H. Nam, Y. Lum, J. Wicks, B. Chen, Z. Wang, J. Chen, Y. Wen, T. Zhuang, M. Luo, X. Du, T. K. Sham, B. Zhang, E. H. Sargent, D. Sinton, *Nat. Commun.* **2020**, *11*, 3685.

[38] A. A. Permyakova, J. Herranz, M. El Kazzi, J. S. Diercks, M. Povia, L. R. Mangani, M. Horisberger, A. Pătru, T. J. Schmidt, *ChemPhysChem* **2019**, *20*, 3120–3127.

[39] W. W. Wang, W. Z. Yu, P. P. Du, H. Xu, Z. Jin, R. Si, C. Ma, S. Shi, C. J. Jia, C. H. Yan, *ACS Catal.* **2017**, *7*, 1313–1329.

[40] L. Liu, Z. Yao, Y. Deng, F. Gao, B. Liu, L. Dong, *ChemCatChem* **2011**, *3*, 978–989.

[41] Y. Wang, Y. Zhang, Y. Feng, X. Zhang, J. Liu, W. Hou, J. Jia, B. Zhang, *IOP Conf. Ser. Mater. Sci. Eng.* ***2019**, 490, 022067.*

[42] I. S. Zhidkov, A. F. Akbulatov, A. I. Kukharenko, S. O. Cholakh, K. J. Stevenson, P. A. Troshinb, E. Z. Kurmaev, *Mendeleev Commun.* **2018**, *28*, 381–383.

[43] C. J. Yang, L. X. Zhao, X. Zhang, D. C. Zhai, Y. Gu, Prot. Met. Phys. Chem. Surfaces 2020, 56, 302–310

[44] Z. Jin, C. Liu, K. Qi, X. Cui, *Sci. Rep.* **2017**, *7*, 39695.

[45] X. P. Cui, K. J. Jiang, J. H. Huang, X. Q. Zhou, M. J. Su, S. G. Li, Q. Q. Zhang, L. M. Yang, Y. L. Song, *Chem. Commun.* **2015**, *51*, 1457–1460.

[46] S. Yang, Q. He, C. Wang, H. Jiang, C. Wu, Y. Zhang, T. Zhou, Y. Zhou, L. Song, *J. Mater. Chem. A* **2018**, *6*, 11281–11287.

[47] J. Wu, R. M. Yadav, M. Liu, P. P. Sharma, C. S. Tiwary, L. Ma, X. Zou, X. D. Zhou, B. I. Yakobson, J. Lou, P. M. Ajayan, *ACS Nano* **2015**, *9*, 5364–5371.

[48] M. Łukaszewski, M. Soszko, A. Czerwiński, *Int. J. Electrochem. Sci.*, **2016**, *11*, 4442–4469.

[49] H. An, L. Wu, L. Mandemaker, S. Yang, J. de Ruiter, J. Wijten, J. Janssens, T. Hartman, W. van der Stam, B. M. Weckhuysen, *Angew. Chem. Int. Ed.* **2021**, *60*, 16576– 16584.

[50] L. D. Burke, M. J. G. Ahern, T. G. Ryan, J. Electrochem. Soc. 1990, 137, 553–561.

[51] M. Ma, K. Djanashvili, W. A. Smith, *Phys. Chem. Chem. Phys.* **2015**, *17*, 20861–20867.

[52] P. Panagiotopoulou, A. Christodoulakis, D. I. Kondarides, S. Boghosian, *J. Catal.* **2006**, *240*, 114–125.

[53] C. H. Lee, M. W. Kanan, *ACS Catal.* **2015**, *5*, 465–469.

[54] M. J. W. Blom, V. Smulders, W. P. M. van Swaaij, S. R. A. Kersten, G. Mul, *Appl. Catal. B:* Environmental **2020**, *268*, 118420.

[55] B. Innocent, D. Liaigre, D. Pasquier, F. Ropital, J. M. Léger, K. B. Kokoh, *J. Appl. Electrochem.* **2009**, *39*, 227–232.

[56] S. Ha, R. Larsen, R. I. Masel, *J. Power Sources* **2005**, *144*, 28–34.

[57] S. Chu, S. Hong, J. Masa, X. Li, Z. Sun, *Chem. Commun.*, **2019**, *55*, 12380−12383.

[58] L. Lin, H. Li, C. Yan, H. Li, R. Si, M. Li, J. Xiao, G. Wang, X. Bao, *Adv. Mater.* **2019**, *31*, 1903470.

[59] W. Xie, H. Li, G. Gui, J. Li, Y. Song, S. Li, X. Zhang, J. Y. Lee, M. Shao, M. Wei, *Angew. Chem. Int. Ed.* **2021**, *60*, 7382–7388.

[60] Y. Li, B. Wei, M. Zhu, J. Chen, Q. Jiang, B. Yang, Y. Hou, L. Lei, Z. Li, R. Zhang, Y. Lu, *Adv. Mater.* **2021**, *33*, 2102212.

2

Chapter 3

Near Unity Electrochemical CO_2 Conversion to CO over Tin−Doped Copper Oxide Nanoparticles

Abstract

Bimetallic electrocatalysts have emerged as a viable strategy to tune the electrocatalytic CO_2 reduction reaction (eCO_2RR) for the selective production of valuable base chemicals and fuels. However, obtaining high product selectivity and catalyst stability remain challenging, which hinders the practical application of eCO_2RR. In this Chapter, it was found that a small doping concentration of tin (Sn) in copper oxide (CuO) has profound influence on the catalytic performance, boosting the Faradaic Efficiency (FE) up to 98% for carbon monoxide (CO) at –0.75 V vs. RHE, with prolonged stable performance (FE > 90.0%) up to 15 h. Through a combination of *ex situ* and *in situ* characterization techniques, the *in situ* activation and reaction mechanism of the electrocatalyst at work was elucidated. *In situ* Raman Spectroscopy measurements revealed that the binding energy of the crucial adsorbed *CO intermediate was lowered through Sn doping, thereby favoring gaseous CO desorption. This observation was confirmed by Density Functional Theory (DFT), which further indicated that hydrogen adsorption and subsequent hydrogen evolution was hampered on the Sn−doped electrocatalysts, resulting in boosted CO formation. It was found that the pristine electrocatalysts consisted of CuO nanoparticles decorated with SnO_2 domains, as characterized by *ex situ* high−resolution scanning transmission electron microscopy (STEM) and X−ray Photoelectron Spectroscopy (XPS) measurements. These pristine nanoparticles were subsequently *in situ* converted into a catalytically active bimetallic Sn−doped Cu phase. This Chapter sheds light on the intimate relationship between bimetallic structure and catalytic behavior, resulting in stable and selective oxide−derived Sn−doped Cu electrocatalysts.

3.1 Introduction

The electrochemical carbon dioxide (CO_2) reduction reaction (eCO_2RR) to value−added chemicals and fuels, possibly powered by renewable electricity, has emerged as a promising strategy to valorize CO_2 emissions from the chemical industry.[1] The pioneering contributions by Hori *et al.* have inspired numerous researchers over the past decades and many efforts have been made to develop new catalyst compositions, formulations and structures with boosted eCO_2RR performance. It is generally accepted that eCO_2RR depends heavily on catalyst structure and composition, and can be influenced by external factors (*e.g.,* composition of the electrolyte).[2,3] Copper (Cu) stands out as electrode material, because it has displayed the unique capability to reduce CO_2 to hydrocarbon products, such as ethylene and methane. However, high material cost, low product selectivity and poor stability remain big challenges that need to be resolved before electrocatalysis can be implemented into industrial applications.[4,5] Higher production rates and Faradaic Efficiencies (FE) have been reported for two−electron products, such as carbon monoxide (CO), by utilization of silver (Ag) and gold (Au) based electrocatalysts. Compared to multi−electron products, such as ethylene (C_2H_4) and ethanol (C_2H_5OH), which suffer from large overpotentials and limited selectivity, production of two−electron products potentially offers more immediate opportunities for practical application.[6] For example, CO is one of the main components of syngas (CO + H_2), used in Fischer−Tropsch synthesis (FTS) reactions, which generates synthetic petroleum and other fuels.[7] Therefore, developing advanced and stable electrocatalysts for selective CO generation is of practical importance in the field of electrochemical CO_2 conversion.

Unfortunately, the electrocatalytically active metals for CO production, such as Ag and Au, require large overpotentials and their widespread implementation is limited by their high cost.[8,9] Cu can also catalyze the electrochemical CO_2 to CO conversion reaction, but due to the intermediate adsorption strength of CO at the Cu surface, these electrocatalysts still suffer from poor selectivity towards CO, and often a wide distribution of reaction products is observed.[10] It has been reported that the selectivity of Cu for CO and ethylene can be tuned via synergistic effects through doping with precious secondary metals, such as Ag and Au.[11,12] However, it would be beneficial if high selectivity for eCO_2RR products can be achieved through doping of Cu with cheaper metals to form bimetallic catalysts.

Appealing candidates would be post−transition metals, such as indium (In), lead (Pb), bismuth (Bi) and tin (Sn). Due to their d^{10} electronic configuration, these metals selectively promote CO_2 to formate conversion and suppress the competing Hydrogen Evolution Reaction (HER).[13,14] Among these formate−selective metals, Sn−based catalysts have attracted a lot of attention in synergy with Cu due to their solid state miscibility, the low cost and toxicity of Sn, and the optimized electrocatalytic behavior.[15–21] Nevertheless, control over stability and selectivity of Cu−Sn bimetallic systems in eCO_2RR remains a challenge.[22–27] In addition, although Sn is more abundant and cheaper than Ag and Au, there is still a possibility that Sn could become endangered due to its increasing demand in a variety of manufacturing industries.[28,29]

In this Chapter, we report the synthesis and *in situ* activation of bimetallic Sn−doped Cu electrocatalysts with near unity CO_2 to CO conversion for elongated time periods (FE>90% for 15 h). *Ex situ* characterization through high−resolution High Angle Annular Dark Field Scanning Transmission Electron Microscopy (HAADF−STEM) and X−ray Photoelectron Spectroscopy (XPS) indicated small SnO_2 domains at the surface of CuO nanostructures. In the electrochemical CO_2 conversion measurements, these electrocatalysts showed a boosted selectivity towards CO and required low overpotentials (as low as –0.55 V vs. RHE) compared to pure CuO electrocatalysts. The maximum FE for CO could reach up to 98% at –0.75 V vs. RHE for CuO nanoparticles doped with 0.4%Sn, on par with the most selective CO_2 to CO conversions reported to date for bimetallic Cu−Sn electrocatalysts (**Table A2**). *In situ* Raman Spectroscopy and X−ray Diffraction (XRD) measurements revealed that the pristine Cu−Sn oxide nanoparticles were *in situ* reduced into their metallic phase, and that Sn−doping tunes the *CO binding strength. From this we conclude that the active sites for selective electrochemical CO_2 to CO conversion are Sn−doped Cu metallic sites. Furthermore, time−resolved *in situ* Raman measurements and Density Functional Theory (DFT) calculations implied that the adsorption strength of the main intermediate *CO was weakened due to the Sn doping, facilitating the desorption of CO, resulting in boosted CO formation. Furthermore, DFT calculations revealed that Sn doping weakened the hydrogen adsorption, thereby effectively suppressing the competing HER and boosting CO_2 to CO conversion to near unity. This work provides insights into nanoscale synergistic effects in bimetallic Sn−doped Cu electrocatalysts, and possibly paves the way to novel design strategies for stable and selective bimetallic Cu−based electrocatalysts.

3.2 Methods

3.2.1 Catalyst Preparation

CuO nanoparticles were synthesized by a wet chemical method, modified from a previously reported work. [30] First, 998 mg $CuSO_4.5H_2O$ (Sigma−Aldrich, trace metals basis, 99.999%) was dissolved in 100 mL ultrapure water, followed by the addition of 30 mL 0.15 M NH_4OH (Sigma−Aldrich, trace metals basis ≥99.99%) solution. After stirring for 15 min, 6 mL 1.2 M NaOH (Sigma−Aldrich, powder, reagent grade, ≥ 98.0%) solution was added into the above solution dropwise, followed by stirring for another 20 min at room temperature. Subsequently, the obtained suspension containing blue sediment was separated by filtration. The sample collected from filtration was dried in the air at room temperature. When the samples were fully dried, the powder was annealed in an air furnace at 400 °C for 2 h, with a heating rate of 1 °C min^{-1}. The preparation of Sn doped CuO was achieved through galvanic replacement. 10 mg, 20 mg and 30 mg of $SnCl_2$ (Sigma−Aldrich, trace metals basis, ≥99.99%) was dispersed in 40 mL absolute ethanol under ultrasonication for 5 min, followed by the addition of 30 mg CuO nanoparticles, to form CuO−0.4%Sn, CuO−0.6%Sn and CuO−0.8%Sn, respectively. After ultrasonication for another 5 min, the samples were collected and washed with a mixture of ultrapure water and ethanol and dried in the air overnight.

3.2.2 Characterization

3.2.2.1 Basic Characterization

The elemental composition of the pristine samples was characterized by Inductively Coupled Plasma−Optical Emission Spectrometry (ICP−OES, PerkinElmer Optima 8300 Optical Emission Spectrometer). The calibration solutions were prepared by diluting standard calibration solutions (PerkinElmer, N9300233 and N9300234) by 5% HNO_3 solution into different concentrations: 0.0 ppm, 0.2 ppm, 0.4 ppm, 0.6 ppm, 0.8 ppm and 1.0 ppm. Then, the prepared catalysts were dissolved by 1 mL 65% HNO_3 and diluted to the same pH as calibration solutions. An average of three samples was used. The phase structure of studied materials was determined by X−ray Diffraction (XRD) measurements on a Bruker D2 Phaser diffractometer for *ex situ* measurement and Bruker D8 Phaser diffractometer for *in situ* measurement, equipped with a Co Kα source (λ = 1.78 Å) and a Cu Kα source (λ = 1.54 Å), respectively. The morphology and elemental distribution were investigated by Transmission Electron Microscopy (TEM, Tecnai20, 200 keV) and High Angle Annular Dark Field Scanning Transmission Electron Microscopy (HAADF−STEM) and coupled STEM Energy Dispersive X−ray Spectroscopy (STEM−EDS) measurements (ThermoFischer Scientific Titan, equipped with the ChemiSTEM system, 200 keV). To do this with the catalyst after catalysis, the particles were scraped of the carbon paper with the help of a scalpel, dispersed in EtOH and dropcasted on the TEM grid. In the X−ray Photoelectron Spectroscopy (XPS) measurements, a K−Alpha X−ray photoelectron spectrometer by ThermoFisher scientific with an aluminum (K= 1486.68 eV) X−ray source was used to collect the X−ray photoelectron spectra. All spectra were calibrated with reference to the C 1s at 284.5 eV. The curve fitting was carried out using Shirley background and Gaussian function.

3.2.2.2 *In situ* Raman Spectroscopy Measurements

A Renishaw InVia Raman microscope and 785 nm excitation laser were used for the *in situ* Raman Spectroscopy measurements, coupled with a Nikon N40X−NIR water−dipping objective. The laser power was set to below 1.5 mW in order to avoid laser damage. The time interval for each spectrum is 1 s for all measured samples. The potential−dependent *in situ* Raman spectroscopy measurements were coupled with CV, for which an Autolab PGSTAT 101 potentiostat was used with a scanning rate of 50 mV s^{-1} in CO_2 saturated 0.1 M $KHCO_3$ electrolyte solution (pH 6.8), from 1.0 V to −0.95 V vs. RHE. The time−dependent *in situ* Raman Spectroscopy measurements were coupled with chronoamperometry (CA) test at potential of −0.75 V vs. RHE.

3.2.2.3 *In situ* X−ray Diffraction Measurements

A Bruker D8 Phaser diffractometer was employed for the *in situ* X−ray Diffraction (XRD) measurements. In a custom−made *in situ* cell, a glassy carbon wafer (SIGRADUR K films, diameter 22 mm, thickness 180 μm) coated with catalysts, a Pt wafer and an Ag/AgCl electrode were used as working electrode, counter electrode and reference electrode, respectively. Back−illumination configuration was used in the measurement under Bragg mode. The electrolyte (*i.e.*, a CO_2 saturated 0.1 M $KHCO_3$ solution) was introduced into the cell with a flow rate of 10 mL/min, using a peristaltic pump (Ismatec 78001−49). The Ivium compactstat.h10800 potentiostat was used for the CA test with a potential fixed at −0.75 V vs. RHE.

3.2.3 Electrochemical Measurements

The Ivium compactstat.h10800 potentiostat was used for electrochemical performance measurements. In a

gas−tight H−cell with two separated chambers, a standard three−electrode system was built with a proton exchange membrane (Nafion 117, Dupont). An Ag/AgCl (ET069−1, −0.205 V vs. SHE) and a Pt−mesh were employed as reference electrode and counter electrode, respectively. Before starting the measurement, 0.1 M KHCO$_3$ (Sigma−Aldrich, powder, ACS reagent, 99.7%) aqueous solution was saturated with CO$_2$ for at least 30 min to obtain an electrolyte with pH of 6.8. During the experiments, CO$_2$ was continuously delivered into the cathodic chamber at a constant rate of 10 mL min^{-1}. To prepare working electrodes, 5 mg catalyst powder was mixed with 20 µL of Nafion solution (5 wt.%) and 500 µL methanol to form catalyst ink after ultrasonication for 2 h. The working electrode was fabricated by drop casting the catalyst ink onto carbon paper (effective electrode area 2 cm^2). The Electrochemical Surface Area (ECSA) was evaluated by the double layer capacitance (C$_{dl}$) through the Cyclic Voltammetry (CV) measurements at different scan rates in the non−Faradaic region by a linear fit of the charging current. The solution resistance (Rs) was determined by Electrochemical Impedance Spectroscopy (EIS) with a frequency range of 10 Hz to 100 kHz for the *iR* correction. The measured potential values were converted to the Reversible Hydrogen Electrode (RHE) using Equation 3.1:

$$E \text{ (vs. RHE)} = E \text{ (vs. Ag/AgCl)} + 0.205 \text{ V} + 0.059 \times pH - iR \qquad (3.1)$$

3.2.4 Products Analysis

In this work, an online Gas Chromatography (GC) was used for gas products analysis, which is equipped with a Thermal Conductivity Detector (TCD) and a Flame Ionization Detector (FID). For liquid products determination, ^{1}H Nuclear Magnetic Resonance (NMR) spectroscopy was employed using water suppression mode. After catalysis, 0.5 mL of electrolyte was extracted and mixed with 0.1 mL of deuterated water (D$_2$O) as lock solvent. 0.05 µL of dimethyl sulfoxide (DMSO) was added as the internal reference.

The Faradaic Efficiency (FE) of gas products was calculated using Equation 3.2:

$$FE = (n \cdot F \cdot c \cdot f) / (Vm \cdot I \cdot 60 \text{ sec/min} \cdot 1000000 \text{ ppm}) \times 100\% \qquad (3.2)$$

Where *n* represents the number of electrons involved to produce the related products from CO$_2$ or H$_2$O (*e. g.,* 2 for CO and H$_2$, 12 for C$_2$H$_4$); *F* is the Faraday constant (96485 C mol^{-1}); *c* is the concentration of the product measured by GC; *f* is the gas flow rate (mL min^{-1}); *I* is the average measured current in 1 min (A); *Vm* is the volume of 1 mol gas at reaction temperature and pressure (24451 mL mol^{-1}).

The FE of liquid products was calculated by using Equation 3.3.

$$FE = (n \cdot F \cdot M \cdot V) / (I \cdot t) \times 100\% \qquad (3.3)$$

Where *n* is the number of electrons transferred to form the desired product (*e. g.,* 2 for HCOOH); *F* is the Faraday constant (96485 C mol^{-1}); *M* is the Molar concentration of the liquid product (mol L^{-1}); *V* is the liquid volume (L); *I* is the average measured current in 1 minute (A); *t* is the duration time (s).

Production rate of all products were calculated by using Equation 3.4:

$$production \ rate = (FE \cdot I) / (n \cdot F \cdot S) \qquad (3.4)$$

Where *n* represents the number of electrons needed to produce the related products; *F* is the Faraday

constant (96485 $C\,mol^{-1}$); I is the average measured current in 1 min (A); S represents the geometric area of the electrode (cm^2).

3.2.5 Density Functional Theory Calculations

The Density Functional Theory (DFT) calculations were conducted by the collaborators. For the modeling of the CuSn surfaces, the models were a periodic ceria slab with a (4×3) surface supercell containing four layers, in which the bottom two layers were frozen. According to the atomic ratios obtained in the XPS measurements results, Cu(111) surface with 48 Cu atoms was constructed, one or two of the Cu atoms at the top layer of the surface were replaced by Sn, describing the structure of $Cu_{x-1}Sn_1$, and $Cu_{x-2}Sn_2$, respectively.

3.3 Results and Discussion

3.3.1 Catalyst Preparation and Characterization

The pristine CuO catalysts were prepared by a simple wet chemical method (**Figure 3.1a**). In this reaction, copper(II) sulfate was dissolved in water, after which ammonia was added to form $[Cu(NH_3)_4]^{2+}$ complexes.[31] The NH_3 ligands were replaced by OH^- through the addition of sodium hydroxide, and the resulting $Cu(OH)_2$ nanowire precursors were precipitated (**Figure 3.1b**). The
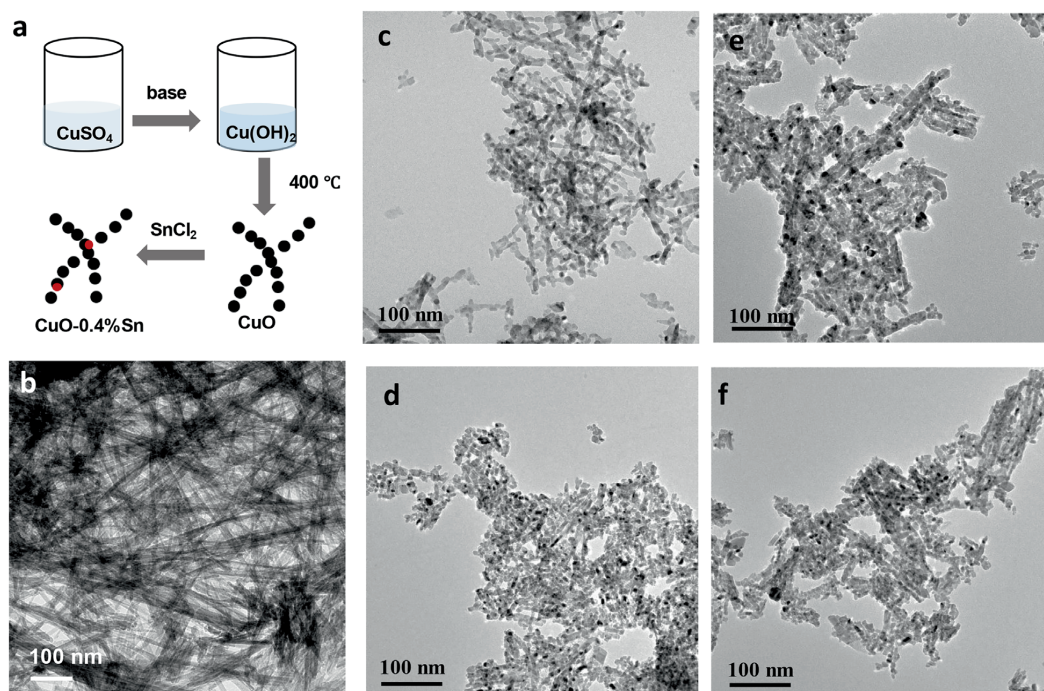
Figure 3.1. Schematic illustration of the catalyst preparation process in this work (a); Transmission Electron Microscopy (TEM) image of the $Cu(OH)_2$ nanowire precursors (b); TEM images of CuO (c), CuO−0.4%Sn (d), CuO−0.6%Sn (e) and CuO−0.8%Sn (f).

Table 3.1. Overview of the Inductively Coupled Plasma−Optical Emission Spectrometry (ICP−OES) results of molar percentage of Sn in the different Sn doped CuO samples under study.

Samples	Cu (mol%)		Sn (mol%)	
	99.59		0.41	
CuO−0.4%Sn	99.55	96.60 (±0.05)	0.45	0.40 (±0.05)
	99.60		0.45	
	99.40		0.60	
CuO−0.6%Sn	99.39	99.40 (±0.05)	0.61	0.60 (±0.05)
	99.44		0.56	
	99.25		0.75	
CuO−0.8%Sn	99.21	99.20 (±0.05)	0.79	0.80 (±0.05)
	99.18		0.82	

CuO nanoparticles were obtained through a thermal treatment, in which the Cu(OH)$_2$ nanowire precursors decomposed at 400 °C. Afterwards, the CuO nanoparticles were doped with Sn by dispersing CuO nanoparticles in an ethanol solution containing SnCl$_2$ under ultrasonication for 10 min. The Sn species formed at the surface of the pristine CuO nanoparticles through a galvanic replacement mechanism.[32] Varying SnCl$_2$ concentrations were used to obtain different degrees of Sn doping, and the Cu:Sn molar ratios were analyzed through Inductively Coupled Plasma Optical Emission Spectroscopy (ICP−OES) measurements (samples are abbreviated as CuO−x%Sn, with x = 0.4, 0.6, 0.8, see **Table 3.1**). Transmission Electron Microscopy (TEM) was applied to study the morphology of the prepared materials. In **Figures 3.1c−f** it can be seen that the pristine CuO and Sn−doped CuO nanoparticles have a similar morphology, with an average size of ~25 nm. This observation already rules out morphology as a possible explanation for variations in catalytic performance, which allows us to selectively study the effect of the dopant on the catalytic behavior. [33]

To get more detailed information about the morphological structure and elemental distribution of the pristine and Sn−doped catalysts, the nanoparticles were investigated by High Angle Annular Dark Field Scanning Transmission Electron Microscopy (HAADF−STEM) and coupled STEM Energy Dispersive X−ray Spectroscopy (STEM−EDS) measurements. HAADF−STEM image of pure CuO and the corresponding elemental analysis are given in **Figures 3.2a, b**, from which high crystallinity and a uniform distribution of Cu and O can be seen. A similar morphology is observed in CuO−0.4%Sn (**Figure 3.2c**), in line with the previous result of TEM characterization. **Figure 3.2d** shows the elemental distribution in the CuO−0.4%Sn sample, where Sn domains can be discerned despite the low Sn content. Besides, it can be seen that the Sn domains are located at the surface of the CuO nanoparticles. The Sn domains are further analyzed with high−resolution HAADF−STEM. Apart from the typical lattice fringe of crystalline CuO (**Figure 3.2e**), lattice fringe of SnO$_2$ can
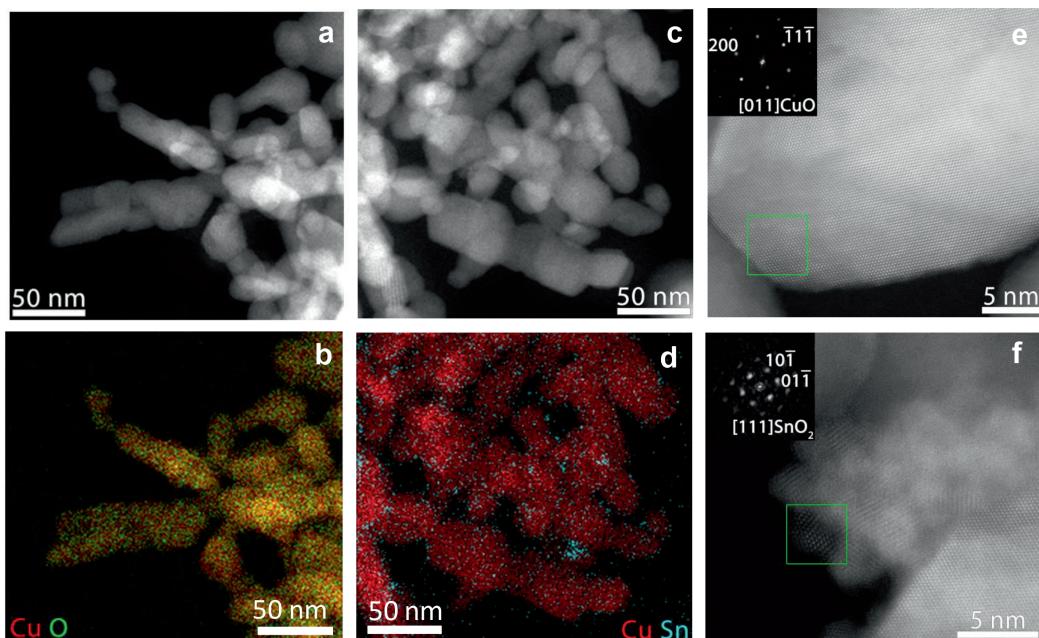
Figure 3.2. High Angle Annular Dark Field Scanning Transmission Electron Microscopy (HAADF–STEM) overview images of CuO (a) and CuO–0.4%Sn (c); The corresponding Energy Dispersive X–ray Spectroscopy (EDS) elemental maps of CuO (b) and CuO–0.4%Sn (d), revealing the distribution of Cu and Sn; (e, f) High–resolution HAADF–STEM images of CuO–0.4%Sn and the corresponding Fourier Transform (FT) patterns (insets). Crystalline domains of SnO_2 and CuO were observed in (e) and (f), respectively.

also be detected (**Figure 3.2f**) at CuO–0.4%Sn, which are further confirmed by the corresponding Fourier Transform (FT) patterns (insets). It can be concluded that Sn doping of CuO nanoparticles resulted in small SnO_2 domains at the surface of the catalyst, suggesting the Sn^{4+} oxidation state.[34]

The crystalline structure of the prepared pristine samples was determined by X–ray Diffraction (XRD) measurements. As shown in **Figure 3.3a**, no peaks related to crystalline Sn species could be found in the different Sn–doped CuO samples under study, and only the diffraction peaks of CuO without any shifts compared to pure CuO are observed. X–ray Photoelectron Spectroscopy (XPS) was further employed to determine the surface chemical state of the different catalyst materials under study. Compared with the bulk Sn/Cu ratios derived from ICP–OES, XPS measurements point to higher Sn/Cu ratios for all Sn–doped samples (**Table 3.2**), suggesting Sn is mainly present at the surface of CuO.

The Cu $2p_{3/2}$ region show that all catalysts have a main line at 933 eV and a prominent satellite, both characteristic of Cu^{2+} (**Figure 3.3b**). From analysis of the Cu $2p_{3/2}$ region, we can exclude the

Table 3.2. Overview of the X−ray photoelectron spectroscopy (XPS) results of atomic percentage of Cu and Sn in the different Sn doped CuO materials under study.

Samples	Cu (at%)	Sn (at%)
CuO−0.4%Sn	98.206	1.794
	98.209	1.791
CuO−0.6%Sn	97.597	2.403
	97.578	2.422
CuO−0.8%Sn	95.923	4.077
	96.123	3.877

presence of $Cu^{0/+}$. [35,36] These observations are confirmed by inspection of the Cu LMM Auger region of the catalysts (**Figure 3.3c**). In **Figure 3.3d**, Sn 3d spectra of all Sn−doped CuO samples evidence the presence of Sn oxides with a main $3d_{5/2}$ feature at 486.6 eV. Metallic Sn (485 eV) species are not observed.[37,38] From the Sn 3d spectra, we can derive that Sn is in the oxidized state, but due to the small separation of the corresponding 3d lines, we cannot unambiguously determine the presence of either Sn^{2+} or Sn^{4+}. However, according to the results in high−resolution HAADF−STEM, the
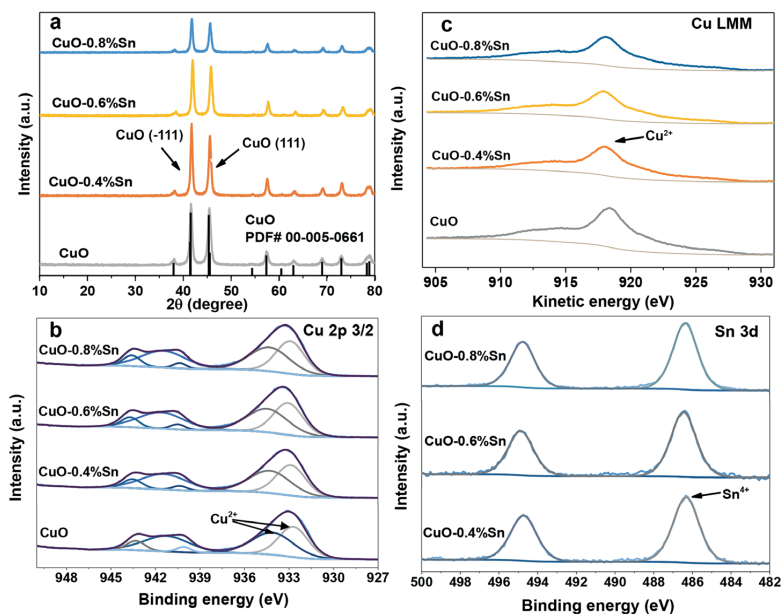
Figure 3.3 Comparison of the X−ray Diffraction (XRD) patterns of CuO and CuO doped with different amounts of Sn using Co Kα1 1.78896 Å(a); XPS measurements of different Sn doped CuO materials for Sn 3d (b) and Cu $2p_{3/2}$ (c); Cu LMM Auger spectra of different Sn doped CuO materials.

oxidation state of element Sn is identified as Sn^{4+}. Together, these findings indicate that Sn is presentin a highly dispersed form at the surface of the CuO particles.

3.3.2 Electrocatalytic Performance

The electrochemical CO_2 conversion behavior was evaluated in CO_2−saturated 0.1 M $KHCO_3$ solution (pH 6.8) by using a gas−tight H−cell, in a standard three−electrode configuration (Ag/AgCl reference electrode, Pt counter electrode and (Sn−doped) CuO nanoparticles on carbon paper as working electrode). Linear Sweep Voltammetry (LSV) was employed on the pristine electrocatalysts in a N_2−saturated electrolyte to analyze the ability of the nanoparticles to catalyze the HER. The pristine CuO nanoparticles displayed the smallest onset potential for HER compared to the Sn− doped CuO catalysts, suggesting a high HER activity, whereas less active HER was observed in
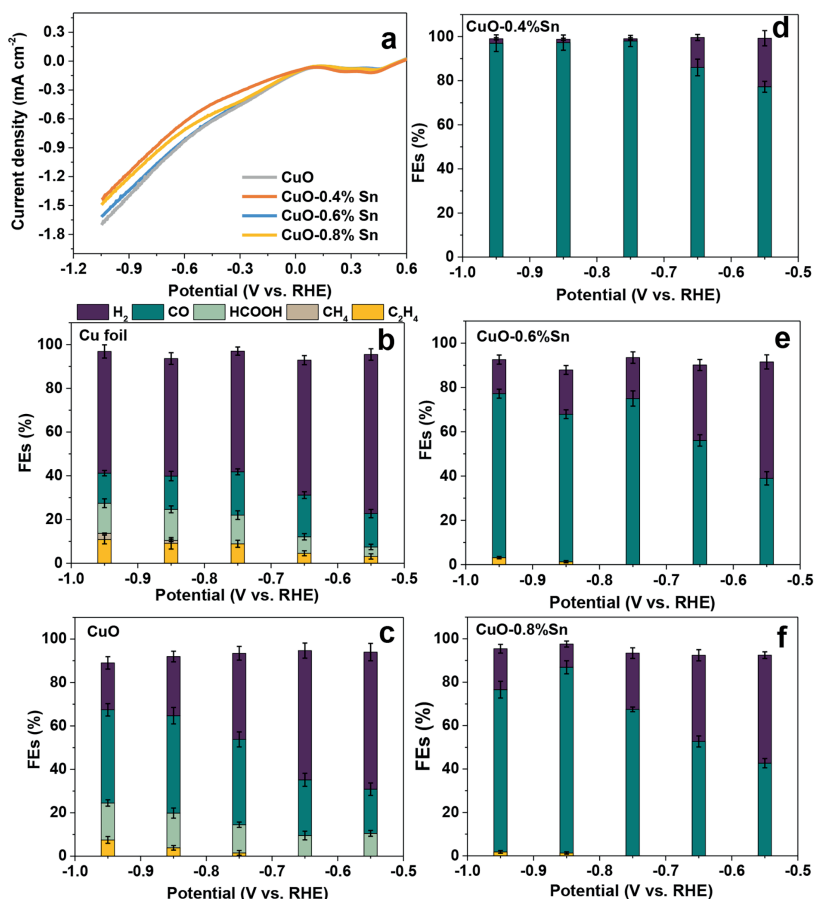
Figure 3.4. Linear Sweep Voltammetry (LSV) curves of CuO, CuO−0.4%Sn, CuO−0.6%Sn and CuO−0.8%Sn in 0.1 M $KHCO_3$ electrolyte saturated with N_2 with a scan rate of 50 mV s^{-1} (a); Potential− dependent Faradaic Efficiencies (FEs) of different products in Cu foil (b), CuO (c), CuO−0.4%Sn (d), CuO−0.6%Sn (e) and CuO−0.8%Sn (f).
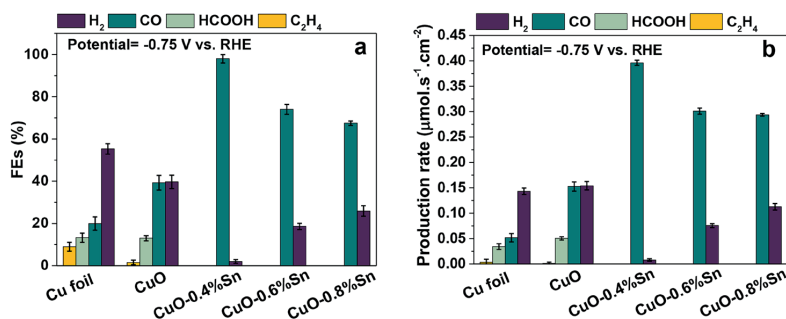
Figure 3.5. Faradaic Efficiencies (FEs) (a) and production rate (b) comparisons of different products at −0.75 V vs. RHE in Sn−doped CuO catalysts, pure CuO and Cu foil.

Sn doped CuO samples (**Figure 3.4a**). No additional pretreatment of the electrocatalysts was performed prior to eCO_2RR analysis, which was conducted on freshly prepared electrodes. To analyze the selectivity toward different eCO_2RR products under various potentials, we applied stepped−potential electrolysis across a potential range from −0.55 to −1.05 V vs. RHE and detected the gaseous products with online Gas Chromatography (GC) and liquid products with offline Nuclear Magnetic Resonance (NMR). In contrast to Cu foil (**Figure 3.4b**) and pure CuO (**Figure 3.4c**) which produced a wide variety of products and substantial HER (>50.0%), all Sn−doped CuO samples (**Figures 3.4d−f**) under study showed boosted selectivity for CO and suppressed HER (<10.0%) in the same potential window.

At an applied potential of –0.75 V vs. RHE (**Figure 3.5a**), the CuO−0.4%Sn sample stands out with a FE of 98.0% for CO_2 conversion to CO. This FE is five−fold and two−fold higher than that of Cu foil (20.0%) and pure CuO (40.0%), respectively. In addition to the improved CO generation, other common products over Cu−based catalysts, such as ethylene, formic acid, and methane, are effectively inhibited and especially the competitive HER was suppressed. The improvement of the CO selectivity clearly depends on the Sn amount. When a higher amount of Sn was introduced into the CuO (CuO−0.6%Sn and CuO−0.8%Sn), HER was only suppressed to a maximum of 20.0%−25.0% (**Figure 3.5a**) and minor hydrocarbon product formation (<3.0%) was observed at increased cathodic bias (**Figures 3.4e, f**). This is probably caused by some bare CuO nanoparticles within the ensemble that remain unaffected by the addition of Sn. The CO enhancement and H_2 suppression on the investigated Sn−doped CuO samples was further verified by comparing their production rates (**Figure 3.5b**). Similarly, the most pronounced production rate enhancement is found for CuO−0.4%Sn, while higher amount of Sn doping leads to lower reaction rates.

Moreover, a significant difference in the stability test was observed between pure CuO and Sn−doped CuO catalysts. Compared to the pure CuO (**Figure 3.6a**), which shows a degradation in CO FE by half after 8 h operation, the Sn−doped CuO samples (**Figures 3.6b−d**) are more stable for CO
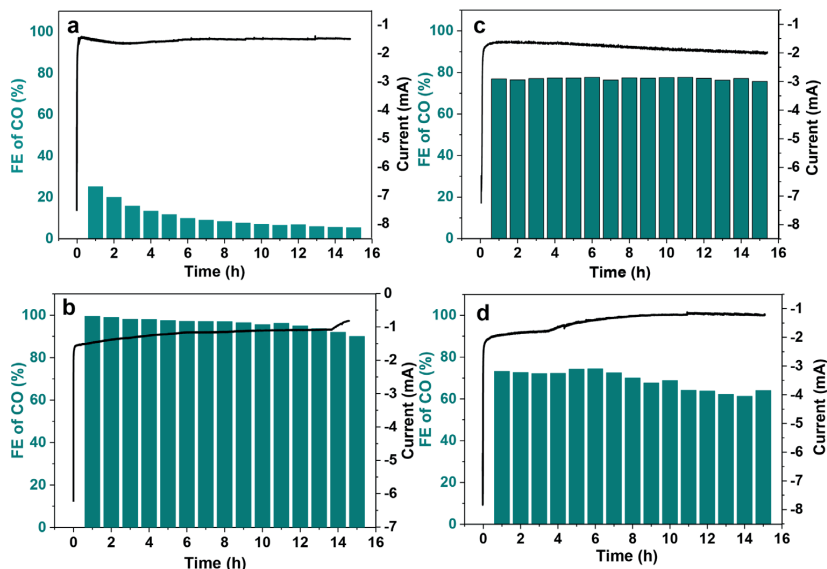
Figure 3.6. Long−term chronoamperometry (CA) test results (line) and the corresponding Faradaic Efficiency (FE) of CO (column) in pristine CuO (a), CuO−0.4%Sn (b), CuO−0.6%Sn (c) and CuO−0.8%Sn (d) at −0.75 V vs. RHE.

formation during prolonged electrochemical reduction of CO_2 (15 h, applied cathodic bias –0.75 V vs. RHE). The current density also remains stable over the course of hours, whereas a significant change in current density is observed during the *in situ* activation of the CuO−Sn particles to the metallic active phase in the first minutes. The decrease in current of CuO−0.8%Sn (**Figure 3.6d**) was observed, which could be attributed to the slight catalyst detachment during the long−lasted measurement. Also here, CuO−0.4%Sn stands out with a FE > 90% CO for 15 h, in contrast to pure CuO nanoparticles which deteriorated over the course of 8 h, after which they only produced half of their initial FE towards CO. Similar trends can be observed in the intrinsic activity. In **Figures 3.7a**,
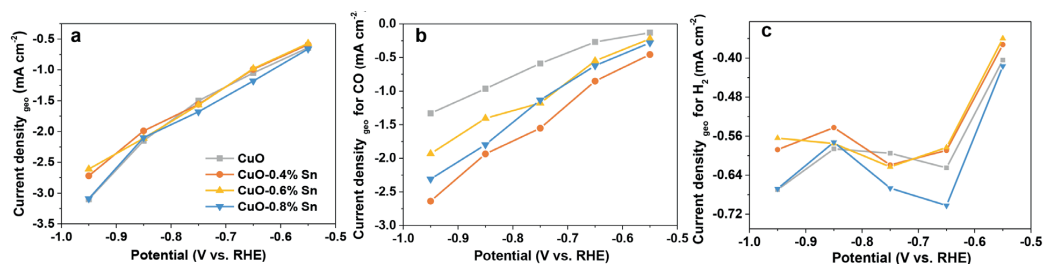
Figure 3.7. Geometric total current densities (a) and partial current densities of CO (b) and H_2 (c) in CuO, CuO−0.4%Sn, CuO−0.6%Sn and CuO−0.8%Sn at different potentials (V vs. RHE).
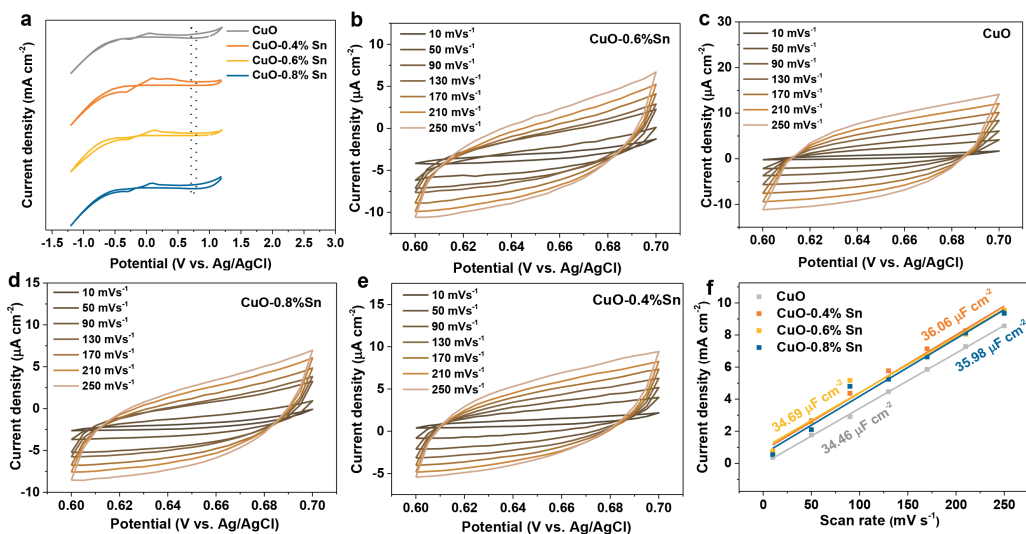
Figure 3.8. Cyclic Voltammetry (CV) curves of the different Sn doped CuO samples at scan rate of 50 mV s^{-1} in CO_2 saturated 0.1 M $KHCO_3$ solution (a); CV curves collected at different scan rates for ECSA measurements of CuO (b), CuO−0.4%Sn (c), CuO−0.6%Sn (d) and CuO−0.8%Sn (e). The potential was chosen from the non−Faradaic region based on the full CV scan (a). (f) Charging current differences at 0.65 V vs. Ag/AgCl for all samples against scan rate for determining double layer capacitance (C_{dl}).

it can be seen that the Sn−doped CuO and pristine CuO samples have similar total geometric current densities. The partial current density of CO over the applied potentials on Sn doped CuO catalysts have higher values than that of CuO (**Figures 3.7b**), which share a similar comparison in FE of CO. However, the H_2 current density of CuO−0.8%Sn is higher than the others whose H_2 current densities are roughly the same (**Figures 3.7c**).

Generally, current densities need to be corrected for the electrochemical active surface area (ECSA) as nanostructures often have enlarged specific surface area which can contribute to catalysis performance due to more active site exposed.[39,40] The ECSA measurement was conducted within the non−Faradaic region in this work, which was determined by the Cyclic Voltammetry (CV) scan shown in **Figure 3.8a**. In **Figures 3.8b−e**, the CV curves were collected with different scan rates. The small difference in C_{dl} (**Figure 3.8f**) for the different samples suggests very similar active surface areas, which is consistent with the trends observed in the total geometric current density analysis. These results imply that morphology is not the critical factor for the boosted catalytic performance of Sn−doped CuO, which is in line with the electron microscopy results described above.

3.3.3 *In situ* Raman Spectroscopy Measurements

To investigate the mechanism behind the CO_2 to CO promotion in the studied Sn−doped Cu bimetallic systems, *in situ* Raman Spectroscopy measurements were conducted in time−dependent and potential−dependent modes (scan speed: one spectrum per second). In **Figure 3.9a** and **3.9b,** the time−dependent Raman spectra of CuO and CuO−0.4%Sn are compared at different stages of catalysis at a fixed potential of –0.75 V vs. RHE. On pure CuO (**Figure 3.9a**), surface CuO_x species are initially present, which are readily reduced at sufficient cathodic bias, evidenced by the disappearance of the CuO_x Raman signal within 5 seconds. Subsequently, a Cu−C band starts to appear around 360 cm^{-1}, which remains constant for the duration of the experiment.[8,41–43] This suggests that the pristine CuO nanoparticles are first *in situ* reduced to metallic Cu, which binds CO. Consistent with this, both the low−frequency band (LFB) and high−frequency band (HFB) of adsorbed CO (*CO) are observed as well at 2050 cm^{-1} and 2090 cm^{-1}, respectively. These LFB and HFB *CO bands have been related to C_2H_4 formation and CO formation in the previous work in our group, respectively.[44] Their coexistence is in line with the catalytic behavior of the CuO nanoparticles, which produce both C_2H_4 and CO. Similarly, in CuO−0.4%Sn (**Figure 3.9b**), CuO_x reduction can be seen at the beginning of the reaction, after which SnO_x (with a characteristic band around 578 cm^{-1}) is observed during the first 10 s, which is readily reduced after ~30 s.[45–49] The observed band around 578 cm^{-1} is attributed to SnO_x, because many reports have shown that the vibrational modes of SnO_x species are very complex.[50–52] The 578 cm^{-1} band could correspond to the S1 mode of SnO_2 (which would be in line with the observed SnO_2 islands in the electron microscopy and XPS analysis), but due to the absence of other vibrational modes of SnO_2, we refer to these bands as SnO_x hereafter.

The SnO_x bands only become apparent after complete removal of CuO_x, because the CuO_x vibrations
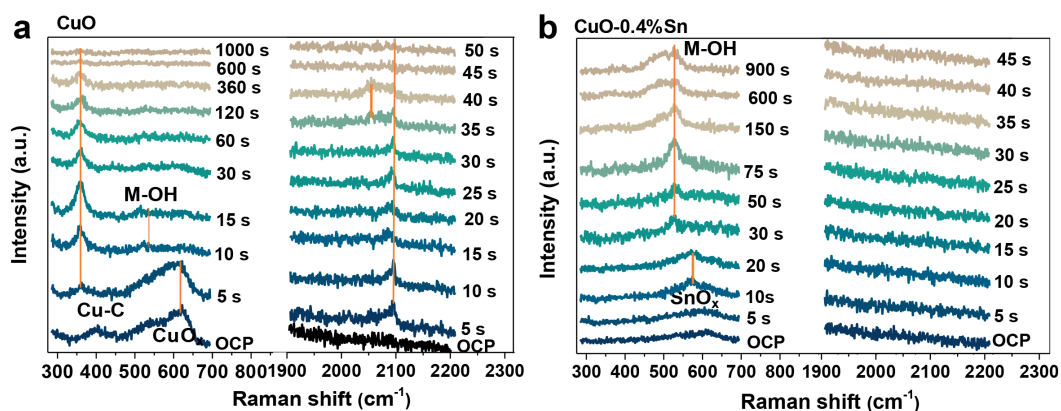
Figure 3.9. Time−dependent *in situ* Raman spectra of (a) CuO and (b) CuO−0.4%Sn. The measurements were employed at −0.75 V vs. RHE in CO_2−saturated 0.1 M $KHCO_3$ electrolyte solution.

initially dominate over the SnO_x signal due to the larger CuO_x volume compared to the SnO_x islands and the formed metallic Cu enhances the SnO_x signal through the Surface Enhanced Raman (SER) effect.[53] The characteristic Cu−C band that was observed for CuO is absent on CuO−0.4%Sn, and a M−OH vibration (with M=Sn or Cu) appears at ~520 cm^{-1} instead.[54–57] Vibrational features around 500 cm^{-1} have been debated in literature,[55] but often species in this region are attributed to hydroxides generated during catalytic conversion reactions. We attribute the band observed around 500 cm^{-1} to metal−hydroxides, which can be stable at moderate cathodic bias according to literatures. [44,54] We note that these hydroxide bands are present in both the pristine CuO and Sn−doped CuO samples, but that the relative intensity varies due to the presence of dominant Cu−C vibrations in the case of *in situ* activated CuO. In addition to the absence of the Cu−C band, both LFB *CO and HFB *CO cannot be detected for the CuO−0.4%Sn sample. Based on the observations above, we hypothesize that the Cu−C, LFB *CO and HFB *CO bands become invisible in our Raman Spectroscopy measurements due to the fast desorption of surface absorbed *CO on timescales faster than our time resolution of one second.
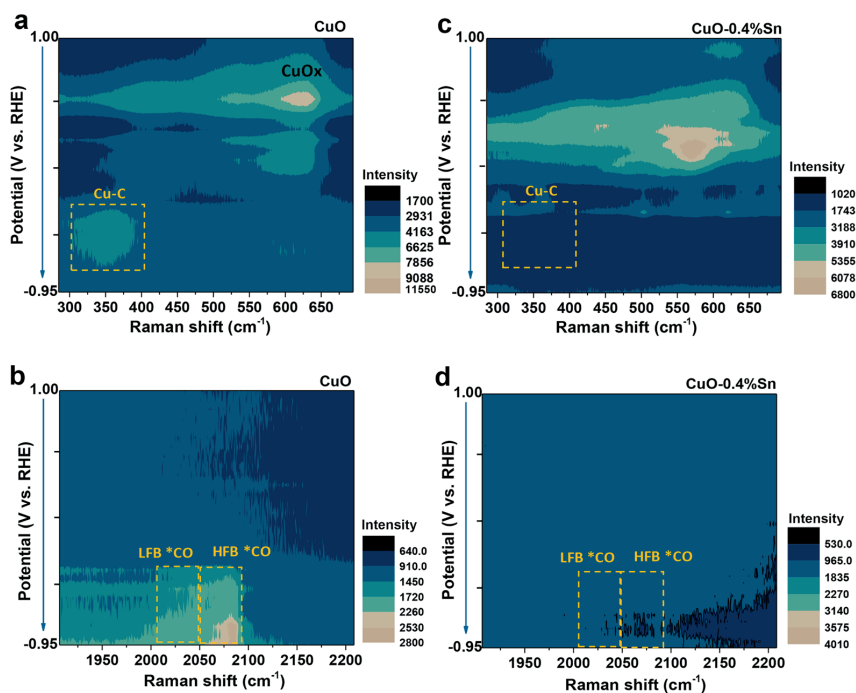
Figure 3.10. Potential−dependent *in situ* Raman spectra heatmaps for CuO in oxide region (a) and CO region (b) and CuO−0.4%Sn in oxide region (c) and CO region (d). The measurements were employed by scanning the potential from 1.0 V vs. RHE to −0.95 V vs. RHE in CO_2−saturated 0.1 M $KHCO_3$ electrolyte solution (pH = 6.8).
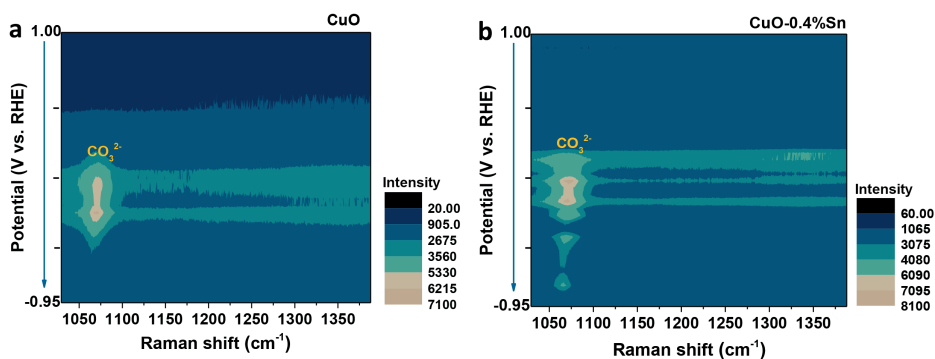
Figure 3.11. Potential−dependent *in situ* Raman spectra heatmap of CuO (a) and CuO−0.4%Sn (b) in the CO_3^{2-} region, with potentials scanning from 1.0 V to −0.95 V vs. RHE in CO_2 saturated 0.1 M $KHCO_3$ solution.

Potential−dependent Raman heatmaps were acquired to gain insights into the dynamics of catalyst activation during cyclic voltammetry scans. Scans were acquired from 1.0 V vs. RHE to –0.95 V vs. RHE under *in situ* conditions. As shown in **Figure 3.10a**, a similar change in electrocatalyst structure is found for the pristine CuO nanoparticles during the cathodic scan from 1.0 V to –0.95 V vs. RHE: initially, CuO is reduced to Cu_2O, followed by Cu_2O reduction to metallic Cu.[58] Reduction to metallic Cu is directly followed by the appearance of the band associated with Cu−C at 360 cm^{-1}, evidencing the presence of *CO as confirmed by the spectra in the CO region (**Figure 3.10b**), around 2000 cm^{-1}). Likewise, we observe LFB *CO and HFB *CO, similar to the time−dependent
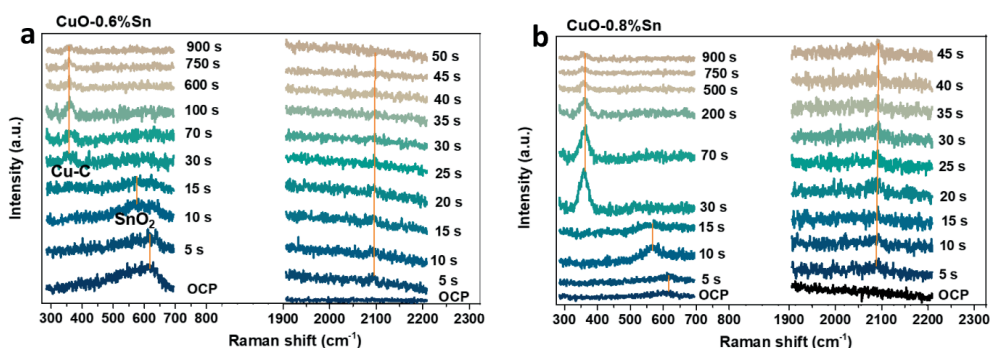
Figure 3.12. Time−dependent *in situ* Raman spectra of CuO−0.6%Sn (a) and CuO−0.6%Sn (b) in the oxide region and the CO region. The measurement was performed at −0.75 V vs. RHE in CO_2 saturated 0.1 M $KHCO_3$ solution.
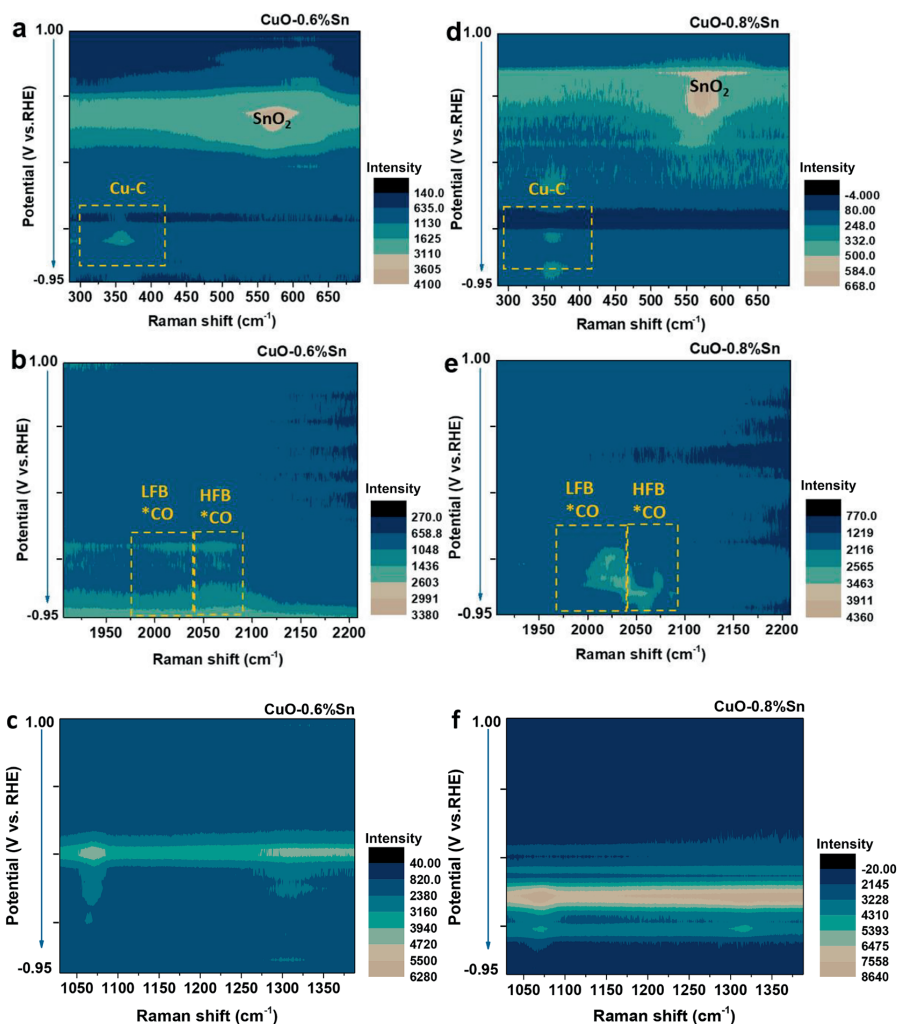
Figure 3.13. Potential−dependent *in situ* Raman spectra heatmap of CuO−0.6%Sn in the oxide region (a), CO region (b) and CO_3^{2-} region (c), and CuO−0.8%Sn in the oxide region (d), CO region (e) and CO_3^{2-} region (f), with potentials scanning from 1.0 to −0.95 V vs. RHE in CO_2 saturated 0.1 M $KHCO_3$ solution.

measurement (**Figure 3.9a**). For CuO−0.4%Sn, similar changes are observed in time−dependent and potential−dependent Raman Spectroscopy (**Figure 3.10c, d**), where bands associated with SnO_2 (at 576 cm^{-1}) appear after copper oxide reduction. These SnO_2 bands disappear around a potential of 0 V vs. RHE, indicating full reduction of the Sn−doped CuO nanoparticles to their metallic counterparts. As was found for the time−dependent Raman measurements, no surface bound *CO was present in the potential−dependent measurements. The absence of surface adsorbed *CO in

both time−dependent and potential−dependent Raman spectra suggests that the adsorption strength of intermediate *CO on activated bimetallic Sn−doped Cu nanoparticles is weakened, resulting in enhanced CO generation. Furthermore, we observe a sharp band around 1075 cm^{-1}, associated with carbonate ions (CO_3^{2-}) in proximity to the electrocatalyst surface of pristine CuO and CuO−0.4%Sn (**Figure 3.11**).[59,60] The main difference between these samples is that the CO_3^{2-} signal persists longer on CuO−0.4%Sn than on the pristine CuO, which implies that the adsorbed *CO on the surface is less dominant so that CO_3^{2-} can approach the electrode for a longer time period.

The samples with different amounts of Sn added (CuO−0.6%Sn and CuO−0.8%Sn) were also investigated with *in situ* Raman Spectroscopy under the same conditions. These samples exhibited high CO selectivity as well, but also showed some activity for ethylene formation (**Figure 3.4**). In their time−dependent *in situ* Raman spectra (**Figure 3.12**), the Cu−C and HFB *CO can be clearly discerned, which indicates that the presence of surface absorbed *CO can be attributed to hydrocarbon formation over activated Sn−doped Cu nanoparticles, which requires long−lived *CO intermediates in order to obtain deeper reduction products (*e.g.*, hydrocarbons). Furthermore, these results imply that *CO is more strongly bound to the nanoparticle surface, resulting in lower FE for CO and reactions beyond CO.

Their potential−dependent *in situ* Raman heatmaps (**Figures 3.13a, d**) prove the presence of SnO_2 species and subsequent metal oxide reduction, immediately followed by the appearance of the Cu−C band on these catalysts under cathodic potentials. Besides, the LFB *CO and HFB *CO are found at high overpotentials (**Figures 3.13b, e**), in accordance with the observations of CO formation along with a little C_2H_4 production at high overpotentials for these catalysts. Similarly, the presence of CO_3^{2-}, which is an indicator for deprotonation close to the surface due to local alkalinity, is observed to persist longer on CuO−0.6%Sn and CuO−0.8%Sn than on pure CuO (**Figures 3.13c, f**).

3.3.4 *In situ* X−ray Diffraction Measurements

In situ XRD measurements were employed to track possible phase changes during catalysis and gain more information about the structure evolution and the activation of the Sn−doped CuO nanoparticles under reaction conditions. For this purpose, an *in situ* XRD cell was designed in house, as depicted in **Figure 3.14a**. In this cell, the bulk structure of the active material is probed in back illumination mode, ensuring optimal signal to noise and hence time resolution due to suppression of X−ray attenuation caused by water−X−ray interactions. Before the *in situ* investigations, *ex situ* XRD was performed prior to and after catalysis to get an idea about possible structural changes induced by the applied negative potential. As shown in **Figure A5** a strong Cu(111) reflection and a small Cu(200) reflection can be observed after catalysis, whereas the reflections of pristine CuO have disappeared. The dynamics of these structural changes were followed by *in situ* XRD measurements, with a time resolution of one diffractogram per minute. In the *in situ* measurements (**Figures 3.14b, c**), the original CuO(−111) and CuO(111) reflections are observed at open circuit potential (OCP). These CuO reflections are still vaguely observed after 3 min of –0.75 V vs. RHE, indicating that full reduction of the CuO nanoparticles is relatively slow, in contrast to the sudden surface oxide
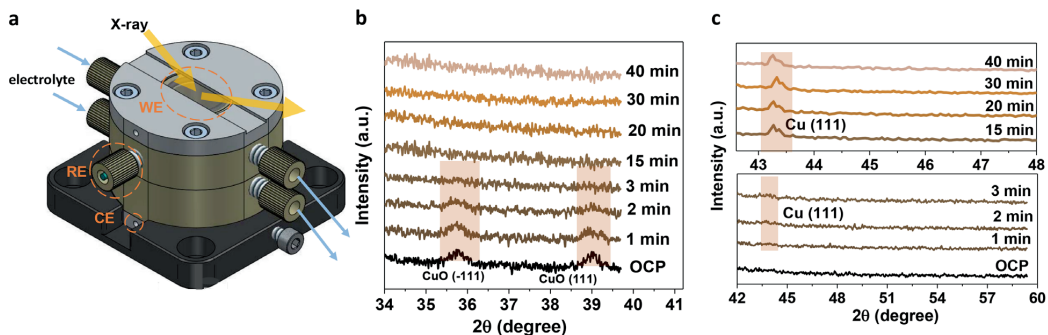
Figure 3.14. Technical drawing of the *in situ* X−ray Diffraction (XRD) cell (a); *In situ* XRD measurements of the CuO−0.4% Sn sample (b), showing the disappearance of the CuO reflections over time at applied cathodic bias of −0.75 V vs. RHE. *In situ* XRD measurements of the CuO−0.4% Sn sample (c), showing the emergence of the Cu(111) reflection after approximately 3 min of −0.75 V vs. RHE cathodic bias.

reduction observed with Raman Spectroscopy. In the diffractogram acquired after 2 min of cathodic bias, a weak reflection is observed at 43.8°, typically associated with metallic Cu(111). This reflection grows in intensity and becomes sharper over time, indicating full reduction of the CuO nanoparticles to metallic Cu and an increase in crystalline domain size, evidenced by a decrease in peak width. These observations are in good agreement with the *in situ* Raman Spectroscopy results, which indicated that surface CuO would be reduced within seconds at onset potential. However, the *in situ* XRD results show that it takes at least 3 min of applied cathodic bias to fully convert the bulk phase of CuO−0.4%Sn to metallic Cu, evidenced by the disappearance of CuO reflections and the emergence of Cu(111).

The electrochemical reduction of CuO and structure reconstruction was confirmed by the HAADF−STEM measurements after catalysis. In **Figure 3.15**, it is observed that both the CuO and the Sn−doped CuO nanoparticles become hollow after catalysis (potentially due to the nanoscale Kirkendall effect).[61] The lattice fringes of metallic Cu can be clearly discerned (**Figures 3.16a, b**) and a thin CuO layer is also observed on the surface of the Sn doped CuO catalyst (**Figure 3.16c**), which can be attributed to the inevitable contact with air during sample transfer. From the STEM− EDS measurements (**Figures 3.16d, e**), it can be seen that Sn signal is absent after catalysis. One possible reason is that the elements redistribute during catalysis in the bimetallic system.[62,63] In this case, the Sn domain of the pristine catalyst dissolved and homogeneously redistributed over the catalyst surface, leading to a lower local Sn concentration that falls below the typical detection limit of the technique (0.1−1.0 at%). This hypothesis is confirmed by ICP−OES measurements after catalysis (**Table 3.3**), which shows that no Sn is leached during catalysis and similar total concentrations of Sn are observed (<1.0%).
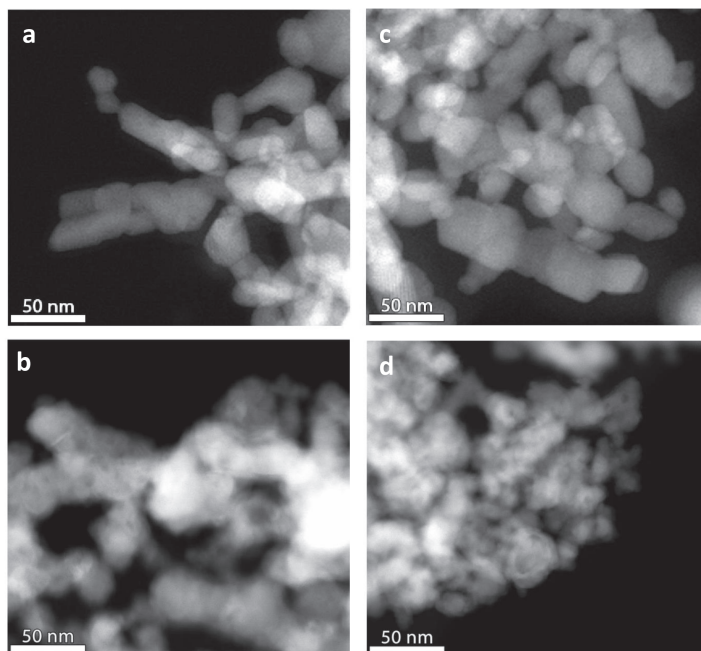
Figure 3.15. High Angle Annular Dark Field Scanning Transmission Electron Microscopy (HAADF–STEM) overview images of CuO before (a) and after eCO$_2$RR (b) catalysis, and CuO−0.4%Sn before (c) and after eCO$_2$RR (d) catalysis.

The combination of *in situ* Raman Spectroscopy and XRD results have indicated that the pristine CuO nanoparticles are activated *in situ* and form metallic Cu and Sn active sites for selective CO$_2$ conversion to CO. By comparison of the activity of undoped and doped nanoparticles and our *in situ* investigations, it becomes evident that Sn doping tunes the adsorption strength of intermediate *CO on the Cu−based catalyst surface. This is evidenced by the *in situ* Raman Spectroscopy measurements, in which sharp Cu−C bands and surface adsorbed *CO are discerned on CuO, whereas *CO is not observed when CO formation is close to unity over CuO−0.4% Sn. It is likely that the desorption of CO on activated Sn−doped Cu nanoparticles is too fast to be detected with the time resolution of our *in situ* Raman Spectroscopy measurements (*i.e.,* one second).

3.3.5 Density Functional Theory Calculations

In order to understand possible mechanistic differences between the reduced CuO and Sn−doped CuO electrocatalysts, Density Functional Theory (DFT) calculations were conducted within the computational hydrogen electrode approach developed by Nørskov's group, while additionally taking into account the solvent implicitly. [64,65] As structural models, Cu(111), Cu$_{x-1}$Sn(111) and Cu$_{x-2}$Sn$_2$(111) were used, in which Sn substituted Cu in the surface Cu layer, representing the active phases of Cu electrodes at varying Sn−dopant levels (**Figure 3.17a**). These structural models are
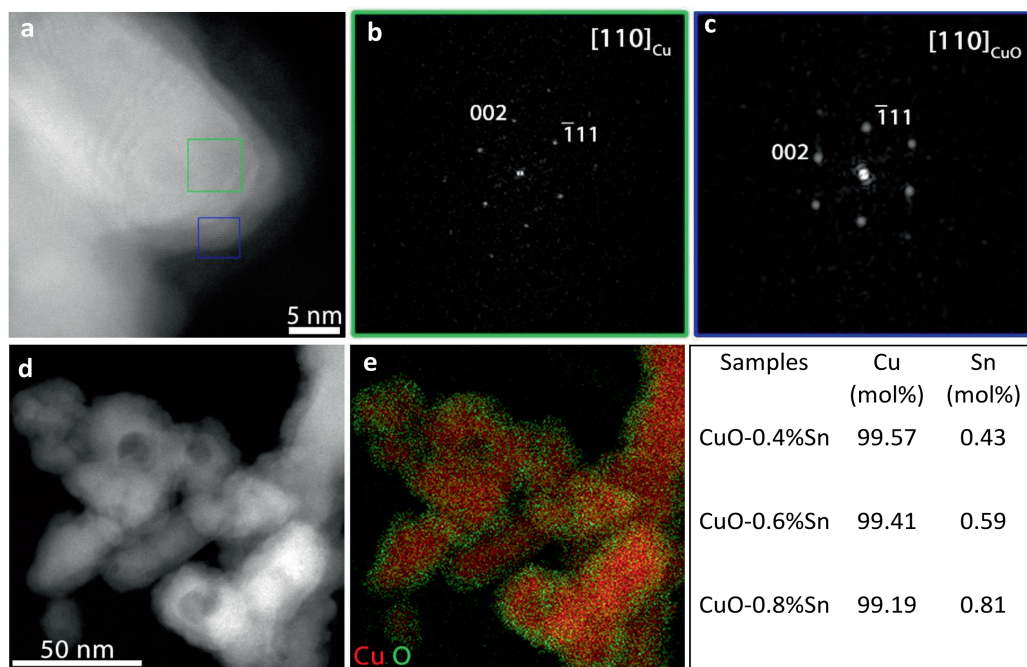
Figure 3.16. Magnified High Angle Annular Dark Field Scanning Transmission Electron Microscopy (HAADF−STEM) image (a) of the spent CuO−0.4%Sn and the corresponding Fourier Transform (FT) patterns from the regions indicated by the green (b) and blue (c) rectangles respectively. The CuO found on the outer layer is attributed to the inevitable oxidation during sample transfer; HAADF−STEM image of the CuO−0.4%Sn sample after eCO$_2$RR catalysis (d) and the corresponding EDS elemental maps (e) of Cu and O, showing the distribution of the elements. Overview of the Inductively Coupled Plasma−Optical Emission Spectrometry (ICP−OES) results of molar percentage of Sn in the different Sn doped CuO samples after catalysis (insert, **Table 3.3**).

in line with the experimental observations, which showed dominant Cu(111) surfaces with <1% Sn doping. Two Cu/Sn ratios were selected for the theoretical models (Cu/Sn 48:1 and 24:1), which roughly correspond to the atomic ratios at the surface for experimental samples CuO−0.4%Sn and and CuO−0.8%Sn as observed with XPS (2.0% and 4.0%, respectively). The distribution of the Sn dopants in the models was investigated, and the influence of Sn distribution was found to be minimal in the Cu$_{x-2}$Sn$_2$(111) models. Using DFT, Gibbs free energies were computed for the key steps involved in electrochemical reduction of CO$_2$ to CO and the competing HER (**Figures 3.17b−c**). According to **Figure 3.17b**, the Gibbs free energies for the formation of *COOH on Cu$_{x-1}$Sn (111), Cu$_{x-2}$Sn$_2$ (111), and Cu (111) are respectively 0.66 eV, 0.69 eV, and 0.61 eV, indicating that Sn doping does not significantly affect the initial protonation step of CO$_2$. According to the computed energy diagrams (**Figure 3.17b**), the desorption of *CO to CO(g) is favored on the Sn−doped models: the
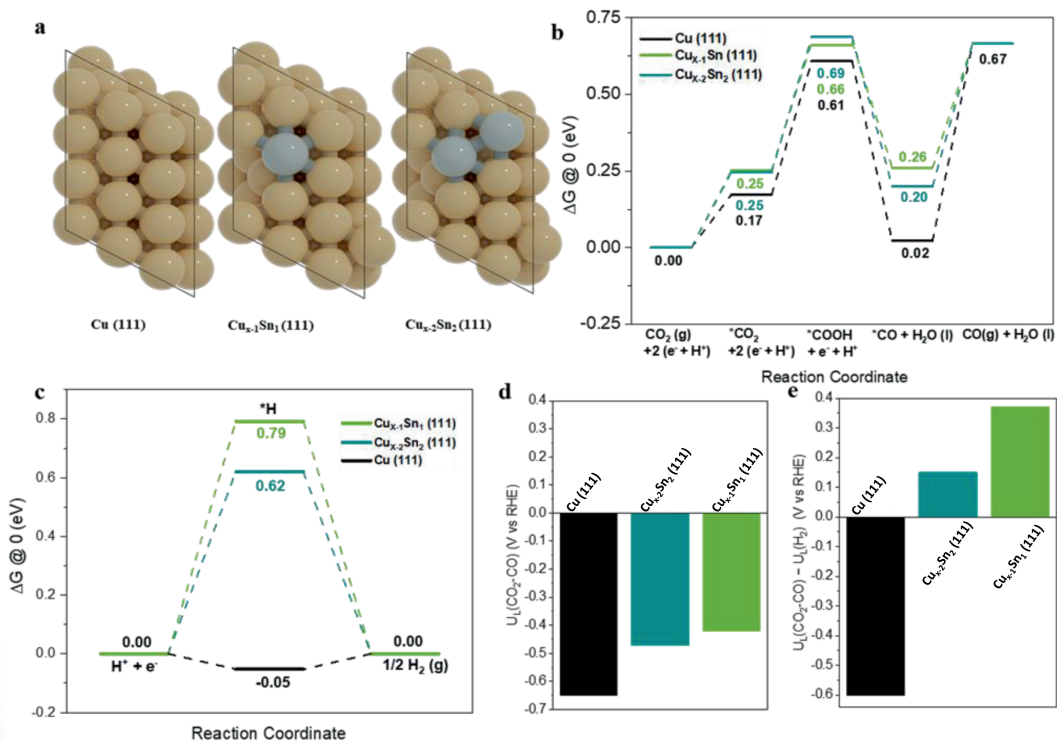
Figure 3.17. Density Functional Theory (DFT) calculations of the electrochemical CO_2 reduction reaction (eCO_2RR) and Hydrogen Evolution Reaction (HER) on CuSn and Cu surfaces: Top views of model 111 slabs for Cu, Cu_{x-1}Sn, and $Cu_{x-2}Sn_2$ (a). Gibbs free energy (ΔG) diagrams for CO_2 reduction to CO (b) on model systems, and H_2 evolution (c) on model systems. Computed limiting potentials (d) for CO_2 reduction. The difference in limiting potentials for CO_2 reduction and H_2 evolution (e).

calculated desorption energies of *CO are 0.41 eV, 0.47 eV and 0.65 eV for the Cu_{x-1}Sn (111), $Cu_{x-2}Sn_2$ (111), and Cu (111) facets, respectively. These differences correlate well with the experimentally observed differences in the CO formation rate, where the Sn−doped CuO nanoparticles displayed higher partial current densities for CO production than CuO nanoparticles. As the HER is the main reaction that competes with CO_2 reduction, the Gibbs free energy for *H formation was also computed for the studied surface models (**Figure 3.17c**). The corresponding values for Cu_{x-1}Sn(111), $Cu_{x-2}Sn_2$(111) are found to be 0.79 eV and 0.62 eV, which are significantly higher than that on Cu(111) (−0.05 eV). The substantial destabilization of *H on the Sn−doped Cu models with respect to Cu(111) can explain the experimentally observed suppressed hydrogen formation for the bimetallic Sn−doped Cu nanoparticle electrodes.

It is also worthwhile to compare the *in situ* Raman spectroscopy data to computed CO adsorption on Cu sites in the models. It has been earlier established that CO adsorption on Sn is very weak.[66] The
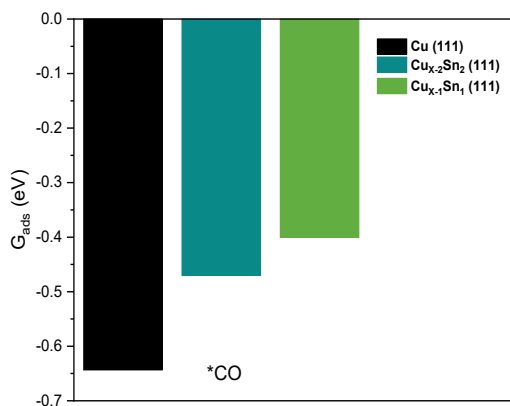
Figure 3.18. The adsorption energy of *CO species on various surface models, showing the weaker adsorption of *CO on the surface of $Cu_{x-1}Sn(111)$ and $Cu_{x-2}Sn_2(111)$ than Cu(111).

data in **Figure 3.17d** shows that *CO adsorption by $Cu_{x-1}Sn(111)$, and $Cu_{x-2}Sn_2(111)$ is weaker than by Cu(111). Notably, the experimental data suggests that CO is weakly adsorbed on the catalytic surface of the Sn−doped CuO nanoparticles. This may be interpreted as a significant part of the Cu surface being terminated by Sn sites, because either no Cu ensembles are available or these sites bind CO weaker because of the nearby presence of Sn. Thus, the presence of Sn at the surface of the *in situ* activated electrocatalyst tunes the adsorption strength of the key intermediate *CO.

These results can also be discussed in terms of the limiting potential U_L, which is the potential at which a reaction step becomes exergonic. The limiting potential U_L equals $-\Delta G/e$ with ΔG being the Gibbs free energy change for the potential−limiting step. Since the activation barriers scale with such Gibbs free reaction energies, trends in U_L follow trends in activity.[67] **Figure 3.17d** shows the thermodynamic limiting potentials $U_L(CO_2-CO)$ for the three model systems. $U_L(CO_2-CO)$ is the most positive for $Cu_{x-1}Sn(111)$ followed by $Cu_{x-2}Sn_2(111)$ and Cu(111), consistent with the order in overall current densities observed in the experiments. The difference between the limiting potentials for CO_2 reduction and H_2 evolution, *i.e.* $U_L(CO_2-CO) - U_L(H_2)$, reflects the difference in reaction rates towards CO and H_2 and, henceforth, the CO selectivity.[68] As shown in **Figure 3.17e**, the computed differences in $U_L(CO_2-CO) - U_L(H_2)$ can explain well the decrease in FE to CO when going from CuO−0.4% Sn to CuO−0.8%Sn and CuO. Overall, the DFT calculations help to understand why CuO−0.4%Sn is the catalyst with the highest electrocatalytic activity and increased CO selectivity due to a lower binding energy of CO and H.
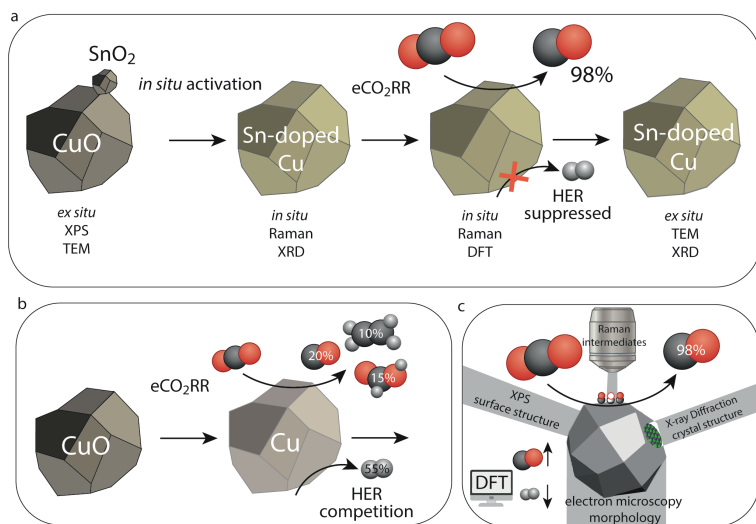
Figure 3.19. Summary of the *in situ* activation and electrocatalytic CO$_2$ reduction performance of (a) Sn−doped CuO nanoparticles and (b) pristine CuO nanoparticles, as evidenced by (c) a combination of *ex situ* and *in situ* techniques and DFT calculations.

Figure 3.19 summarizes the *in situ* activation of the pristine electrocatalysts and the differences in performance between pure CuO and Sn−doped CuO electrocatalysts, as analyzed by a combination of *ex situ* and *in situ* characterization techniques and DFT calculations.

3.4 Conclusions

In this Chapter, Sn−doped Cu bimetallic electrocatalysts are activated *in situ* from pristine SnO$_2$−decorated CuO nanoparticles, which displayed near unity selectivity for CO$_2$ to CO conversion with stable performance up to 15 h. The pristine morphology and structure were elucidated through *ex situ* electron microscopy and X−ray spectroscopy and diffraction measurements, which revealed that CuO nanoparticles were decorated with SnO$_2$ domains. The *in situ* activated Sn−doped Cu electrocatalysts displayed improved electrochemical CO$_2$ conversion to CO, with a record Faradaic Efficiency of 98.0% for CuO−0.4%Sn at an applied potential of –0.75 V vs. RHE. Time− and potential−dependent *in situ* Raman Spectroscopy and *in situ* X−ray Diffraction measurements were utilized to reveal the activation of the catalyst, and the adsorbed species at the catalyst surface. We find that pristine surface CuO is readily reduced within a few seconds, resulting in the presence of *CO and Cu−C vibrations in the Raman spectra, whereas full reduction of bulk CuO takes at least 3 min according to the *in situ* X−ray Diffraction measurements. Sn−doping resulted in the absence of *CO vibrations in the Raman spectra, suggesting fast desorption of gaseous CO, in line with the near unity electrocatalytic performance. This was confirmed by Density Functional Theory (DFT)

calculations, which revealed that the secondary component (Sn) strongly suppresses the hydrogen evolution reaction and weakens the adsorption strength of the key intermediate *CO on the catalyst surface, leading to boosted CO generation. This work opens up an attractive avenue to develop high−performance and low−cost electrocatalysts through doping of Cu−based electrocatalysts with post−transition metals, and provides insights into nanoscale synergistic events and *in situ* activation of oxide−derived Sn−doped Cu nanoparticles.

3.5 Acknowledgements

3.6 References

3

[1]   Y. Y. Birdja, E. Pérez−Gallent, M. C. Figueiredo, A. J. Göttle, F. Calle−Vallejo, M. T. M. Koper, *Nat. Energy* **2019**, *4*, 732–745.

[2]   M. C. O. Monteiro, F. Dattila, N. López, M. T. M. Koper, *J. Am. Chem. Soc.* **2022**, *144*, 1589–1602.

[3]   L. Wu, K. E. Kolmeijer, Y. Zhang, H. An, S. Arnouts, S. Bals, T. Altantzis, J. P. Hofmann, M. C. Figueiredo, E. J. M. B. Hensen, B. M. Weckhuysen, W. van der Stam, *Nanoscale*, **2021**, *13*, 4835−4844.

[4]   D. Gao, R. M. Arán−Ais, H. S. Jeon, B. Roldan Cuenya, *Nat. Catal.* **2019**, *2*, 198–210.

[5]   S. Nitopi, E. Bertheussen, S. B. Scott, X. Liu, A. K. Engstfeld, S. Horch, B. Seger, I. E. L. Stephens, K. Chan, C. Hahn, J. K. Nørskov, T. F. Jaramillo, I. Chorkendorff, *Chem. Rev.* **2019**, *119*, 7610–7672.

[6]   S. Jin, Z. Hao, K. Zhang, Z. Yan, J. Chen, *Angew. Chem. Int. Ed.* **2021**, *60*, 20627–20648.

[7]   I. C. ten Have, B. M. Weckhuysen, *Chem. Catal.* **2021**, *1*, 339–363.

[8]   W. Akemann, A. Otto, *J. Raman Spectrosc.* **1991**, *22*, 797–803.

[9]   T. Zheng, K. Jiang, H. Wang, *Adv. Mater.* **2018**, *30*, 1802066.

[10]   M. Ma, K. Djanashvili, W. A. Smith, *Angew. Chem. Int. Ed.* **2016**, *55*, 6680–6684.

[11]   Z. Tao, Z. Wu, X. Yuan, Y. Wu, H. Wang, *ACS Catal.* **2019**, *9*, 10894–10898.

[12]   J. Huang, M. Mensi, E. Oveisi, V. Mantella, R. Buonsanti, *J. Am. Chem. Soc.* **2019**, *141*, 2490–2499.

[13]   J. E. Pander, M. F. Baruch, A. B. Bocarsly, *ACS Catal.* **2016**, *6*, 7824–7833.

[14]   Z. Yang, F. E. Oropeza, K. H. L. Zhang, *APL Mater.* **2020**, *8*, 060901.

[15]   Y. Chen, M. W. Kanan, *J. Am. Chem. Soc.* **2012**, *134*, 1986–1989.

[16]   Q. Li, J. Fu, W. Zhu, Z. Chen, B. Shen, L. Wu, Z. Xi, T. Wang, G. Lu, J. J. Zhu, S. Sun, *J. Am. Chem. Soc.* **2017**,

139 (12), 4290–4293.

[17]   Y. Zhao, C. Wang, G. G. Wallace, *J. Mater. Chem. A,* **2016**, *4*, 10710–10718.

[18]   S. Sarfraz, A. T. Garcia−Esparza, A. Jedidi, L. Cavallo, K. Takanabe, *ACS Catal.* **2016**, *6*, 2842–2851.

[19]   S. Zhao, S. Li, T. Guo, S. Zhang, J. Wang, Y. Wu, Y. Chen, *Nano−Micro Lett.* **2019**, *11*, 62.

[20]   M. Zhang, Z. Zhang, Z. Zhao, H. Huang, D. H. Anjum, D. Wang, J. H. He, K. W. Huang, *ACS Catal.* **2021**, *11*, 11103–11108.

[21]   L. C. Pardo Pérez, A. Arndt, S. Stojkovikj, I. Y. Ahmet, J. T. Arens, F. Dattila, R. Wendt, A. Guilherme Buzanich, M. Radtke, V. Davies, K. Höflich, E. Köhnen, P. Tockhorn, R. Golnak, J. Xiao, G. Schuck, M. Wollgarten, N. López, M. T. Mayer, *Adv. Energy Mater.* **2022**, *12*, 2103328.

[22]   M. Schreier, F. Héroguel, L. Steier, S. Ahmad, J. S. Luterbacher, M. T. Mayer, J. Luo, M. Grätzel, *Nat. Energy* **2017**, *2*, 1–9.

[23]   W. Ren, X. Tan, J. Qu, S. Li, J. Li, X. Liu, S. P. Ringer, J. M. Cairney, K. Wang, S. C. Smith, C. Zhao, *Nat. Commun.* **2021**, *12*, 1–8.

[24]   W. Ju, F. Jiang, H. Ma, Z. Pan, Y. B. Zhao, F. Pagani, D. Rentsch, J. Wang, C. Battaglia, *Adv. Energy Mater.* **2019**, *9*, 1901514.

[25]   A. Vasileff, X. Zhi, C. Xu, L. Ge, Y. Jiao, Y. Zheng, S. Z. Qiao, *ACS Catal.* **2019**, *9*, 9411–9417.

[26]   W. J. Dong, Lim, W. J. D. M. Hong, J. Y. Park, W. S. Cho, S. Baek, C. J. Yoo, W. Kim, J. L. Lee, *ACS Appl. Energy Mater.* **2020**, *3*, 10568–10577.

[27]   C. J. Yoo, W. J. Dong, J. Y. Park, J. W. Lim, S. Kim, K. S. Choi, F. O. Odongo Ngome, S. Y. Choi, J. L. Lee, *ACS Appl. Energy Mater.* **2020**, *3*, 4466–4473.

[28]   B. B. K. Sovacool, S. H. Ali, M. Bazilian, B. Radley, B. Nemery, J. Okatz, D. Mulvaney, *Science* **2020**, *367*, 30–33.

[29]   S. Stojkovikj, G. A. El−Nagar, F. Firschke, L. C. Pardo Pérez, L. Choubrac, M. Najdoski, M. T. Mayer, *ACS Appl. Mater. Interfaces* **2021**, *13*, 38161–38169.

[30]   W. Z. Wang, G. H. Wang, X. S. Wang, Y. K. Zhan, Y. K. Liu, C. L. Zheng, *Adv. Mater*. **2002**, *14*, 67−69.

[31]   B. Morosin, A. C. Larson, *Acta Cryst.* **1969**, *B25*, 1417–1419.

[32]   X. Xia, Y. Wang, A. Ruditskiy, Y. Xia, *Adv. Mater.* **2013**, *25*, 6313–6333.

[33]   A. A. Permyakova, J. Herranz, M. El Kazzi, J. S. Diercks, M. Povia, L. R. Mangani, M. Pătru, A. Horisberger, T. J. Schmidt, *ChemPhysChem* **2019**, *20*, 3120–3127.

[34]   W. W. Wang, W. Z. Yu, P. P. Du, H. Xu, Z. Jin, R. Si, C. Ma, S. Shi, C. J. Jia, C. H. Yan, *ACS Catal.* **2017**, *7*, 1313–1329.

[35]   B. Babu, I. Neelakanta Reddy, K. Yoo, D. Kim, J. Shim, *Mater. Lett.* **2018**, *221*, 211–215.

[36]   J. Wu, X. Bai, Z. Ren, S. Du, Z. Song, L. Zhao, B. Liu, G. Wang, H. Fu, *Nano Res.* **2021**, *14*, 1053–1060.

[37]   S. Back, M. S. Yeom, Y. Jung, *J. Phys. Chem. C* **2018**, *122*, 4274–4280.

[38]   X. Jiang, X. Wang, Z. Liu, Q. Wang, X. Xiao, H. Pan, M. Li, J. Wang, Y. Shao, Z. Peng, Y. Shen, M. Wang, *Appl. Catal. B Environ.* **2019**, *259*, 118040.

[39]   Y. Yoon, B. Yan, Y. Surendranath, *J. Am. Chem. Soc.* **2018**, *140*, 2397–2400.

[40]   Z. Q. Liang, T. T. Zhuang, A. Seifitokaldani, J. Li, C. W. Huang, C. S. Tan, Y. Li, P. De Luna, C. T. Dinh, Y. Hu, Q. Xiao, P. L. Hsieh, Y. Wang, F. Li, R. Quintero−Bermudez, Y. Zhou, P. Chen, Y. Pang, S. C. Lo, L. J. Chen, H. Tan, Z. Xu, S. Zhao, D. Sinton, E. H. Sargent, *Nat. Commun.* **2018**, *9*, 3823.

[41]   C. J. Hirschmugl, G. P. Williams, F. M. Hoffmann, Y. J. Chabal, *Phys. Rev. Lett.* **1990**, *65*, 480–483.

[42]   W. Akemann, A. Otto, *Surf. Sci.* **1993**, *287–288*, 104–109.

[43]   C. M. Gunathunge, X. Li, J. Li, R. P. Hicks, V. J. Ovalle, M. M. Waegele, *J. Phys. Chem. C* **2017**, *121*, 12337–12344.

3

[44]   H. An, L. Wu, L. D. B. Mandemaker, S. Yang, J. de Ruiter, J. H. J. Wijten, J. C. L. Janssens, T. Hartman, W. van der Stam, B. M. Weckhuysen, *Angew. Chem. Int. Ed.* **2021**, *60*, 16576–16584.

[45]   K. Yu, Y. Xiong, *Phys. Rev. B* **1997**, *55*, 2666–2671.

[45]   C. H. Shek, G. M. Lin, J. K. L. Lai, *Nanostructured Mater.* **1999**, *11*, 831–835.

[47]   C. Meier, S. Lüttjohann, V. G. Kravets, H. Nienhaus, A. Lorke, P. Ifeacho, H. Wiggers, C. Schulz, M. K. Kennedy, F. E. Kruis, *J. Appl. Phys.* **2006**, *99*, 113108.

[48]   L. Z. Liu, X. L. Wu, F. Gao, J. C. Shen, T. H. Li, P. K. Chu, *Solid State Commun.* **2011**, *151*, 811–814.

[49]   X. Chen, D. A. Henckel, U. O. Nwabara, Y. Li, A. I. Frenkel, T. T. Fister, P. J. A. Kenis, A. A. Gewirth, *ACS Catal.* **2020**, *10*, 672–682.

[50]   A. Diéguez, A. Romano−Rodríguez, A. Vilà, J. R. Morante, *J. Appl. Phys.* **2001**, *90*, 1550–1557.

[51]   M. Batzill, U. Diebold, *Prog. Surf. Sci.* **2005**, *79*, 47–154.

[52]   N. Bodappa, M. Su, Y. Zhao, J. B. Le, W. M. Yang, P. Radjenovic, J. C. Dong, J. Cheng, Z. Q. Tian, J. F. Li, *J. Am. Chem. Soc.* **2019**, *141*, 12192–12196.

[53]   A. Dutta, A. Kuzume, M. Rahaman, S. Vesztergom, P. Broekmann, *ACS Catal.* **2015**, *5*, 7498–7502.

[54]   G. Niaura, *Electrochim. Acta* **2000**, *45*, 3507–3519.

[55]   L. Mandal, K. R. Yang, M. R. Motapothula, D. Ren, P. Lobaccaro, A. Patra, M. Sherburne, V. S. Batista, B. S. Yeo, J. W. Ager, J. Martin, T. Venkatesan, *ACS Appl. Mater. Interf.* **2018**, *10*, 8574–8584.

[56]   C. J. Chang, S. C. Lin, H. C. Chen, J. Wang, K. J. Zheng, Y. Zhu, H. M. Chen, *J. Am. Chem. Soc.* **2020**, *142*, 12119–12132.

[57]   A. Kudelski, *Surf. Sci.* **2009**, *603*, 1328–1334.

[58]   J. de Ruiter, H. An, L. Wu, Z. Gijsberg, S. Yang, T. Hartman, B. M. Weckhuysen, W. van der Stam, *J. Am. Chem. Soc.* **2022**, 144, 15047–15058.

[59]   I. V. Chernyshova, P. Somasundaran, S. Ponnurangam, *Proc. Natl. Acad. Sci. U. S. A.* **2018**, *115*, E9261–E9270.

[60]   Z. Pan, K. Wang, K. Ye, Y. Wang, H. Y. Su, B. Hu, J. Xiao, T. Yu, Y. Wang, S. Song, *ACS Catal.* **2020**, *10*, 3871–3880.

[61]   L. Mu, F.Wang, B. Sadtler, R. A. Loomis, W. E. Buhro, *ACS Nano* **2015**, *9* (7), 7419–7428.

[62]   A. Herzog, A. Bergmann, H. S. Jeon, J. Timoshenko, S. Kühl, C. Rettenmaier, M. Lopez Luna, F. T. Haase, B. Roldan Cuenya, *Angew. Chem. Int. Ed.* **2021**, *60*, 7426–7435.

[63]   J. Vavra, F. Dattila, A. Kormányos, S. Cherevko, N. Lopéz, R. Buonsanti, *ChemRxiv.* **2022**.

[64]   J. K. Nørskov, J. Rossmeisl, A. Logadottir, L. Lindqvist, J. R. Kitchin, T. Bligaard, H. Jónsson, *J. Phys. Chem. B* **2004**, *108*, 17886−17892.

[65]   K. Mathew, R. Sundararaman, K. Letchworth−Weaver, T. A. Arias, R. G. Hennig, *J. Chem. Phys.* **2014**, *140*, 084106.

[66]   A. Bagger, W. Ju, A. S. Varela, P. Strasser, J. Rossmeisl, *ChemPhysChem* **2017**, *18*, 3266−3273.

[67]   S. Wang, V. Petzold, V. Tripkovic, J. Kleis, J. G. Howalt, E. Skúlason, E. M. Fernández, B. Hvolbæk, G. Jones, A. Toftelund, H. Falsig, M. Björketun, F. Studt, F. Abild−Pedersen, J. Rossmeisl, J. K. Nørskov, T. Bligaard, *Phys. Chem. Chem. Phys.* **2011**, *13*, 20760–20765.

[68]   C. Shi, H. A. Hansen, A. C. Lausche, J. K. Nørskov, *Phys. Chem. Chem. Phys.* **2014**, *16*, 4720–4727.

3

Chapter 4

Halide−Guided Active Site Exposure in Bismuth Electrocatalysts for Selective CO$_2$ Conversion to Formic Acid

Abstract

It remains a challenge to identify the active sites of bismuth catalysts in the electrochemical CO$_2$ reduction reaction. Here we show through *in situ* characterization that the activation of bismuth oxyhalide electrocatalysts to metallic bismuth is guided by the halides. *In situ* X-ray diffraction results show that bromide promotes the selective exposure of planar bismuth surfaces, whereas chloride and iodide result in more disordered active sites. Furthermore, we find that bromide-activated bismuth catalysts outperform the chloride and iodide counterparts, achieving high current density (>100 mA cm^{-2}) and formic acid selectivity (>90%), suggesting that planar bismuth surfaces are more active for the electrochemical CO$_2$ reduction reaction. In addition, *in situ* X-ray absorption spectroscopy measurements reveal that the reconstruction proceeds rapidly in chloride-activated bismuth and gradually when bromide is present, facilitating the formation of ordered planar surfaces. These findings show the pivotal role of halogens on selective facet exposure in activated bismuth-based electrocatalysts during the electrochemical CO$_2$ reduction reaction.

4.1 Introduction

The electrocatalytic conversion of carbon dioxide (CO_2) into industrial feedstocks, chemicals and fuels is considered as a powerful tool to store intermittent renewable energy in chemical bonds. [1–4] However, there remain several challenges that need to be faced before the full potential of electrocatalytic CO_2 conversion can be used. Among these challenges, a lot of research has been devoted to optimization of three key descriptors of catalysis: selectivity, activity and stability.[5–9] Despite the fact that C_{2+} products (*e.g.,* ethylene and ethanol) have a greater industrial value than C_1 products (*e.g.,* carbon monoxide and formic acid), the complicated reaction mechanism for C_{2+} products hampers the selectivity and activity.[10] Furthermore, recent techno−economic analysis suggests that the synthesis of CO or formic acid as base chemicals is economically and practically more feasible due to their high production rates and superior adaptability to future industrial implementation compared to C_{2+} products.[11–13] In numerous chemical processes, including electrowinning, leather tanning, and aviation de−icing, formic acid (HCOOH) has been extensively investigated as chemical feedstock[14–16] with a sizable economic market.[17],[18]

Over the past decades, efforts have been aimed at the optimization of electrocatalysts for HCOOH production.[19] Post−transition metal−based electrocatalysts like tin (Sn), indium (In), bismuth (Bi), and lead (Pb) have been extensively investigated as the typical catalysts for selective CO_2 to HCOOH electrochemical conversion due to their strong adsorption of the key intermediates to formate and suppression of the competing Hydrogen Evolution Reaction (HER).[15,20–22] Among the post−transition metals, Sn and In have been studied extensively due to their low cost, relative abundance and easy processability. Due to toxicity reasons, Pb is not vastly studied for electrochemical CO_2 conversion, but has shown promise in combination with Cu for selective CO production.[23] Bi−based electrocatalysts for CO_2 conversion were first reported in 1995, but since then research into Bi−based electrocatalysts has stagnated.[24,25] Recently, Bi−based electrocatalysts are receiving increasing attention because of the low toxicity and abundance of Bi,[26,27] but there is still a lot of room for improvement in terms of activity, selectivity and stability of Bi−based electrocatalysts.[28]

Various strategies, such as nanostructures, defects and selective facet exposure, have been investigated to boost selectivity and activity of electrocatalysts. However, the actual active site, its stability and reaction mechanism under operating conditions are still up for debate.[29] By employing *in situ* Attenuated Total Reflection−Infrared (ATR−IR) Spectroscopy to observe the unaltered oxide layer on the Bi surface, Pander *et al.* concluded that Bi is an oxide−independent electrocatalyst, although other researchers found the Bi−O interaction to be crucial for the effectiveness of Bi−based electrocatalysts in eCO$_2$RR.[30,31] Along with the debate regarding the participation of oxide species, Density Functional Theory (DFT) findings have suggested that the basal Bi(003) plane is less active than the edge plane Bi(012) in the HCOOH formation,[31] while some other work stated that basal sites are more active.[15,32–34] Furthermore, it has been reported that the use of two−dimensional metallic Bi electrocatalysts is beneficial in eCO$_2$RR since the layered structure often results in improved performance.[35–39] Identification of the active sites and disclosure of the restructuring during operation are crucial in the study of Bi−catalyzed eCO$_2$RR in order to logically design a catalyst with improved

activity, selectivity and stability to satisfy the requirement of practical applications. X−ray radiation is ideally suited for this purpose, because it can probe structural features over multiple length scales, depending on the X−ray technique of choice. However, online monitoring of structural changes and distinguishing between the sites responsible for the CO_2 conversion reaction requires dedicated *in situ* X−ray characterization cells due to the attenuation of X−rays by the aqueous electrolyte.[40,41]

In this Chapter, layered {001}−oriented Bi oxyhalide (BiOX, X = Cl, Br, I) nanoplatelets were synthesized and applied as a platform to *in situ* monitor the structure and active sites of Bi−based electrocatalysts in eCO_2RR. Through *in situ* X−ray Diffraction (XRD) and *in situ* Raman Spectroscopy measurements, we follow the dynamics of the *in situ* transformation of the prepared BiOX catalysts into activated metallic Bi electrocatalysts. It was found that the *in situ* activated Bi electrocatalysts selectively exposed specific facets during catalysis, guided by the choice of halide: Br^- promotes Bi(003) exposure, Cl^- results in dominant Bi(012) facets, whereas I^- creates a mixture. Furthermore, we link the facet exposure to catalytic performance. BiOBr (BOB) exhibited a maximum HCOOH selectivity of 91.0% with a current density of 148 mA cm^{-2} at –1.05 V vs. RHE. At the similar applied potential of –1.09 V vs. RHE, BiOCl (BOC) displayed 69.0% HCOOH Faradaic Efficiency (FE) at 88 mA cm^{-2} current density, whereas BiOI (BOI) demonstrated a HCOOH selectivity of 76.0% at –1.08 V vs. RHE with a current density of 95 mA cm^{-2}, in between BOB and BOC. This suggests that the *in situ* formed basal Bi(003) facet is more catalytically active than the stepped Bi(012) site in eCO_2RR. In addition, *in situ* X−ray Absorption Spectroscopy (XAS) measurements revealed that the reconstruction of BOC proceeded rapidly after reduction onset, as indicated by the short−lived transition state, while the transition state in BOB and BOI persists longer. It implies that halogens in BiOX affect the selective facet exposure of the formed Bi during catalysis by tuning the reconstruction rate.

4.2 Methods

4.2.1 Catalyst Preparation

The studied BiOX materials (with X = Br, Cl, and I) were synthesized by hydrothermal synthesis, modified from previously reported works.[42–44] In the procedure to obtain BiOBr, 5 mmol $Bi(NO_3)_3.5H_2O$ (Sigma−Aldrich, reagent grade, 98.0%) and 5 mmol cetyltrimethylammonium bromide (CTAB, Sigma−Aldrich, ≥ 98.0%) were dissolved in 100 mL ultrapure water at room temperature for 40 min with stirring, followed by the addition of 1 M NaOH (Sigma−Aldrich, reagent grade, ≥ 98.0%) solution to adjust the pH to 7. After 1 h stirring, the mixed solution was poured up to 80.0% of the total volume into a 100 mL Teflon−lined stainless autoclave. The autoclave was then heated to 170 °C for 17 h before being cooled to room temperature in air. The sample was centrifuged and washed three times with ethanol and ultrapure water. Finally, the powders obtained were dried in the air at room temperature. Similarly, 4 mmol $Bi(NO_3)_3.5H_2O$ and 4 mmol KCl (Sigma−Aldrich, BioXtra, ≥ 99.0%) were added to 60 mL ultrapure water at room temperature with continuous stirring in a typical procedure for preparing BiOCl. After stirring for 1 h, the suspension was poured into a 100 mL Teflon−lined stainless autoclave. The autoclave was heated to 160 °C for 24 hours.

4

After cooling, the precipitates were centrifuged and washed with ethanol and ultrapure water three times. Finally, the powders were air dried at room temperature. For synthesis of BiOI, 1.5 mmol $Bi(NO_3)_3.5H_2O$ was dissolved in a solution of 20 mL ethanol (Sigma−Aldrich, ACS reagent, ≥ 99.5%), and stirred for 30 min to form solution A. 1.5 mmol KI (Sigma−Aldrich, ACS reagent, > 99.0%) was dissolved into 40 mL ultrapure water to form solution B. Solution A and B were mixed together under vigorous stirring. Then, the mixed solution was transferred into a 100 mL Teflon−lined stainless autoclave. The autoclave was heated at 80 °C for 3 h. After cooling down, the resulting precipitates were collected by centrifugation and washed with ethanol and ultrapure water three times. Finally, the sample was dried in an oven at 60 °C for 12 h before further characterization.

4.2.2 Characterization

4.2.2.1 Basic Characterization

The phase structure of studied materials was determined by X−ray Diffraction (XRD) measurements on a Bruker D8 Phaser diffractometer for *in situ* measurements, equipped with a Cu Kα source (λ = 1.54056 Å). Grazing Incidence X−ray Diffraction (GIXRD) measurement was also conducted in the Bruker D8, using a theta of 0.3°. The morphology was first studied by Scanning Electron Microscopy (SEM, Phenom ProX). Atomic Force Microscopy (AFM) measurements were performed with a Bruker Multimode microscope instrument, using silicon NSC−16 SCANASYST−AIR in ScanAsyst mode. The local crystal structure, morphology and elemental distribution within the particles were determined by conducting High Angle Annular Dark Field Scanning Transmission Electron Microscopy (HAADF−STEM) and STEM Energy Dispersive X−ray Spectroscopy (STEM−EDS) measurements at an aberration corrected ThermoFischer Scientific Titan electron microscope operated at 300 kV, equipped with the ChemiSTEM system. [45]

4.2.2.2 *In situ* Raman Spectroscopy Measurements

A Renishaw InVia Raman microscope and 532 nm excitation laser were used for the *in situ* Raman Spectroscopy measurement, coupled with a Nikon N40X−NIR water−dipping objective. The laser power was set to below 1.5 mW in order to avoid laser damage. The time interval for each spectrum is 10 second for all measured samples. The *in situ* Raman Spectroscopy measurement was coupled with chronoamperometry (CA), for which an Autolab PGSTAT 101 potentiostat was used in CO_2−saturated 0.1 M $KHCO_3$ electrolyte solution (pH 6.8), at potential of −1.15 V vs RHE.

4.2.2.3 *In situ* X−ray Diffraction Measurements

A Bruker D8 Phaser diffractometer was employed for the *in situ* XRD measurements. In a custom−made *in situ* cell, a glassy carbon wafer (SIGRADUR K films, diameter 22 mm, thickness 180 μm) coated with catalysts, a Pt wafer and an Ag/AgCl electrode were used as working electrode, counter electrode and reference electrode, respectively. Back−illumination configuration was used in the measurement under Bragg mode. The electrolyte (CO_2−saturated 0.1 M $KHCO_3$ solution) was introduced into the cell with a flow rate of 10 mL/min, using a peristaltic pump (Ismatec 78001−49). The Ivium compactstat.h10800 potentiostat was used for the CA tests in time−and potential−dependent *in situ* XRD measurements.

4.2.2.4 *In situ* X−ray Absorption Near Edge Spectroscopy Measurements

The Bi L_3−edge High−Energy Resolution Fluorescence Detection X−ray Absorption Spectroscopy (HERFD

–XAS) measurements were performed at the high−brilliance beamline ID26 of the European Synchrotron Radiation Facility (ESRF) in Grenoble, France. The storage ring operated in uniform multi−bunch mode with an electron current of 200 mA. Three undulators (u35) generated the incoming radiation, which was monochromated using a cryogenically cooled Si (111) double crystal monochromator. The X−rays were focused by two bent Pd mirrors to a size of ~210 x 105 μm^2 (horizontal x vertical) at the sample position. The detector was Si Avalanche Photo−Diode (APD) with 200 μm thickness and 10 x 10 mm^2 active area. The *in situ* and *ex situ* measurements were performed at room temperature. The size of an X−ray focus spot on sample surface was 1 μm ×1 μm. For each spectrum, the acquisition time was set to 2 min. The same home−made *in situ* cell which was used for *in situ* XRD measurements with back−illumination configuration was used again for the *in situ* XANES measurements, however, vertically tilted 90 degrees. A glassy carbon wafer (SIGRADUR K films, diameter 22 mm, thickness 180 μm) coated with catalysts, a Pt wafer and an Ag/AgCl electrode were used as working electrode, counter electrode and reference electrode, respectively. The electrolyte (CO_2−saturated 0.1 M $KHCO_3$ solution) was introduced into the cell with a flow rate of 10 mL/min. The Ivium compactstat.h10800 potentiostat was used for the CA tests in time−and potential−dependent *in situ* XAS measurements. Mass−flow controllers (Bronkhorst) controlled the gas atmosphere in the reactor. The preliminary data analysis and normalization was performed using Data Analysis X−ray spectroscopy (DAXS) program available at the ESRF. The Athena software from the Demeter package was used for the Linear Combination Fitting (LCF).

4.2.3 Electrochemical Measurements

The Ivium compactstat.h10800 potentiostat was used for electrochemical performance measurements. In a gas−tight H−cell with two separated chambers, a standard three−electrode system was built with a proton exchange membrane (Nafion 117, Dupont). An Ag/AgCl (ET069−1, 5 mm) and a Pt−mesh were employed as reference electrode and counter electrode, respectively. Before starting a measurement, 0.1 M $KHCO_3$ (Sigma−Aldrich, ACS reagent, 99.7%) aqueous solution was saturated with CO_2 for at least 30 min to obtain an electrolyte with pH of 6.8. During the experiments, CO_2 was continuously delivered into the cathodic chamber at a constant rate of 10 mL min^{-1}. In a Gas Diffusion Electrode (GDE) flow cell, the same type of membrane was used. An Ag/AgCl (LF−1, 1 mm) and a platinized Ti electrode were employed as reference electrode and counter electrode, respectively. 1 M $KHCO_3$ solution was used as electrolyte in GDE flow cell. To prepare working electrodes, 5 mg catalyst powder was mixed with 20 μL 5 wt. % Nafion (Alfa Aesar, Nafion® D−520 dispersion) solution and 500 μL methanol (Sigma−Aldrich, ≥ 99.9%) to form catalyst ink after ultrasonication for 2 h. The working electrode was fabricated by drop casting the catalyst ink onto carbon paper (effective electrode area 2 cm^2 in H−cell and 0.5 cm^2 in GDE flow cell). The Electrochemical Surface Area (ECSA) was evaluated by the double layer capacitance (C_{dl}) through the Cyclic Voltammetry (CV) measurements at different scan rates in the non−Faradaic region by a linear fit of the charging current. The solution resistance (Rs) was determined by Electrochemical Impedance Spectroscopy (EIS) with a frequency range of 10 Hz to 100 kHz for the *iR* correction. The measured potential values were converted to the Reversible Hydrogen Electrode (RHE) using Equation 4.1:

$$E \ (vs. \ RHE) = E \ (vs. \ Ag/AgCl) + 0.205 \ V + 0.059 \times pH - iR \tag{4.1}$$

The potential−dependent catalytic performance was probed by potentiostatic test at different cathodic potentials. Each potential was held for at least 40 min.

4.2.4 Products Analysis

Online Gas Chromatography (GC) was used for gas products analysis, which is equipped with a Thermal Conductivity Detector (TCD) and a Flame Ionization Detector (FID). For liquid products determination, ^{1}H Nuclear Magnetic Resonance (NMR) spectroscopy was employed using water suppression mode. After catalysis, 0.5 mL of electrolyte was extracted and mixed with 0.1 mL of deuterated water (D$_2$O, Sigma− Aldrich, ≤1 ppm) as lock solvent. 0.05 μL of dimethyl sulfoxide (DMSO, Sigma−Aldrich, ACS reagent, ≥99.9%) was added as the internal reference.

The Faradaic Efficiency (FE) of gas products was calculated using Equation 4.2:

$$FE = (n \cdot F \cdot c \cdot f) / (Vm \cdot I \cdot 60\ sec/min \cdot 1000000\ ppm) \times 100\% \tag{4.2}$$

Where n represents the number of electrons involved to produce the related products from CO$_2$ or H$_2$O (*e.g.*, 2 for CO and H$_2$, 12 for C$_2$H$_4$); F is the Faraday constant (96485 C mol^{-1}); c is the concentration of the product measured by GC; f is the gas flow rate (mL min^{-1}); I is the average measured current in 1 min (A); Vm is the volume of 1 mol gas at room temperature and pressure (24451 mL mol^{-1}).

The FE of liquid products was calculated by using Equation 4.3:

$$FE = (n \cdot F \cdot M \cdot V) / (I \cdot t) \times 100\% \tag{4.3}$$

Where n is the number of electrons transferred to form the desired product (*e.g.,* 2 for HCOOH); F is the Faraday constant (96485 C mol^{-1}); M is the molar concentration of the liquid product; V is the liquid volume; I is the average measured current in 1 minute (A); t is the duration time (s).

Production rate of all products were calculated by using Equation 4.4:

$$production\ rate = (FE \cdot I) / (n \cdot F \cdot S) \tag{4.4}$$

Where n represents the number of electrons needed to produce the related products; F is the Faraday constant (96485 C mol^{-1}); I is the average measured current in 1 min (A); S represents the geometric area of the electrode (cm^2).

4.3 Results and Discussion

4.3.1 Catalyst Preparation and Structural Characterization

Figure 4.1a depicts a typical BiOX (X = Cl, Br, and I) layered structure. Through weak van der Waals interactions, the neighboring halogen layers in the BiOX stack and the [Bi$_2$O$_2$]$^{2+}$ slab are sandwiched between two layers of halogen atoms.[46] The studied BiOBr (BOB), BiOCl (BOC) and BiOI (BOI) catalysts were prepared through hydrothermal synthesis (see more details in 4.2 Methods section). To determine the electronic structure of the obtained materials and the crystal phase, X−ray Absorption Near Edge Spectroscopy (XANES) and X−ray Diffraction (XRD) were
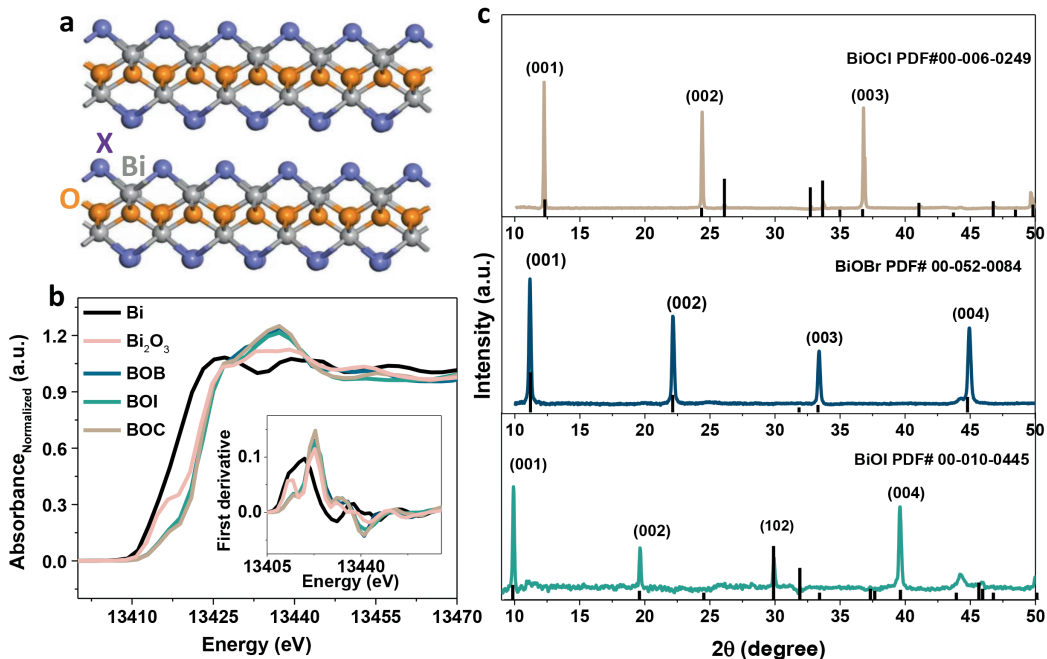
Figure 4.1. The representative schematic crystal structure of BiOX (a); X–ray Absorption Near Edge Spectroscopy (XANES) spectra of BiOCl (BOC), BiOBr (BOB), and BiOI (BOI), compared with references Bi powder and Bi_2O_3 (b); X–ray Diffraction (XRD) patterns of the studied BOC, BOB and BOI electrocatalysts (c).

employed. In **Figure 4.1b**, the XANES spectra of the studied BOB, BOI and BOC are compared with reference metallic Bi powder and Bi_2O_3. BOB, BOI and BOC show a similar shape of XANES spectra to Bi_2O_3, suggesting a shared electronic structure. It is clear that the Bi L_3–edge position of the studied materials differs from metallic Bi, but closely resembles Bi_2O_3. This is further confirmed by the first derivative of the XANES spectra (**the insert in Figure 4.1b**), showing that the studied BOB, BOI and BOC have a similar oxidation state as Bi_2O_3, *i.e.,* Bi^{3+}. As shown in **Figure 4.1c**, a typical layered BiOCl structure is observed with (001), (002), and (003) planes dominating the XRD pattern. The XRD patterns for BiOBr (BOB) and BiOI (BOI) show similar layered structures, with the reflections slightly shifted to smaller diffraction angles due to the size of the halogen (BOC < BOB < BOI). Similar to BOC, a series of {001} facets dominate the XRD patterns, with negligible reflections of other facets.

To gain more insights into the structure of the prepared Bi–based catalysts, morphological structure and elemental distribution were investigated through Scanning Electron Microscopy (SEM), High–Angle Annular Dark Field Scanning Transmission Electron Microscopy (HAADF–STEM) and coupled STEM Energy Dispersive X–ray Spectroscopy (STEM–EDS) measurements.
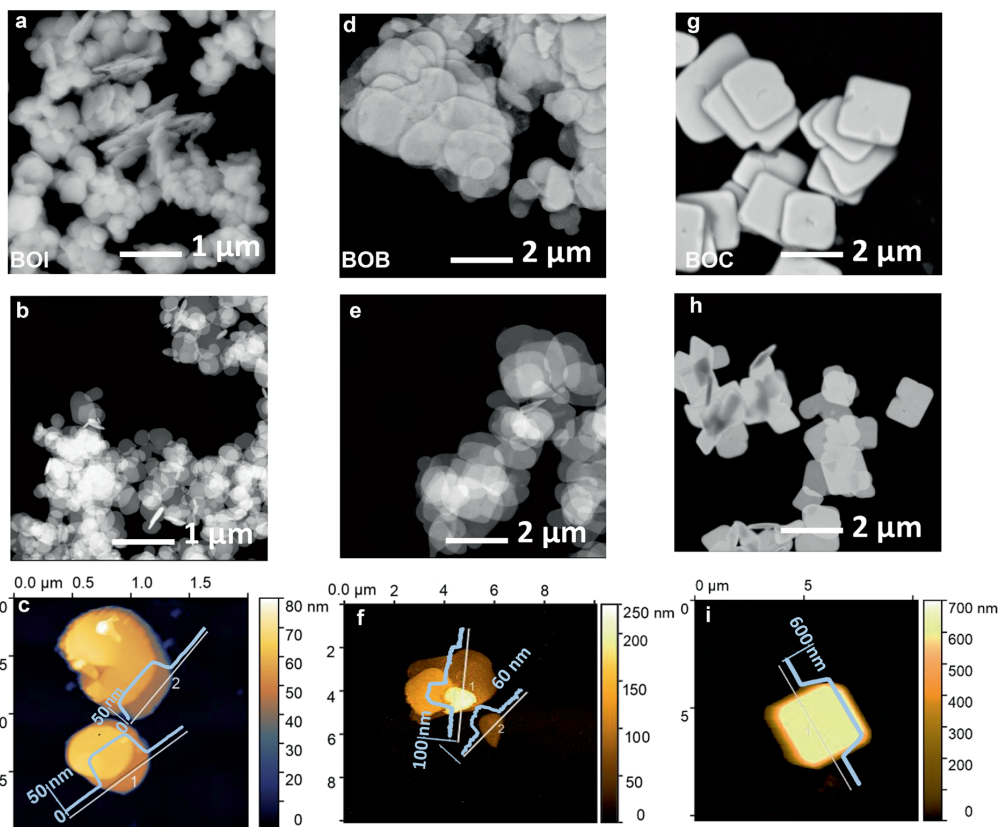
Figure 4.2. Scanning Electron Microscopy (SEM), High−Angle Annular Dark Field Scanning Transmission Electron Microscopy (HAADF−STEM) and Atomic Force Microscopy (AFM) images of the studied BOI (a, b, c), BOB (d, e, f) and BOC (g, h, i) electrocatalysts, respectively.

4

The representative SEM images in **Figure 4.2** show that all BiOX materials have a layered morphology, which is consistent with the XRD results. BOI has an irregular film structure that ranges in lateral size from 100 nm to 300 μm (**Figure 4.2a**). This is similar to the morphology of BOB (**Figure 4.2d**), which also exhibits an irregular film structure with smaller lateral dimensions, ranging from 100 nm to 3 μm. In BOC (**Figure 4.2g**), uniform squares are observed with edge length around 1 μm. We hypothesize that BOC grows more isotropically due to the stronger Bi−Cl bonds, compared to the Bi−Br and Bi−I bonds, similar to the growth mechanism for other 2D compositions.[47,48] The lower bond energy makes it energetically favorable for BOB and BOI to grow anisotropically based on the layered crystal structure, whereas in BOC additional Bi−Cl bonds are created by growing thicker 2D structures. The representative HAADF−STEM image of BOI, BOB and BOC are shown in **Figures 4.2b, e, h**, respectively, confirming their layered crystal structures. The morphology and thickness
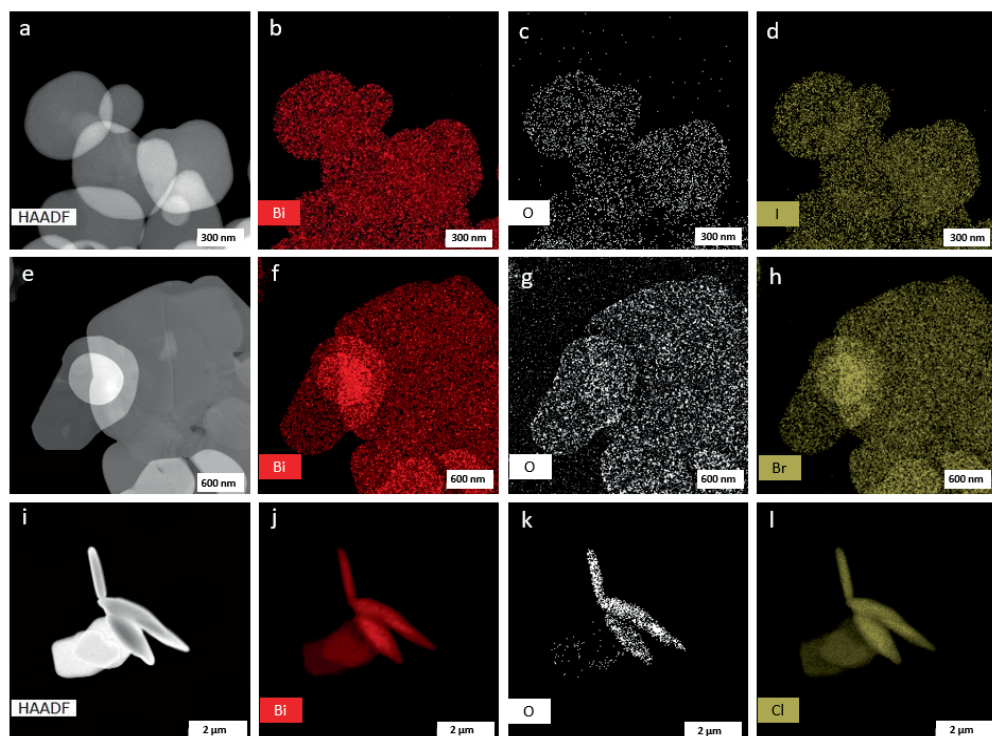
Figure 4.3. High−Angle Annular Dark Field Scanning Transmission Electron Microscopy (HAADF−STEM) overview image from BOI (a) and the corresponding Energy Dispersive Spectroscopy (EDS) elemental maps of Bi (b), O (c) and I (d); HAADF−STEM overview image from BOB (e) and the corresponding EDS elemental maps of Bi (f), O (g) and Br (h); HAADF−STEM overview image from BOC (i) and the corresponding EDS elemental maps of Bi (j), O (k) and Br (l).

of the studied materials was further studied by Atomic Force Microscopy (AFM). In BOI (**Figure 4.2c**), overlapping irregular layers are observed with thicknesses ranging from 40 nm to 50 nm, confirming the layered structure. BOB has a similar irregular layered structure, but its thickness is estimated to be around $60 - 90$ nm (**Figure 4.2f**), based on AFM. BOC, on the other hand, is much thicker than both BOB and BOI, with a regular square shape and an approximate thickness of 600 nm (**Figure 4.2i**). **Figures 4.3a−d** shows the overlapped Energy Dispersive Spectroscopy (EDS) elemental distribution for BOI, confirming the homogeneous distribution of Bi, O, and I. Similar to BOI, uniform element distribution of Bi, O and Br or Cl are seen in BOB (**Figures 4.3e−h**) and BOC (**Figures 4.3i−l**), respectively. From High−resolution HAADF−STEM images and the corresponding FT patterns of BOB (**Figure A6**), two types of lattice fringes can be found in the plane and edge area of BOB, which is identified as typical BiOBr and $Bi_2O_2CO_3$, respectively. The presence of $Bi_2O_2CO_3$ at the surface is attributed to inevitable air exposure during sample transport.

4.3.2 Electrocatalytic Performance

The electrocatalytic performance of the BiOX electrocatalysts in eCO$_2$RR is first explored using an H−type cell with a typical three−electrode configuration in 0.1 M KHCO$_3$ aqueous electrolyte (see 4.2 Methods for details). This concentration for the electrolyte was chosen in this work because it allows for direct comparison between different studies into the structure−performance relationships for electrocatalysts, and the potentials reported were automatically iR−corrected to account for the solution resistance.[49,50] Linear Sweep Voltammetry (LSV) measurements were estimate the activity of the studied catalysts. In **Figure 4.4a**, the current densities for these three catalysts in the CO$_2$−saturated electrolyte are plotted as function of applied potentials, and it is observed that all current densities are larger than the corresponding current density in the N$_2$ atmosphere, indicating their intrinsic activity for eCO$_2$RR. Besides, BOB has a larger current density difference in CO$_2$ and N$_2$ than BOI and BOC, while the difference between BOI and BOC is minor, indicating that the activity of BOB in eCO$_2$RR is better than that of BOI and BOC, and the production of H$_2$ increased over time.

To analyze the selectivity of different eCO$_2$RR products under various potentials, we applied stepped−potential electrolysis across a potential range from −0.85 V to –1.25 V vs. RHE and detected the gaseous products with online Gas Chromatography (GC) and liquid products with offline Nuclear Magnetic Resonance (NMR) after 1 h of eCO$_2$RR. From **Figure 4.5a**, it can be seen that the HCOOH Faradaic Efficiency (FE) of BOB is higher than 80.0% over the entire potential region and it reaches up to 96.0% from −0.95 V to −1.15 V vs. RHE in the H−type cell, with effective suppression of Hydrogen Evolution Reaction (HER) and CO production. BOI (**Figure 4.5b**) has a maximum HCOOH FE of 85.0% at −1.15 V vs. RHE, slightly lower than BOB, while BOC (**Figure 4.5c**) displayed a maximum HCOOH FE of 81.0% at −1.05 V vs. RHE.
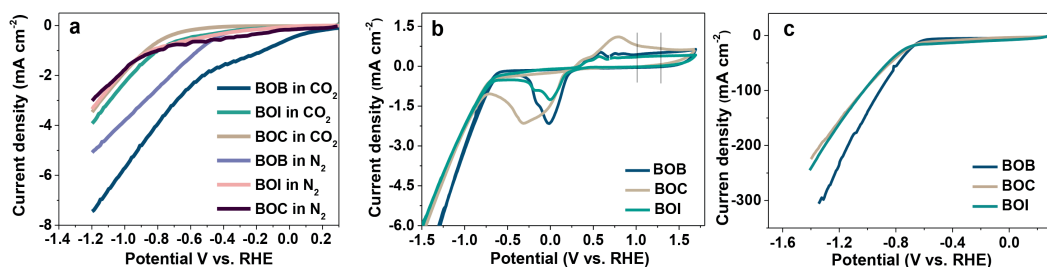
Figure 4.4. Linear Sweep Voltammetry (LSV) curves of BOB, BOI, and BOC in N$_2$ saturated 0.1 M KHCO$_3$ solution and CO$_2$−saturated 0.1 M KHCO$_3$ solution using a H−type cell at the scan rate of 50 mV s^{-1} (a). Cyclic Voltammetry (CV) curves of BOB, BOI, and BOC in CO$_2$−saturated 0.1 M KHCO$_3$ solution using a H−type cell at the scan rate of 50 mV s^{-1} (b); LSV curves of BOB, BOI, and BOC in CO$_2$−saturated 1 M KHCO$_3$ solution using a Gas Diffusion Electrode (GDE) flow cell at the scan rate of 50 mV s^{-1} (c).
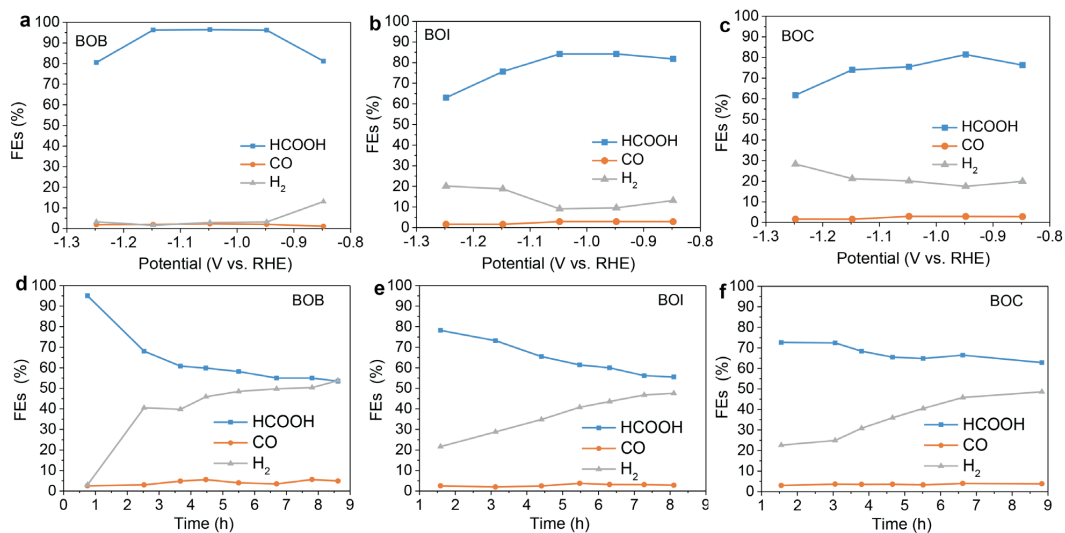
Figure 4.5. Potential−dependent Faradaic Effciencies (FEs) of BOB (a), BOI (b) and BOC (c); Stability performance of BOB (d), BOI (e) and BOC (f) at −1.15 V vs. RHE, using an H−type cell in CO_2−saturated 0.1 M $KHCO_3$ solution.

Despite the difference in selectivity of HCOOH, there is not much difference in their stability performance. As shown in **Figure 4.5**, after prolonged operation at −1.15 V vs. RHE around 8 h, the HCOOH FE of BOB decreases from 96.0% to 53.0% (**Figure 4.5d**), which is similar to BOI (**Figure 4.5e**) dropping from 80.0% to 55.0%. In contrast, BOC (**Figure 4.5f**) shows a higher FE of HCOOH after the long−term operation, only dropping from 72.0% to 62.0%. This could be attributed to the thicker layered structure of BOC, compared to BOB and BOI, which helps slow down the structure degradation.

To evaluate the electrocatalytic CO_2 conversion performance of the as−prepared BiOX under industrially relevant conditions,[51] a Gas Diffusion Electrode (GDE) flow cell was utilized with 1 M $KHCO_3$ solution as electrolyte. Within the GDE flow cell configuration (**Figure 4.6a**), continuous gaseous CO_2 feedstock can be supplied through the porous carbon support to the catalyst surface so that the gas solubility limitation in the aqueous electrolyte is circumvented. On the other side of the porous electrode, electrolyte is flowing over the catalyst surface with the help of a peristaltic pump, hereby diluting the HCOOH accumulation at the catalyst surface and buffering the electrolyte pH change, in order to minimize the mass transfer limitations. The minimization of mass transfer limitations is confirmed by the fact that the current densities using the GDE flow cell (**Figure 4.4c**) are 60 times higher than using the H−type cell (**Figure 4.4a**). It can be seen that using GDE flow cell the FE of HCOOH in BOB remains as high using H−cell over the measured potential window (**Figures 4.6b**). BOB shows a FE of HCOOH up to 91.0% at −1.05 V vs. RHE, which is higher than that of BOI (76.0%, −1.08 V vs. RHE) and BOC (69.0%, −1.09 V vs. RHE) at a similar potential.

4

The production rate of BOB also outperforms the other two compositions in the investigated potential range (**Figures 4.6c**). Current density is commonly used as the main indicator to evaluate catalyst activity. BOB has the highest total current density over the applied potential window of the studied catalysts, as shown in **Figure 4.6d**. When solely formic acid FE is considered, there is a large difference in partial current density between BOB, BOI, and BOC (**Figure 4.6e**). At an applied potential of -1.05 V vs. RHE, a HCOOH partial current density of 148 mA cm^{-2} is achieved for BOB, whereas BOI and BOC only reach 95 mA cm^{-2} and 88 mA cm^{-2} at -1.08 V vs. RHE and -1.09 V vs. RHE, respectively.
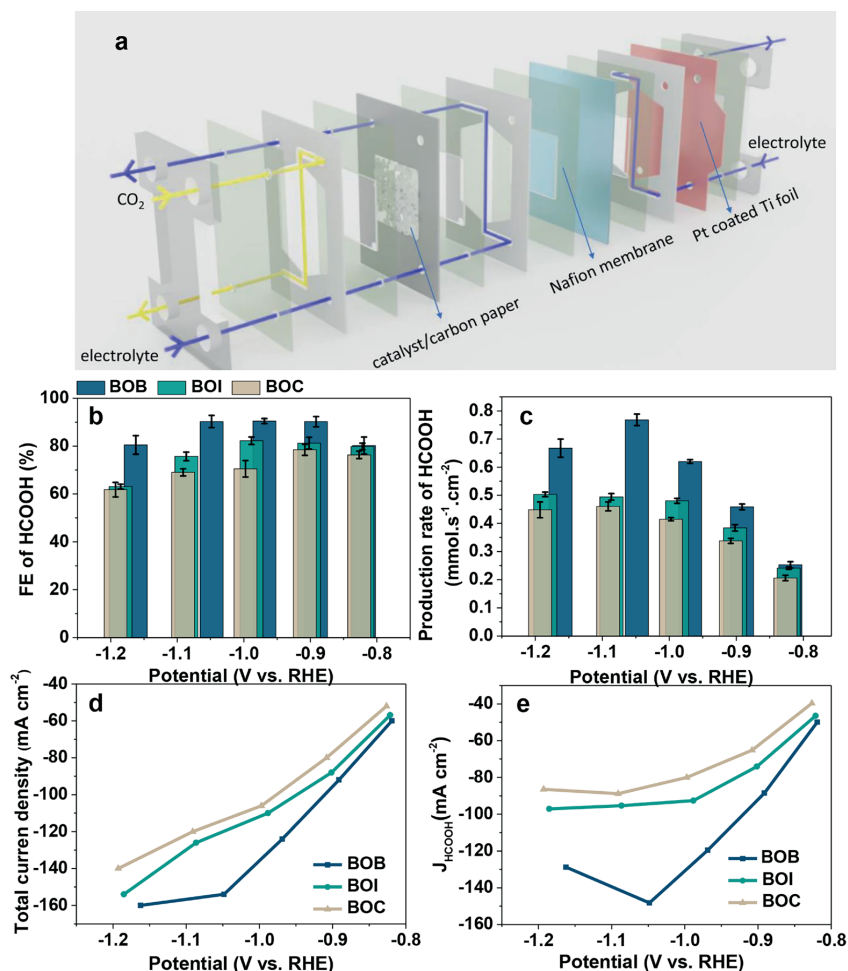
Figure 4.6. Schematic of the used Gas Diffusion Electrode (GDE) flow cell (a); Potential−dependent Faradaic Efficiency (FE) (b) and production rate (c) of formic acid for BOB, BOI, and BOC, using a GDE flow cell in CO_2−saturated 1M KHCO$_3$ solution; Total current density (d) and the corresponding HCOOH partial current density (e) of BOB, BOI, and BOC.
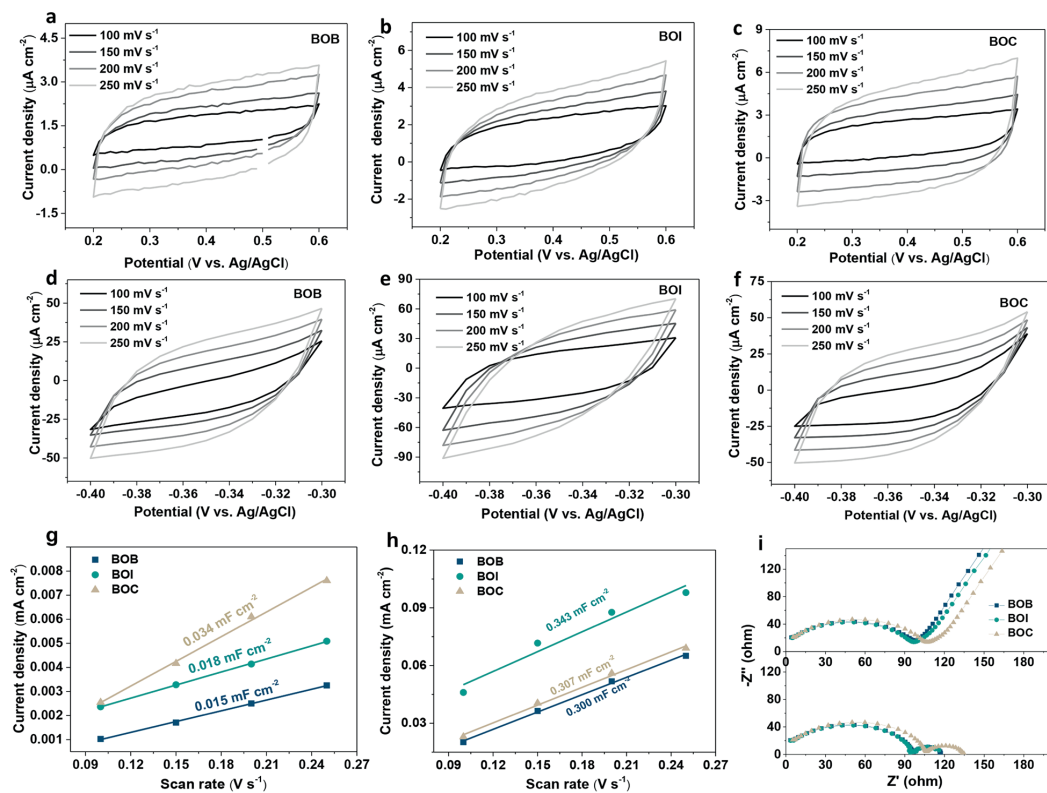
Figure 4.7. Cyclic Voltammetry (CV) curves collected at different scan rates before and after catalysis of BOB (a, d), BOI (b, e) and BOC (c, f), respectively. Charging current differences (g) at 0.40 V vs. Ag/AgCl for all catalysts before catalysis against scan rate for determining double layer capacitance (C_{dl}); Charging current differences (h) at −0.35 V vs. Ag/AgCl for all samples after catalysis against scan rate for determining double layer capacitance (C_{dl}); The Electrochemical Impedance Spectra (EIS) at open circuit potential (OCP) and −1.15 V vs. RHE, respectively (i).

Different morphological features are known to result in different catalytic behaviors, and larger specific surface areas usually expose more active sites.[52] In order to accurately define the contribution of the nature and number of active sites during electrolysis, we evaluated the electrochemical surface area (ECSA) of the as−prepared and spent catalysts by measuring the double layer capacitance in the non−Faradaic potential area in a H−type cell.[53] In **Figure 4.4b**, the Cyclic Voltammetry (CV) results indicate the non−Faradaic region, in which the CV curves with different scan rates (**Figures 4.7a−f**) were collected. Before catalysis (**Figure 4.7g**), BOC has a C_{dl} of 0.034 mF cm^{-2}, which is almost twice the double layer capacitance of BOB (0.015 mF cm^{-2}) and BOI (0.018 mF cm^{-2}), suggesting a larger ECSA than that of BOB and BOI. After catalysis all investigated catalysts
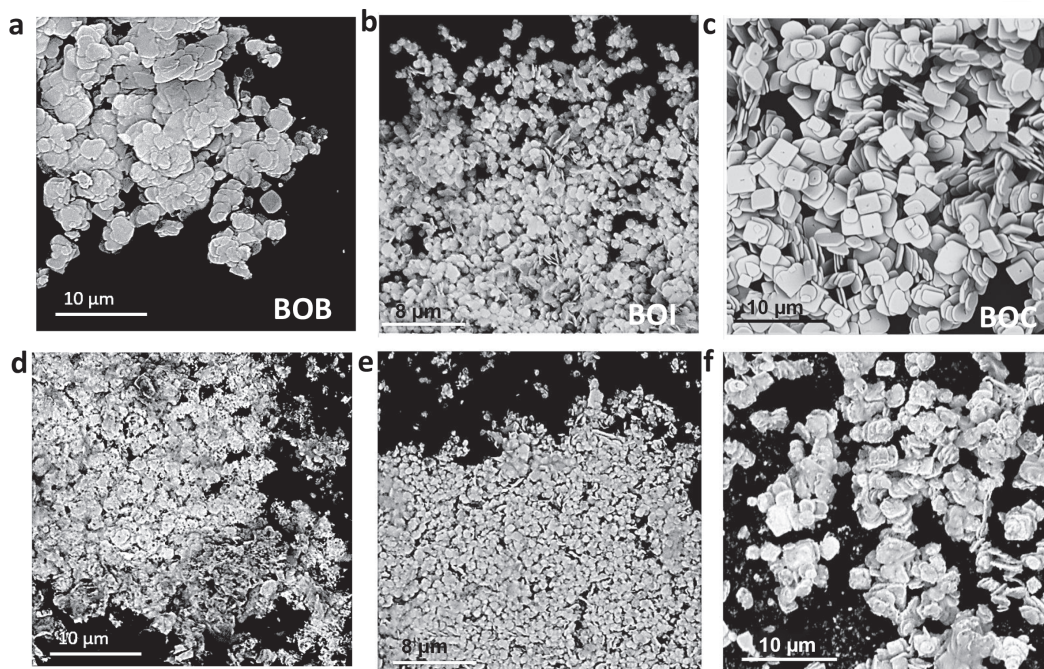
Figure 4.8. Scanning Electron Microscopy (SEM) images of BOB before (a) and after (b) catalysis at −1.15 V vs. RHE for 1 h, BOI before (c) and after (d) catalysis at −1.15 V vs. RHE for 1 h, and BOC before (e) and after (f) catalysis at −1.15 V vs. RHE for 1 h. It can be seen that all BiOX catalysts have more rough surfaces after catalysis, compared to their pristine morphology.

showed similar values (**Figure 4.7h**). Considering that BOC resulted in lower selectivity and activity than BOB and BOI, we conclude that the larger electrochemical surface area did not contribute much to catalytic performance. Besides, the catalyst structures underwent reconstruction during catalysis, resulting in similar ECSA after catalysis. This is also supported by Electrochemical Impedance Spectroscopy (EIS, **Figure 4.7i**). It can be seen that BOB, BOC, and BOI have a similar semicircle area at the open circuit potential (OCP) in the high frequency region, implying a similar charge transfer property. When a reaction potential (−1.15 V vs. RHE) was applied, they all formed a second semicircle, which is the signal of the generation of a second interface, suggesting the structure of the catalysts studied changed at such a potential. This can be confirmed by their SEM images before and after catalysis (**Figure 4.8**), that the BOB, BOI and BOC all show a rougher surface after catalysis compared to their fresh surface.

4.3.3 *In situ* Raman Spectroscopy Measurements

Based on the observations above, we have used *in situ* techniques to monitor the structural evolution of the catalyst materials under reaction conditions and to elucidate the relationship between catalyst. reconstruction and catalytic activity. *In situ* Raman Spectroscopy measurements were performed at

a rate of 10 s per spectrum. As shown in **Figure 4.9a**, BOB exhibits BiOBr characteristics at the start of the reaction (A_{1g} Bi−Br band at 110 cm^{-1}, E_g Bi−Br band at 158 cm^{-1}) and these characteristics all fade away after 80 s at a fixed applied potential of –1.15 V vs. RHE.[54] The peak at 384 cm^{-1} is attributed to the E_g and B_{1g} band produced by the motion of oxygen atoms.[51,56] The peak located at 478 cm^{-1} is related to the Bi−O vibration, which disappeared around 150 s (**Figure 4.9b**) in BOB. [57] Similarly, BiOI features (A_{1g} Bi−I band at 107 cm^{-1}, E_g Bi−I band at 150 cm^{-1}) are observed in BOI at the onset of catalysis, which disappear after 30 s of cathodic bias (**Figure 4.9c**).[58] The Bi−O
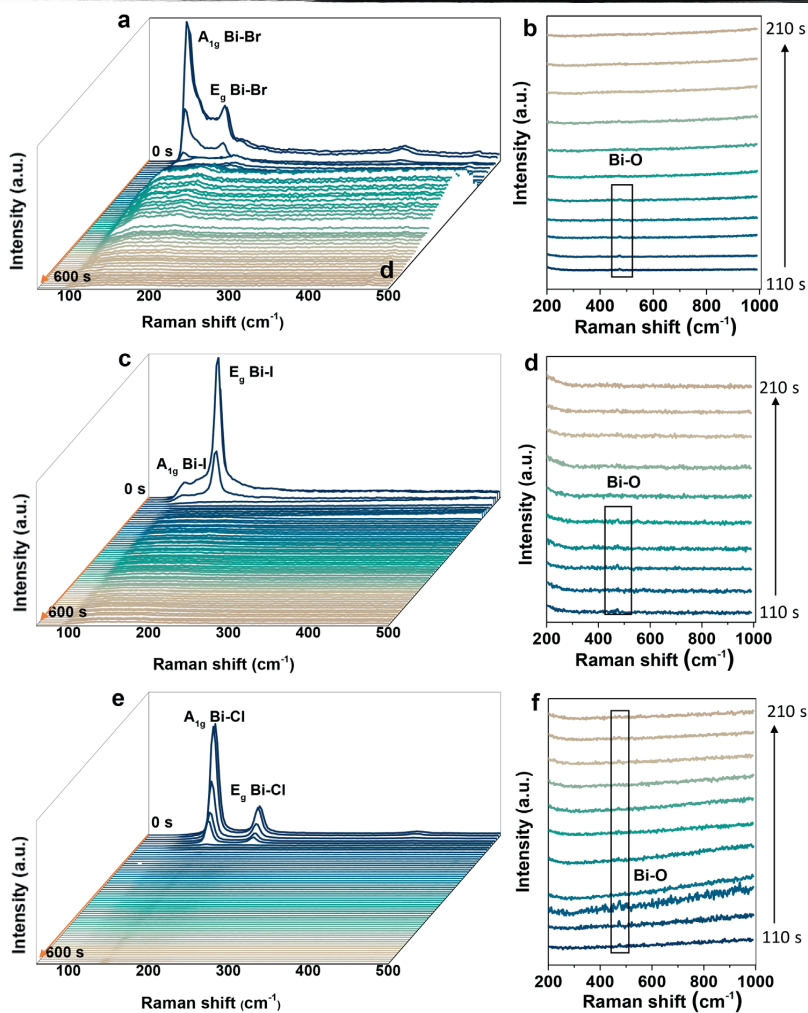
Figure 4.9. Time−dependent *in situ* Raman spectra within 600 s and the detailed Raman spectra within 210 s of BOB (a, b), BOI (c, d) and BOC (e, f) at −1.15 V vs. RHE, measured in CO_2−saturated 0.1 M KHCO$_3$ solution. The pristine structure of BOB and BOI disappear faster than that in BOC, evidenced by both their Bi−X characteristic Raman peaks and Bi−O vibration at 478 cm^{-1}.

band at 478 cm^{-1} in BOI also disappeared around 150 s (**Figure 4.9d**). In BOC, BiOCl features (A$_{1g}$ Bi−Cl band at 145 cm^{-1}, E$_g$ Bi−Cl band at 200 cm^{-1}) fade away after 80 s of catalysis, similar to BOB (**Figure 4.9e**). However, the Bi−O band persists in BOC even after 210 s (**Figure 4.9f**), indicating that the reduction of BOC is hampered compared to BOB and BOI.[59] This implies that reconstructions occur in the pristine Bi oxyhalides during catalysis, and the conversion of BOB and BOI is easier than that of BOC under the same applied cathodic potential. The relatively poor reducibility of BOC can be attributed to the larger size and thickness than the other Bi oxyhalide nanoplatelets.[60] Due to detection limitations and a low signal−to−noise ratio, it is difficult to see other formed species, such as reaction intermediates, during catalysis using *in situ* Raman Spectroscopy.

4.3.4 Time−dependent *in situ* X−ray Diffraction Measurements

Dynamic structural information is gained by performing *in situ* XRD measurements to reveal the structure evolution during catalysis. The time−dependent *in situ* XRD pattern was collected every 3 min, except the first two XRD patterns (each minute) in order to catch the small changes in the beginning of the reaction. In **Figure 4.10a** and **Figure A7a** it can be seen that BiOBr {001} facets dominate in BOB at OCP, which quickly fade away within 7 min at an applied potential of −1.15 V vs. RHE, while peaks of metallic Bi (PDF # 00−004−1246) begin to appear after 1 min already with dominant arrangements of Bi(003) and Bi(006) at 22.4° and 45.8°, respectively. Another constant peak located at 44.3° is from the cell cover. The quantified peak intensity of Bi(003) and Bi(012)
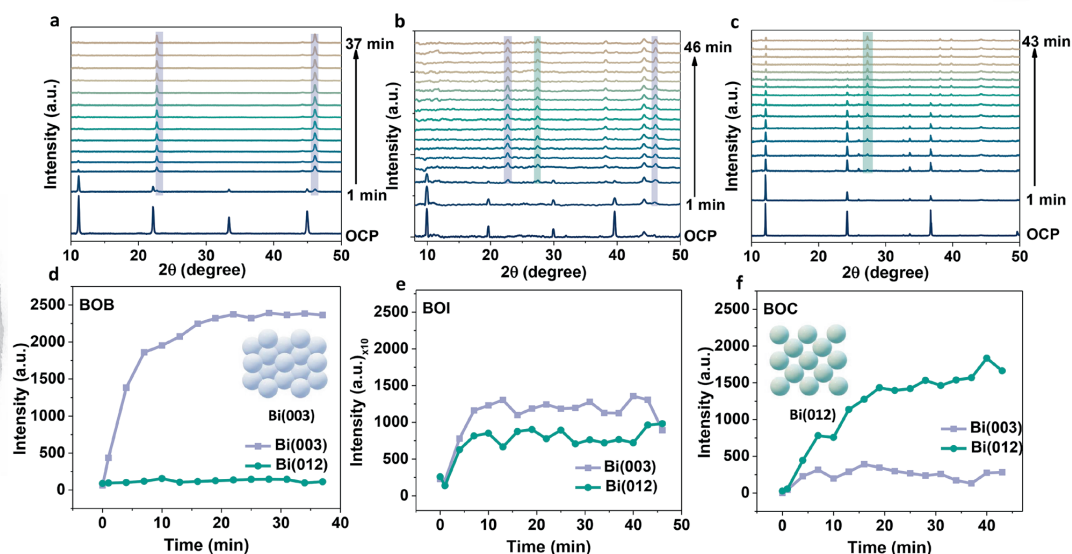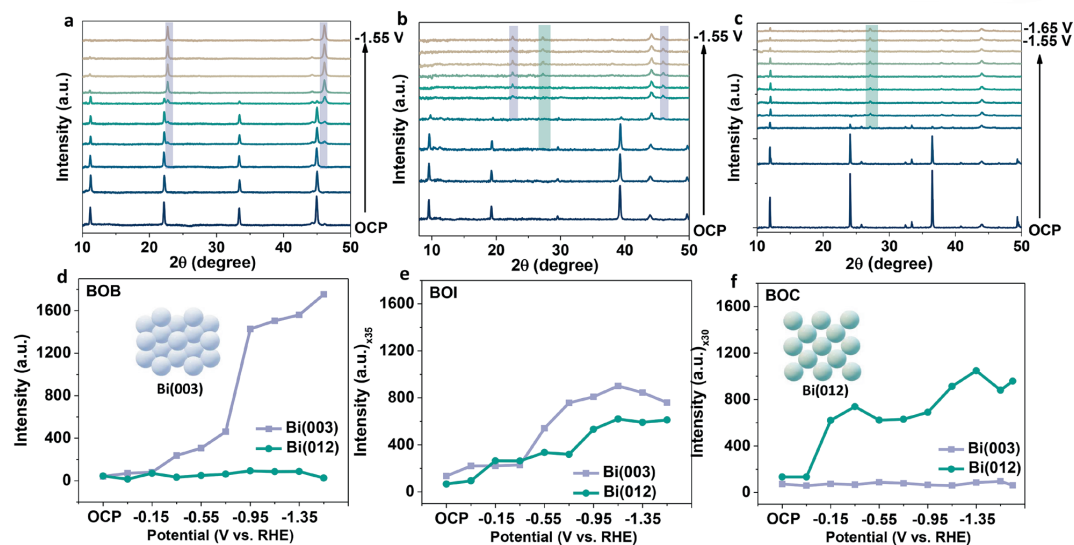

Figure 4.10. Time−dependent *in situ* X−ray Diffraction (XRD) patterns and the diffraction intensity of Bi(003) and Bi(012) facets as a function of reaction time of BOB (a, b), BOI (c, d) and BOC (e, f) in CO$_2$−saturated 0.1 M KHCO$_3$ solution, at a fixed potential of −1.15 V vs. RHE. Bi(003) and Bi(006) facets dominate in BOB during catalysis, while in BOC Bi(012) facet is found to be main structure.

is compared in **Figure 4.10b**, in which the Bi(003) slowly increases during catalysis and becomes stable at 16 min, in contrast to Bi(012) whose intensity stays close to zero during catalysis. Under the same conditions, distinct characteristic BiOI peaks can be seen in BOI (**Figure 4.10c** and **Figure A7b**) at the start of the reaction, which also disappear in the first 4 min. Simultaneously, Bi(003) and Bi(006) appear in the XRD patterns, with the same contribution from Bi(012), Bi(104) and Bi(110) facets located at 27.1°, 37.9°, and 39.6°, respectively. The diffraction intensity of Bi(003) is found to be similar to that of Bi(012) (**Figure 4.10d**). Furthermore, BOC exhibits BiOCl peaks at the start of the reaction, which gradually decline during catalysis (**Figure 4.10e** and **Figure A7c**). Contrary to BOB, the intensity of Bi(003) is negligible compared to the pronounced Bi(012) in BOC during catalysis (**Figure 4.10f**). These *in situ* time−dependent XRD measurements indicate that an applied potential of –1.15 V vs. RHE is sufficient driving force to reduce BOB and BOI, whereas for BOC higher applied potentials are required.

4.3.5 Potential−dependent *in situ* X−ray Diffraction Measurements

Since the studied catalyst materials have shown potential−dependent catalytic performance, potential−dependent *in situ* XRD was also conducted to reveal the structure evolution as a function of applied potential, in which a diffraction pattern is collected every –0.20 V vs. RHE. **Figure 4.11a** and **Figure A8a** illustrate the same trend as the result in time−dependent measurements, with BOB showing characteristic BiOBr reflections at OCP, which convert to metallic Bi at an onset

Figure 4.11. Potential−dependent *in situ* X−ray Diffraction (XRD) patterns and the diffraction intensity of Bi(003) and Bi(012) facets as a function of applied potentials of BOB (a, b), BOI (c, d) and BOC (e, f) in CO_2−saturated 0.1 M $KHCO_3$ solution. Bi(003) and Bi(006) facets dominate in BOB during catalysis, while in BOC Bi(012) facet is found to be main structure.

potential of −0.15 V vs. RHE. This is consistent with the CV result (**Figure 4.4b**), in which the two reduction peaks of Bi^{3+}/Bi locate at potentials of −0.02 V vs. RHE and −0.15 V vs. RHE. The BiOBr reflections fully disappear at an applied cathodic bias that is slightly more negative than in the CVs (<−0.15 V vs. RHE). A possible reason for this is that CV mainly measures the surface redox properties, whereas XRD detects structural changes of the bulk electrode. As the potential−dependent catalysis proceeds, Bi(003) and Bi(006) facets remain the main exposed facets for the BOB−derived electrocatalysts. In **Figure 4.11b**, the diffraction intensity of Bi(003) gradually grows as the reaction proceeds, while the intensity of Bi(012) is strongly suppressed. Likewise, BOI also shows typical BiOI reflections at OCP (**Figure 4.11c**), but with increasing negative potentials, these peaks gradually decrease in intensity (**Figure A8b**). Metallic Bi peaks already appear at a potential of −0.15 V vs. RHE, which is also in agreement with the CV result for Bi^{3+}/Bi reduction at this potential. Furthermore, this result indicates that the reducibility of BOI is higher compared to BOB, since the characteristic BOI reflections have faded out at a lower cathodic bias. A similar intensity of Bi(003) and Bi(012) facets is observed in BOI during catalysis (**Figure 4.11d**), just as in the time−dependent *in situ* XRD measurements, indicating that the activated Bi catalysts have the same conformation regardless of time− or potential−dependent electrocatalytic reflections are observed at OCP and they gradually fade away when larger cathodic potentials are activation. **Figure 4.11e** and **Figure 4.11f** show the *in situ* XRD patterns of BOC at different potentials applied. The most striking difference between BOC and BOB/BOI is that the Bi(012) facet is the most pronounced in BOC during catalysis, along with the less pronounced Bi(104) and Bi(110) facets, while Bi(003) and Bi(006) are effectively suppressed. The reflections of BiOCl remain at −1.35 V vs. RHE (**Figure A8c**), which is consistent with the observation in the CV curve (**Figure 4.4b**) that the Bi^{3+}/Bi reduction peak requires a more negative potential compared to BOB and BOI. As mentioned above, this could be due to the relatively large thickness of BOC, which normally requires more energy to be fully reduced. The observed residue of BiOCl is attributed to the uneven catalyst layer on the glassy carbon wafer, as the drop−casting method was used to prepare the electrode.
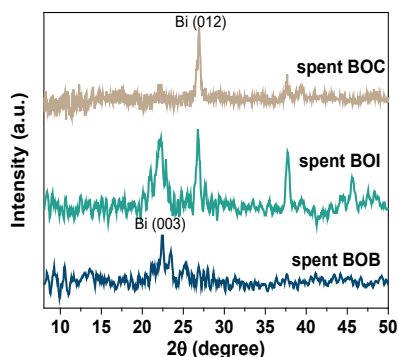
Figure 4.12. The Grazing Incidence X−ray Diffraction (GIXRD) patterns of BOB, BOI and BOC after catalysis at −1.15 V vs. RHE for 1 h, indicating that the surface structure of the studied BiOX all became metallic phase after catalysis.

Results of the *ex situ* Grazing Incidence X−ray Diffraction (GIXRD) (**Figure 4.12**) measurement, which was used to determine surface structures, confirm that all of the studied BiOX materials have been reduced to metallic Bi after catalysis. In addition, on the surface of the spent BOB, only Bi(003) can be observed, while on the surface of the spent BOC, Bi(012) dominates, and on the surface of the spent BOI, both facets can be observed. From these results, it is inferred that Bi(003) and Bi(012) facets contribute differently to electrochemical CO_2 conversion reaction, with Bi(003) resulting in superior formic acid production. Considering their catalytic performance in terms of activity and selectivity, we conclude that in the studied *in situ* activated Bi catalyst system, the *in situ* formed Bi(003) facet is more catalytically active than Bi(012). Furthermore, we conclude that bromide promotes exposure of the active Bi(003) surface sites, whereas chloride results in preferred exposure of a less active Bi(012) surface. Iodide has a less profound influence on the facet exposure, resulting in an equal contribution of Bi(003) and Bi(012) and intermediate performance for formic acid production.

4.3.6 *In situ* X−ray Absorption Spectroscopy Measurements

To further investigate the dynamic electronic structure of the studied BiOX catalysts during catalysis, *in situ* XANES was applied under time−dependent and potential−dependent conditions (time resolution = 2 min per spectrum). The measurement spot in the *in situ* XANES measurement was 1×1 μm and moved around during catalysis, in order to minimize possible beam damage effects. In **Figures 4.13a**, BOB shows a typical BiOBr XANES spectrum at OCP. When a cathodic bias of −1.15 V vs. RHE is applied, the Bi L_3−edge gradually moves to lower energy region and the shape of XANES curve starts changing, indicating restructuring and a change in oxidation potential. As a function of time, the Bi L_3−edge moves close to the edge energy of metallic Bi (13419 eV),
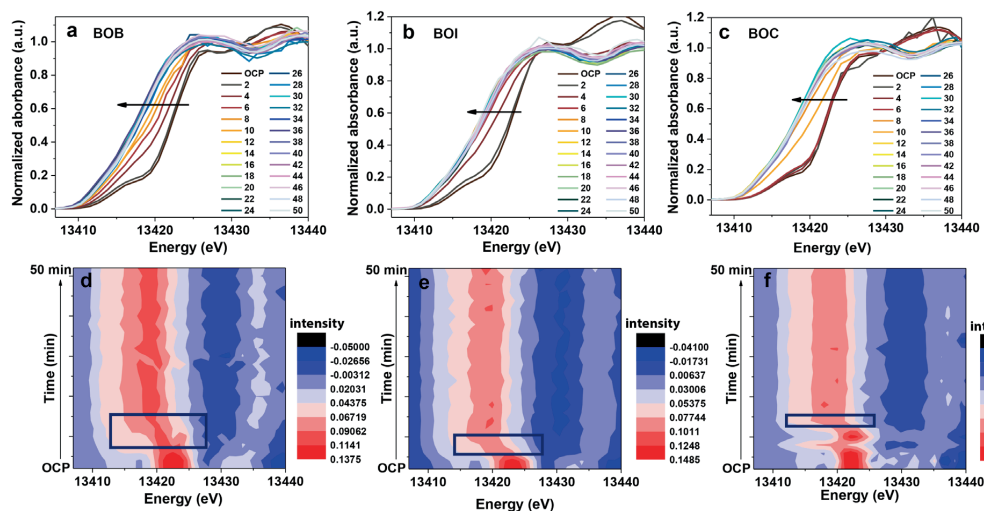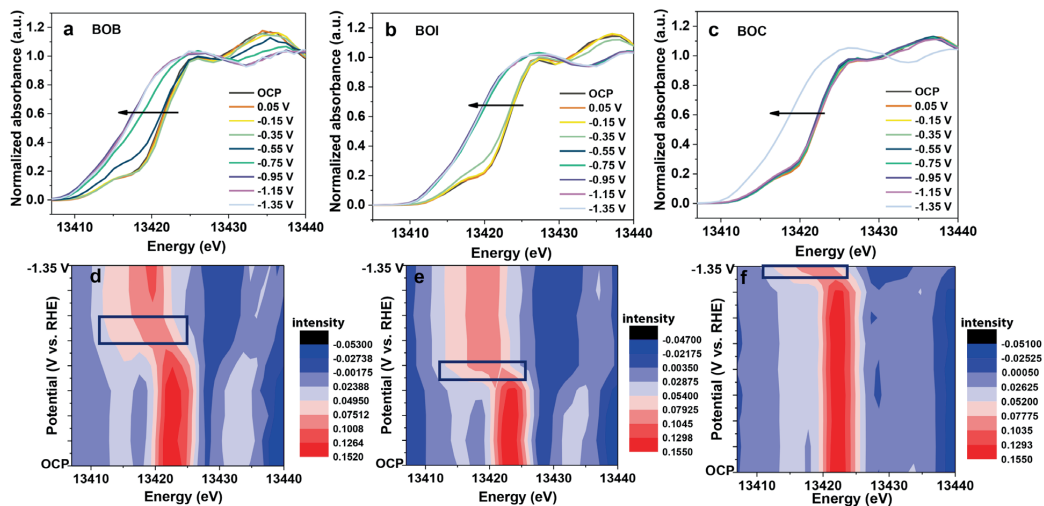

Figure 4.13. Time−dependent *in situ* X−ray Absorption Near Edge Spectroscopy (XANES) Bi L_3−edge spectra and the heat−map of the corresponding first−derivative of XANES in BOB (a, d), BOI (b, e) and BOC (c, f), measured at −1.15 V vs. RHE for 50 min (2 min per spectrum).
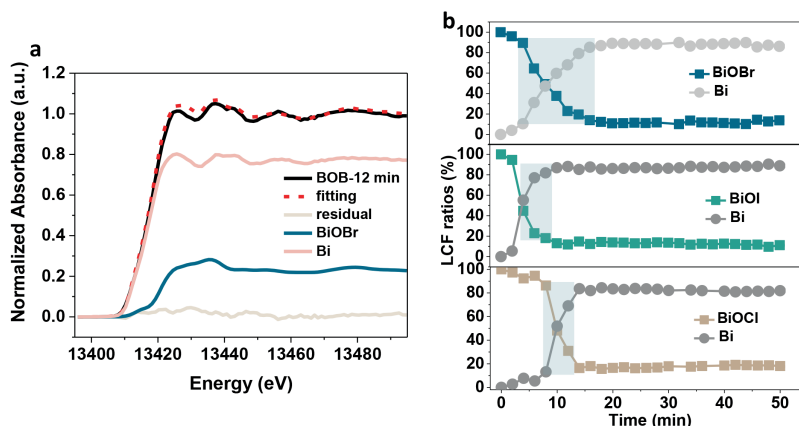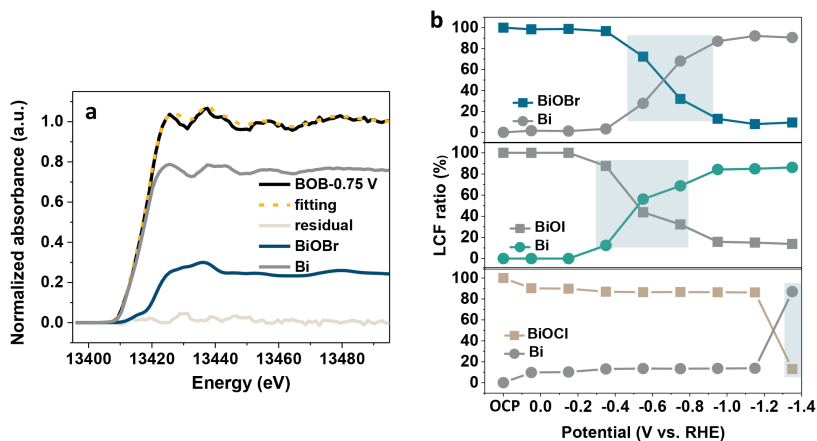
Figure 4.14. The example of Linear Combination Fitting (LCF) analysis of BOB at 12 min and the time−dependent *in situ* X−ray Absorption Near Edge Spectroscopy (XANES) spectra (b) for BOB, BOI and BOC shown in Figure 4.13. It shows that the different transition state (marked with light blue rectangle) lasts longer in BOB and BOI, compared to BOC.

suggesting that BOB is being gradually converted into the metallic Bi phase under reaction conditions. A similar trend is observed for BOI and BOC (**Figures 4.13b and c**), in which the Bi L_3−edge also gradually shifts to lower energy toward the edge position of metallic Bi. Next to the observation BiOX reconstruction toward metallic Bi during catalysis, the rate of the structure transformation varies from each other depending on the halide. The difference in rate of reconstruction can be seen more obvious in the heatmaps of the first derivative of XANES spectra. It can be seen that the structure evolution has an earlier onset in BOB (**Figure 4.13d**) and BOI (**Figure 4.13e**), compared to BOC (**Figure 4.13f**). This is in line with the *in situ* XRD and Raman Spectroscopy measurements. Through Linear Combination Fitting (LCF), the dynamic composition change during catalysis can be better quantified. **Figure 4.14a** shows the LCF example of BOB in 12 min. In **Figure 4.14b**, the LCF analysis was applied to the time−dependent *in situ* XANES spectra, with Bi powder and BiOX as reference materials. It becomes evident that the structural evolution (BiOBr < 90.0% and Bi > 10.0%) has an earlier onset in BOI and BOB than in BOC at an applied potential of −1.15 V vs. RHE, *i.e.*, 4 min, 4 min, 8 min, respectively. The difference in onset time compared to the *in situ* XRD and Raman Spectroscopy measurements could be due to the difference in their detection accuracy and signal−to−noise ratio, whereas the overall trend is unaffected by the choice of characterization technique. The transition state is defined as the intermediate state between the two stable reference states: pristine Bi oxyhalide and metallic Bi. The transition state is determined to last for 14 min in BOB, while full transformation from pristine Bi oxyhalide to metallic Bi is achieved in 6 min for BOI and BOC.

In the potential−dependent *in situ* XANES spectra (**Figure 4.15**), the same trend as in XRD can be

Figure 4.15. Potential−dependent *in situ* X−ray Absorption Near Edge Spectroscopy (XANES) Bi L$_3$−edge spectra and the heat−map of the corresponding first−derivative in BOB (a, d), BOI (b, e) and BOC (c, f) measuring from OCP to −1.35 V vs. RHE.

found: the onset potential for BOB and BOI is lower than for BOC. In **Figure 4.15a**, no obvious change in the Bi L$_3$−edge of BOB is observed upon changing the applied potential from OCP to −0.35 V vs. RHE, but the edge shifts to lower energy at −0.55 V vs. RHE and onward. Upon scanning the potential more negative, both the shape and edge position become similar to that of metallic Bi. Likewise, BOI has a structure evolution onset potential at −0.35 V vs. RHE, and quickly turns to a metallic−like structure at higher cathodic bias (**Figure 4.15b**). On the contrary, BOC seems to be more difficult to be converted into the metallic counterpart, evidenced by the delayed reconstruction onset potential at −1.35 V vs. RHE (**Figure 4.15c**). This indicates that the rate of reconstruction in BOI and BOB is faster than in BOC. The potential−dependent transition state behavior also has a similar trend as the time−dependent *in situ* XAS measurement seen in **Figure 4.13** and **Figure 4.14**. The different reconstruction rate is confirmed in the heatmaps of the first derivative of XANES spectra (**Figures 4.15d−f**). It can be seen that in all the studied BiOX catalysts Bi L$_3$−edge position shifts to lower energy as the potential goes more negative. This structure reconstruction happens earlier in BOI and BOB, compared to BOC which only shows the shift at −1.35 V vs. RHE. **Figure 4.16a** shows the LCF example of BOB at −0.75 V vs. RHE. The LCF results of the potential−dependent *in situ* XANES spectra are shown in **Figure 4.16b**. The onset potential of structure evolution in BOB is identified to be −0.55 V vs. RHE, and the transition state is found in the range of −0.55 V to −0.95 V vs. RHE. In BOI, the potential window that the transition state could be discerned ranges from −0.35 V to −0.75 V vs. RHE, while in BOC the restructuring occurs at −1.35 V vs. RHE. In addition to the different size of the pristine BiOX, the onset of structure evolution during catalysis can also be

Figure 4.16. The example of Linear Combination Fitting (LCF) analysis of BOB at −0.75 V vs. RHE and the potential−dependent *in situ* X−ray Absorption Near Edge Spectroscopy (XANES) spectra (b) for BOB, BOI and BOC shown in Figure 4.15. It shows that the different transition state (marked with light blue rectangle) lasts in a larger potential window in BOB and BOI, compared to BOC.

explained by the Hard−Soft−Acid−Base (HSAB) theory which states that soft acids form stronger bonds with soft bases, whereas hard acids form stronger bonds with hard bases.[57] The proposed mechanism is shown in **Figure 4.17**. Bi^{3+} is an intermediate Lewis acid, which tends to form a stronger bond with the intermediate Lewis base Cl^- compared to the soft bases Br^- and I^-, in line with the Raman Spectroscopy results. Therefore, more energy is needed to break Bi−Cl bonds and to further form metallic Bi. Furthermore, when the Bi–Cl bonds are finally broken and Bi monomers are formed, a sudden burst of nucleation and growth of metallic Bi occurs, evidenced by the short–lived transition state in in situ XANES results, causing the preferred formation of edge planes (Bi(012) in this case over ordered basal planes, *e.g.,* Bi(003)). The long–lived transition state indicated that BOB and BOI could be continuously reduced into metallic Bi, which is inferred to be beneficial for the formation of ordered basal plane structures with optimized catalytic performance for CO_2 conversion to formic acid.[33]

4
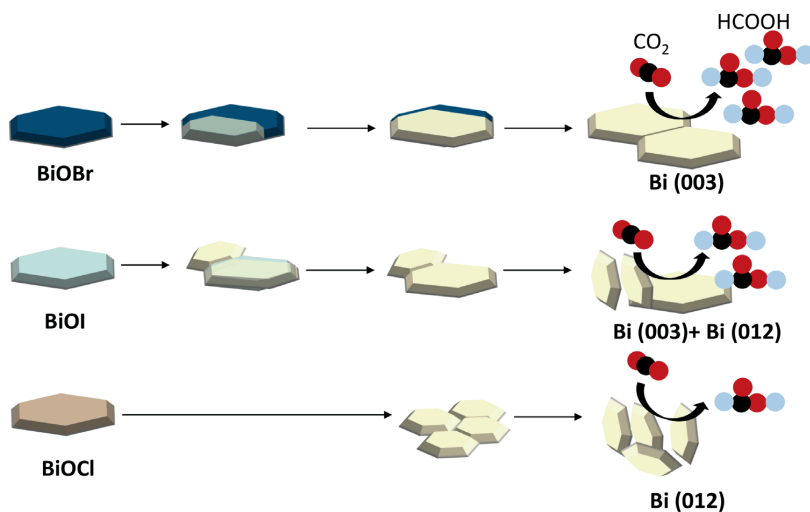
Figure 4.17. Schematic illustration of the BiOX electrocatalysts and their structure reconstruction under eCO$_2$RR conditions. Based on the HSAB theory, BOB and BOI have weak Bi−Br and Bi−I bonds, while the Bi−Cl bond in BOC is stronger. With these less strong Bi−Br or Bi−I bonds, structure reconstructions can be triggered earlier, and the transition state can last longer, resulting in more chances to form plane structure Bi(003) facets and better CO$_2$ to formic acid conversion. It takes a longer time to trigger the structure reconstruction in BOC due to the strong Bi−Cl bond. The transition state does not last long, resulting in edge structure Bi(012) facets and worse CO$_2$ to formic acid conversion.

4.4 Conclusions

Layered {001} oriented Bi oxyhalides (*i.e.,* BiOX, with X = Cl, Br, or I) electrocatalysts were synthesized and utilized as template for *in situ* formation of Bi electrocatalysts in the selective CO$_2$ reduction reaction to HCOOH. Using a Gas Diffusion Electrode flow cell, the partial current density of HCOOH in the prepared BiOBr (BOB) catalyst could reach up to 148 mA cm^{-2} with a selectivity of 91.0% at −1.05 V vs. RHE. Furthermore, HCOOH selectivities of 76.0% and 69.0% were observed for BiOI (BOI) and BiOCl (BOC) at a similar potential (−1.08 V vs. RHE for BOI and −1.09 V vs. RHE for BOC), along with current densities of 95 mA cm^{-2} and 88 mA cm^{-2}, respectively. Through *in situ* Raman Spectroscopy and X−ray Diffraction, it is found that the pristine BiOX electrocatalysts are converted into metallic Bi, but that the formation of the active sites is heavily influenced by the halide: bromide promotes Bi(003), chloride results in preferred Bi(012) exposure, and iodide has an equal contribution of Bi(003) and Bi(012). This result combined with the catalytic

performance trends suggests a structure−sensitivity, in which the Bi(003) facet is more selective and active toward formic acid formation relative to the Bi(012) surface. *In situ* X−ray Absorption Spectroscopy (XAS) measurements showed that the reconstruction of BOC proceeded rapidly, but at a higher cathodic bias, as compared to BOB and BOI. This suggests that the reconstruction rate of BiOX could determine facet exposure during catalysis in the presence of halides. This work provides insights in the active site of *in situ* activated Bi−based electrocatalyst in eCO$_2$RR through multiscale *in situ* X−ray characterization, and potentially paves the way for the rational design of other electrocatalysts for renewable production of chemicals and fuels.

4.5 Acknowledgements

4.6 References

[1]   S. Chu, A. Majumdar, *Nature* **2012**, *488*, 294–303.

[2]   M. B. Ross, P. De Luna, Y. Li, C. T. Dinh, D. Kim, P. Yang, E. H. Sargent, *Nat. Catal.* **2019**, *2*, 648–658.

[3]   S. E. Renfrew, D. E. Starr, P. Strasser, *ACS Catal.* **2020**, *10*, 13058–13074.

[4]   Y. Y. Birdja, E. Pérez−Gallent, M. C. Figueiredo, A. J. Göttle, F. Calle−Vallejo, M. T. M. Koper, *Nat. Energy* **2019**, *4*, 732–745.

[5]   D. Gao, R. M. Arán−Ais, H. S. Jeon, B. Roldan Cuenya, *Nat. Catal.* **2019**, *2*, 198–210.

[6]   A. Wagner, C. D. Sahm, E. Reisner, *Nat. Catal.* **2020**, *3*, 775–786.

[7]   J. de Ruiter, H. An, L. Wu, Z. Gijsberg, S. Yang, T. Hartman, B. M. Weckhuysen, W. van der Stam, *J. Am. Chem. Soc.* **2022**, *144*, 15047–15058.

[8]   L. Wu, K. E. Kolmeijer, Y. Zhang, H. An, S. Arnouts, S. Bals, T. Altantzis, J. P. Hofmann, M. Costa Figueiredo, E. J. M. Hensen, B. M. Weckhuysen, W. Van Der Stam, *Nanoscale* **2021**, *13*, 4835–4844.

[9]   H. An, L. Wu, L. D. B. Mandemaker, S. Yang, J. de Ruiter, J. H. J. Wijten, J. C. L. Janssens, T. Hartman, W. van der Stam, B. M. Weckhuysen, *Angew. Chem. Int. Ed.* **2021**, *60*, 16576–16584.

[10] S. Nitopi, E. Bertheussen, S. B. Scott, X. Liu, A. K. Engstfeld, S. Horch, B. Seger, I. E. L. Stephens, K. Chan, C. Hahn, J. K. Nørskov, T. F. Jaramillo, I. Chorkendorff, *Chem. Rev.* **2019**, *119*, 7610–7672.

[11] S. Jin, Z. Hao, K. Zhang, Z. Yan, J. Chen, *Angew. Chem* **2021**, *133*, 20795–20816.

[12] S. Verma, B. Kim, H. R. M. Jhong, S. Ma, P. J. A. Kenis, *ChemSusChem* **2016**, *9*, 1972–1979.

[13] O. S. Bushuyev, P. De Luna, C. T. Dinh, L. Tao, G. Saur, J. van de Lagemaat, S. O. Kelley, E. H. Sargent,

Joule **2018**, *2*, 825–832.

[14]   M. Wesselmark, C. Lagergren, G. Lindbergh, *J. Appl. Electrochem.* **2008**, *38*, 17–24.

[15]   J. H. Koh, D. H. Won, T. Eom, N. K. Kim, K. D. Jung, H. Kim, Y. J. Hwang, B. K. Min, *ACS Catal.* **2017**, *7*, 5071–5077.

[16]   E. Huttunen−Saarivirta, V. T. Kuokkala, J. Kokkonen, H. Paajanen, *Mater. Chem. Phys.* **2011**, *126*, 138–151.

[17]   S. Enthaler, J. Von Langermann, T. Schmidt, *Energy Environ. Sci.* **2010**, *3*, 1207–1217.

[18]   J. M. Spurgeon, B. Kumar, *Energy Environ. Sci.* **2018**, *11*, 1536–1551.

[19]   C. W. Lee, N. H. Cho, K. T. Nam, Y. J. Hwang, B. K. Min, *Nat. Commun.* **2019**, *10*, 3139.

[20]   Q. Li, J. Fu, W. Zhu, Z. Chen, B. Shen, L. Wu, Z. Xi, T. Wang, G. Lu, J. J. Zhu, S. Sun, *J. Am. Chem. Soc.* **2017**, *139*, 4290–4293.

[21]   S. Wang, B. Y. Guan, X. W. D. Lou, *J. Am. Chem. Soc.* **2018**, *140*, 5037–5040.

[22]   C. X. Zhao, Y. F. Bu, W. Gao, Q. Jiang, *J. Phys. Chem. C* **2017**, *121*, 19767–19773.

[23]   S. Yang, H. An, D. Anastasiadou, W. Xu, L. Wu, H. Wang, J. de Ruiter, S. Arnouts, M. C. Figueiredo, S. Bals, T. Altantzis, W. van der Stam, B. M. Weckhuysen, *ChemCatChem* **2022**, *14,* e202200754.

[24]   K. Fan, Y. Jia, Y. Ji, P. Kuang, B. Zhu, X. Liu, J. Yu, *ACS Catal.* **2020**, *10*, 358–364.

[25]   Y. Guan, M. Liu, X. Rao, Y. Liu, J. Zhang, *J. Mater. Chem. A* **2021**, *9*, 13770–13803.

[26]   D. Xia, H. Yu, H. Xie, P. Huang, R. Menzel, M. M. Titirici, G. Chai, *Nanoscale* **2022**, *14*, 7957–7973.

[27]   R. Mohan, *Nat. Chem.* **2010**, *2*, 336.

[28]   D. Yao, C. Tang, A. Vasileff, X. Zhi, Y. Jiao, S. Z. Qiao, *Angew. Chem. Int. Ed.* **2021**, *60*, 18178–18184.

[29]   Z. Yang, F. E. Oropeza, K. H. L. Zhang, *APL Mater.* **2020**, *8*, 060901.

[30]   J. E. Pander, M. F. Baruch, A. B. Bocarsly, *ACS Catal.* **2016**, *6*, 7824–7833.

[31]   R. J. Walker, A. Pougin, F. E. Oropeza, I. J. Villar−Garcia, M. P. Ryan, J. Strunk, D. J. Payne, *Chem. Mater.* **2016**, *28*, 90–96.

[32]   W. Zhang, Y. Hu, L. Ma, G. Zhu, P. Zhao, X. Xue, R. Chen, S. Yang, J. Ma, J. Liu, Z. Jin, *Nano Energy* **2018**, *53*, 808–816.

[33]   D. Wang, K. Chang, Y. Zhang, Y. Wang, Q. Liu, Z. Wang, D. Ding, Y. Cui, C. Pan, Y. Lou, Y. Zhu, Y. Zhang, *Appl. Catal. B: Environ.* **2021**, *299*, 120693.

[34]   A. Walsh, D. J. Payne, R. G. Egdell, G. W. Watson, *Chem. Soc. Rev.* **2011**, *40*, 4455–4463.

[35]   P. Su, W. Xu, Y. Qiu, T. Zhang, X. Li, H. Zhang, *ChemSusChem* **2018**, *11*, 848–853.

[36]   N. Han, Y. Wang, H. Yang, J. Deng, J. Wu, Y. Li, Y. Li, *Nat. Commun.* **2018**, *9*, 1320.

[37]   H. Yang, N. Han, J. Deng, J. Wu, Y. Wang, Y. Hu, P. Ding, Y. Li, Y. Li, J. Lu, *Adv. Energy Mater.* **2018**, *8*, 1–6.

[38]   F. P. García de Arquer, O. S. Bushuyev, P. De Luna, C. T. Dinh, A. Seifitokaldani, M. I. Saidaminov, C. S. Tan, L. N. Quan, A. Proppe, M. G. Kibria, S. O. Kelley, D. Sinton, E. H. Sargent, *Adv. Mater.* **2018**, *30*, 6–11.

[39]   L. Wang, D. Lv, Z. Yue, H. Zhu, L. Wang, D. Wang, X. Xu, W. Hao, S. X. Dou, Y. Du, *Nano Energy* **2019**, *57*, 398–404.

[40]   S. Yang, Z. Liu, H. An, S. Arnouts, J. De Ruiter, F. Rollier, S. Bals, T. Altantzis, M. C. Figueiredo, I. A. W. Filot, E. J. M. Hensen, B. M. Weckhuysen, W. Van Der Stam, *ACS Catal.* **2022**, 15146–15156.

[41]   A. D. Handoko, F. Wei, Jenndy, B. S. Yeo, Z. W. Seh, *Nat. Catal.* **2018**, *1*, 922–934.

[42]   H. Feng, Z. Xu, L. Wang, Y. Yu, D. Mitchell, D. Cui, X. Xu, J. Shi, T. Sannomiya, Y. Du, W. Hao, S. X. Dou, *ACS Appl. Mater. Interfaces* **2015**, *7*, 27592–27596.

[43]   L. Wang, K. Xu, W. Cui, D. Lv, L. Wang, L. Ren, X. Xu, F. Dong, S. X. Dou, W. Hao, Y. Du, *Adv. Funct. Mater.* **2019**, *29*, 1–8.

[44]   D. Shao, L. Zhang, S. Sun, W. Wang, *ChemSusChem* **2018**, *11*, 527–531.

[45]   P. Schlossmacher, D. O. Klenov, B. Freitag, H. S. von Harrach, *Micros. Today* **2010**, *18*, 14–20.

4

[46] Y. Zheng, T. Zhou, X. Zhao, W. K. Pang, H. Gao, S. Li, Z. Zhou, H. Liu, Z. Guo, *Adv. Mater.* **2017**, *29*, 1700396.

[47] R. G. Parr, R. G. Pearson, *J. Am. Chem. Soc.* **1983**, *105*, 7512–7516.

[48] A. Riedinger, F. D. Ott, A. Mule, S. Mazzotti, P. N. Knüsel, S. J. P. Kress, F. Prins, S. C. Erwin, D. J. Norris, *Nat. Mater.* **2017**, *16*, 743–748.

[49] G. Marcandalli, M. C. O. Monteiro, A. Goyal, M. T. M. Koper, *Acc. Chem. Res*. **2022**, *55*, 1900–1911.

[50] W. Zheng, *ACS Energy Lett.* **2023**, *8*, 1952–1958.

[51] K. Yang, R. Kas, W. A. Smith, T. Burdyny, *ACS Energy Lett.* **2021**, *6*, 33–40.

[52] K. D. Yang, W. R. Ko, J. H. Lee, S. J. Kim, H. Lee, M. H. Lee, K. T. Nam, *Angew. Chem. Int. Ed.* **2017**, *129*, 814–818.

[53] Y. Yoon, B. Yan, Y. Surendranath, *J. Am. Chem. Soc.* **2018**, *140*, 2397–2400.

[54] D. Zhang, J. Li, Q. Wang, Q. Wu, *J. Mater. Chem. A* **2013**, *1*, 8622–8629.

[55] M. Jiang, Y. Zhang, J. Chen, Q. Liang, S. Xu, C. Yao, M. Zhou, Z. Li, *Cellulose* **2020**, *27*, 8843–8858.

[56] D. Wu, S. Yue, W. Wang, T. An, G. Li, H. Y. Yip, H. Zhao, P. K. Wong, *Appl. Catal. B: Environ.* **2016**, *192*, 35–45. **1989**, *70*, 885–888.

[57] M. E. Kazyrevich, M. V. Malashchonak, A. V. Mazanik, E. A. Streltsov, A. I. Kulak, C. Bhattacharya, *Electrochim. Acta* **2016**, *190*, 612–619.

[58] S. Weng, Z. Pei, Z. Zheng, J. Hu, P. Liu, *ACS Appl. Mater. Interf.* **2013**, *5*, 12380–12386.

[59] P. Panagiotopoulou, A. Christodoulakis, D. I. Kondarides, S. Boghosian, *J. Catal.* **2006**, *240*, 114–125.

[60] R. G. Parr, R. G. Pearson, *J. Am. Chem. Soc.* **1983**, *105*, 7512–7516.
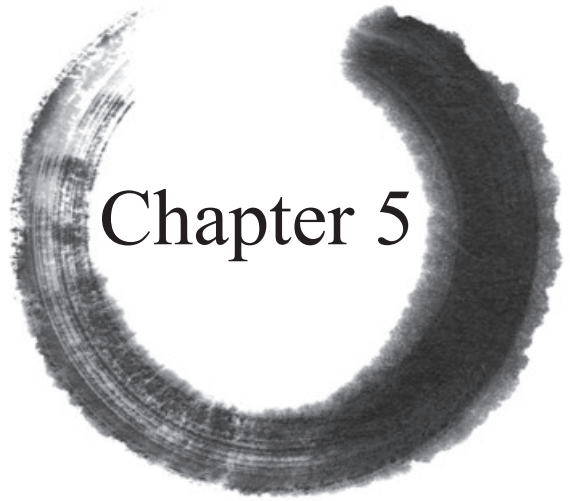
Chapter 5

Summary and Outlook

5.1 Summary

This PhD Thesis began with a general introduction of electrochemical CO_2 reduction reactions (eCO_2RR) in **Chapter 1**, discussing the motivation and challenges first and then introducing transition metal Cu and post−transition metal (Pb, Sn, Bi, In) electrocatalysts and related state−of−the−art *in situ* characterization techniques. The motivation was the ability of eCO_2RR to convert CO_2 into value−added chemicals and fuels, which can mitigate environmental problems and facilitate the sustainable development of energy. One of the challenges of the eCO_2RR application to be addressed is the low product selectivity and stability. Another challenge is the limited advanced electrocatalyst design due to unclear structure−composition−performance relationships for most electrocatalyst materials. Thus, designing new or more effective electrocatalysts and understanding the principles behind their catalytic behavior are crucial for developing eCO_2RR. Transition metal Cu has a unique ability to produce C_{2+} products, however, often with low product selectivities and high hydrogen selectivity. On the contrary, post−transition metals are highly selective for formic acid production and relatively inert for Hydrogen Evolution Reaction (HER). Therefore, in this PhD Thesis, the combination of the transition metal Cu with post−transition metals were applied to catalyze eCO_2RR to improve product selectivity and stability. Meanwhile, multiscale *in situ* characterization were utilized to systematically explored the structure−composition−performance relationship of the studied electrocatalyst materials.

In **Chapter 2**, we synthesized a series of Cu_xPb_y (X + Y = 10) electrocatalysts from industrial residue Fayalitic slags through complexing with ammonium chloride, and subsequent electrodeposition under various cathodic potentials, in which Cu to Pb ratios were tuned to be $Cu_{9.20}Pb_{0.80}$, $Cu_{9.00}Pb_{1.00}$, and $Cu_{8.65}Pb_{1.35}$. Electrochemical performance evaluation results showed that the selectivity of CO
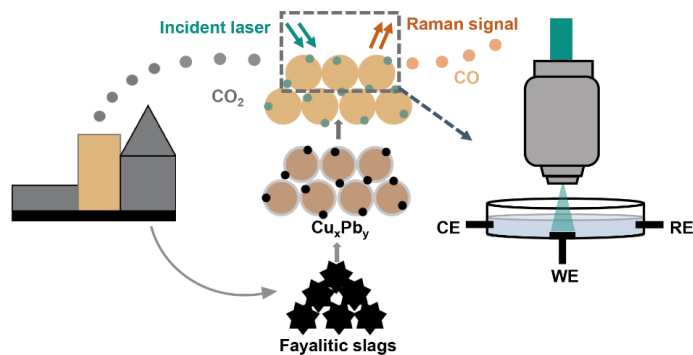
Figure 5.1. Main findings of Chapter 2. Cu_xPb_y (X + Y = 10) electrocatalysts were fabricated from industrial residue Fayalitic slags. The prepared Cu_xPb_y showed an improved CO_2 to CO selectivity in eCO_2RR. Furthermore, *in situ* Raman Spectroscopy revealed the enhancement mechanism to be a synergistic effect between Cu and Pb.

was effectively improved in the Cu_xPb_y, in contrast to pure Cu. Additionally, a volcano−shaped relationship was discovered between eCO_2RR selectivity for CO and the Cu/Pb elemental ratio. The inclusion of a small quantity of Pb in Cu electrodes ($Cu_{9.20}Pb_{0.80}$) resulted in an around two−fold increase in eCO_2RR selectivity towards CO, *i.e.,* 22.8%, respectively, compared to 9.7% for pure Cu electrodes (Cu−1). Moreover, $Cu_{9.20}Pb_{0.80}$ showed a lower H_2 production (30.1% compared to 70.9% for Cu−1). The addition of a slightly greater amount of Pb ($Cu_{9.00}Pb_{1.00}$) further increased the CO production to 41.1% Faradaic Efficiency (FE), which was four times greater than that of pure Cu under similar electrocatalytic conditions. However, $Cu_{8.65}Pb_{1.35}$ exhibited hindered production of CO and a significant increase in H_2 FE (60.6%, compared to 70.8% for Cu−1). Through *In situ* Raman Spectroscopy measurement, it was revealed that the reducibility of pristine Cu^+ and Pb^{2+} species into metallic Cu^0 and Pb^0 played a crucial role in the enhanced formation of CO. The mechanism was proposed that when an appropriate amount of Pb is present with Cu, a synergistic effect between the *in situ* reduced Cu and Pb helps increase CO selectivity. However, when the amount of Pb species is increased, the reduction processes are obstructed due to the aggregation of Pb species, resulting in a decrease of CO selectivity and a more pronounced hydrogen production.

In **Chapter 3**, a series of bimetallic Sn doped CuO electrocatalysts (CuO−0.4%Sn, CuO−0.6%Sn and CuO−0.8%Sn) were fabricated through galvanic replacement. The electrochemical performance evaluation showed that the Sn doped CuO nanoparticles could enhance the CO_2 to CO formation near unity at low cathodic potentials, compared to pure CuO. At −0.75 V vs. RHE, the CuO−0.4%Sn
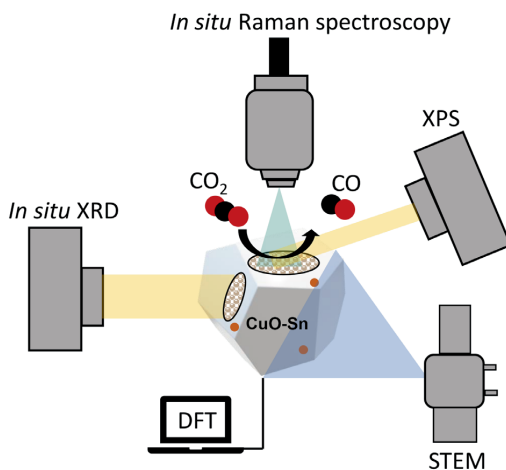
Figure 5.2. Main findings of Chapter 3. Sn−doped CuO bimetallic electrocatalysts were fabricated as electrocatalysts for eCO_2RR, showing a near unity CO selectivity. Multiscale characterization (*in situ* X−ray Diffraction (XRD), *ex situ* X−ray Photoelectron Spectroscopy (XPS), *in situ* Raman Spectroscopy, and *ex situ* Scanning Electron Transition Microscopy (STEM) measurements) revealed that the high CO selectivity could be attributed to the weakened adsorption strength of intermediate *CO, which was further confirmed by Density Functional Theory (DFT).

5

showed a FE of 98.0% of CO with suppressed H_2 production to 2.0%. This FE was found to be 5−fold and 2−fold higher than that of Cu foil (20.0%) and pure CuO (40.0%), respectively. When a higher amount of Sn was introduced into the CuO (CuO−0.6% Sn and CuO−0.8% Sn), HER was only suppressed to a maximum of 20.0%–25.0% and minor hydrocarbon product formation (<3.0%) was observed at increased cathodic potentials. *In situ* Raman Spectroscopy and *in situ* X−ray Diffraction (XRD) measurements were employed in this study to uncover the catalyst activation and adsorbed species at the catalyst surface. The results revealed that pristine CuO surface and SnO_2 were quickly reduced, leading to the presence of *CO and Cu−C vibrations in the Raman spectra. However, full reduction of bulk CuO took at least 3 minutes, as indicated by the *in situ* XRD measurements. The optimal amount of Sn−doping (0.4%) caused the absence of *CO vibrations in the Raman spectra, indicating fast desorption of gaseous CO, which corresponds to the near unity CO selectivity. Density Functional Theory (DFT) calculations confirmed that the introduction of a secondary component (Sn) strongly inhibited the HER and reduced the adsorption strength of the key intermediate *CO on the catalyst surface, leading to enhanced CO generation. Both Chapter 2 and Chapter 3 showcase the huge potential and feasibility of mitigating product selectivity in eCO_2RR by combining transition metal Cu with post−transition metals.

Similar to other post−transition metals, which are known to be active for electrochemical CO_2 to formic acid production, Bi−based electrocatalysts have attracted a lot of attention due to their low toxicity and high earth abundance.[1] Despite the high selectivity towards formic acid, the active site of Bi−based electrocatalysts remain unclear. In **Chapter 4**, a series of layered Bi oxyhalides (BiOX, X = Cl, Br, or I) with {001} orientation was synthesized through hydrothermal synthesis and applied as a template to *in situ* study the structure−performance relationship of Bi−based electrocatalysts in eCO_2RR. The prepared BiOBr (BOB) catalyst showed HCOOH FE around 91.0% with a partial current density of up to 148 mA cm^{-2} at −1.05 V vs. RHE, using a Gas Diffusion Electrode (GDE) flow cell. Similarly, BiOI (BOI) and BiOCl (BOC) showed formic acid FE of 76.0% (−1.08 V vs. RHE) and 69.0% (−1.09 V vs. RHE), respectively, with corresponding current densities of 95 mA cm^{-2} and 88 mA cm^{-2}. *In situ* Raman Spectroscopy and *in situ* XRD were employed to discover catalyst structure change during catalysis. It was found that the pristine BiOX electrocatalysts were *in situ* transformed into metallic Bi during catalysis, and the formation of active sites depended heavily on the halide used. In BiOBr, Bi(003) was observed as the main structure during catalysis, whereas Bi(012) exposure was preferred in BiOCl and an equal contribution of Bi(003) and Bi(012) was found in BiOI. These findings, combined with the observed catalytic performance trends, suggest a structure−sensitivity that the Bi(003) facet is more selective and active toward formic acid formation than the Bi(012) surface. *In situ* X−ray Absorption Spectroscopy (XAS) measurements revealed that the structure reconstruction rate in BiOCl was faster than that in BOB and BOI, evidenced by its shorter transition time and narrower potential window for the transition state. This suggests that the reconstruction rate of BiOX could be tuned by the type of halogen, which has further influence on determining facet exposure during catalysis. The results of this study provide insights into the active site of *in situ* activated Bi−based electrocatalysts in eCO_2RR through multiscale *in situ* characterization and have the potential to facilitate the rational design of other electrocatalysts
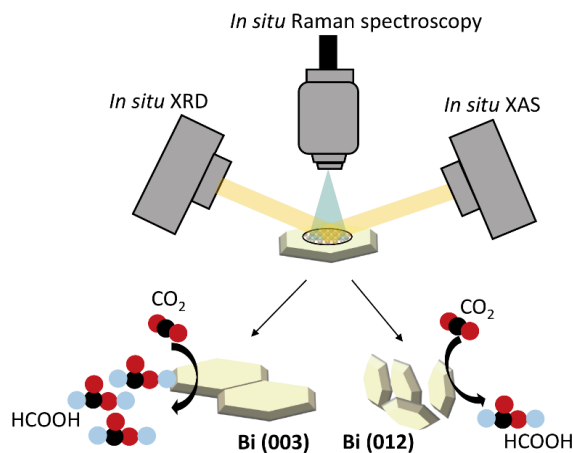
Figure 5.3. Main finding of Chapter 4. Bi oxyhalides (BiOX, X = Cl, Br, and I) were applied to electrochemically catalyze CO_2 to HCOOH conversion, with high HCOOH selectivity and activities (BiOBr > BiOI > BiOCl). Through multiscale characterization (*in situ* X−ray Diffraction (XRD), *in situ* X−ray Absorption Spectroscopy (XAS), and *in situ* Raman Spectroscopy), it was found that the *in situ* formed metallic Bi acted as the active phase during catalysis. Additionally, the *in situ* formed Bi(003) facets were more catalytically active than Bi(012) facets.

for the renewable production of chemicals and fuels.

5.2 Outlook

This PhD Thesis explored a series of electrocatalysts composed of the transition metal Cu and post−transition metals for eCO_2RR. Enhanced catalytic performances were observed on these studied electrocatalysts compared to their corresponding counterparts. In addition, the catalytic performance and catalyst structure were correlated through multiscale characterization techniques, and the related catalytic active site was identified. However, most involved synthesis methods required a super clean environment, and the catalyst yield was low, which is not practical for large−scale applications. Moreover, the catalytic activity was still not up to the industrial level. Therefore, future catalyst design must align with industrial requirements, such as low−cost materials, compatible synthesis conditions, and high conversion efficiency, particularly long−term stability.

In **Chapter 2**, a series of CuPb electrocatalysts were fabricated by electrodeposition from industrial residues with tunable Cu to Pb ratios. It was found that the synergistic effect between Cu and Pb improved CO_2 to CO conversion, with four times higher FE compared to Cu alone. However, the studied CuPb ratios were limited by the composition of the industrial waste (Fayalite slags). Using more operable raw materials, such as commercial chemicals with high purities, can extend the

5

range of Cu to Pb ratios to a larger window. Moreover, it was found that a unique Cu (0% Pb) icosahedral crystal (**Figure 5.4**) could be obtained by electrodeposition at −0.4 V vs. Ag/AgCl. This unique structure is of interest for many fundamental studies, such as crystal growth and material physics. However, achieving homogeneous Cu icosahedrons remains challenging due to the complicated chemical environment inside the electrolyte, which was the filtrate from the waste extraction. One of the most feasible strategies to synthesize uniform Cu icosahedrons is to simulate the filtrate with reproducible and controllable composition, and systematically tune the parameters of electrodeposition.
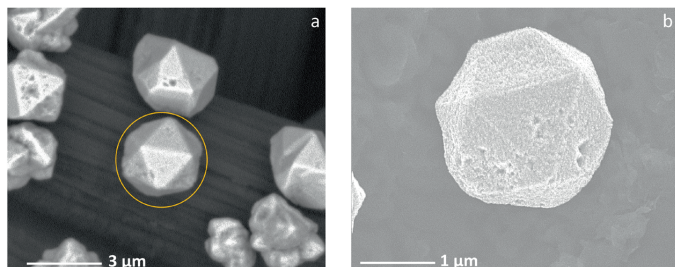
Figure 5.4. Scanning Electron Microscopy (SEM) images of the icosahedral Cu crystal synthesized by electrodeposition at −0.4 V vs. Ag/AgCl, using the filtrate from the waste extraction as electrolyte.

Chapter 3 explored using Sn−doped CuO nanoparticles as electrocatalysts for CO_2 conversion. The results demonstrated that even a small amount of Sn doping could significantly enhance CO_2 to CO conversion with near unity selectivity. The traditional Fischer−Tropsch process is a highly efficient industry standard for converting a mixture of CO and H_2 into liquid hydrocarbons.[2] Future research in this area could involve combining the produced CO with Fischer−Tropsch Synthesis (F−TS) processes to generate more valuable products that cannot be achieved through electrocatalysis alone. Fe, Co, Ni, and Ru transition metals could be promising candidates for the F−TS process. However, the problem of gas purity in the subsequent F−TS process needs to be addressed, such as the possible electrolyte vapor and the mixed CO_2 and CO stream from electrocatalysis. The latter topic has already been researched when combining electrocatalysis with the CO_2 methanation reaction, and we have already an experimental setup in the Utrecht laboratories to make this possible.[3]

In **Chapter 4**, a series of layered Bi oxyhalides (*i.e.,* BiOBr, BiOI, and BiOCl) were utilized as a platform to identify the active phase in eCO_2RR and monitor the structure reconstruction in Bi−based electrocatalysts. *In situ* measurements provided valuable information about the structure−performance relationship on the time and potential scales. However, the *in situ* structure reconstruction has not been well investigated on the spatial scale. A preliminary investigation of *in situ* space−resolved X−ray Absorption Near Edge Spectroscopy (XANES) was carried out to monitor the structural changes in different locations of the BiOBr, BiOI, and BiOCl. It has been suggested that the structure reconstruction is also spatially dependent during catalysis. However, the spatial resolution was only 1 × 1 µm due to technical limitations. Understanding the correlation between

the spatial differences in catalyst structure and catalytic behavior requires higher spatial resolution of XANES mapping measurements and combination with the results from other techniques, such as *in situ* Raman imaging and *in situ* Atomic Force Microscopy (AFM) techniques.

In addition to the combination of Cu and post−transition metals, which were the topic of this PhD Thesis, incorporating other transition metals, such as Ag, Au, and Zn, known to be active for CO_2 to CO conversion due to the weak bonding energy of *CO, has been regarded as a promising way to steer the reaction pathway towards multi−carbon products (C_{2+} products).[5,6] Since Cu and Ag are essentially immiscible, silver is often chosen as the catalyst which would contain a mixture of Ag and Cu phases instead of an alloy phase.[6,7] The creation and maximization of these atomic Ag−Cu interfaces have been suggested to be beneficial for electrochemical CO_2 reduction towards products beyond CO. [8–10] For instance, Ting *et al.* reported an increment in CO_2 conversion to ethanol via a bimetallic catalyst containing Ag particles and oxide−derived Cu nanowires. It is suggested that the
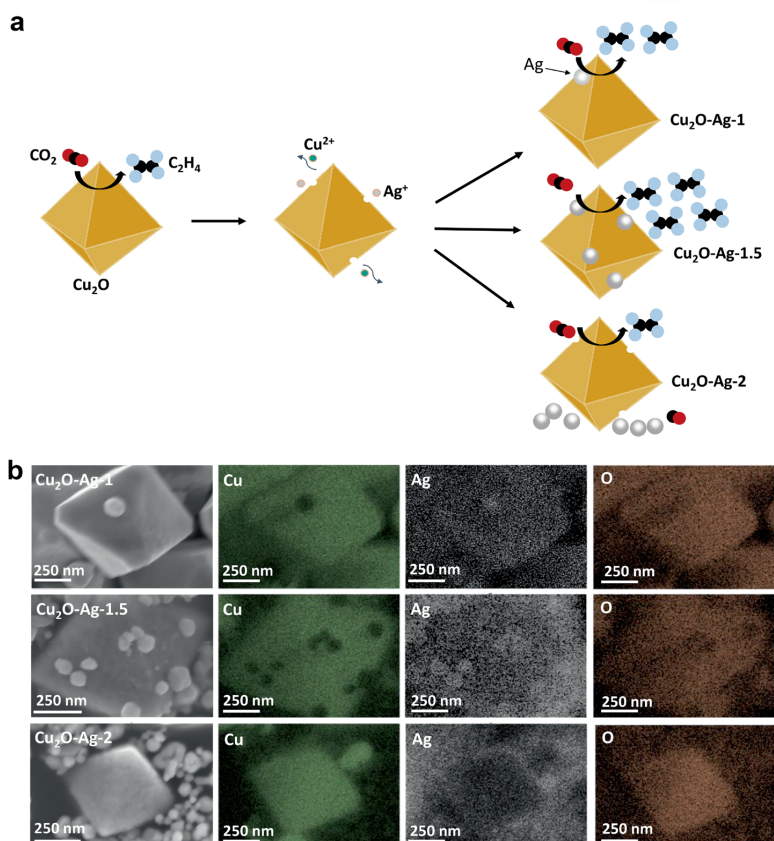
Figure 5.5. Overview of the preparation of Cu_2O−Ag−X (X = 1, 1.5, 2) bimetallic materials and their catalytic ability to produce C_2H_4 in eCO_2RR (a); Scanning Electron Microscopy (SEM) images and the corresponding Energy Dispersive X−ray Spectroscopy (EDS) elemental maps of the prepared Ag−Cu_2O−1 (a), Ag−Cu_2O−1.5 (b) and Ag−Cu_2O−2 (c), revealing the distribution of Cu, Ag, and O.

improved ethanol production benefitted from the CO evolved from Ag sites.[11] However, despite commendable efforts in demonstrating the CO−spillover phenomenon from Ag to Cu sites, directly tuning the Cu−Ag interface and tracing the critical intermediate *CO is rarely reported. In our preliminary work (**Figure 5.5a**), a bimetallic $Cu_2O−Ag$ structure has been investigated as an electrocatalyst for eCO_2RR, which has shown an enhanced C_2H_4 formation.

A series of $Cu_2O−Ag−X$ (X = 1, 1.5, 2) bimetallic structures with different amounts of Ag were prepared through galvanic replacement. The morphology and elemental distribution of the prepared $Cu_2O−Ag−X$ materials were studied by Scanning Electron Microscopy (SEM). As displayed in **Figure 5.5b**, the prepared Cu_2O shows a typical shape of octahedron. Small particles (100 nm) are firmly attached to the surface of Cu_2O octahedrons in $Ag−Cu_2O−1$. The particles become irregular and the surface of Cu_2O tunes corroded and uneven when the addition of Ag increases ($Ag−Cu_2O−1.5$), compared to the $Ag−Cu_2O−1$. When the amount of Ag becomes even more in $Ag−Cu_2O−2$, small particles have fallen off and separated from Cu_2O octahedrons. These particles are confirmed to be Ag, evidenced by the Energy Dispersive X−ray Spectroscopy (EDS) elemental mapping results.

The electrocatalytic performance of the prepared $Cu_2O−Ag−X$ was evaluated in an H−type cell with a standard three−electrode configuration. As shown in **Figures 5.6a, b**, with the increase of
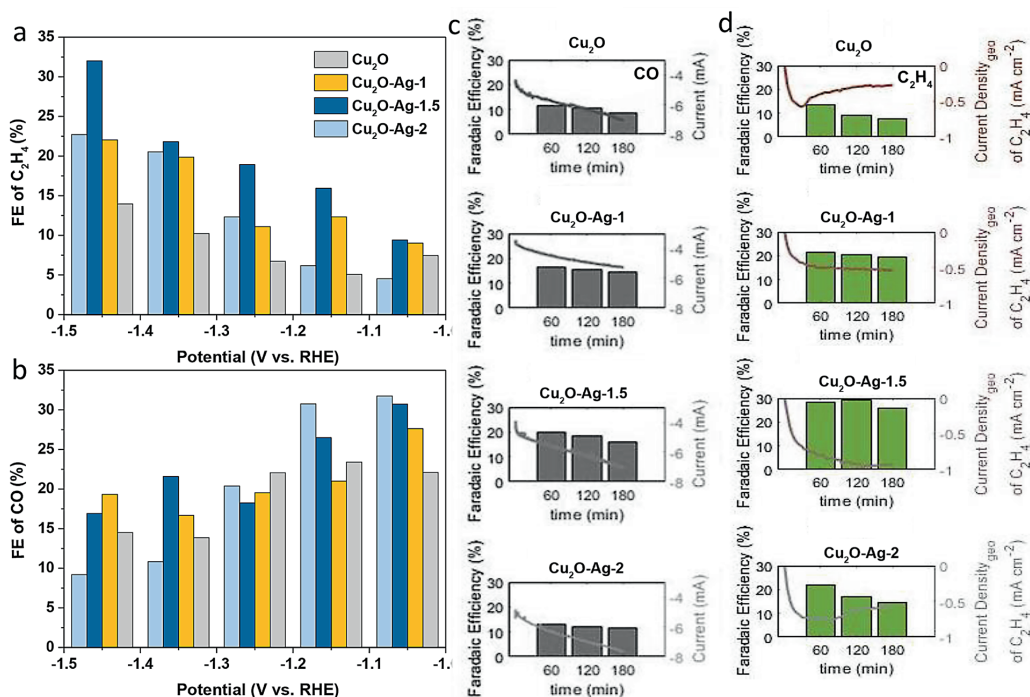
Figure 5.6. Potential−dependent Faradaic Efficiency (FE) comparison of C_2H_4 (a) and CO (b) in $Cu_2O−Ag−X$ catalysts and Cu_2O; Stability comparison of CO (c) and C_2H_4 (d) in $Cu_2O−Ag−X$ catalysts and Cu_2O at −1.25 V vs. RHE.

overpotentials, the Faradaic Efficiencies (FEs) of CO and C_2H_4 in the pure Cu_2O gradually decrease from 22.0% (at -1.05 V vs. RHE) to 14.0% (at -1.45 V vs. RHE) and increases from 7.0% (at -1.05 V vs. RHE) to 14.0% (at -1.45 V vs. RHE), respectively. A similar trend can also be found in Ag$-$Cu$_2$O$-$X catalysts. The FEs of CO and C_2H_4 are found to be 27.0% and 9.0% at -1.05 V vs. RHE in Cu$_2$O$-$Ag-1, which drops to 19.0% and grows to 22.0% at -1.45 V vs. RHE, respectively. This trend is even more evident in Cu$_2$O$-$Ag-1.5, which shows a FE of CO of 30.0% at -1.05 V vs. RHE and 17.0% at -1.45 V vs. RHE. Meanwhile, the FE of C_2H_4 increases from 9.0% at -1.05 V vs. RHE to 32.0% at -1.45 V vs. RHE. In Cu$_2$O$-$Ag-2, where the amount of Ag is maximized, CO production decreases from 31.0% at -1.05 V vs. RHE to 9.0% at -1.45 V vs. RHE. However, the increment of C_2H_4 becomes smaller than that in Cu$_2$O$-$Ag-1.5 and Cu$_2$O$-$Ag-1. It can be found that the C_2H_4 FE reaches highest in Cu$_2$O$-$Ag-1.5 among the studied catalysts over the applied potential window. Compared to Cu$_2$O$-$Ag-1.5, Cu$_2$O$-$Ag-1 and Cu$_2$O$-$Ag-2 have relatively lower FE of C_2H_4 but are still higher than pure Cu$_2$O.

The catalytic stability of CO and C_2H_4 production in Cu$_2$O$-$Ag$-$X catalysts are compared in **Figures 5.6 c** and **d**, respectively. A declining CO selectivity can be seen in all the Cu$_2$O$-$Ag$-$X catalysts and Cu$_2$O during 3 h of catalysis at -1.25 V vs. RHE. The same degradation can be found in C_2H_4 production for Cu$_2$O. However, the FE of C_2H_4 stays more stable in Cu$_2$O$-$Ag-1 and Cu$_2$O$-$Ag-1.5 for 3 h. This suggests the addition of Ag could improve not only the selectivity of C_2H_4 but also stability. In Cu$_2$O$-$Ag-2, the C_2H_4 selectivity drops by 30% within 3 h of catalysis. This is similar to the stability performance of pure Cu$_2$O, implying that the separated Cu and Ag do not enhance and stabilize the C_2H_4 production. It is worth noticing that there is a sudden rise of C_2H_4 in Cu$_2$O$-$Ag-1.5 after 1 h of reaction, which is absent in all other catalysts. SEM images of the studied catalysts at different stages (fresh, spent after 1 h of reaction, spent after 3 h of reaction) are shown in **Figure 5.7**. The octahedron shape is kept for 3 h in pure Cu$_2$O (**Figures 5.7a$-$c).** Similarly, in Cu$_2$O$-$Ag-1 (**Figures 5.7d$-$f**) and Cu$_2$O$-$Ag-2 (**Figures 5.7j$-$l**), the octahedron shape remains after 3 h of reaction, however, with Ag particles aggregated together. Interestingly, obvious dendrite structures are seen in Cu$_2$O$-$Ag-1.5 after 3 h of reaction (**Figures 5.7g$-$i**), and the morphology change is more pronounced than the other three. This is in accordance with the unique rise of C_2H_4 in the stability test, suggesting a possible correlation between the dendrite structure and the boosted C_2H_4 selectivity during long$-$term operation.

Potential$-$dependent *in situ* Raman Spectroscopy measurements were employed to reveal the C_2H_4 enhancement mechanism in the Cu$_2$O$-$Ag$-$X catalyst. In **Figure 5.8**, the $*CO_3^{2-}$ (1068 cm^{-1}) and $*CO^{2-}$ (1543 cm^{-1}) species are present in all studied catalysts.[12] The absorbed $*CO$ could be observed in the range of 2050 cm^{-1} (low$-$frequency band linear CO, LFB$-$CO) to 2100 cm^{-1} (high$-$frequency band linear CO, HFB$-$CO) when reaction potentials are given. Specifically, in pure Cu$_2$O (**Figure 5.8a**), only HFB$-$CO is found at -1.15 V vs. RHE. In Cu$_2$O$-$Ag-1 (**Figure 5.8b**), both the LFB$-$CO and HFB$-$CO can be seen at -1.25 V vs. RHE and -1.35 vs. RHE. The LFB$-$CO and HFB$-$CO appear in a wider potential window for Cu$_2$O$-$Ag-1.5 (**Figure 5.8c**), ranging from -1.15 V to -1.35 V vs. RHE. However, only the HFB$-$CO is observed for Cu$_2$O$-$Ag-2 (**Figure 5.8d**),
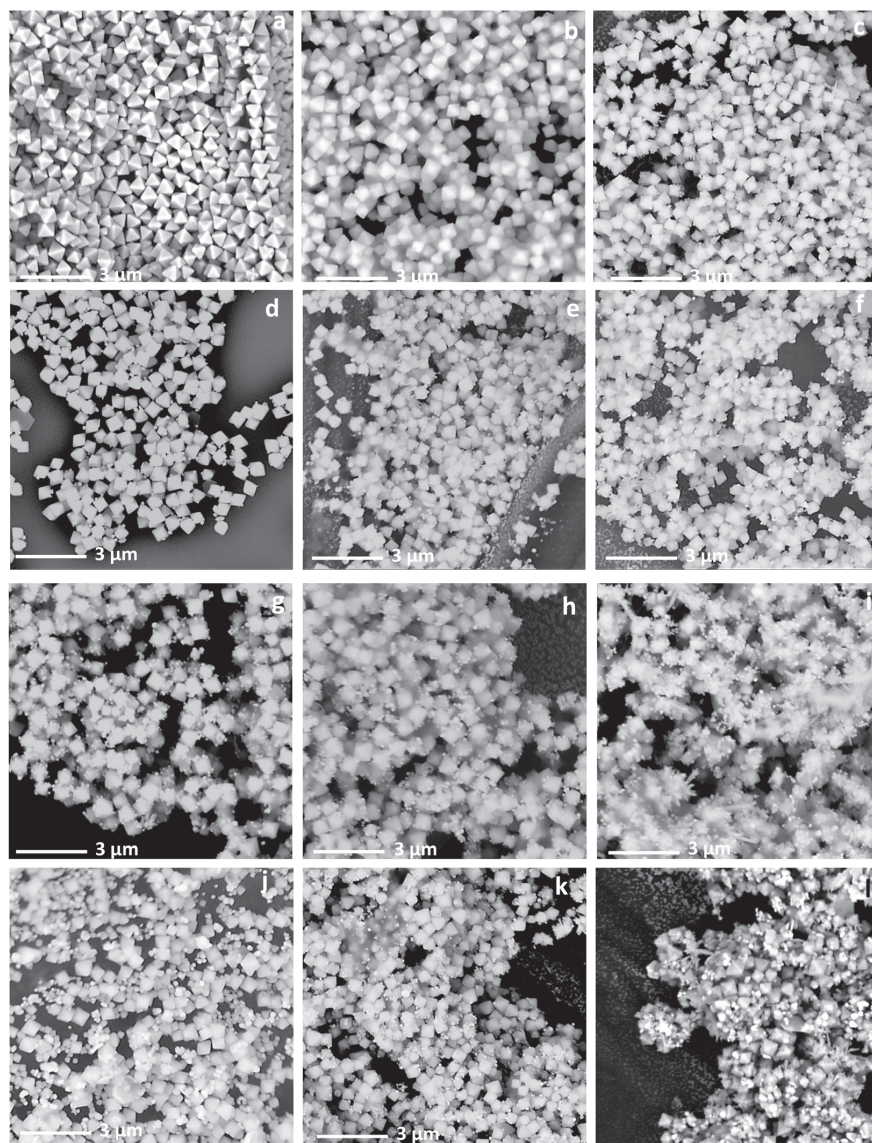
5

Figure 5.7. Scanning Electron Microscopy (SEM) images of fresh Cu_2O (a), $Cu_2O-Ag-1$ (d), $Cu_2O-Ag-1.5$ (g), and $Cu_2O-Ag-1.5$ (j); SEM images of Cu_2O (b), $Cu_2O-Ag-1$ (e), $Cu_2O-Ag-1.5$ (h), and $Cu_2O-Ag-1.5$ (k) after catalysis for 1h; SEM images of Cu_2O (b), $Cu_2O-Ag-1$ (e), $Cu_2O-Ag-1.5$ (h), and $Cu_2O-Ag-1.5$ (k) after catalysis for 3h.

similar to the pure Cu_2O. The intermediate LFB−CO has been reported to be active for C_2H_4 formation, while the HFB−CO is thought to be responsible for CO formation in eCO_2RR.[13]

The active site for the enhanced C_2H_4 selectivity is preliminarily proposed to be the Cu/Ag interface,
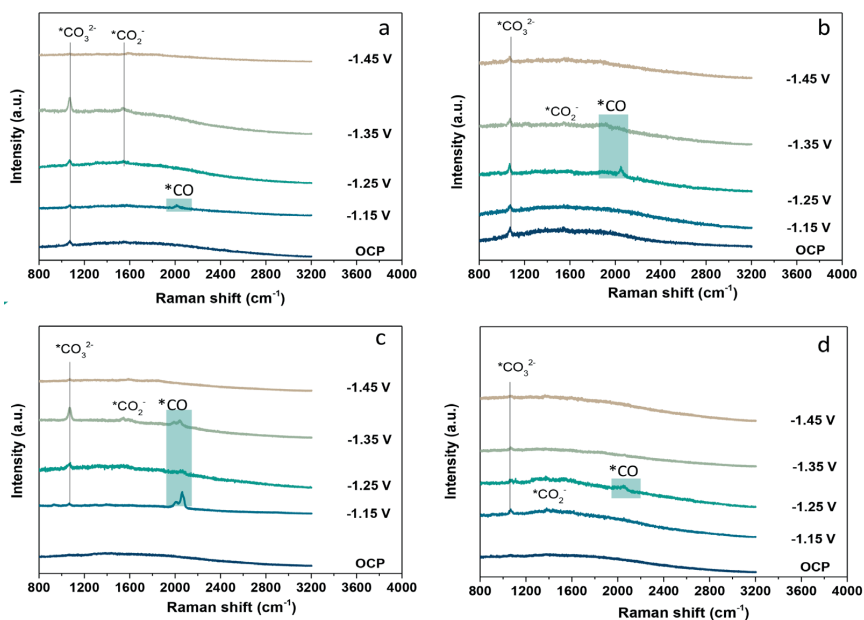
Figure 5.8. *In situ* Raman Spectroscopy measurements of the studied Cu_2O (a), $Cu_2O–Ag–1$ (b), $Cu_2O–Ag–1.5$ (c) and $Cu_2O–Ag–2$ (d) catalysts at different potentials, using 0.1 M CO_2–saturated $KHCO_3$ solution.

where the Ag sites facilitate *CO formation and the adjacent Cu sites process the *CO dimerization to C_2H_4. Therefore, the C_2H_4 formation is maximized in $Cu_2O−Ag−1.5$, where the irregular Ag particles create a large Cu/Ag interface area. While in $Cu_2O−Ag−2$, the Cu/Ag interface area is limited due to the separated Ag and Cu particles, leading to a $Cu_2O−$like catalytic performance. However, understanding the correlation between the dendrite structure and the sudden rise in FE of C_2H_4 is still unclear. Therefore, it is worth tracking the morphology change and the product distribution during catalysis through an *operando* way. *Operando* imaging techniques are recommended for this purpose, such as *operando* AFM. Additionally, more detailed Raman Spectroscopy and Fourier− Transform Infrared (FTIR) Spectroscopy measurements are needed to catch the intermediates in higher time and potential resolutions. Electron Backscatter Diffraction (EBSD), a powerful method to look at the Cu/Ag interface, can also help confirm the proposed mechanism and reveal more structure information, such as the grain boundaries of Cu and Ag.

Unlike traditional crystalline materials, amorphous materials have shown promising potential in eCO_2RR.[14,15] It has been reported that amorphizing of the materials will cause the formation of "dangling bonds" that may provide more reactive sites and, as a result, improve the product activity and selectivity for eCO_2RR.[16] Modified from Chapter 3, amorphous CuO nanosheets have been

5

prepared as electrocatalysts for CO_2 reduction. As shown in **Figures 5.9a, b**, the prepared CuO shows a morphology of porous nanosheets with no obvious characteristic lattice fringes in the high−resolution Transition Electron Microscopy (TEM) image. The amorphous feature is confirmed by the X−ray Diffraction (XRD) patterns at open circuit potential (OCP) in **Figure 5.9d**, which shows a broad reflection peak of CuO(111) peak. The electrocatalytic performance of the prepared CuO nanosheets in eCO₂RR shows a similar product distribution of CuO nanoparticles (see Chapter 3), except for a suppressed hydrogen evolution reaction (HER) and HCOOH formation (**Figure 5.9c**). Preliminary exploration of structural change was determined by *ex situ* XRD (**Figure 5.9d**). It can be seen that the pristine characteristic peak of CuO disappears when a reaction potential is applied and a Cu(111) peak dominates for all applied potentials. This suggests an immediate structural reconstruction happening at the beginning of catalysis, transiting from amorphous CuO to amorphous Cu.

Since regular XRD measurements provide limited structural information regarding amorphous structure, X−ray Pair Distribution Function (PDF) analysis can be introduced to reveal the structural
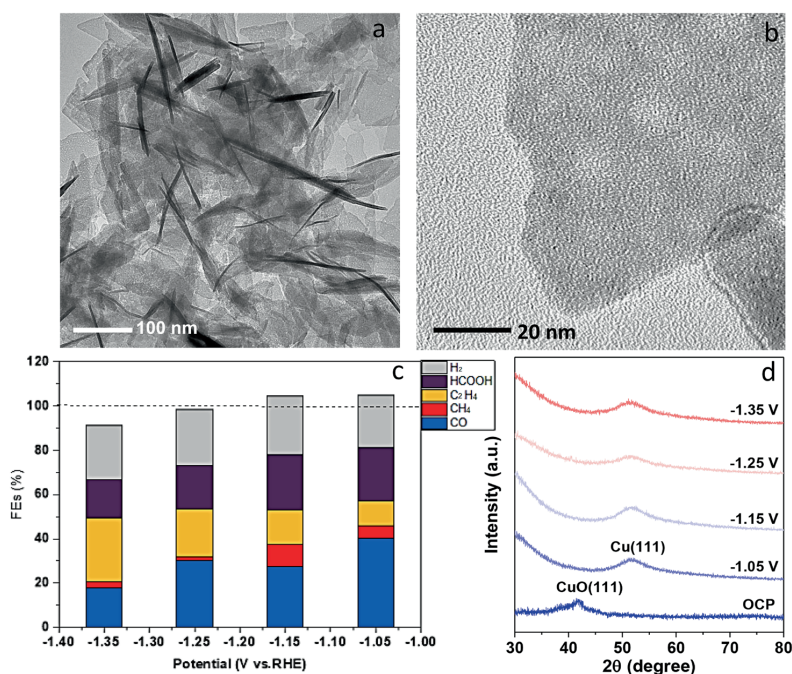
Figure 5.9. Transmission Electron Microscopy (TEM) image (a) and high−resolution TEM image (b) of the prepared CuO amorphous nanosheets. Potential−dependent Faradaic Efficiencies (FEs) distribution of different products using the CuO nanosheets as the electrocatalyst for eCO₂RR (c); *Ex situ* X−ray Diffraction (XRD) patterns of the CuO nanosheets at different potentials, ranging from open circuit potential (OCP) to −1.35 V vs. RHE, using Co Kα source.

change of the amorphous CuO. Unlike XRD and X−ray Absorption Fine Structure (XAFS), PDF analysis can offer structural information over local and long−range structures with atomic resolution. It has been widely used for investigating amorphous materials, such as battery materials, and would also be a strong tool for investigating low−crystalline Cu−based catalysts in eCO₂RR. By recovering the full range of atom−atom distances with this technique online, one can get a clear "image" of dynamic structure evolution during catalysis and greatly help in related mechanism study.

Compared to bimetallic electrocatalysts, trimetallic electrocatalysts have also shown potentials in tuning the product selectivity in eCO_2RR. Cu−Ag−Pd trimetallic nanoplates have been preliminarily studied as the electrocatalyst for eCO_2RR. As shown in **Figures 5.10a** and **c−e**, the prepared Cu−Ag−Pd nanoplate shows a triangular shape, with elements Cu, Ag and Pd homogenously distributed on the surface. The product selectivity of Cu−Ag−Pd is compared with Cu−Ag in **Figure 5.10b**. It can be seen that when having the same total FE of CO and C_2H_4, the as−prepared trimetallic Cu−Ag−Pd catalyst showed a higher proportion of C_2H_4 and a lower proportion of CO than Cu−Ag. This indicates that the addition of Pd helps to improve C_2H_4 at the cost of CO consumption. This early−stage investigation shows the considerable potential of trimetallic electrocatalysts in eCO_2RR, even with a
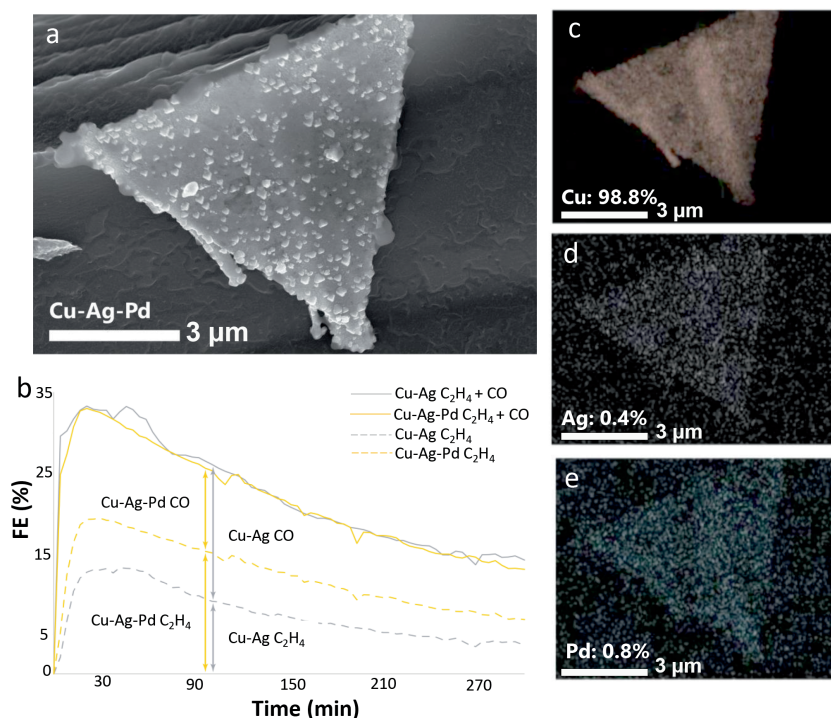
Figure 5.10. Scanning Electron Microscopy (SEM) image of the prepared Cu−Ag−Pd nanoplates (a) and the corresponding Energy Dispersive X−ray Spectroscopy (EDS) elemental mapping of Cu (c), Ag (d) and Pd (e); Faradaic Efficiency (FE) comparison of C_2H_4 and CO in Cu−Ag−Pd and Cu−Ag nanoplates (b).

doping amount of less than 1%. Future work can be extended to explore more types of multi−component electrocatalysts for eCO$_2$RR, *e.g.,* high−entropy alloys (HEAs).

HEAs represent an emerging group of multi−component alloys consisting of more than five major elements, with the atomic percentage of each element being higher than 5% and less than 35%. Unlike conventional alloys, the subject and object elements are blurred in HEAs as all atoms randomly occupy lattice sites, resulting in severe lattice distortions. The electrocatalytic reaction is a multi−step process where the distribution of active sites on the catalyst surface plays a crucial role in enhancing catalytic performance. HEAs offer a unique advantage in this regard. The interactions between adjacent atoms of different elements in HEAs create a wealth of distinct surface binding sites, enabling an almost continuous distribution of associated adsorption energies. This characteristic allows for precise tuning of binding energies to modulate reaction properties effectively. The catalytic behaviors observed in HEAs have been attributed to four main effects: high−entropy effect, lattice distortion effect, sluggish diffusion effect, and cocktail effect.[17] The high−entropy effect, associated with a high entropy configuration, contributes to lowering the Gibbs free energy and enhances material stability.[18] The lattice distortion effect that often occurs at the atomic level modulates the physical and chemical properties of materials, changing the adsorption property of reaction intermediates.[19] In HEAs, the lattice potential energy at different locations exhibits distinct variations, which leads to a high diffusion activation energy that limits the diffusion of atoms and subsequently improves the stability of materials during catalysis.[20] A cocktail effect is a special effect generated by the interaction between multi−component elements, which would eventually reflect in the overall properties of HEA materials, including their mechanical properties, corrosion resistance, and oxidation resistance.[21] Researchers focusing on electrocatalysis often attribute the remarkable electrocatalytic performance of HEAs to the effects mentioned above. For example, Nellaiappan *et al.* synthesized AuAgPtPdCu HEAs and applied them in eCO$_2$RR.[22] A FE of about 100% toward gaseous products is obtained at a low applied potential (−0.3 V vs. RHE). The enhancement was attributed to the reversal in adsorption trends for two out of the total eight intermediates *OCH$_3$ and *O on Cu(111) and HEA surfaces, as revealed by DFT calculations. The design of HEAs catalysts, including element selection, element interactions, and determination of active sites, serves as the core guiding principle for achieving effective electrocatalysis. In spite of the fact that HEAs are still in the early stages of research, they deserve further exploration and investigation.

5.3 References

[1]   Z. Zhang, M. Chi, G. M. Veith, P. Zhang, D. A. Lutterman, J. Rosenthal, S. H. Overbury, S. Dai, H. Zhu, *ACS Catal.* **2016**, *6*, 6255–6264.

[2]   M. E. Dry, *Catal. Today* **2002**, *71*, 227−241.

[3]   C. Vogt, J. Wijten, C. L. Madeira, O. Kerkenaar, K. Xu, R. Holzinger, M. Monai, B. M. Weckhuysen, *ChemCatChem* **2020**, *12*, 2792.

[4]   C. Yin, Q. Li, J. Zheng, Y. Ni, H. Wu, A.−L. Kjøniksen, C. Liu, Y. Lei, Y. Zhang, *Adv. Powder Mater.* **2022**, *1*, 100055.

[5]   A. Vasileff, C. Xu, Y. Jiao, Y. Zheng, S. Z. Qiao, *Chem* **2018**, *4*, 1809–1831.

[6]   A. Herzog, A. Bergmann, H.S. Jeon, J. Timoshenko, S. Kuhl, C. Rettenmaier, M.L. Luna, F.T. Haase, B. Roldan Cuenya, *Angew. Chem. Int. Ed.* **2021**, *60*, 7426-7435.

[7]   L. Wu, K. E. Kolmeijer, Y. Zhang, H. An, S. Arnouts, S. Bals, T. Altantzis, J. P. Hofmann, M. Costa Figueiredo, E. J. M. Hensen, B. M. Weckhuysen, W. van der Stam, *Nanoscale* **2021**, *13*, 4835−4844.

[8]   T. Cheng, H. Xiao, W. A. Goddard, *Proc. Natl. Acad. Sci.* **2017**, *114*, 1795−1800.

[9]   E. D. Goodman, J. A. Schwalbe, M. Cargnello, *ACS Catal.* **2017**, *7*, 7156−7173.

[10]   Z. Chang, S. Huo, W. Zhang, J. Fang, H. Wang, *J. Phys. Chem. C* **2017**, *121*, 11368–11379.

[11]   L. R. L. Ting, O. Piqué, S. Y. Lim, M. Tanhaei, F. Calle−Vallejo, B. S. Yeo, *ACS Catal.* **2020**, *10*, 4059−4069.

[12]   I. V. Chernyshova, P. Somasundaran, S. Ponnurangam. *Proc. Natl. Acad. Sci.* **2018**, *115*, E9261−9270.

[13]   H. An, L. Wu, L. D. B. Mandemaker, S. Yang, J. de Ruiter, J. H. J. Wijten, J. C. L. Janssens, T. Hartman, W. van der Stam, B. M. Weckhuysen, *Angew. Chem. Int. Ed.* **2021**, *60*, 16576–16584.

[14]   T. Yuan, Z. Hu, Y. Zhao, J. Fang, J. Lv, Q. Zhang, Z. Zhuang, L. Gu, S. Hu, *Nano Lett.* **2020**, *20*, 2916–2922.

[15]   P. F. Yin, J. Fu, Q. Yun, B. Chen, G. Liu, L. Li, Z. Huang, Y. Ge, H. Zhang, *Adv. Mater.* **2022**, *34*, 2201114.

[16]   Y. X. Duan, F. L. Meng, K. H. Liu, S. S. Yi, S. J. Li, J. M. Yan, Q. Jiang, *Adv. Mater.* **2018**, *30*, 1706194.

[17]   Y. Zhang, D. Wang, S. Wang, *Small*, **2022**, *18*, 2104339.

[18]   J. W. Yeh, S. Y. Chang, Y. D. Hong, S. K. Chen, S. J. Lin, *Mater. Chem. Phys.* **2007**, *103*, 41.

[19]   S. Chen, H. S. Oh, B. Gludovatz, S. J. Kim, E. S. Park, Z. Zhang, R. O. Ritchie, Q. Yu, *Nat. Commun.* **2020**, *11*, 826.

[20]   K. Y. Tsai, M. H. Tsai, J. W. Yeh, *Acta Mater.* **2013**, *61*, 4887.

[21]   Y. Zhang, T. T. Zuo, Z. Tang, M. C. Gao, K. A. Dahmen, P. K. Liaw, Z. P. Lu, *Prog. Mater. Sci.* **2014**, *61*, 1.

[22]   S. Nellaiappan, N. K. Katiyar, R. Kumar, A. Parui, K. D. Malviya, K. G. Pradeep, A. K. Singh, S. Sharma, C. S. Tiwary, and K. Biswas, *ACS Catal.* **2020,** *10*, 3658−3663.

5

Appendix A. Nederlandse Samenvatting

Dit proefschrift begon met een algemene introductie van elektrochemische CO_2 reductiereacties (eCO_2RR) in **hoofdstuk 1**, waarbij eerst de motivatie en uitdagingen werden besproken en vervolgens het overgangsmetaal koper en post−transitiemetaal elektrokatalysatoren en gerelateerde geavanceerde *in−situ* karakteriseringstechnieken werden geïntroduceerd. De motivatie was het vermogen van eCO_2RR om CO_2 om te zetten in chemicaliën en brandstoffen met toegevoegde waarde, die milieuproblemen kunnen verminderen en de energie transitie kunnen vergemakkelijken. Een van de uitdagingen van eCO_2RR, die moet worden aangepakt, is de lage productselectiviteit en stabiliteit van de katalysator. Een andere uitdaging is het beperkte begrip om een elektrokatalysator te ontwerpen vanwege onduidelijke structuur−samenstelling−prestatierelaties voor de meeste elektrokatalysatormaterialen. Het ontwerpen van nieuwe of effectievere elektrokatalysatoren en het begrijpen van de principes achter hun katalytisch gedrag zijn dus cruciaal voor het ontwikkelen van eCO_2RR. Het overgangsmetaal Cu heeft het unieke vermogen om C_{2+} producten te maken, echter vaak met lage productselectiviteit en hoge waterstofselectiviteit. Post−transitiemetalen zijn daarentegen zeer selectief voor de productie van mierenzuur en relatief inert voor de waterstofevolutiereactie (HER). Daarom werd in dit doctoraatsproefschrift de combinatie van Cu met post−transitiemetalen (Pb, Sn) toegepast om de productselectiviteit en stabiliteit van de elektrokatalytische CO_2 reductie reacties te verbeteren. Daarnaast werd *in−situ* karakterisering op meerdere lengteschalen gebruikt om de structuur−samenstelling−prestatierelaties van de bestudeerde elektrokatalysator materialen systematisch te onderzoeken.

In **Hoofdstuk 2** hebben we een reeks Cu_xPb_y (X + Y =10) elektrokatalysatoren gesynthetiseerd uit afvalresten van de metaalindustrie door middel van complexering met ammoniumchloride en daaropvolgende elektrodepositie onder verschillende kathodische potentialen, waarbij Cu−Pb elektrokatalysatoren in de verhoudingen $Cu_{9.20}Pb_{0.80}$, $Cu_{9.00}Pb_{1.00}$ en $Cu_{8.65}Pb_{1.35}$ werden gemaakt.
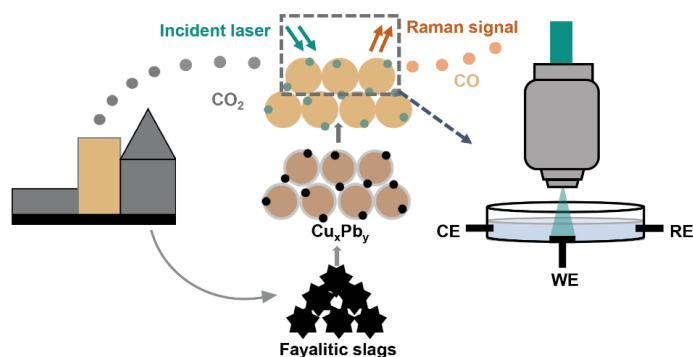
Figuur 5.1. Voornaamste bevindingen van Hoofdstuk 2. Cu_xPb_y (X + Y = 10) elektrokatalysatoren werden vervaardigd uit fayalitische industriële residuen. De bereide Cu_xPb_y vertoonde een verbeterde CO_2 naar CO selectiviteit in eCO_2RR. Bovendien onthulde *in−situ* Raman Spectroscopie dat het versterkingsmechanisme een synergetisch effect is tussen Cu en Pb.

De elektrochemische testen toonden aan dat de selectiviteit van CO effectief was verbeterd door toevoeging van Pb. Bovendien werd een maximum in de relatie tussen de eCO$_2$RR−selectiviteit voor CO en de elementaire verhouding Cu/Pb ontdekt. De opname van een kleine hoeveelheid Pb in Cu−elektroden (Cu$_{9.20}$Pb$_{0.80}$) resulteerde in een tweevoudige toename van de eCO$_2$RR−selectiviteit naar CO, *d.w.z.* respectievelijk 22.8%, vergeleken met 9.7% voor zuivere Cu−elektroden (Cu−1). Bovendien vertoonde Cu$_{9.20}$Pb$_{0.80}$ een lagere waterstof productie (30.1% vergeleken met 70.9% voor Cu−1). De toevoeging van een iets grotere hoeveelheid Pb (Cu$_{9.00}$Pb$_{1.00}$) verhoogde de CO selectiviteit verder tot 41.1% Faraday efficiëntie (FE), wat vier keer groter was dan die van zuiver Cu onder vergelijkbare elektrokatalytische omstandigheden. Cu$_{8.65}$Pb$_{1.35}$ vertoonde echter een verminderde productie van CO en een significante toename van waterstof productie (FE 60.6%, vergeleken met 70.8% voor Cu−1). Door middel van *in−situ* Raman spectroscopiemetingen werd onthuld dat de reduceerbaarheid van Cu$^+$ en Pb^{2+} ionen tot metallisch Cu^0 en Pb^0 een cruciale rol speelde bij de verbeterde vorming van CO. Het mechanisme dat werd voorgesteld houdt in dat de CO selectiviteit wordt verhoogd wanneer een geschikte hoeveelheid Pb aanwezig is met Cu. Dit zorgt voor een synergetisch effect tussen de *in−situ* gereduceerde Cu en Pb atomen. Wanneer de hoeveelheid Pb echter wordt verhoogd, worden de reductieprocessen belemmerd door de aggregatie van Pb deeltjes, wat resulteert in een afname van de CO selectiviteit en een meer uitgesproken waterstofproductie.

In **Hoofdstuk 3** werd een reeks elektrokatalysatoren gemaakt waarin verschillende hoeveelheden tin (Sn) in koper oxide (CuO) werden gebracht (CuO−0.4%Sn, CuO−0.6%Sn en CuO−0.8%Sn) door
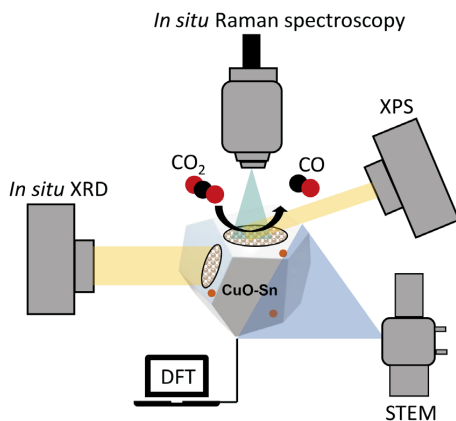
Figuur 5.2. Voornaamste bevindingen van Hoofdstuk 3. Sn−gedoteerde CuO bimetallische elektrokatalysatoren werden gefabriceerd als elektrokatalysatoren voor eCO$_2$RR, die een CO selectiviteit van bijna één tonen. Karakterisering op meerdere schalen (*in−situ* Röntgendiffractie (XRD), *ex−situ* Röntgen Foto−elektronen Spectroscopie (XPS), *in−situ* Raman spectroscopie en *ex−situ* Raster Transmissie Elektronenmicroscopie (STEM)) toonden aan dat de hoge CO selectiviteit kon worden toegeschreven aan de verzwakte adsorptiesterkte van intermediair *CO, wat verder werd bevestigd door Density Functional Theory (DFT).

middel van galvanische vervanging. De elektrochemische prestaties toonden aan dat de met Sn−gedoteerde CuO−nanodeeltjes de vorming van CO_2 tot CO naar bijna honderd procent selectiviteit konden verbeteren bij lage kathodische potentialen: bij −0.75 V vs. RHE vertoonde de CuO−0.4%Sn een FE van 98.0% CO met onderdrukte H_2 productie tot 2.0%. Deze FE bleek 5−voudig en 2−voudig hoger te zijn dan die van respectievelijk Cu−folie (20.0%) en zuiver CuO (40.0%). Toen een grotere hoeveelheid Sn in de CuO werd geïntroduceerd (CuO−0.6% Sn en CuO−0.8% Sn), werd HER slechts onderdrukt tot een maximum van 20.0% −25.0% en werd een geringe vorming van koolwaterstofproducten (< 3.0%) waargenomen bij verhoogde kathodische potentialen. In−situ Raman spectroscopie en in−situ Röntgendiffractie (XRD) metingen werden in deze studie gebruikt om de activatie van de katalysator en de geadsorbeerde moleculen aan het katalysatoroppervlak waar te nemen. De resultaten toonden aan dat het oorspronkelijke CuO−oppervlak en SnO_2 snel werden gereduceerd tot metallisch Cu en Sn, wat leidde tot de aanwezigheid van *CO en Cu−C vibraties in de Raman spectra. De volledige reductie van bulk CuO duurde echter minstens 3 minuten, zoals blijkt uit de in−situ XRD metingen. De optimale hoeveelheid Sn−dotering (0.4%) veroorzaakte de afwezigheid van *CO vibraties in de Raman spectra, wat wijst op een snelle desorptie van gasvormig CO, wat overeenkomt met de CO selectiviteit van bijna 100%. Berekeningen met behulp van Density Functional Theory (DFT) bevestigden dat de introductie van een secundaire component (Sn) de HER sterk remde en de adsorptiesterkte van het belangrijkste tussenproduct *CO op het katalysatoroppervlak verminderde. Dit leidde tot een verbeterde CO vorming, zoals experimenteel waargenomen. Zowel Hoofdstuk 2 als Hoofdstuk 3 demonstreren het enorme potentieel om de productselectiviteit in eCO_2RR te verhogen door het overgangsmetaal Cu te combineren met post−transitiemetalen.

Net als andere post−transitiemetalen, waarvan bekend is dat ze actief zijn voor elektrochemische CO_2 productie, hebben Bi−gebaseerde elektrokatalysatoren veel aandacht gekregen vanwege hun lage toxiciteit en veelvoorkomendheid op aarde.[1] Ondanks de hoge selectiviteit naar mierenzuur, blijft het actieve centrum van Bi−gebaseerde elektrokatalysatoren onduidelijk. In **Hoofdstuk 4** werd een reeks gelaagde Bi−oxyhalogeniden (BiOX, = Cl, Br of I) met {001} oriëntatie gesynthetiseerd en toegepast precursor om in−situ de structuur− prestatierelatie van Bi−gebaseerde elektrokatalysatoren in eCO_2RR te bestuderen. De BiOBr (BOB) katalysator toonde een mierenzuur FE rond 91.0% met een partiële stroomdichtheid van maximaal 148 mA cm^{-2} bij −1.15 V vs. RHE, met behulp van een Gas Diffusie Elektrode (GDE) cel. Daarnaast vertoonden BiOI (BOI) en BiOCl (BOC) een mierenzuur FE van respectievelijk 76.0 % en 69.0 % bij dezelfde potentiaal, met overeenkomstige stroomdichtheden van 95 mA cm^{-2} en 88 mA cm^{-2}. In−situ Raman spectroscopie en in−situ Röntgendiffractie werden gebruikt om veranderingen in de katalysatorstructuur tijdens katalyse te ontdekken. Er werd ontdekt dat de oorspronkelijke BiOX elektrokatalysatoren tijdens de katalyse in−situ werden omgezet in metallisch Bi, en dat de vorming van de actieve oppervlakken sterk afhing van het gebruikte halogenide. In BOB werd Bi(003) waargenomen als de voornaamste structuur tijdens de katalyse, terwijl Bi(012) als oppervlak de voorkeur had in BOC. In BOI werd een gelijke bijdrage van Bi(003) en Bi(012) waargenomen. Op basis van deze bevindingen, gecombineerd met de waargenomen katalytische prestatietrends, kan geconcludeerd worden dat

het Bi(003) oppervlak selectiever en actiever is voor de vorming van mierenzuur dan het Bi(012) oppervlak. In−situ Röntgenabsorptiespectroscopie (XAS) metingen onthulden dat de snelheid van de reconstructie in BOC sneller was dan die in BOB en BOI, wat blijkt uit de kortere tijd en het smallere potentiaalgebied voor de overgangstoestand. Dit suggereert dat de reconstructiesnelheid van BiOX kan worden beïnvloed door het type halogeen, wat een verdere invloed heeft op het bepalen van de actieve katalysator oppervlakken tijdens de reactie. De resultaten van deze studie geven inzicht in het actieve centrum van in−situ geactiveerde Bi−gebaseerde elektrokatalysatoren in eCO2RR door middel van in−situ karakterisering op meerdere lengteschalen. Daarnaast kunnen deze resultaten helpen voor het ontwerpen van nieuwe elektrokatalysatoren voor de hernieuwbare productie van chemicaliën en brandstoffen met verhoogde selectiviteit, activiteit en stabiliteit.
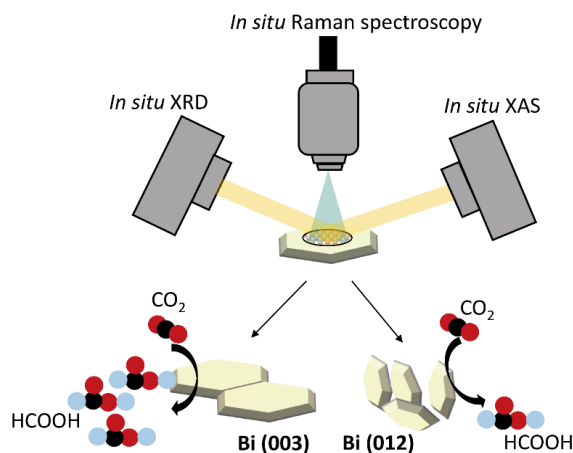
Figuur 5.3. Hoofdbevinding van Hoofdstuk 4. Bi−oxyhalogeniden (BiOX, X = Cl, Br en I) werden toegepast om de conversie van CO_2 naar HCOOH elektrochemisch te katalyseren, met hoge HCOOH selectiviteit en activiteit (BiOBr > BiOI > BiOCl). Door karakterisering op meerdere lengteschalen (*in−situ* Röntgendiffractie (XRD), *in−situ* Röntgenabsorptiespectroscopie (XAS) en *in−situ* Ramanspectroscopie), werd ontdekt dat het *in−situ* gevormde metallische Bi fungeerde als de actieve fase tijdens de katalyse. Bovendien waren de *in−situ* gevormde Bi(003) facetten katalytisch actiever dan Bi(012) facetten.

Appendix B. Supporting Information

Table A1. Cu K–edge and Pb L_3–edge Extended X–ray Absorption Fine Structure (EXAFS) simulation parameters.

Sample	Shell	CN	R (Å)	ΔE (eV)	σ2 (10^{-3} Å^2)
Cu foil	Cu–Cu	12.00	2.54	4.30	8.60
Cu–1	Cu–Cu	8.40	2.54	4.60	8.60
$Cu_{9.00}Pb_{1.00}$	Cu–Cu	5.20	2.54	5.00	8.80
	Pb–O1	2.00	2.28	0.82	3.20
	Pb–O2	1.00	3.50	0.82	3.20
	Pb–Cl	2.00	2.85	0.82	3.40
Pb–1	Pb–O	2.00	2.28	3.90	4.30

Table A2. Summary of the Cu–Sn bimetallic electrocatalysts for CO_2 conversion to CO and formate from literatures.

	Synthesis	Electrolyte	Potential V vs. RHE	FE of CO	FE of formate	References
$Cu_{6.26}Sn_5$	Hydrogen bubble templates	0.1 M $KHCO_3$	−1.08	–	97.80%	*Appl. Catal. B: Environmental* **2021**, *292, 120119*
SnO_2/CuO NCs	Co–precipitation	0.5 M $KHCO_3$	−1.00	–	89.30%	*ChemElectroChem* **2021**, *8, 1150– 1155*
Hollow Cu/Sn	Colloidal synthesis	0.1 M $KHCO_3$	−1.00	20.10%	70.10%	*Nat Commun* **2018**, *9, 4933*
Cu/p–Sn	Physical vapor deposition	0.1 M $KHCO_3$	−1.00	58.10%	24.10%	*ACS Appl. Energy Mater.* **2020**, *3, 11, 10568–10577*
CuNW– Sn15c	Atomic layer deposition	0.1 M $KHCO_3$	−0.70	79.00%	6.70%	*Adv. Energy Mater.* **2022**, *12, 2103328*
Cu_3Sn/Cu	Alloying/ dealloying	0.1 M $KHCO_3$	−0.70	91.50%	–	*Small* **2021**, *17, 2100683*
$Cu_{20}Sn_1$	one–step reduction	0.5 M $KHCO_3$	−1.00	95.30%	–	*ACS Catal.* **2021**, *11, 17, 11103–11108*
$Cu_{97}Sn_3$	one–step reduction	0.5 M $KHCO_3$	−0.70	98.00%	–	*Nat Commun* **2021**, *12, 1449*
CuO–0.4%Sn	Galvanic replacement	0.1 M $KHCO_3$	−0.75	98.00%	–	This work (Chapter 3)
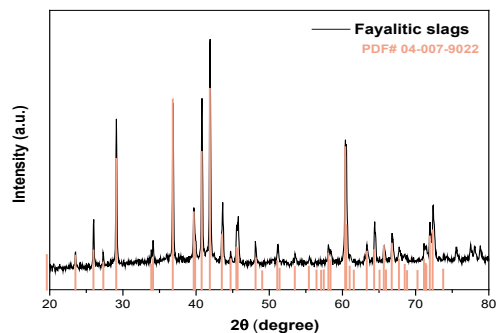
Figure A1. X–ray Diffraction (XRD) pattern of the fayalite slags under study.
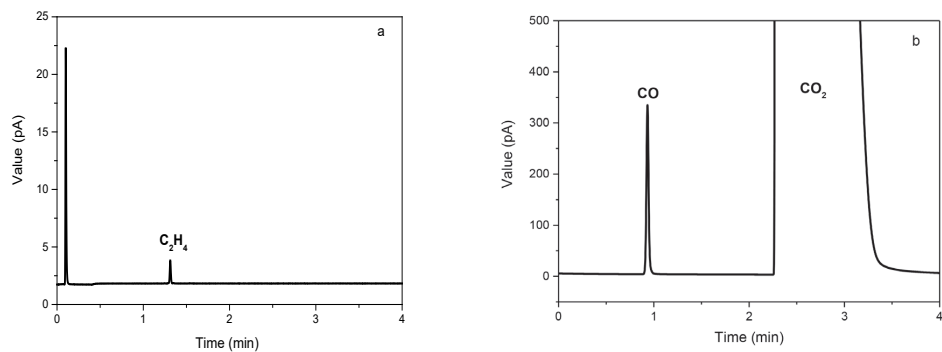
Figure A2. Representative online Gas Chromatography (GC) results of C_2H_4 (a) and CO (b) of $Cu_{9.00}Pb_{1.00}$ at −1.05 V vs. RHE.
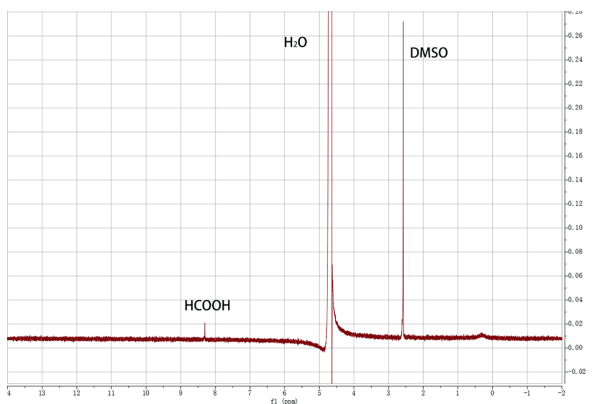
Figure A3. Representative ^1H Nuclear Magnetic Resonance (NMR) result of $Cu_{9.00}Pb_{1.00}$ after electrocatalysis at −1.05 V vs. RHE for 1 h.
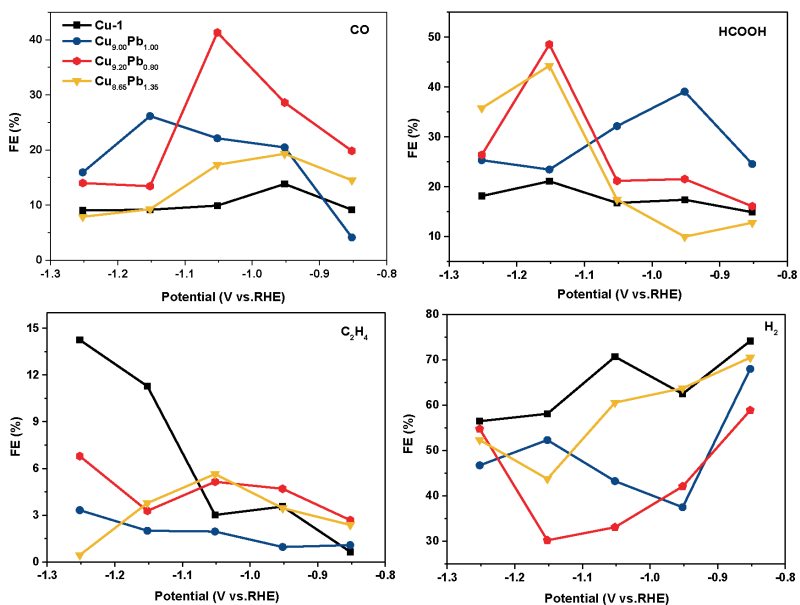
Figure A4. Comparison of potential−dependent Faradaic Efficiencies (FEs) of different samples towards certain products.
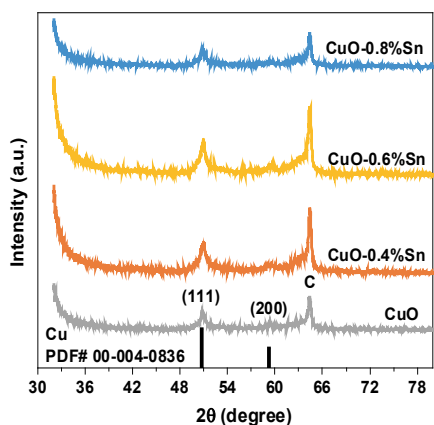
Figure A5. X−ray Diffraction (XRD) patterns after electrochemical CO₂ reduction reaction (eCO₂RR) catalysis of CuO and CuO doped by different amounts of Sn (Co Kα1 1.78896 Å).
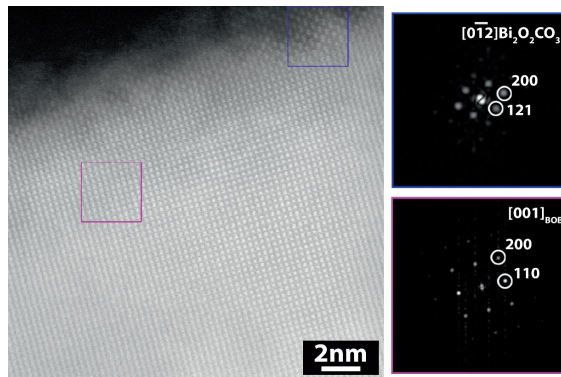
Figure A6. High–resolution High Angle Annular Dark Field Scanning Transmission Electron Microscopy (HAADF–STEM) image of a particle in the BOB sample, together with the corresponding FT patterns from the edge and non–edge areas.
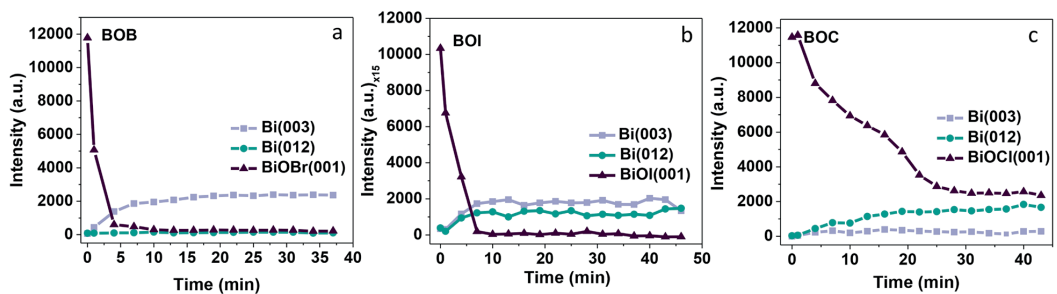
Figure A7. X–ray Diffraction (XRD) intensity of Bi(003), Bi(012) and BiOX (X = Cl, Br, I) as a function of reaction time in the time–dependent *in situ* XRD measurements of BOB (a), BOI (b) and BOC (c).
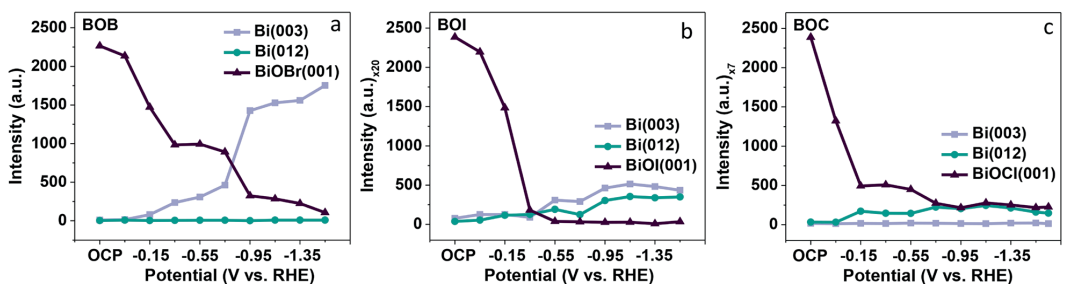
Figure A8. X–ray Diffraction (XRD) intensity of Bi(003), Bi(012) and BiOX (X = Cl, Br, I) as a function of applied potentials in the potential–dependent *in situ* XRD measurements of BOB (a), BOI (b) and BOC (c).
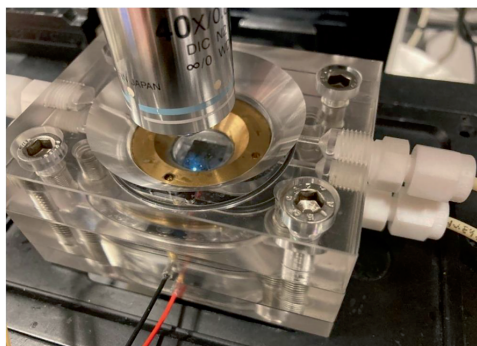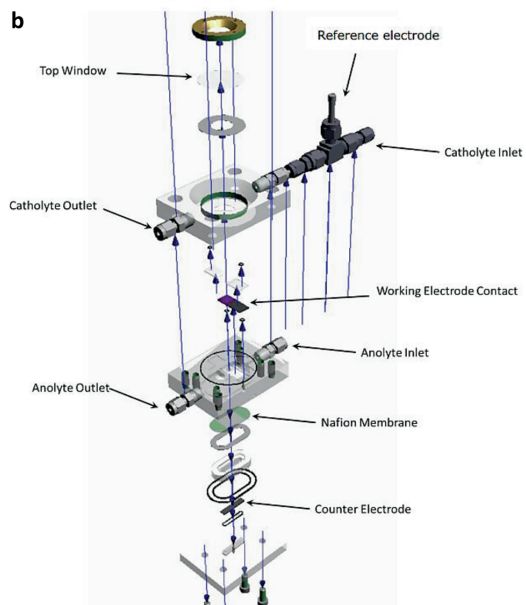
Figure A9. Picture of the *in situ* Raman Spectroscopy cell (a) and schematic illustration of the *in situ* Raman cell configuration (b). The working electrode (WE), counter electrode (CE) and reference electrode (RE) were located at the top, bottom, and side positions of the cell, respectively. The WE was a square glassy carbon plate with a thickness of 2 mm and a width of 10 mm, covered by a catalyst layer. Front illumination mode was employed for all the *in situ* Raman Spectroscopy measurements. Reproduced from An *et al.* (*Angew. Chem. Int. Ed.* **2021**, *60*, 16576–16584).
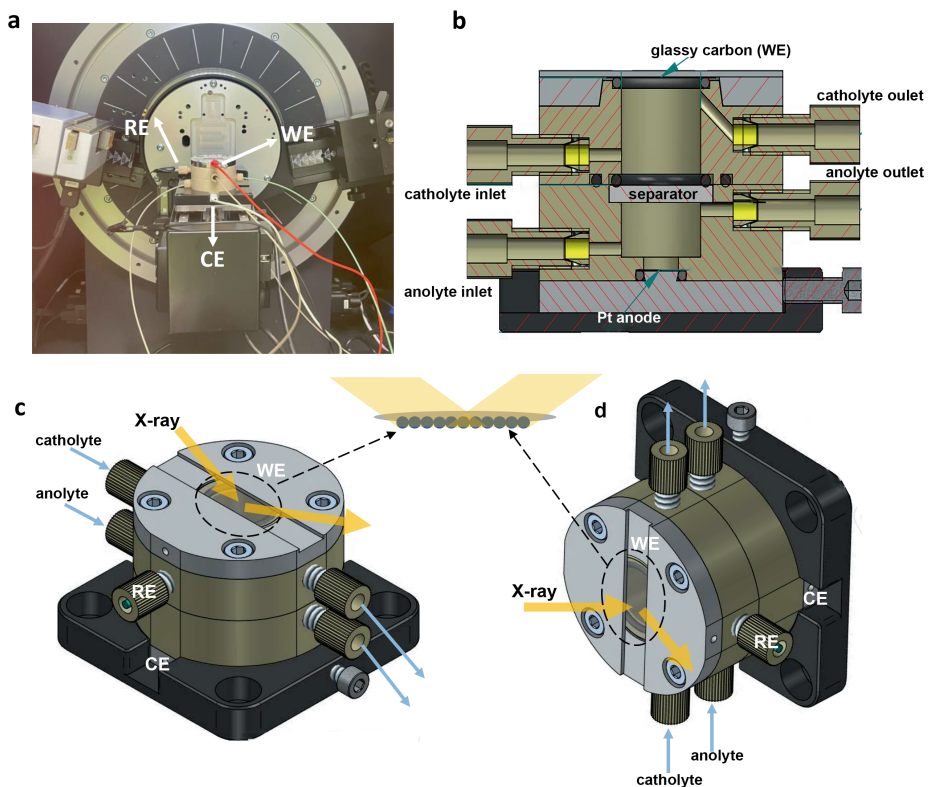
Figure A10. Picture of the *in situ* X−ray Diffraction (XRD) setup (a) and internal schematic of the *in situ* X−ray electrochemical cell (b); External schematic of the *in situ* XRD cell configuration (c) and *in situ* X−ray Absorption Spectroscopy (XAS) cell configuration (d). The Working Electrode (WE), Counter Electrode (CE) and Reference Electrode (RE) were located at the top, bottom, and side position of the cell, respectively. The separator can be an ion−exchange membrane or a quartz filter. The WE was a round glassy carbon wafer with a thickness of 180 µm and a diameter of 20 mm, covered by a catalyst layer. Back illumination mode was employed for all the *in situ* XRD and XAS measurements.

Appendix C. List of Publications & Presentations

This Thesis is based on the following publications:

1. **S. Yang**, H. An, D. Anastasiadou, W. Xu, L. Wu, H. Wang, J. de Ruiter, S. Arnouts, M.C. Figueiredo, S. Bals, T. Altantzis, W. van der Stam, B. M. Weckhuysen, Waste−Derived Copper−Lead Bimetallic Nanoparticles for the Electrocatalytic Reduction of CO_2. *ChemCatChem* **2022**, *14*, e2022007.

2. **S. Yang**, Z. Liu, H. An, S. Arnouts, J. de Ruiter, F. Rollier, S. Bals, T. Altantzis, M. C. Figueiredo, I. A. W. Filot, E. J. M. Hensen, B. M. Weckhuysen, W. van der Stam, Near Unity Electrochemical CO_2 to CO Conversion over Sn−Doped CuO Nanoparticles with Prolonged Stability. *ACS Catal.* **2022**, *12*, 15146−15156.

3. **S. Yang**, H. An, S. Arnouts, H. Wang, X. Yu, J. de Ruiter, S. Bals, T. Altantzis, B. M. Weckhuysen, W. van der Stam. Halide−Guided Active Site Exposure in Bismuth Electrocatalysts for Selective CO_2 Conversion to Formic Acid, *Nat Catal*. **2023**, *6*, 796–806.

Other publications by the author:

4. **S. Yang**, H. Wang, R. Kwaaitaal, H. An, J. de Ruiter, B. M. Weckhuysen, W. van der Stam. Spillover Effect in Copper−Silver Tandem Structures for Electrochemical CO_2 Conversion, in preparation.

5. **S. Yang**, Q. He, C. Wang, H. Jiang, C. Wu, Y. Zhang, T. Zhou, Y. Zhou, L. Song. Confined Bimetallic Phosphide within P, N co−doped Carbon Layers towards Boosted Bifunctional Oxygen Catalysis. *J. Mater. Chem. A* **2018**, *6*, 11281−11287.

6. **S. Yang**, K. Zhang, C. Wang, Y. Zhang, S. Chen, C. Wu, A. Vasileff, S. Z. Qiao, L. Song. Hierarchical 1T−MoS_2 Nanotubular Structures for Enhanced Supercapacitive Performance. *J. Mater. Chem. A* **2017**, *5*, 23704−23711.

7. J. de Ruiter, H. An, L. Wu, Z, Gijsberg, **S. Yang**, T. Hartman, B. M. Weckhuysen, W. van der Stam. Probing the Dynamics of Low−Overpotential CO_2−to−CO Activation on Copper Electrodes with Time−Resolved Raman Spectroscopy, *J. Am. Chem. Soc*. **2022**, 144, *33*, 15047–15058

8. H. An, L. Wu, L. D. B. Mandemaker, **S. Yang**, J. de Ruiter, J. H. J. Wijten, J. Janssens, T. Hartman, W. van der Stam, B. M. Weckhuysen. Sub-second Time-resolved Surface Enhanced Raman Spectroscopy Reveals Dynamic CO Intermediates during Electrochemical CO_2 Reduction on Copper, *Angew. Chem. Int. Ed*. **2021**, *60*, 16576– 16584.

9. K. Zhang, Y. Lin, Z. Muhammad, C. Wu, **S. Yang**, Q. He, X. Zheng, S. Chen, B. Ge, L. Song. Active {010} facet−exposed Cu_2MoS_4 Nanotube as High−Efficiency Photocatalyst. *Nano Research*

2017, *10*, 3817−3825.

10.   K. Zhang, Y. Lin, C. Wang, **S. Yang**, Chen, S. Yang, W. Xu, H. Chen, Q. Fang, G. Zhang, G. Li, L. Song, Facile Synthesis of Hierarchical Cu_2MoS_4 Hollow Sphere/Reduced Graphene Oxide Composites with Enhanced Photocatalytic Performance. *J. Phys. Chem. C* **2016**, *120*, 13120−13125.

11.   X. Lv, J. Wu, **S. Yang,** D. Xiao, J. Zhu. Identification of Phase Boundaries and Electrical Properties in Ternary Potassium−Sodium Niobate−Based Ceramics. *ACS Appl. Mat. Interfaces* **2016**, *8*, 18943−18953.

Oral presentations

1.   **S. Yang**, H. An, H. Wang, X. Yu, W. van der Stam, B. M. Weckhuysen, Elucidating the Facet−Guided Activation of Bi−based Electrocatalysts for Selective CO_2 to Formic Acid Conversion. *NCCC*, **2023**, Noordwijkerhout, The Netherlands

2.   **S. Yang**, H. An, W. van der Stam, B. M. Weckhuysen, Near Unity Electrochemical CO_2 to CO Conversion over Sn−doped CuO Nanoparticles with Prolonged Stability. *CHAINS*, **2021**, online

3.   **S. Yang**, H. An, W. van der Stam, B. M. Weckhuysen, Near unity electrochemical CO_2 to CO conversion over Sn−doped CuO nanoparticles with prolonged stability. *NanoGe Fall Meeting*, **2021**, online

Poster presentations

1.   **S. Yang**, H. An, W. van der Stam, B. M. Weckhuysen, Facet−Guided Activation of Bi−based Electrocatalysts in CO_2 Conversion, *CHAINS*, **2022**, Veldhoven, The Netherlands.

2.   **S. Yang**, H. An, W. van der Stam, B. M. Weckhuysen, Near Unity Electrochemical CO_2 to CO Conversion over Sn−Doped CuO Nanoparticles with Prolonged Stability. *International Conference on Frontiers in Electrocatalytic Transformations*, **2021**, Valencia, Spain.

3.   **S. Yang**, H. An, W. van der Stam, B. M. Weckhuysen, Waste-Derived Cu/Pb Nanoparticles for Effectively Selective Formation of C_1 Products in CO_2 Electroreduction. *International Conference on Electrocatalysis for Energy Applications and Sustainable Chemicals,* **2020**, online.

4.   **S. Yang**, H. An, J. H. J. Wijten, W. van der Stam, B. M. Weckhuysen, Electrochemical Conversion of CO_2 to C_2H_4 and CO in Industrial Waste−Derived Bimetallic Cu/Pb Nano−catalysts, *Structure−function Relationships in CO_2 Electrocatalysis*, **2020**, online.

Acknowledgements

Four years ago, I had a recurring dream that lasted for weeks before I started pursuing a doctoral degree in the Netherlands. Though I had never been to Utrecht, I saw the city's streets and dazzling shops in my dream. I recall it was a snowy Christmas Eve. The accumulated snow reached my knees as I trudged alone in the dark snowy street. The warm yellow lights cast a gentle glow onto the snow outside and me. This dream has always remained with me, for it seemed to have turned into a reality since I arrived in the Netherlands. The COVID−19 pandemic began in early 2020 and had raged for two and half years, and it was like the snowstorm in my dream. Due to quarantine, people were separated, which for most people was the first time in their life. Everyone struggled to walk through the snow. The passion for science was like a force that helped us persist in moving forward in the snow. We believed we could reach our warm home as long as we kept going.

Bert is like the warm light emitted from the shop all along my journey. Without your guidance, it is difficult for me to see the road ahead in the darkness, and I may not even be able to reach my destination. I am grateful to you for giving me a chance to come to the Netherlands to do a PhD. In China, there is an old saying: "The master points the way; The practice and training are over to you." As the master in scientific research, you have pointed me in a good direction, electrocatalysis. You have given me enough freedom to explore this field and enough trust and support, allowing me to focus on science wholeheartedly for these four years. I sincerely appreciate the top−notch scientific research resources you provided me, including well−equipped labs, high−knowledge platforms, free and equal academic interactions, and open cooperation opportunities. Your long−term vision and hard work profoundly influenced me, and your decisive style cured my procrastination. You are a leader and a promotor in scientific research and an inspirer of my professional life.

My great gratitude also belongs to my daily supervisor **Ward**. As I always said, I probably would have quit my PhD without you. I still remember the first time I asked you for help when you were not my daily supervisor, and we had not met before. Your friendly, dedicated, and proactive attitude and professional advice made me feel your enthusiasm for scientific research. I felt a sense of belonging to this research group for the first time. Being encouraged by this collaboration, I decided to join your electro−buzz team. I was incredibly fortunate to have had you, a kind, generous, and compassionate supervisor, by my side. You have always gone above and beyond to support me, both academically and personally. I have learned so much from you, not just in terms of scientific skills and knowledge but also in integrity, humility, and passion for research. Your unwavering belief in my potential has given me the confidence to pursue my goals and overcome challenges. You have been being the source of creativity and passions for me, offering me other perspectives and teaching me how to do research systematically and effectively step by step. I cannot express how grateful I am for your guidance and mentorship, which have significantly impacted my academic and personal growth. Thank you for being my daily supervisor, believing in me, and making this journey more meaningful and rewarding. I will always cherish the memories and lessons learned under your supervision.

Joyce, **Jim**, and **Matt**, your warm smiles and optimism are like a little sun that brightens everyone's day. Thank you for always warming people's hearts. And to **Marisol, Fabiane, Sirada, Katarina**, I am grateful for your kindness and help at the start of my PhD. It was your support that helped me overcome the challenges that I faced when I first joined the group.

In closing, I want to express my gratitude to my parents, younger brother, and **Yanqi** for their support as my backbone throughout my journey. Thank you for always being there for me.

About the Author

Shuang Yang obtained her Bachelor degree in Advanced Energy Materials and Devices from Sichuan University (China). During her Bachelor Thesis, she studied the synthesis and performance of $1T-MoS_2$ nanosheets for Li−ion batteries. Apart from the project Bachelor Thesis, she also joined other research projects, including metal hydrides for hydrogen storage and the synthesis of lead−free piezoelectric ceramics. Subsequently, she moved to the National Synchrotron Radiation Laboratory (NSRL), University of Science and Technology of China (China), for her Master study. She obtained her Master degree in July 2019 in Materials Science and Engineering, focusing on electrochemistry in supercapacitors and water splitting. Her Master Thesis was entitled "Synthesis and Performance of Layered Materials in Electrochemical Applications." Afterward, she started her PhD research in August of the same year and moved to the Netherlands, where she worked under the supervision of prof. dr. ir. Bert M. Weckhuysen and dr. Ward van der Stam, at the Inorganic Chemistry and Catalysis (ICC) group of Utrecht University. The content of her research work has been described in this PhD Thesis.